The Pennsylvania State University

The Graduate School

The Eberly College of Science

INVESTIGATION OF CHARGE-CARRIER DYNAMICS IN ORGANO-HALIDE PEROVSKITE AND COLLOIDAL QUANTUM DOT SEMICONDUCTORS

A Dissertation in

Chemistry

by

Robert J. Stewart

Submitted in Partial Fulfillment
of the Requirements
for the Degree of

Doctor of Philosophy

August 2016

The dissertation of Robert J. Stewart was reviewed and approved* by the following:

John B. Asbury
Associate Professor of Chemistry
Dissertation Advisor
Chair of Committee

Mark Maroncelli
Distinguished Professor of Chemistry

Raymond E. Schaak
DuPont Professor of Materials Chemistry

Chris Giebink
Assistant Professor of Electrical Engineering

Kenneth S. Feldman
Professor of Chemistry
Graduate Program Chair

*Signatures are on file in the Graduate School.

ABSTRCT

Crystallite surfaces often dominate the optical and electronic properties of nanocrystalline semiconductors because the fraction of atoms at the surface experience different crystal field environments than bulk atoms, and as a consequence, surfaces influence the energetic landscape of the entire crystallite. Contributing electronic states that are either isoenergetic or below the semiconductor band edges, surface states mediate charge conduction and recombination - two critical processes in optoelectronic device performance. Utilizing a combination of inorganic synthesis, surface characterization, and time-resolved optical spectroscopy, the research presented herein begins to identify the link between charge carrier dynamics and the underlying surface chemistry in two emerging, yet promising, nanocrystal semiconductor systems: organo-halide perovskites and colloidal quantum dots (CQD).

Notably, my research provided one of the first reports that charge recombination centers in lead halide perovskite films are localized almost exclusively on the surface of crystallites. Passivation of these nanocrystal surfaces with small molecules that contain strongly coordinating functional groups caused charge-carrier lifetimes in perovskite thin-films to approach the bulk radiative limit reported for single crystal analogues. Likewise, my research contributed to an understanding that surfaces in lead sulfide (PbS) CQDs produce electronic energy levels that are sufficiently delocalized to provide charge conduction pathways in CQD thin-film arrays. Given the strong coupling to the QD surface, charge carrier diffusion lengths were shown to be highly sensitive to the character of surface-bound ligands. My PhD research highlights the importance of understanding the interplay between surface chemistry and nanocrystal semiconductor photophysics as well

as the importance of selecting surface treatment strategies capable of passivating diverse surfaces to eliminate energetic inhomogeneity while simultaneously allowing strong electronic coupling across interfaces.

TABLE OF CONTENTS

LIST OF FIGURES

LIST OF TABLES

LIST OF ABBREVIATIONS

OA Oleic acid

EDT Ethanedithiol

MPA 3-mercaptopropionic acid

TRIR Microsecond Transient Infrared Spectroscopy

PL Photoluminescence spectroscopy

CQD Colloidal quantum dot

TRPL Time-resolved photoluminescence spectroscopy

ITO indium tin oxide

P3HT poly(3-hexylthiophene)

FTIR Fourier transform infrared

FWHM full width at half maximum

MCT mercury cadmium telluride

OD optical density

MIR mid-infrared

NIR near-infrared

UV ultraviolet

PV photovoltaic

MLCT metal-to-lignad charge-transfer

LMCT ligand-to-metal charge-transfer

M molar (moles/liter)

YAG yttrium aluminum garnet

ACKNOWLEDGMENTS

I wish to express the most sincere gratitude and appreciation to every individual who has helped me get to this current point in my life – I can truly say that life would have no meaning without *you*. The past decade spent in higher education has, without a doubt, been the most challenging period in my life, and I am greatly indebted to a number of advisors, mentors, collaborators, acquaintances, friends, and family members who have helped me succeeded. In advance, I offer my deepest apologies to anyone that I have mistakenly omitted.

I would like to begin by thanking my Ph.D. adviser, Dr. John Asbury, whose knowledge, creativity, motivation, and passion have inspired me to challenge myself in science and in all future endeavors I will undertake. I would like to thank him for providing financial support for my research as well as for all his advice which has strongly influenced my professional development, technical and scientific capabilities, writing and presenting style, and numerous intangibles I have become accustomed to over the last five years. I thank John for allowing me to design and carry out my own independent research projects and for providing an environment where I felt comfortable taking projects in their directions, thinking outside the box, and occasionally disagreeing with him on matters of science. He also kept me grounded and focused in seeing projects through to completion. Furthermore, I would like to thank the members of my graduate committee: Professors Giebink, Maroncelli, and Schaak for their support, encouragement, and feedback which greatly facilitated my professional and intellectual development.

I would like to thank all of my collaborators who were kind enough to answer all my questions, bring me up to speed on project initiatives, and keep me inspired to this day.

A special thank you is offered to Professors: Giebink, Gomez, and Jackson for creating a supportive yet informal collaborative environment where I could openly discuss research ideas, and for opening my eyes to the vast landscape of optoelectronic materials research. Your guidance has truly inspired me to always seek different ways of approaching problems.

I wish to thank all my colleagues in the Asbury lab: Chris Greico, Eric Kennehan, Grayson Doucette, Alec Larsen, Chris Averill, Ryan Pensack, Kwang Jeong, Jihye Kim, Mike Kellogg, Julian Paige, Kimberly Lundberg, and the rest of the Asbury lab crew. Additionally, I would like to thank Derek Keefer, Jesse Bischof, Steve Aro, Tom Fitzgibbons, Todd Day, Subhasis "Sub" Chaudhuri, Justin Sparks, Haoyu Li, Alyssa Brigeman, Rijul Dhanker, Jared Price, Brooke Kuei, and Thinh Le for your friendship, research support, and for providing amusement through grad school. I would also like to extend a heartfelt thank you to the Penn State MRI staff whose knowledge and support provided strength to my research: Greg Barber, Vince Bojan, Josh Stapleton, Trevor Clark, Josh Maier, Dan Veghte, and Bangzhi Liu.

I would like to thank my family for supporting me through the entirety of educational career. Thank you to my mom and dad, Sharon and Bob, who made a lifetime of sacrifices which allowed me to pursue my academic and intellectual passions, and who taught me to always offer my best to others. Thank you to my mother- and father-in-law, Christine and Brian Alsford, who showed me unconditional love and support and what it means to be truly passionate about career achievements.

Last but certainly not least, I give my thanks, praise, and love to my best friend and wife, Catherine, for her continued love and support. She has always been there for me even while pursuing her own doctoral degree. I know it has been a long-time coming, but I'm excited about our future together, and all the adventures we will have now that we are finished with school. The words "thank you" do not begin to express the gratitude and appreciation I owe you for putting up with me and my rigorous work schedule over the last decade.

CHAPTER 1

Motivation and Background

1.1 The Future of Solar Energy Conversion and Promise of Solution-Processed Semiconductors

Humans use approximately 4.6 x 10^{20} joules of energy in one year[3] which corresponds to a consumption rate of 1.5 x 10^{13} J/s or 15 TW of power. By the year 2035 this consumption rate is expected to reach 26 TW[4] The only single energy resource (renewable or nonrenewable) that can provide us with enough power to match the expected consumption rate in future decades is the sun.

To demonstrate the scale of energy delivered by the sun we draw a few parallels: in one second, the sun provides more energy than is released by a 7.8 magnitude earthquake (~10^7 joules),[3] and in one hour, the sun irradiates Earth with enough power to meet the total global demand for a full year (15 TW).[5] To highlight the promise of harnessing solar energy for utility electric power, Michael Grätzel so eloquently says: "covering 0.1% of the Earth's surface with solar cells capable of converting only 10% of the sun's energy to electricity would satisfy our present needs."[6] Given the immense energy that strikes the Earth's surface from the sun, it's not surprising that approximately 30% of new electricity generated worldwide between 2016 and 2030 is expected to be delivered by solar cells,[7] nor is it surprising that the solar electricity industry already represents a $10 billion/year market and is growing at a rate of 30% per year.[8]

Moving towards a society which obtains the majority of its energy from renewable, carbon-neutral, sources such photovoltaic and photochemical devices[8] is absolutely necessary; especially when considering: a) the finite supply of nonrenewable recourses (coal and oil), which currently supplies more than 80% of the global energy,[9-10] and b) the exponentially increasing levels of CO_2, and other harmful pollutants released into the atmosphere upon burning fossil fuels; the effects of which could have unprecedented, catastrophic, and irreversible environmental impacts.[11-13] However, the adaptation of solar energy conversion methods in a *cost-effective* and *cost-competitive* manner is complicated. In order for PV devices to be economical for individual consumers and cost-competitive to fossil fuels and natural gas, significant reductions in the costs of photovoltaic (PV) module manufacturing, installation, and ancillary equipment are absolutely necessary and must be accompanied by an increase in the solar-to-electric conversion efficiency.

To accurately compare the cost of electricity obtained from photovoltaic systems with traditional sources such as fossil fuels and natural gas, we invoke a metric called Levelized Cost of Electricity (LCOE). LCOE is calculated as the ratio of the sum of costs for the expected unit's lifetime to the sum of the electrical energy generated over the unit's lifetime – the ratio has units of $/KW-hr.[14] A quick comparison of LCOE for solar cell modules versus fossil fuel-based sources shows that cost of manufacturing and maintenance of solar cell modules must decrease while solar power conversion efficiency increases in order for solar energy to be cost-competitive with fossil-fuel energy. The estimated LCOE for terrestrial, solar energy conversion is between $0.11 per KW-hr to $0.16 per kWh for utility-scale systems and between $0.19 per KW-hr to $0.29 per KW-hr for residential systems. In contrast, the average LCOE for coal sources is $0.096 per KW-hr and natural gas is $0.066 per KW-hr,[15-16] which is less costly than solar energy by roughly a factor of five!

Researchers in the field of solar energy conversion realize this uphill battle against the relatively low price of fossil fuel energy, and are appropriately working towards the next-generation of photovoltaic materials and other creative, low cost solutions for solar-energy conversion. The photovoltaic field can be divided roughly into three generations of materials according to module cost per area and corresponding solar-to-electric power conversion efficiency – an idea which has been popularized by Lewis,[8, 10] and Green.[17] Figure 1.1A shows a correlation of PV efficiency versus price per area for three generations of solar cells.

The first generation (G1) represents the most mature PV technology – cells made from thick crystalline silicon wafers (~20μm) which demonstrate about 15-20 % efficiency. This technology is costly to manufacture because it requires high temperature processing and nearly complete removal of crystalline defects in order to give high PCEs; additionally, a large quantity of this high purity silicon is required to provide a long absorption path length due to the indirect band gap and weak absorption of Si. However, this first generation technology represents ~90% of the cells in production today.[16]

The second generation (G2) of solar cells is based on thin-film technologies such as copper-indium-gallium-selenide (CIGS) and CdTe, where typical power conversion efficiencies are between 10 - 15%. Semiconductors used in thin-film, G2, solar cells have absorption coefficients two to three orders of magnitude greater than crystalline Si, and as a consequence do not require such long optical path lengths as G1 cells. Thin-film G2 PVs have lower material consumption that G1 cells which decreases the cost per area relative to the Si-wafer G1 cells. However, the fabrication of G2 solar cells is still costly because they often require high temperatures and vacuum processing techniques. As such, these thin-film cells constitute about 10% of the solar cell devices manufactured today.[18]

Third generation (G3) solar cells represent emerging materials that are primarily at the laboratory-scale, research and development stage. As shown in Figure 1.1A, these emerging solar cells are expected to have low production, installation, and maintenance costs, while simultaneously exhibiting power conversion efficiencies > 15-20%. Some of the materials that can be categorized as G3 cells are organic small molecule and polymer PVs,[19-20] solar concentrator PVs,[21] and high performance multi-junction solar cells – although the later are often as costly as $10,000 - $100,000 per square meter. The work in this dissertation focuses on two classes of semiconductors for third generation photovoltaics: organohalide perovskites and colloidal quantum dots. We believe these two materials represent the next generation of low-cost, high performance solar cells because thin-films are fully processable from solution at low temperatures.[22-25] As shown in Figure 1.1B, deposition of solution-processed electronics can invoke similar processing to printing newspapers. A continuous, flexible substrate (about as thin as a sheet of paper) moves at a constant rate through machinery precursor solutions of absorbers or other complementary electronic layers are deposited by painting or blade coating where in one stage and dried in another stage. Fabricating photovoltaic devices in this roll-to-roll printing fashion opens the possibility of using a continuous, light-weight, flexible substrates thereby eliminating factory handing costs associated with moving heavy substrates from one processing stage to another, but more importantly eliminates the high costs associated with ridged mounts used to stabilize heavy PV modules. Furthermore, by controlling the chemical composition, and casting-conditions one can tune the absorption and charge conduction properties of both organohalide perovskites and colloidal quantum dots across the solar spectrum allowing for efficient harvesting of the sun’s energy from UV to near-IR wavelengths.

Organohalide perovskites warrant particular research investment because cells fabricated from these semiconductors are the first solution-processed PVs to achieve 20% power conversion efficiency.[26] As such, we dedicate chapters 3 and 4 of this dissertation to our research into the fundamental, physical understanding of charge-carriers dynamics following photoexcitation in organo-halide perovskites. The conclusions of our research will enable and guide design rules for future material by way of stabilizing nanocrystal surfaces and grain boundaries, which have been found to facilitate electron-hole recombination and are susceptible to attack from atmospheric water and oxygen. Our research found one of many possible routes to protect or passivate crystallite surface in order to enhance charge-carrier lifetimes as well as protect the material from atmospheric degradation. The physical principles that underlie photovoltaic operation will be presented in the following section.

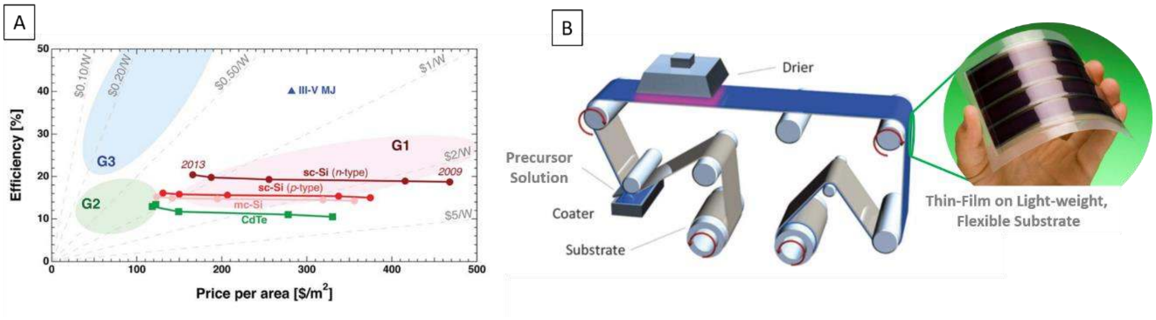

Figure 1.1: A) Correlation of power conversion efficiency with price per area for three generations of photovoltaics. Organohalide perovskites and colloidal quantum dot solar cells beginning to bridge the gap between G2 and G3 devices. B) Schematic for roll-to-roll printing of thin-film, solution-processed photovoltaic devices in a similar fashion to newspaper printing where an “ink” is deposited on a continuous, flexible substrate moving through the “printer” at a constant rate. Figures are adapted from references: 16 and 27.

1.2 Semiconductor and Photovoltaic Device Physics

1.2.1 The Solar Spectrum and Photovoltaic Effect

The sun has a spectrum that can be approximated as a blackbody emitter with a temperature of 5,800 K, as shown in Figure 1.2A. Comparison of the spectra measured above Earth's atmosphere (yellow) with the spectrum measured at sea level (red) reveals the effect of Earth's atmosphere on attenuating the power that reaches Earth's surface. Atmospheric chemicals such as O_3, N_2, and O_2 have strong absorption bands in the UV, whereas molecules like water and CO_2 absorb strongly in the infrared spectral regime. Other conditions such as latitude, cloud coverage, and direct or diffuse light can influence the solar spectrum and optical power at sea level. However, for laboratory testing of terrestrial solar cells, scientists and engineers have agreed to use a standardized solar spectrum. The most commonly used spectrum is called AM (air mass) 1.5 which corresponds to sun light passing through Earth's atmosphere 1.5 times thicker than the thickness of the atmosphere normal to Earth's surface at the equator. The AM 1.5 spectrum is used because it simulates sunlight at an angle 41.8^o above the horizon, which accurately represents the overall yearly average of sea-level sunlight at mid-latitudes, and it conveniently integrates to a power density of 1 KW/m^2 across all wavelengths shown in Figure 1.2A.[28-29]

Materials that generate a voltage or current upon exposure to light exhibit the photovoltaic effect. As such, photovoltaic devices revolve around the ability of a semiconductor (or absorbing dye) to absorb light from the sun and efficiently convert the resultant photogenerated electron-hole pair into current that gets passed through an external circuit with sufficiently high power (power = I×V) to perform work. A schematic of a photovoltaic device diagram is shown in Figure 1.2B consisting of a semiconductor grown or deposited between two electrodes. In this case, the cathode is a semi-transparent electrode (typically a conductive oxide such as indium tin oxide [ITO]) and the back anode is typically a thick, reflective metal such as gold. Light passes through the transparent cathode and is absorbed by the semiconductor to generate an excited state electron-hole pair. Some mechanism of "photovoltaic action" is present which provides rectification and causes the electron and hole to overcome their Columbic attraction and be collected at separate electrodes: the cathode and anode, respectively. Mechanisms of photovoltaic action can be a p-n junction, a built-in electric field (as shown in Figure 1.2B), or even a solid-liquid junction. More details will be presented in section 1.2.2, below.

If the absorber layer consists of conductive polymers or small molecules, molecular orbital terminology is employed, and it is said that excited state electrons reside within and are transported through the lowest-unoccupied molecular orbital (LUMO) whereas holes are transported through the highest-occupied molecular orbital (HOMO). However, in the context of this dissertation, we will be discussing solid-state semiconductors which have defined conduction (CB) and valance (VB) bands separated by a band gap (E_g), as shown in Figure 1.2B.

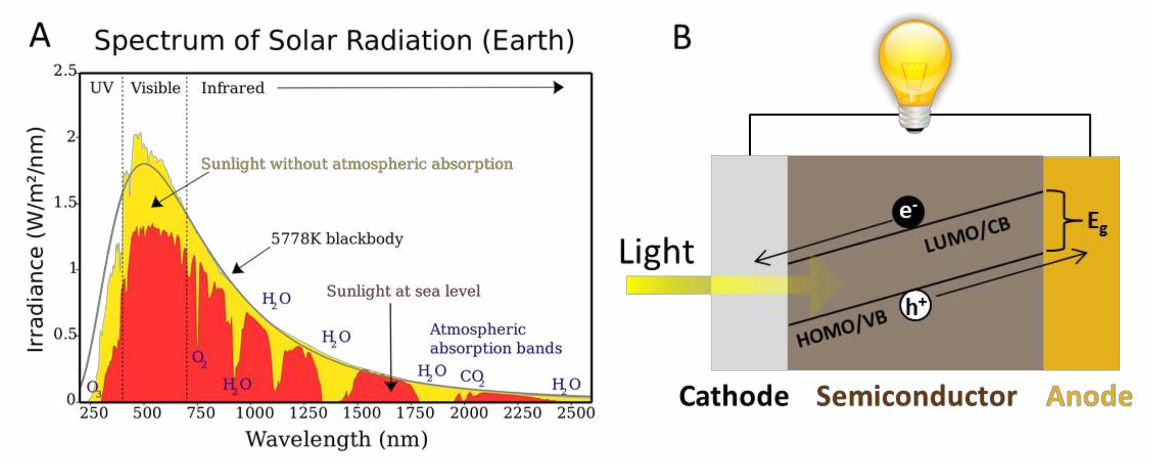

Figure 1.2: A) Solar spectra above Earth's atmosphere (yellow) and at sea level (red) which spans the UV-Visible-Infrared wavelength regimes. B) Shows a simplified photovoltaic device where a semiconductor with defined conduction (CB) and valance (VB) bands responsible for transporting electrons and holes to respective electrodes following optical absorption. In this geometry, light and pass through the semitransparent cathode without significant attenuation before being absorbed by the semiconductor.

1.2.2 Energy Levels in Semiconductors

The HOMO-LUMO or VB-CB energetic splitting can be controlled by tuning the chemistry, composition, and/or casting conditions of the semiconductor used as the primary absorber in Figure 1.2B. Significant research effort has gone into selecting the correct conditions to yield semiconductors and dyes that have correct band-gaps and absorption profiles in order to match the solar spectrum (Figure 1.2A) and efficiently capture solar energy. In addition to determining the photon wavelengths absorbed, the semiconductor electronic structure sets the maximum energy (voltage) that can be extracted from photogenerated carriers because electrons and holes very quickly relax to the lowest energy states before undergoing charge transfer processes across semiconductor junctions (to cathode and anode electrodes, for instance). There is a critical tradeoff between effectively absorbing the solar spectrum and generating charge carries with sufficient voltage to drive external devices. In the case of a large band-gap material, the extracted photocurrent will have a large voltage but, the semiconductor will only absorb high energy photons (UV and short wavelength visible) and will not effectively use a majority of photons in the long wavelength visible and infrared regions. In contrast, engineering a material with a small band-gap will allow for complete absorption of the entire solar spectrum, but the cost of doing so will result in a small voltage drop across the device in Figure 1.2B – preventing such a solar cell from doing any useful work when connected to an external circuit. From this brief introduction, one can see that tuning the chemistry and composition of the primary absorber in a solar cell is of the utmost importance for both the absorption and electronic properties of a solar cell. Therefore, a discussion of the origin of the band-gap in semiconductors is warranted.

Figure 1.3 shows the evolution of atomic orbitals into continuous electronic bands by considering the interaction of sequentially more atoms, beginning with one containing atomic orbitals (s, p, d, f, etc.) and bringing it in close contact with many other atoms as in a semiconducting solid. All atomic nuclei are represented as blue dots in Figure 1.3. According to Valance Bond Theory, the atomic valance and bonding arrangements of atoms in molecules can be rationalized by considering the overlap or “hybridization” of two or more atomic orbitals, as shown by the sp^3 hybrid orbital in Figure 1.3, which consists of 33% “s” atomic orbital and 66% “p” atomic orbital. Furthermore, chemical Lewis structures and molecular geometries can be rationalized by considering the three-dimensional overlap of two or more hybrid orbitals. Bringing two sp^3 hybridized atoms together, and solving the Schrödinger equation while satisfying quantum mechanical stipulations, it is found that the resultant wave functions are linear combinations of the hybrid atomic orbitals. The even or symmetric addition of the two hybrid orbitals produces a molecular orbital (MO) where significant electron density exists between the two nuclei, producing a bonding (σ) MO that is lower in energy than the constituent sp^3 orbitals. The odd or antisymmetric addition of two hybrid orbitals produces an MO that is higher in energy than the constituent hybrid orbitals and contains a node (area with no electron density) between the two nuclei. As such, this MO is called antibonding (σ^*) because occupation of this orbital does not result in the stabilization of electrons through bonding. In this case of small molecules where few (< 100) atoms interact, populating molecular orbitals with electrons from low energy to increasingly higher energy – following the Pauli and Aufbau Principles – it is typical that the σ bonding MO is the highest-energy orbital filled with electrons (HOMO) and the following higher-energy MO is the lowest level to be unoccupied by electrons (LUMO).

From the simple discussion above, it can be seen that electronic states in isolated, non-interaction atoms can have identical energies and wave functions, but as two or more atoms are brought together, electron wave functions overlap to form new functions characterized by an energetic split between the symmetric and anti-symmetric linear combinations as well as delocalization of electrons over all atoms making up the new MOs. Bringing increasingly more atoms together until a small cluster ($10 - 10^3$ atoms, for instance) is formed, discrete energy levels are produced, where the highest energy orbital in the σ (symmetric addition) band is the HOMO level and the lowest energy orbital in the σ* (anti-symmetric addition) band produces the LUMO level. Such an electronic scheme gives the characteristic electronic structure of semiconducting quantum dots. By extending this argument to larger crystallites (> 10^5 atoms) we reach a bulk crystal where the HOMO level becomes the valance band edge and the LUMO levels becomes the conduction band edge with a band gap (E_g) separating the two bands. Therefore, a semiconductor at zero kelvin, in the absence of doping and photoexcitation, will have a valance band completely occupied with electrons and the conduction band will be completely unoccupied.

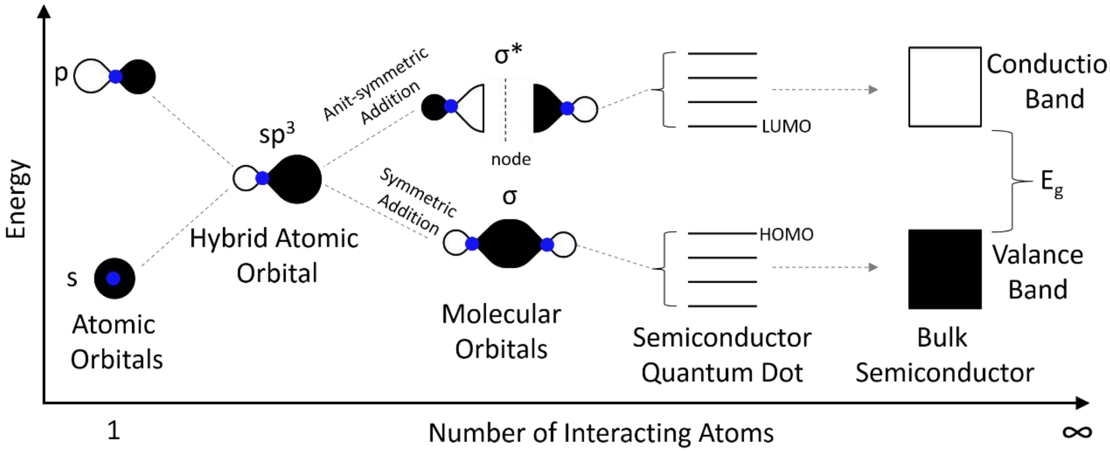

Figure 1.3: Orbital energy level diagram showing the evolution of electron wave functions in systems with one atom giving rise to atomic orbitals, two atoms forming σ and σ* Molecular Orbitals, many atoms (< 10^3 atoms) forming discreet energy levels following orbital overlap, and finally reaching the limit of a bulk crystal where continuous levels (valance and conduction bands) are formed and a band gap energy separates the two bands. It is this band gap that dictates the optical absorption onset and maximum voltage obtainable from solar cells. Figure was adapted from reference 30.

1.2.3 Photogenerated Carriers in Semiconductors

In a photovoltaic device, such as the one shown in Figure 1.2B, there are four processes that need to occur in order to convert solar energy into electric energy:[28] 1) an absorption event which promotes the semiconductor from a ground state to an excited state; 2) overcoming the exciton (neutral quasi-particle consisting of Coulombically bound electron/hole pair) binding energy to form an individual electron and hole; 3) directional charge transport that discriminates the transport direction of an electron and a hole; and 4) extraction of photogenerated charge carrier by appropriate electrodes and passage through an external circuit to power some electrical load. Some semiconductors such as silicon and organo-halide perovskites have such low exciton binding energies (lower than thermal energy, k_BT, at room temperature)[29, 31] that the primary absorption event is said to result in "free" electrons and holes. The low exciton binding energy is a strong advantage for these systems over excitonic materials such as organic polymer-based semiconductor. The details of light absorption will be addressed in Chapter 2, and the details of charge extraction at metal/semiconductor junctions and transport through external circuits is beyond the scope of this dissertation. My dissertation work sought to use optical spectroscopy and supporting materials processing and characterization to understand the fundamental processes taking place during electron and hole transport in semiconductors. By identifying and understanding the competing processes to charge transport, such as charge trapping and recombination, we provided strategies to eliminate and overcome these deleterious loss mechanisms which do not lead directly to enhancing the efficiency of solar-to-electric energy conversion.

The charge-carrier lifetime (τ), or inversely, the charge-carrier recombination rate (r_n) limits the time window for which charges are able to be extracted from a semiconducting layer before they undergo a recombination process to regenerate the ground state. Three primary recombination mechanisms exist in direct band gap semiconductors following photoexcitation: a) unimolecular, trap-mediated recombination, b) bimolecular, band-to-band recombination, and c) higher-order Auger recombination – all three mechanisms are detailed in Figure 1.4. In Figure 1.4, the band energies are plotted as a function of the wave vector (k), a parameter which requires a brief introduction. Solving the Schrödinger equation for an approximate system where an electron is placed in a periodically repeating crystal lattice, the electron or hole wave function takes the form of a Bloch function which propagates in direction, x, with a constant, k, according to the wave function:

$$\psi_k(x) = U(k_x, x)e^{jk_x x} \qquad \boxed{1.1}$$

where $U(k_x,x)$ describes the periodicity of the semiconductor crystal lattice.[32] The energy of such a system is given by:

$$E = \frac{1}{2}mv^2 = \frac{1}{2}\frac{p^2}{m} = \frac{\hbar^2}{2m}\mathbf{k}^2 \qquad \boxed{1.2}$$

where m is the effective mass of the electron, v is the velocity of the electron, p is momentum, ħ is Planck’s constant divided by 2π. Equation 1.2 shows that the wave vector is proportional to particle momentum and energy is proportional to the wave vector squared, which gives rise to the parabolic shape to the bands appearing in Figure 1.4.[33] It should be noted that Bloch functions and the periodically repeating crystal lattices extend in three dimensions; therefore, complete band diagrams are shown in three dimensional “reciprocal space” in order to visualize the full relationship between E and k. However, Figure 1.4 is only meant to show the band diagram near the conduction band minimum (CBM) and valance band maximum (VMB) for direct band gap semiconductors where the CBM and VBM occur at the same k value.

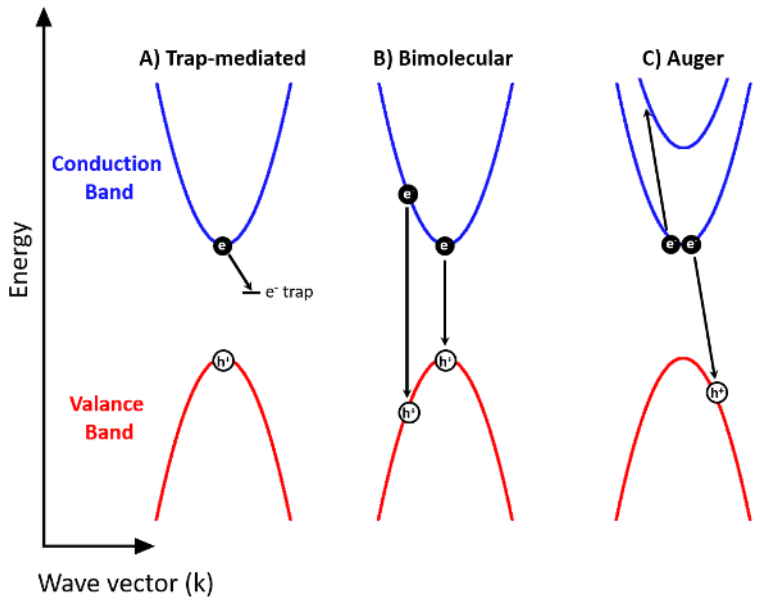

Figure 1.4: Band diagrams for a direct band gap semiconductor were the CBM and VBM are at identical wave vectors. A) Shows the process of unimolecular, trap-mediated recombination. Recombination through traps is rarely radiative because trapping often changes the momentum of the electron when it is transferred to some localized defect. B) Shows biomolecular, band-to-band recombination can occur at the CBM and VBM or at higher energy. Band-to-band recombination is often radiative because no change in momentum occurs. Band-to-band recombination, such as that shown in Fig 1.4B gives rise to photoluminescence in organo-halide perovskite semiconductors. C) Auger recombination is a higher order process involving three or more particle. The energy from one electron-hole pair recombination event is transferred to exciting another electron to a higher excited state, and as a result, Auger recombination is never radiative. Note that energy and momentum are conserved. Figure is adapted from reference 34.

As stated above, the charge-carrier lifetime, or charge recombination rate, limits the time window following photoexcitation for which free electrons and holes can be harvested at their respective electrodes. The rate of decay for all carriers, n, can be expressed as the sum of the rates for each process shown in Figure 1.4 as the differential (eq 1.3) or integrated (eq 1.4) rate equations:[31, 35]

$$\frac{\mathrm{dn}}{\mathrm{dt}} = -\mathrm{k}_{\mathrm{Auger}}(\mathrm{n}^3) - \mathrm{k}_{\mathrm{Bimol}}(\mathrm{n}^2) - \mathrm{k}_{\mathrm{Trap}}(\mathrm{n}) \qquad \boxed{1.3}$$

$$\mathrm{r}(\mathrm{n}) = \mathrm{k}_{\mathrm{Auger}}(\mathrm{n}^2) + \mathrm{k}_{\mathrm{Bimol}}(\mathrm{n}^2) + \mathrm{k}_{\mathrm{Trap}} \qquad \boxed{1.4}$$

In equations 1.3 and 1.4, n is the charge density, t is time, and k_{Auger}, k_{Bimol}, and k_{Trap} are the rate constants for: Auger recombination (Fig 1.4C), nongeminate, band-to-band recombination (Fig 1.4B), and trap-mediated recombination (Fig 1.4A), respectively. The charge carrier recombination rate is inversely related to the charge carrier diffusion length (L_D) according to:

$$\mathrm{L}_{\mathrm{D}} = \sqrt{\frac{\mu \mathrm{k}_{\mathrm{B}}\mathrm{T}}{\mathrm{r}(\mathrm{n})\mathrm{q}}} \qquad \boxed{1.5}$$

where μ us the charge carrier mobility (expressed in units of $cm^2V^{-1}s^{-1}$), k_B is Boltzmann's constant, T is temperature, q is the elementary charge, and r(n) is given by equation 1.4.[24, 31, 36-37]

When employing solution-processed semiconductors such as organo-halide perovskites or colloidal quantum dots for photovoltaic applications, trap states can be a result of defects or imperfections in the crystalline habit, bonding geometry, or incomplete "dangling" bonding at crystallite surfaces. Because these materials are deposited or synthesized in solutions where chemistry cannot be as precisely controlled as in high-vacuum equipment where ultra-pure, thin-films are grown one atomic layer at a time, solution processed materials are highly susceptible to trap state formation. As a result, the charge-carrier dynamics, recombination, and ultimate the performance in solution-processed semiconductors are often dominated by defects and trap states.

In organo-halide perovskites, trap densities have been experimentally determined to be in the range of 10^{16}-10^{20} cm^{-3} for nanocrystalline thin-films,[35, 38-39] and 10^{9}-10^{10} cm^{-3} for bulk, single crystals.[40-41] Correspondingly, the charge carrier dynamics appear to be dominated by the nongeminate, biomolecular, band-to-band electron-hole recombination at photoexcitation densities in the range of 10^{17}-10^{18} cm^{-3} where all trap states have been occupied and carriers generated in excess of the trap densities are able to able to undergo band-to-band recombination.[37, 39] Furthermore, the regime where Auger recombination dominates the charge carrier dynamics in organo-halide perovskites isn't expected to be achieved until optical excitation densities in excess of 10^{18}-10^{19} cm^{-3} are reached.[42] In the experiments we highlight in later chapters of this dissertation, where we intend to probe charge carrier dynamics in the trap-mediated-recombination regime, we intentionally use optical excitation densities in the range of 10^{15}-10^{17} cm^{-3}, where the charge recombination rates extracted from transient photoluminescence kinetics are linear in this range (Figures 3.15 B and C).[43]

Much of the research presented in this dissertation will focus on using spectroscopic techniques to identify and characterize the effects of trap states, while wet-chemistry processing strategies are developed to overcome the effects of charge trapping and recombination in an effort to enhance the carrier diffusion length (equation 1.5) and boost power conversion efficiencies for solution-processed PVs.

1.3 Thesis Overview

The current chapter represents an introduction for the remainder of this dissertation. Motivation for the development of novel solar cell technologies has been established, and a brief background on semiconductor and solar cell device physics was presented. Given below is a brief summary of the remaining chapters in this dissertation.

Chapter 2 presents a fundamental understanding for a variety of optical spectroscopic techniques as well as thin-film processing and characterization methodologies. This background knowledge will serve as the foundation for the material and topics what will appear consistently throughout the remainder of this dissertation. Fundamental aspects of the following topics will be introduced: steady-state, absorption spectroscopy; time-resolved, absorption and emission spectroscopy; x-ray diffraction; and thin-film processing techniques such as spin-coating. For each technique introduced in this chapter, appropriate examples will be given to draw tangible connections to the materials presented in the later chapters.

Chapter 3 presents our work in tuning the morphology and crystallite domain size of nanocrystalline organohalide perovskite thin-films by controlling deposition conditions and precursor concentrations. We show that the crystallite size is related to the photogenerated electron-hole recombination rate, and that recombination is limited by photocarrier diffusion to crystallite surfaces and/or grain boundaries. Furthermore, we demonstrate one of the first literature reports that bulk-crystal, electron-hole recombination rates can be achieved by treating nanocrystal films with strongly coordinating molecules such as 1,2-ethanedithiol known to eliminate the effects of trap-mediated recombination in semiconductor quantum dots.

In Chapter 4 we present an in-depth study of solution-phase chemistry occurring in solutions preceding organohalide perovskite film casting. Given the low-temperature, solution-processed nature of organohalide perovskites, we hypothesize that species formed in solution could result in defects in the final crystalline film capable of producing electronic states that facilitate carrier trapping and electron-hole recombination. We find that a series of higher-order coordination compounds of PbI_x^{2-x} exist in solution when a Pb^{2+} source and CH_3NH_3I are mixed at concentrations relevant to perovskite film deposition. Furthermore, we control and quantify the competing association equilibria between all the PbI_x^{2-x} complexes in solution by varying the mole ratio of PbX_2:CH_3NH_3I. Casting films from all solutions, we can extract electron-hole recombination rates from careful analysis of transient photoluminescence spectroscopy kinetics. We report that the solution concentration of PbI_4^{2-} is uniquely correlated with film trap density and provide strong evidence that other species (I^-, PbI_3^-, PbI_2) suggested by computational experiments to result in trap states are not in fact not well correlated.

In Chapter 5, my contribution to a collaborative research effort is presented wherein we assign the optical transition giving rise to transient, mid-IR absorption observed for PbS colloidal quantum dots and tune the mid-IR TA absorption by controlling nanocrystal surface chemistry. My work supported a broader project goal of understanding how sub-band gap states in PbS quantum dots mediate charge transport and influence achievable photovoltage in thin-film arrays.

The work in Chapter 6 also presents my role in a collaborative project, however, on a tangential research effort to the solution-processed electronic materials. The goal of the project was to determine if and how electrostatic environments in enzyme active sites influence the chemical reaction catalyzed by the protein. Using infrared spectroscopy, we investigated the changing electrostatic environment in the active site of dihydrofolate reductase (DHFR), a protein responsible for catalyzing the reduction of dihydroholate to tetrahydrofolate. Our results illustrate a changing electrostatic environment as a result of conformational changes facilitates the hydride transfer reaction. Furthermore, we find that electrostatic environments not only aid in reducing the activation barrier for the catalytic step, but also aid in substrate binding, release, and alignment within the active site throughout the entire catalytic cycle of DHFR.

In Chapter 7, the conclusions of this dissertation research are discussed and the prospects for future research direction in solution-processed photovoltaics with special emphasis on organo-halide perovskites and colloidal quantum dots are presents.

CHAPTER 2

Instrumentation, Techniques, and Methods

The intention of this chapter is to provide a fundamental understanding of the spectroscopic techniques and thin-film processing and characterization methodologies that will be appear consistently throughout the remainder of this dissertation. Fundamental aspects of the following topics will be introduced: steady-state absorption spectroscopy; time-resolved, absorption and emission spectroscopy; and thin-film processing techniques such as spin-coating. For each technique introduced in this chapter, appropriate examples will be given to draw tangible connections to the materials presented in the later chapters.

2.1 Steady State Spectroscopic Methods

The term "steady-state spectroscopy" refers to the interaction of electromagnetic radiation with matter on a long timescales (seconds or longer), and chemical or physical systems typically reach an equilibrated state under the timescales of these measurements. Therefore, these "steady-state" spectroscopic experiments probe time-averaged, ensemble information and provide information about the sample's electronic structure, chemical structure, chemical composition, dielectric or solvent environment under equilibrium conditions. The instrumentation and information that can be gleaned from a steady-state measurements is much different than in transient spectroscopic techniques which will be examined in Section 2.2. As such, it is typical that all steady-state, optical spectrometers have the same basic components: light source, wavelength selector, sample compartment, photon detector, and signal processer or digitizer,[44-45] and the schematic of several steady-state spectrometers will be detailed below.

2.1.1 Absorption Spectroscopy

Light can be absorbed by a sample when the photon energy is resonant with the energy difference between two states involved in the transition – given that all other quantum mechanical requirements or "selection rules" are simultaneously satisfied. Optical transitions can occur between electronic, vibrational, or rotational energy levels, but this dissertation will only focus on electronic and vibrational absorption spectroscopy.

In a steady-state absorption experiment, a narrow wavelength region is selected from a broadband light source using a wavelength selecting element such as a diffraction monochromator. This monochromatic light (realistically, a narrow wavelength band) is passed (transmitted) through an absorbing sample of thickness *l*, containing molar (moles/liter) concentration *c* of absorbing species or "chromophores." The fraction of light which passes through the sample is described by the Beer-Lambert law (equation 2.1),[46-47] which relates the intensity of light before the sample, I_{before}, to the intensity of light after the sample, I_{after}:

$$\frac{I_{after}}{I_{before}} = 10^{-c\varepsilon l} = T \qquad \boxed{2.1}$$

where ε is the molar absorption coefficient – a constant that is intrinsic to a chromophore and depends sensitively on the wavelength of light, but does not depend on optical path, and T is the sample transmittance. The sample absorbance (A) can be calculated from equation 2.1 according to:

$$A = -\log(T) = c\varepsilon l. \qquad \boxed{2.2}$$

When discussing absorption for solid samples, such as thin-film semiconductors, where the density of absorbing centers is fixed, the molar absorption coefficient cannot be defined because the molar concentration of the chromophore has no meaning. Therefore, for solid samples, equation 2.2 becomes:

$$A = -\log(T) = \varepsilon t \qquad \boxed{2.3}$$

where t is the film thickness, and ε has units of cm^{-1}, which defines the thickness required to absorb all light of a given wavelength. Typical absorbance coefficients for PV-relevant semiconductors are $\sim 10^4 - 10^6$ cm^{-1} at wavelengths above the bandgap.[29] As reference, the absorption coefficients for two semiconductor materials which are the main focus of this dissertation, organo-halide perovskites and colloidal quantum dots, are 8.8×10^4 cm^{-1} (532nm)[48-49] and $< 1 \times 10^4$ cm^{-1} (532nm),[50-51] respectively.

It should be noted that there are realistic limitations to the Beer-Lambert law eq(2.1) and absorbance spectroscopy measurements. For instance, it is necessary to use low analyte concentrations to avoid strong anaylte-analyte or analyte-solvent interactions, which can drastically influence the chromophore environment and absorbance.[45] Additionally, the refractive index, η, of a sample is related to the concentration, and therefore the absorptivity of a sample can be significantly altered by changes in concentration.[52] If this effect is expected, then the following correction term[45] should be included in equation 2.2:

$$A = c\varepsilon l\left(\frac{\eta}{(\eta^2 + 2)^2}\right) \qquad \boxed{2.4}$$

However, changes in refractive index are rarely expected for samples with concentrations less than 0.01 M.

2.1.1.1 Ultraviolet and Visible Absorption Spectroscopy

The ultraviolet and visible regions of the electromagnetic spectrum consist of wavelengths between 0.2 µm and 0.7 µm – corresponding to photon energies of 6.2 eV and 1.8 eV, respectively. This optical range matches the energetic spacing between electronic energy levels in molecular and coordination compounds, and absorption of wavelengths in this spectral range gives rise to colors visible to the human eye. For instance: electronic transitions occurring in metal coordination compounds often give rise to spectacular colors as a result of metal-to-ligand or ligand-to-metal charge transfer absorption events (abbreviated MLCT or LMCT, respectively). Strong absorption of UV and visible light is one of the many reasons that transition-metal coordination compounds, such as cis-bis(isothiocyanato)bis(2,2'-bipyridyl-4,4'-dicarboxylato) ruthenium(II) are used as the primary absorbing "dye" in dye-sensitized solar cells (DSSCs).[53-54]

Using the Beer-Lambert law expressed in eq(2.2) and highly sensitive UV-Visible spectrometers, my dissertation research was able to provide quantitative analysis of metal coordination compounds in solution and to characterize the absorption properties of novel semiconductors for photovoltaics across the critical UV, Visible, and near-IR regions of the solar spectrum. The assignment and quantification of iodoplumbate coordination compounds and characterization of their complex solution chemistry[38] appearing in chapter five of this dissertation was made possible by the sensitive and reproducible absorption measurements conducted on the two-channel PerkinElmer Lambda 950 Spectrophotometer (PerkinElmer, Inc. Waltham, MA) capable of making UV, visible, and near-infrared absorption measurements.

Figure 2.1 shows a simplified schematic of a two-channel spectrophotometer similar to the PerkinElmer Lambda 950 instrument used for this work. Light from a broadband, blackbody emitter (commonly, a deuterium lamp for UV or a tungsten-halogen lamp for visible and NIR wavelengths)[45] is collected and focused into a monochromator. The output from the monochromator represents a narrow wavelength band that is collimated by a matching mirror and this collimated beam is split into two monitoring beams of equal intensity by a 50/50 beam splitter (BS). The origin of increased sensitivity achievable with two-channel spectrophotometers lies in the detection scheme where the monitoring beams simultaneously pass through the sample and reference cells before being focused on identical detectors – often photomultiplier tubes (PMTs). The two PMT signals are amplified and the logarithmic ratio (equation 2.2) is calculated electronically before the reference-corrected, or "blanked," absorbance spectrum is displayed. This two-channel or double-beam absorption experiment is preferable to single-beam spectrometers because it is not necessary for the user to make two separate measurements of the reference and the sample, but more importantly by measuring the sample and reference transmittance simultaneously, two-channel instruments overcome the effect of thermal fluctuations that are a major source of error and limit the sensitivity of single-channel spectrometers.[47]

Given the sensitivity of the two-channel, PerkinElmer Lambda 950 spectrometer, we were able to interpret small absorbance changes in solutions containing two organo-halide perovskite precursors: lead (II) iodide/chloride and methylammonium iodide. Solutions of PbI_2 in the presence of excess iodide are known to undergo complex association equilibria forming a series of higher order iodoplumbate PbI_x^{2-x} species, and the ability to detect small changes in absorbance as a result of changes in composition allowed us to provide quantitative detail of the competing equilibrium reactions (equation 5.5) and correlate solution metrics with crystalline defects in solid-state, thin-films of organo-halide perovskite semiconductors.

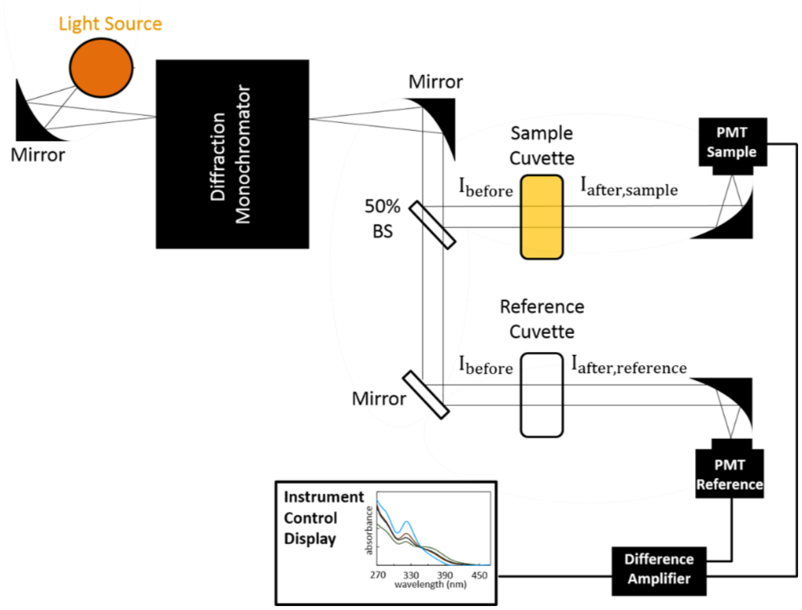

Figure 2.1: Simplified schematic of a two-channel absorbance spectrometer similar to the PerkinElmer Lambda 950 instrument used to quantify small absorbance changes as a result of tuning the composition of organo-halide perovskite precursors in solution (see chapter 5 of this dissertation). The instrument consists of a UV or visible/NIR light source, focusing mirror, diffraction monochromator, collimating mirror, 50% beam splitter, sample and reference chamber, matching detectors, and ancillary electronics to amplify, digitize, calculate the absorbance spectrum of the sample.

2.1.1.2 Infrared Absorption Spectroscopy

Like UV and visible absorption phenomena, infrared absorption obeys similar quantum mechanical selection rules and the degree of IR light absorbed by a sample is described by the Beer-Lambert law. However, due to differences in application and instrumentation, the infrared spectral regime is usually divided into three sub-regions: near-infrared (NIR), mid-infrared (MIR), and far-infrared (FIR). In this section, and the remainder of the dissertation, the focus will almost exclusively be on the MIR region because most compounds containing some degree of covalent bonding will absorb selectively in the mid-infrared spectral window, which extends from 2.5 μm to 25 μm wavelengths. Chemists often identify MIR radiation in a unit called wavenumber ($\tilde{\nu}$) which has units of inverse wavelength expressed as inverse centimeters (cm^{-1}) because wavenumber is directly proportional to frequency and gives convenient values for covalent bond vibration frequencies: 2.5 μm and 25 μm wavelengths correspond to 4000 cm^{-1} and 400 cm^{-1}, respectively.

Chemical bond vibration can be described semi-classically by the harmonic oscillator approximation where a bond is considered as two masses (atoms) connected by a spring that can stretch or compress with natural oscillation frequency:

$$\nu_{classical} = \frac{1}{2\pi}\sqrt{\frac{K}{\mu}} \tag{2.5}$$

where K is the force constant of the spring or bond and μ is the reduced mass of the two atoms (m_1 and m_2) connected by the spring:

$$\mu = \frac{m_1 m_2}{m_1 + m_2}. \tag{2.6}$$

In contrast to a mechanical oscillator that can access any energy, chemical bond vibrations can only access discrete or quantized energy states and the harmonic oscillator approximation much be altered to account for this quantized nature of molecular, vibrational energies. By solving the wave equations of quntum mechanics, the potential energy of the semi-classical harmonic oscillator is:

$$\mathrm{E} = \left(\mathrm{v} + \frac{1}{2}\right)\frac{h}{2\pi}\sqrt{\frac{\mathrm{K}}{\mu}} \qquad \boxed{2.7}$$

where v is the vibrational quantum number ($\mathrm{v} \geq 0$) and h is Planck’s constant. It is possible to substitue equation 2.5 into equation 2.7 to obtain an expression for the energy of the quantum system in terms of the classical vibrational frequency ($\nu_{classical}$):

$$\mathrm{E} = \left(\mathrm{v} + \frac{1}{2}\right) h\nu_{classical}. \qquad \boxed{2.8}$$

Although simple, the semi-classical, harmonic oscillator model of a chemical bond is not capable of fully describing all observables of experimental vibrational spectra. Chemical bond dissocation and overtone absorption bands are just two deviations that cannot be captured by the harmonic oscillator model. To overcome many deviations, vibrational anharmonicity must be accounted for in the potential energy in the form of a Morse potential:

$$\mathrm{E(r)} = \mathrm{D_e}\left(1 - \mathrm{e}^{-(\mathrm{r}-\mathrm{r_e})}\right)^2 \qquad \boxed{2.9}$$

where D_e is the energy required for bond dissociation, r is the interatomic distance and r_e is the equilibrium bond distance. The harmonic oscillator and Morse potentials are shown graphically in Figure 2.2, where it is apparent the harmonic potential is a close approximation to the Morse potential at low energy, but quickly deviates at higher energies. By not including anharmonicity, the harmonic oscillator model is unable to descibe bond dissocation and overtone absorption bands (transitions between 0 → 2, 0 → 3, etc.). Furthermore, the Harmonic oscillator model is inacapble of describing the sensitivity of a bond vibrational frequecy to an applied electric field (electrochromism) or various dielectic or solvent environments (solvatochromism). It becomes necessary to invoke the anharmonic Morse potential to descibe these phenemea, as we will see in Chapter 6, where we use calibrated, vibrational sensitivies to measure the electrostatic environement in the active site of biological enzymes by measuring small changes in bond vibrational frequencies via infrared absorption spectroscopy.

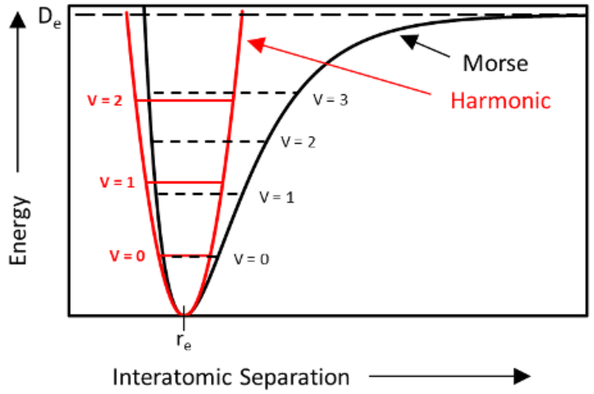

Figure 2.2: Harmonic Oscillator (red) and Anharmonic, Morse (black) potential. The harmonic oscillator model is a close approximation to the Morse potential at low energy, but quickly deviates. Also, the Morse potential is necessary to explain overtone absorptions, bond dissociation, and decreasing transition energy between sequential quantum states.

Early infrared spectrometers had instrument schemes similar to UV/visible spectrophotometers (Figure 2.1) where light from a broad-band infrared source would be passed through an IR diffraction monochromator, and the monochromatic beam would transmit a sample, be collected, and focused onto an MIR detector. A full spectrum would be built-up by rotating the diffraction grating to tune the wavelength of light passing though the sample, and the spectrometer would read-out the intensity of light (measured as a voltage) on the detector element as a function of wavelength. Although many of these "dispersive" IR instruments are found in laboratories today, this section and the remainder of this dissertation will focus on the more efficient, reproducible, and sensitive Fourier-transform infrared (FTIR) spectrometers. FTIR spectroscopy was used to provide qualitative compositional information for thin-film materials[48] in Chapters 4 and 5, and provide a quantitative measure of electric fields in enzyme active sites[55] in Chapter 8.

Unlike dispersive IR spectrometers that build up a spectrum by measuring the intensity of transmitted light through a sample one wavelength at a time, FTIR spectrometers allow the entire spectrum of MIR radiation to transmit the sample and hit the detector. Due to an experimental design that will be discussed in more detail, all wavelengths are collected simultaneously in the time domain, and using a mathematical operation called a "Fourier-transform," the time-domain data is converted to a frequency domain which is displayed as transmission versus wavelength (or wavenumber). The data acquisition scheme employed by FTIR instruments allows for the collection of an entire spectrum with high resolution in a very short time – as brief as one second in some cases.[56]

The instrument schematic for a single-beam, FTIR spectrometer is shown in Figure 2.3, which is similar to the Mattson Galaxy Series (Madison Instruments, Inc. Middleton, WI) FTIR spectrometer used for measurements in later chapters. At the heart of all FTIR instruments is the interferometer which is responsible for generating the time-domain data, called an interferogram. An interferometer consists of a beam-splitter and two mirrors – one at a fixed position and one on a movable base. As seen in Figure 2.2, the broad-band emission from a blackbody emitter (silicon carbide Globar) is split into two beams by the interferometer beam-splitter (BS). The length of one IR path is modulated by the moving mirror, and the other path is held constant by the fixed mirror. After reflection off the respective mirrors, the IR light of both the fixed path and modulated path overlap at the beam-splitter, and when the position of the moving mirror an identical distance from the beam splitter as the fixed mirror, light from the two paths constructively interferes. If the distance of the moving mirror does not match the distance of the fixed mirror, there will be a phase difference between light of the two optical paths at the beam-splitter; this phase discrepancy will produce destructive interference. The broad-band, collimated light exits the interferometer, transmits the sample, and is focused on the MIR detector. The intensity of light hitting the detector is monitored as a voltage, and the spectrometer plots the signal voltage versus position of the moving mirror to obtain an interference pattern represented as a blue data in the top right corner of Figure 2.3. The largest amplitude is shown in the center of the interferogram and this point represents the position where the moving mirror distance matches the fixed mirror distance – total constructive interference.

Also shown in the instrument schematic in Figure 2.2 is a continuous wave (CW) laser that is passed through the interferometer and has an independent detector. The CW

He-Ne laser (633nm fundamental wavelength) is responsible for providing the interferometer fringe reference and sampling interval information.[45] In other words, the CW laser tracks the position of the moving mirror and provides a feedback loop to maintain a constant scanning velocity for the mirror/drive system.

FITR spectrometers have numerous advantages over dispersive IR instruments: signal-to-noise ratios of FTIR spectrometers are usually an order of magnitude better than dispersive instruments.[57] The enhancement in S/N is related to decreased scan durations, as FITR spectrometers can collected high resolution spectra (less than 0.1 cm^{-1}) in a fraction of the time achievable with an instrument featuring a diffraction monochromator (~1 to 10 cm^{-1} spectral resolution). Furthermore, the optics of an FTIR spectrometer are amenable to high optical throughput whereas the diffraction grating and narrow monochromator slit widths required in dispersive measurement significantly decrease the optical energy throughput thus decreasing the sensitivity. The resolution and sensitivity of FTIR vibrational spectroscopy has enabled numerous experiments in this dissertation, including two experiments highlighted in the next section: vibrational, electro- and solvatochromic spectroscopy.

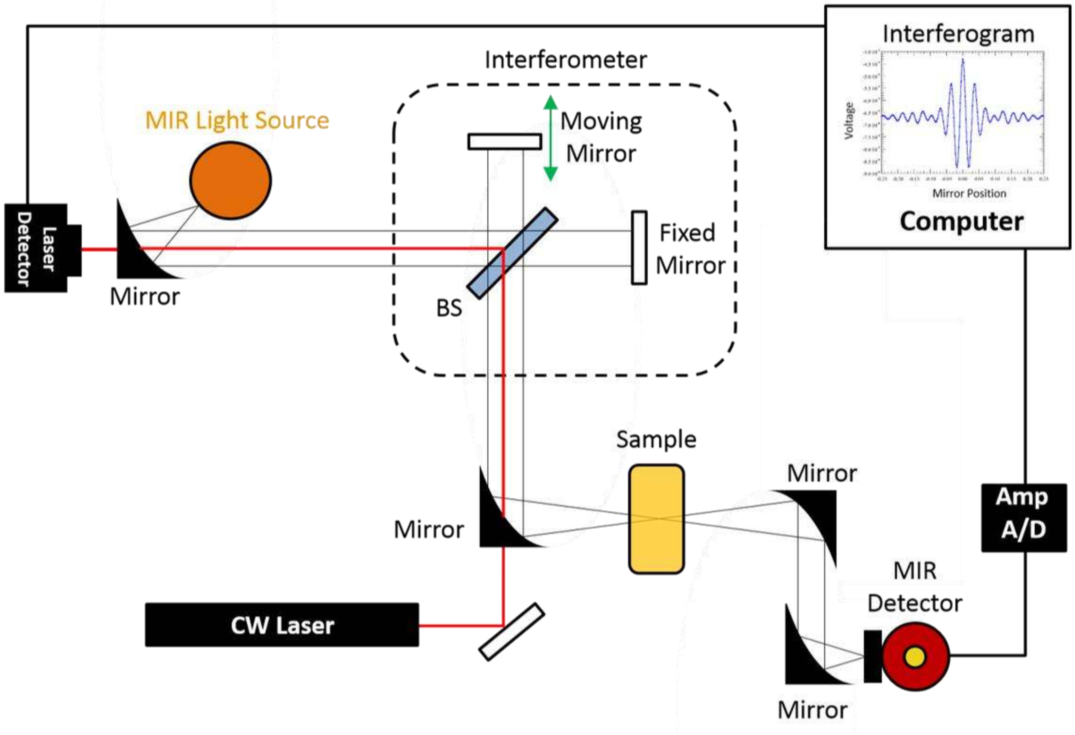

Figure 2.3: Schematic of a single-channel FTIR spectrometer similar to the Mattson Galaxy Series instrument used to for qualitative chemical identification of thin-films in Chapter 4 and 5 and quantitative analysis of dielectric environments in enzymes in Chapter 6 of this dissertation. The instrument consists of a Globar IR source, interferometer, sample chamber, infrared detector, and ancillary electronics to calculate the Fourier-transform of the interferogram to give a frequency-domain spectrum.

2.2 Transient Spectroscopic Methods

In Section 2.1, we examined the fundamentals, instrumentation, and uses of two powerful, steady-state absorbance spectrometric techniques: UV/Visible/NIR and FTIR spectroscopy. By using pulsed light sources, detectors with appropriately fast time responses, and fast ancillary electronics, one can measure dynamic properties of chemical and physical systems that are displaced from equilibrium conditions that are probed in the aforementioned steady-state experiments. In this section, we will examine two transient spectroscopic techniques: time-resolved photoluminescence (TRPL) and transient absorbance (TA) spectroscopies because these time-resolved methods will figure prominently in the remainder of the dissertation as the means for assigning transient photophysical phenomena occurring in organo-halide perovskites and colloidal quantum dots.

2.2.1 Transient Photoluminescence Spectroscopy

Photoluminescence is the physical process by which light is emitted from a material following optical excitation to an electronic excited state. Photoluminescence can be classified as fluorescence (transition between states of the same multiplicity) or phosphorescence (transition between states of different multiplicity). However, in complicated systems, such as thin-film semiconductors, the spin multiplicity of the emissive state is not always known, and as such, we will refer to optical emission experiments in this dissertation by the all-encompassing nomenclature: photoluminescence. In the same light as absorption spectroscopy, it is possible to make steady-state photoluminescence spectroscopy measurements. However, much of the research in this dissertation will leverage time-resolved data to assign the mechanism by which excited-state carriers relax to the ground state in semiconductor materials. Assignment of decay mechanisms and quantitative decay rates/lifetimes will be obtained by fitting photoluminescence kinetics curves with models developed for specific systems[58] as well as with less complex, phenomenological functions such as exponential, multi-exponential, or power law decays. Furthermore, we only focus on transient experiments in this section because "steady-state" photoluminescence information can be obtained from these transient experiments by simply integrating the time domain to achieve a time-averaged spectrum.

Figure 2.5 shows a schematic of the home-built TRPL instrument fabricated in the Asbury lab. A frequency doubled $Nd^{3+:}$YAG laser (10ns pulse duration, 30 Hz repetition rate, 532 nm wavelength, Continuum, CA, USA) is used as the excitation source, where excitation densities in the range of 10 nJ/cm^2 to 1 mJ/cm^2 can be achieved. If other excitation wavelengths are required for a specific experiment, the Asbury lab is equipped with a High Resolution Dye Laser (Photon Technology International, NJ, USA). As shown in Figure 2.5, sample emission is collected at a right angle relative to excitation, coupled into a monochromator (DK240, Spectral Products) with lenses and passed through appropriate long pass filters to discriminate the excitation wavelength and other orders of diffraction from the monochromator. The diverging light is focused onto a photodiode where for most experiments in this dissertation a biased silicon photodiode with high sensitivity from 200 – 1100 nm and a 1 ns rise time (DET10A, Thorlabs) was used. The signal was amplified using a 200 MHz preamplifier (HVA-200M-40-B, FEMTO) and was digitized using a 250 MHz computer-mounted oscilloscope (Pico-5000, Picotech), which was synchronized to the trigger output from the Nd^{3+}:YAG laser. The quantity measured in experiment is a voltage on the photodiode, and we are unfortunately limited in our ability to provide quantitative interpretation of emission intensity or absolute quantum yield. However, if care is taken when aligning the sample, matching excitation energy densities between experiments, normalizing the signal amplitude to account for the number of absorbed photons, as assuming that emitting species are isotropically distributed in samples, then this instrument can provide relative quantum yields from sample to sample and absolute quantum yield upon comparison to a known standard.

The combination of a 30 Hz repetition rate laser with 10 ns pulse duration, fast electronics, and a tunable resolution oscilloscope allowed us to electronically resolve photoluminescence kinetics traces from 10 ns to > 10 ms. This adaptable and high resolution instrument enabled the measurement of significantly different radiative recombination events, such as diffusion-limited, bulk-crystal charge recombination kinetics in organohalide perovskites with an average emission lifetime of $\tau = 230$ ns[48] to radiative emission from highly defective perovskite materials with average emission lifetimes as short as $\tau < 20$ ns. The sensitivity and resolution of this instrument is perhaps best displayed by the data shown in Figure 4.14 of this dissertation. The ability to precisely and consistently resolve small differences in PL kinetics enabled us to correlate small changes in organohalide perovskite precursor solution composition to even smaller changes in electron-hole radiative recombination rates in thin-films prepared from these solutions to begin to understand the chemical origin of defects and charge recombination centers in these emerging solution-processed optoelectronic materials. Transient photoluminescence spectroscopy is a power characterization tool, but it is limited by its intrinsic ability to only measure optically bright transitions. In the next section, we will discussion a complementary technique which can probe both optically bright and dark states – both of which play significant roles in optoelectronic materials.

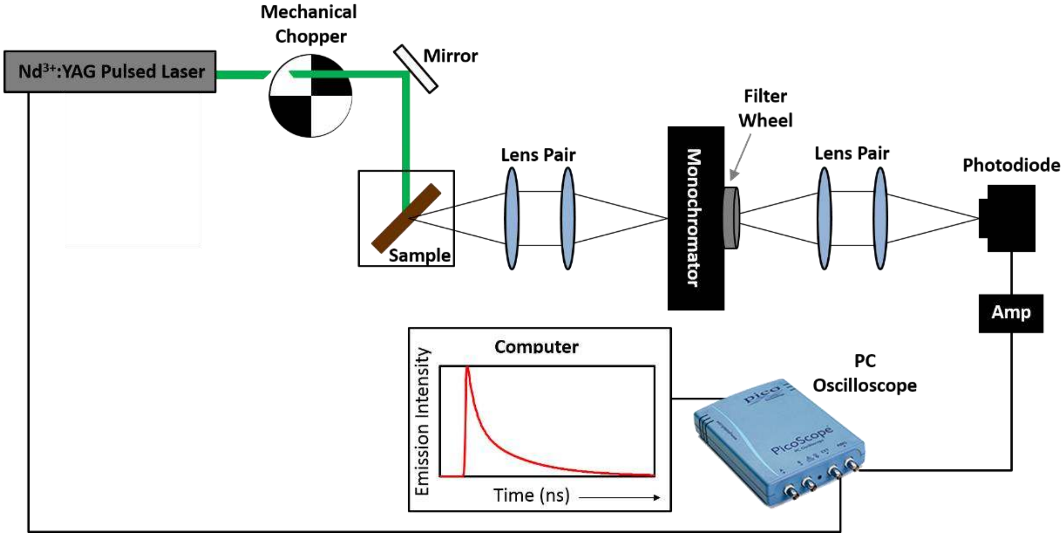

Figure 2.4: Schematic for a home-built, nanosecond, transient photoluminescence spectrometer based on a pulsed Nd^{3+}:YAG laser (30 Hz repetition rate, 10 ns pulse duration).

2.2.2 Transient Absorption Spectroscopy

The purpose of transient absorption spectroscopy is to measure a temporal change in the sample absorbance following perturbation by a short excitation pulse of light.[47] Following excitation, the sample can undergo a variety of spontaneous photophysical or photochemical reactions, and by tracking the changes in absorbance of a probe beam one can understand the pathways undergone by excited states in order to return the system to thermal equilibrium. For instance, the excited species can return to the ground state by a direct transition, or by intermediate states such as singlet or triplet excited states or by charge trapping and recombination mediated by defect states. Alternatively, it is possibly for the excited species to undergo photophysical or photochemical reactions such as charge transfer or chemical isomerization reactions. Provided that intermediate states and photophysical, or photochemical products have distinct absorption bands in a measurable spectral window, interpretation of transient spectra and their time evolution can provide detailed information about excited state processes and dynamics.

Similar to steady-state absorbance measurements, transient absorbance (TA) experiments measure the degree of light absorbed by the sample; however, in TA spectroscopy experiments, sample absorbance has a time-dependence as well as a wavelength dependence. The quantity more often displayed in TA measurements is the change is absorbance (ΔA), which is the normalized change in absorption of a monitoring (probe) beam of light induced by an excitation (pump) pulse of light. ΔA is obtained by the following equation:

$$\Delta\mathrm{A}(\lambda,\mathrm{t}) = -\log\left(1+\frac{\Delta\mathrm{U}(\mathrm{t},\lambda)}{\mathrm{U}_0(\lambda)}\right) \quad \boxed{2.10}$$

$$\text{where: } \Delta U(t,\lambda) = U(t,\lambda) - U_0(\lambda) \qquad \boxed{2.11}$$

$\Delta U(t,\lambda)$ is the time-dependent difference in the probe signal level on the detector – that is the difference between the probe signal in the presence [$U(t,\lambda)$] and absence [$U_0(\lambda)$] of the pulsed excitation. The home-built transient absorbance spectrometer of the Asbury lab (Figure 2.6) calculates $\Delta U(t,\lambda)$ using a sequential subtraction method which is detailed in recent publications.[59-60] Briefly, sequential subtraction and calculation of $\Delta U(t,\lambda)$ is achieved by chopping the pulsed light beam at a frequency half the repetition rate of the laser (30 Hz) while continuously measuring the probe signal intensity and triggering the digitizer on every laser shot. In this scheme, every other laser pulse excites the sample, but the digitizer acquires the probe signal for every laser shot. By using a fast, two channel digitizer (250 MHz computer-mounted Pico-5000 oscilloscope) the oscilloscope uses on board memory to distinguish the two probe signals: when the sample is irradiated with the excitation pulse [$U(t,\lambda)$] versus when the sample is not irradiated [$U_0(\lambda)$]. The program source code can then calculate $\Delta U(t,\lambda)$ and $\Delta A(t,\lambda)$ using equations 2.11 and 2.10, respectively, for a preallocated time window and at a wavelength specified by the monochromator.

A schematic for the home-built transient absorbance spectrometer is depicted in Figure 2.6. The instrument uses an identical optical layout and Nd^{3+}:YAG pulsed laser as the transient photoluminescence spectrometer described above (Figure 2.5), with the only modification being the addition of a continuous-wave, broad-band light source used as the probe which is focused on the sample, collected and refocused on the monochromator slits, and then refocused on a photodiode. All ancillary electronics are identical to the TRPL instrument described in section 2.2.1. To ensure that the probe beam is monitoring an area of the sample that has been uniformly excited by the pump beam, the excitation and probe beams must be overlapped at the sample and the area of the excitation beam must be larger than the area of the probe beam, as shown by the inset in Figure 2.6.

Two nanosecond transient absorbance instruments are employed in this dissertation: a visible/NIR instrument and a mid-infrared instrument. The optical layout of the two spectrometers is identical, and the only differences between the two instruments are in the broad-band light source, the optical materials used, the grating for the monochromator, and detector. The visible/NIR instrument employs a tungsten halogen light source, a visible/NIR monochromator grating, and silicon photodiodes. The mid-IR spectrometer uses a silicon nitride mid-IR emitter, a mid-IR monochromator grating, and a liquid nitrogen cooled MCT, mid-IR detector. Additionally, the visible/NIR spectrometer requires an automated shutter or beam block to temporarily block the probe light. The reason for blocking the probe light is for the subtraction of emission from the transient absorbance signal which is expected to overlap some transient absorption features in the visible and near-IR spectral regime. Analogous subtraction of emission is not necessary in the mid-infrared regime because it is rare for a sample to absorb visible light and emit mid-IR light – especially for thin-film semiconductors which is the primary material under investigation in this dissertation.

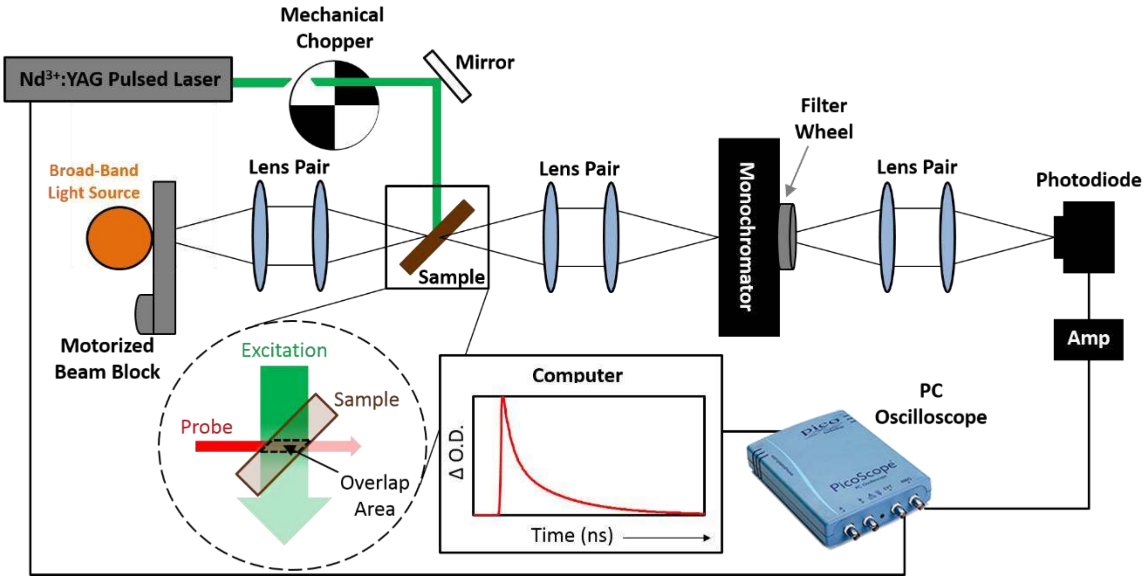

Figure 2.5: Schematic for a home-built, nanosecond, transient absorbance spectrometer, which closely resembles the TRPL instrument shown in Figure 2.5. The same optical scheme is used for both the visible/NIR and mid-IR transient absorbance spectrometers used in this dissertation, with appropriate changes to account for different wavelength regimes.

We will now briefly review a few excited state processes that can be monitored by transient absorption spectroscopy and associated terminology. Additionally, we will give an example where comparison of transient photoluminescence and absorption data can be used to provide a comprehensive picture of decay pathways in thin-film semiconducting materials.

The wavelength chosen for the pulsed excitation in TA measurements must be on resonance with a ground-state absorption band of the sample in order to provide initial excitation from the ground state an excited state, as shown in Figure 2.6A. It is not necessary for the primary absorption event to result in a transition from the ground state to the lowest lying excited state as shown in the figure. However, excitation to higher excited states often results in ultrafast cooling to lower excited states through processes like internal conversion, intersystem crossing, or other thermalization processes by interaction with lattice phonons.[61-62] Following absorption of the pulsed light, the system can undergo one of many possible photophysical or photochemical events. In the simplest case, the excited state will not undergo any reaction, and when broadband probe light interacts with the excited chromophore, appropriate wavelengths will be absorbed and a small fraction of the system will be promoted to higher excited states as shown in Figure 2.6 B. Absorption of the probe in such a way results in lower probe light intensity measured by the detector at the absorbed wavelength; decreased probe intensity following puled excitation results in a negative value for $\Delta U(t,\lambda)$ (equation 2.11) and consequently will be displayed as a positive feature in the $\Delta A(t,\lambda)$ spectrum (equation 2.10). Because the sample absorbs a larger fraction of the probe light following pulsed excitation, this phenomenon is aptly named “photoinduced absorption.” A chromophore in the initial excited state is capable of undergoing a photophysical or photochemical reaction such as charge transfer across an interface or isomerization. The new species which are perturbed as a result of excess charge will absorb more probe light at an appropriate wavelength and will likewise be detected as a photo-induced absorption signal.

Another interaction between the probe beam and an excited chromophore is possible. Consider a molecule in an excited state configuration similar to that shown in Figure 2.6 B. A small fraction of the ground state population has already been promoted to excited state(s) by absorption of the pump beam; therefore, when probe wavelengths resonant with the 0 → 1 transition interact with the this chromophore, light at that wavelength will be attenuated to a lesser extent than prior to photoexcitation – meaning that a larger probe signal will be detected follow pulsed excitation. As a result, $\Delta U(t,\lambda)$ will have a positive sign because $U(t,\lambda) > U_0(\lambda)$ in equation 2.11 and the transient $\Delta A(t,\lambda)$ spectrum will be negative in this region. A transient absorption feature resulting from this phenomenon is called a "bleach." It should be noted that due to the nature of the bleach phenomenon, these features in TA spectra are only observed at identical spectral locations to a ground-state (steady-state) absorption.

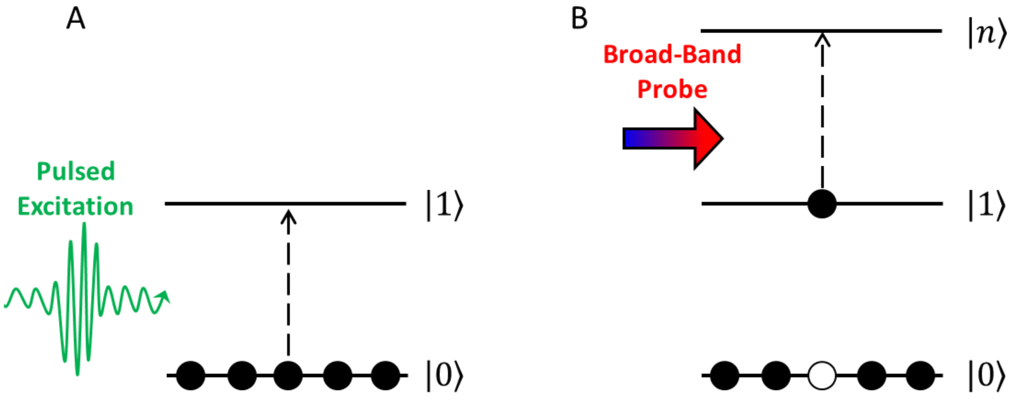

Figure 2.6: A) Two-level energy diagram depicting interaction of ground state chromophore with pulsed excitation. B) Following absorption of the pulsed source, the excited state chromophore can be promoted to higher energy excited states upon absorption of appropriate wavelengths of probe light. It is also shown that the ground state has decreased population following excitation by the pulsed, pump source and therefore will not absorb as much probe light at wavelengths resonate with the 0 → 1 transition.

Using a generic, direct band gap semiconductor with a conduction band (CB) and valance band (VB) separated by a band-gap, we will show an example where comparison of transient photoluminescence (TRPL) and transient absorbance (TA) spectroscopy is required to differentiate between two decay pathways following optical excitation of the semiconductor. Figure 2.7 shows a simplified, spatial band diagram for a generic semiconductor with a band gap sufficiently larger than thermal energy (k_BT) at room temperate so as to prevent thermal population of conduction band. Figure 2.7A shows interaction of the semiconductor with short pulse of light capable of exciting an electron to the conduction band. Also shown in the band diagram, is a localized trap state which does not have significant wave function overlap with the valance band, causing the oscillator strength for a direct absorptive transition between the VB and trap state to be small. In the absence of another material capable of scavenging the excited state electron or hole from this system through a charge transfer process, the electron in the CB and hole in the VB will recombine through one of two pathways shown in Figure 2.7B.

Given that this material is a direct band gap semiconductor, the band-to-band recombination of an electron and hole can result in the emission of a photon with energy equal to the band gap energy. Photoluminescence spectroscopy is capable of measuring the spectrum of this emission event, and with appropriately fast instrumentation, one can measure TRPL kinetics to obtain a rate constant for electron-hole recombination by fitting the kinetics decay with an appropriate model or function. However, photoluminescence spectroscopy is not capable of accessing the other decay pathway proceeding through a trap or defect state because trap-mediated recombination is typically nonradiative. In these cases, comparison of transient PL to transient absorption measurements is a very powerful way to provide thorough characterization of excited state processes that cannot be achieved by the two measurements independently. Measuring the ground state bleach for the semiconductor bandgap with TA spectroscopy gives information about total recovery of the ground state by both radiative and trap-mediated processes simultaneously, so comparison of the two techniques become critical for isolating the pure radiative recombination rate from the pure trap-mediated recombination rate.

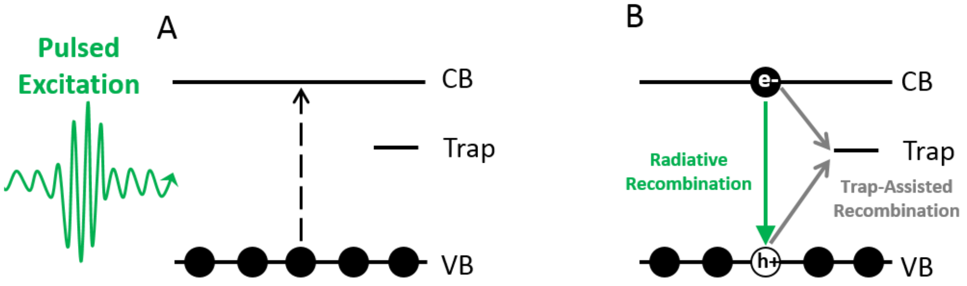

Figure 2.7: A) A simplified, spatial band diagram of a direct band gap semiconductor interacting with a pulsed light source which promotes a valance band (VB) electron to the conduction band (CB). B) Following pulsed excitation, and in the absence of a semiconductor junction or other material capable of undergoing excited-state charge transfer, the electron and hole will recombine with one of two pathways: direct band-to-band recombination or trap-assisted recombination. Comparison of the ground-state bleach kinetics as measured by TA and the radiative emission decay rate as measured by TRPL can be powerful in distinguishing the two mechanisms of recombination.

The following data shown in Figure 2.8 strengthens the argument that comparison of TRPL and TA kinetics measured for a semiconductor known to have trap-states can provide a thorough characterization of excited state processes. It is know that in organo-halide perovskite semiconductors, bimolecular, band-to-band, electron-hole recombination (as discussed in Chapter 1) results in emission of a photon at 765nm.[34, 63] Furthermore, electron-hole recombination through trap states is assumed to occur, but this mechanism is not well understood, and the research presented in this dissertation seeks to find chemical ways to overcome this deleterious trap-mediated recombination. In chapters 3-5 of this dissertation, we demonstrate a post-film-processing route to eliminating the effect of trap-mediated recombination in these materials, and comparison of TRPL and TA kinetics measurement was critical in our demonstration. Figure 2.8 A shows TRPL (red) and TA (blue) kinetics traces for an organo-halide perovskite thin-film before chemical treatment with 1,2-ethanedithiol (ETD) – a crystallite surface treatment which qualitatively passivated crystal defects and eliminates the effect of trap-mediated recombination. TRPL, which tracks the band-to-band recombination of mobile charge carriers, demonstrates a decay lifetime approximately one order of magnitude shorter than the TA band gap bleach kinetics, which probes band-to-band and trap-mediated recombination. In Figure 2.8 A, it should be noted that the shape of the TRPL decay suggests bimolecular charge recombination whereas the TA decay shape would indicate a unimolecuar, trap-mediated process. The difference in the lifetimes and the shapes of the kinetics traces in Fig. 2.8A is due to the slow recombination of trapped, immobile charge carriers.

Following treatment of the organohalide perovskite film with EDT, the TRPL and TA decays converge as seen in Figure 2.8B indicating the elimination of trap-mediated recombination upon EDT treatment. Both TRPL and TA kinetics decays exhibit only one path to the ground state through bimolecular band-to-band, electron-hole recombination. Elimination of trap states by post-film processing methods such as EDT treatment is expected to have significant benefits to the performance of organohalide perovskite semiconductors in photovoltaic applications.

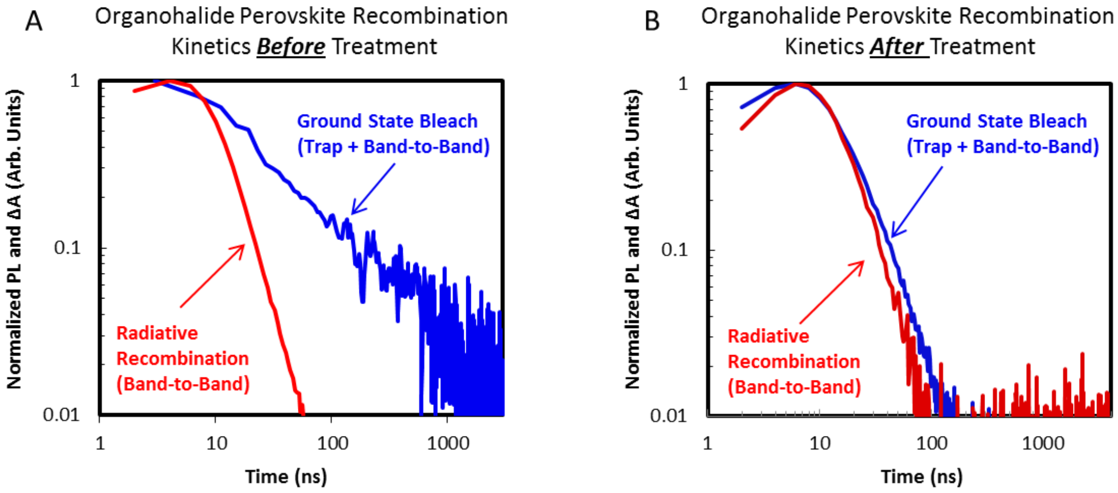

Figure 2.8: A) TRPL (red) and TA (blue) kinetics traces measured for an organohalide perovskite thin-film before treatment with 1,2-ethanedithiol. The order of magnitude difference in lifetime and the different shapes of the kinetics decays are due to significant trap-mediated recombination in this film. B) TRPL (red) and TA (blue) kinetics traces for an identical organohalide perovskite film after it had been treated with 1,2-ethanedithiol. Both decay lifetimes and shapes of the kinetics traces indicate that only a single pathway to the ground states exists in this material: bimolecular, band-to-band, electron-hole recombination.

2.3 Thin-Film Deposition by Spin Coating

For several decades, spin-coating has been used for the deposition of laboratory-scale deposition of thin-films. In this dissertation, organohalide perovskite and colloidal quantum dot films are prepared by spin coating precursor solutions on a variety of substrates and optical flats for spectroscopic measurements and other material characterizations. Spin coating was the deposition methods of choice because used to because it yields films of consistent thickness and uniformity with short dry-down times relative to other film casting methods such as drop coating, blade coating, or spray coating.

The typical spin-coat process involves dripping a small volume aliquot of a solution onto the center of a substrate and then spinning the substrate at high speed. Centripetal acceleration will cause the solution to spread to the edge of the substrate leaving behind a thin, liquid-film and eventually a solid-state film as the solvent evaporates and the solute from the precursor solution dries. The spin coater used in this dissertation work was a single wafer spin processor (WS-400B-6NPP-LITE, Laurell Technologies Corp) capable of spin speeds between 100 – 8000 rpm. The mechanics of spin coating are complicated and, the final film thickness depends on many parameters including: centrifugal and viscous forces, solute diffusion and solvent evaporation, spin speed and acceleration, and initial concentration of the solute in solution.[64] Qualitatively, the thickness (t) of the final film is inversely related to the angular velocity (ω):

$$t \propto \frac{1}{\sqrt{\omega}} \qquad \boxed{2.11}$$

The unfortunate disadvantage of spin coating is that this thin-film processing wastes the majority of material dispensed on the substrate as a solution: roughly 2–5% of the material dispensed onto the substrate goes into making the thin-film, while the remaining 95–98% is flung off the side of the substrate.[64]

CHAPTER 3

Chemical Control of Morphology, Charge-Carrier Recombination, and Crystallite Surface Passivation for Nanocrystalline, Organo-Halide Perovskite Thin-Films

This chapter has been adapted from the following publication:, Robert J. Stewart, Christopher Grieco, Alec V. Larsen, Joshua J. Maier, and John B. Asbury; Approaching Bulk Carrier Dynamics in Organo-Halide Perovskite Nanocrystalline Films by Surface Passivation. *J. Phys. Chem. Lett.*, 2016, 7 (7), pp 1148–1153, which has been adapted for the context of this dissertation.

3.1 Introduction

One of the central narratives in the organo-halide perovskite field has been that material and device performance depend largely on morphology and processing conditions.[65-68] This narrative is exemplified by the correlation of device performance with cuboid size,[69] by the disparity of perovskite crystallization kinetics when $PbCl_2$ versus PbI_2 are used as Pb^{2+} sources,[70-71] and by the influence of $PbCl_2$ on nucleation, growth and electronic structure of perovskite films.[65, 72-74] While there is little doubt that material morphology influences overall photovoltaic device performance, the underlying mechanisms by which morphology or processing conditions affect fundamental properties such as photoluminescence lifetime or charge recombination kinetics have not been fully clarified. Kinetic models have been proposed to predict how photoluminescence lifetime and recombination kinetics depend on the density of charge carriers and charge traps[39, 75] present in the forbidden bandgap of the materials, but the chemical origins of these traps remain unclear.

Recent experimental and computational studies suggest that charge recombination centers in organo-halide perovskites are related to the presence of iodide-rich chemical species[76-78] and that chemical passivation of these species upon coordination with small molecules can improve the performance of perovskite solar cells.[79-81] However, the role that charge recombination centers at the surfaces versus the bulk may have in influencing the electronic properties of perovskites remains unclear. Identifying the chemical origins of defects may provide insight about how to increase the long-term stability of organo-halide perovskite electronic materials and solar cells since many degradation pathways likely originate at the surfaces of perovskite crystals.[82]

We undertook a systematic study of charge recombination kinetics in a series of organo-halide perovskite films in an effort to elucidate the reasons why thin film processing conditions and morphologies influence charge recombination lifetimes in organo-halide perovskites. We utilized a two-step deposition method to form the perovskite films because the resulting materials represent the state of the art in terms of photovoltaic device performance.[66, 68-69, 83-85] A similar two-step spin-coating approach was used to systematically vary the cuboidal morphology of $CH_3NH_3PbI_3$ perovskite films that were deposited from solutions with differing concentrations of CH_3NH_3I.[69] We reasoned that the ability to tune film morphology in a controlled manner would provide an opportunity to explore quantitatively how surfaces and grain boundaries of organo-halide perovskites[65] are related to their electronic structure and mechanisms of charge recombination.

3.2 Materials and Methods

3.2.1 Material Synthesis and Preparation

Materials

Hydroiodic acid (Sigma Aldrich, 57wt% in water, distilled, stabilized, 99.95%), methylamine solution (Sigma Aldrich, 40wt% in water), ethyl alcohol (anhydrous, Fisher Scientific), dimethyl sulfoxide (Acros Organics, extra dry over molecular sieve, 99.7%), lead (II) chloride (Sigma Aldrich, trace metal basis, 99.999%), aluminum oxide (Sigma Aldrich, nanoparticles, <50nm particles, 20wt% in isopropanol), and 2-propanol (Sigma Aldrich, anhydrous, 99.5%).

Synthesis of Methylammonium Iodide

Methylammonium iodide (MAI) was synthesized according to previously reported methods.[86] Hydroiodic acid (aqueous, 57 wt %) was added dropwise to an aqueous solution of methylamine (40 wt %) and was stirred at 0°C for 3 hrs. Following the reaction, the solvent was evaporated under reduced pressure. The white solid was recrystallized from 200 proof ethanol, and the resulting crystals were dried at 150°C in vacuum overnight. The crystalline solid was used without further purification.

Preparation of meso-porous Al_2O_3 Substrates

To prepare the glass/meso-porous alumina substrates, glass microscope slides were sonicated for 5 minutes in each of the following: soap solution, distilled water, 200 proof ethanol, acetone, and isopropyl alcohol before being subjected to an oxygen plasma treatment for 5 minutes. The mesoporous aluminum oxide film was deposited by spin coating a 10 wt % solution of nanoparticles in isopropyl alcohol at 2500 rpm for 30 seconds on cleaned microscope slides. The films were annealed at 450 °C for 1 h. Prior to deposition of the perovskite film, the substrates were again treated with an oxygen plasma for 5 min to ensure complete emoval of stabilizers and other organic materials remaining from the nanoparticle solution.

Perovskite Film Casting Using a Sequential, Two-Step, Dip-Coat Procedure Followed by Treatment with 1,2-ethanedithiol

Our method of two-step, sequential, dip-coat perovskite film deposition followed previously reported methods.[87-89] $PbCl_2$ was dissolved in anhydrous dimethyl sulfoxide at a concentration of 1 mole/L and allowed to stir at 100^oC until fully dissolved. $PbCl_2$ films were cast from the 100^oC solution onto mp-Al_2O_3/glass substrates by spin coating the precursor solution at 3000 rpm for 20s and drying the film for 5 minutes at 100^oC. The resulting white, crystalline film was then dipped into a solution of specified concentration of MAI in 2-propanol. Conversion from a white to black film occurred within a few seconds, indicating very rapid conversion to the perovskite. All $PbCl_2$ films were dipped in the MAI/2-propanol solutions for 20 seconds and immediately dried with a stream of dry nitrogen to remove excess 2-propoanol, and no subsequent annealing was necessary. All film fabrication, dipping, and drying was performed in a dry-air glovebox. Select perovskite films were treated with a solution of 1,2-ethanedithiol (EDT) (1% v/v) dissolved in isopropyl alcohol. The perovskite film was flooded with the EDT/2-propanol solution for 20 seconds before spinning at 2000 rpm for 60 seconds. Excess EDT was removed from the film by washing with neat 2-propanol.

3.2.2 Material Characterization by Scanning Electron Microscopy, UV-Visible and FT-Infrared Absorption Spectroscopies, and X-Ray Diffraction

Scanning Electron Microscopy of Perovskite Films

Scanning Electron Micrographs of perovskite films were acquired with an FEI Helios NanoLab 660 Field Emission Scanning Electron Microscope (FESEM) with an accelerating voltage of 500 V. Figures 3.1 to 3.5 show SEM images of perovskite films synthesized from all concentrations of MAI iodide before and after EDT treatment; no significant film reconstruction occurs upon treatment with EDT.

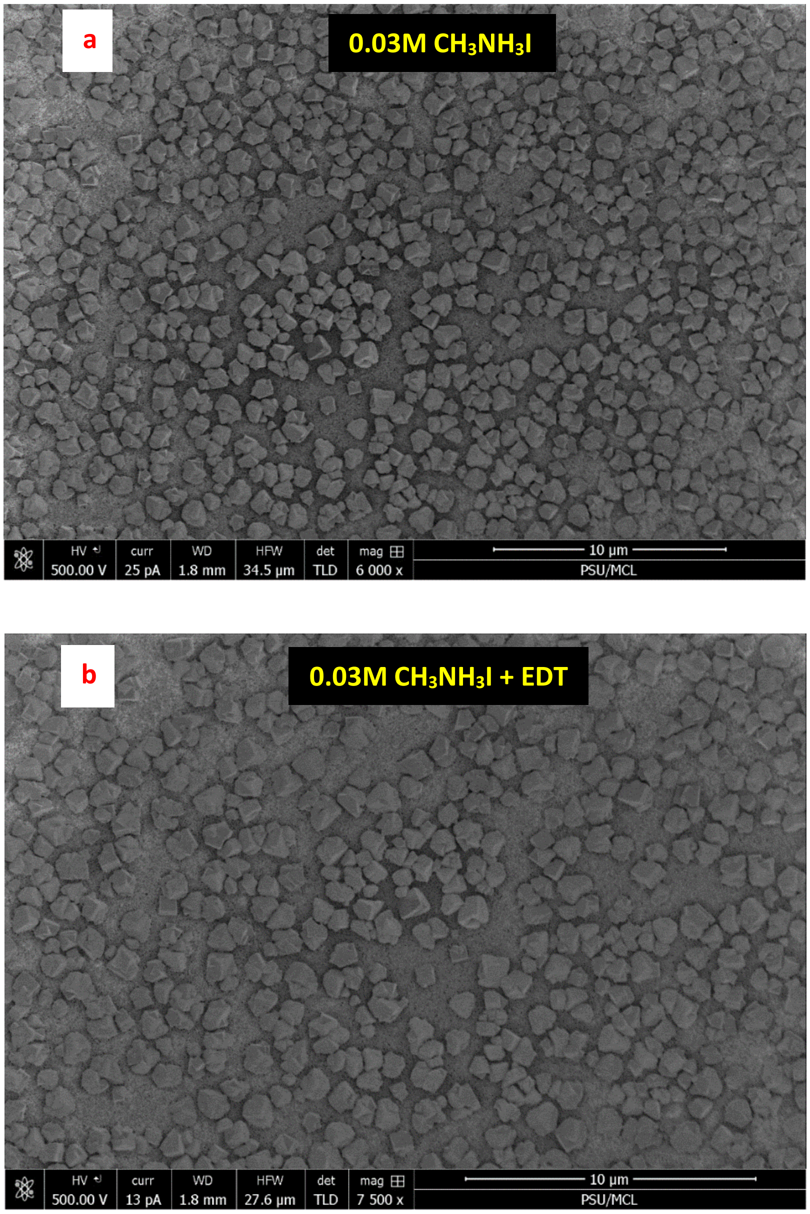

Figure 3.1: SEM Micrographs of perovskite films cast from $PbCl_2$ and 0.03M methylammonium iodide: a) before treatment with EDT and b) after EDT treatment.

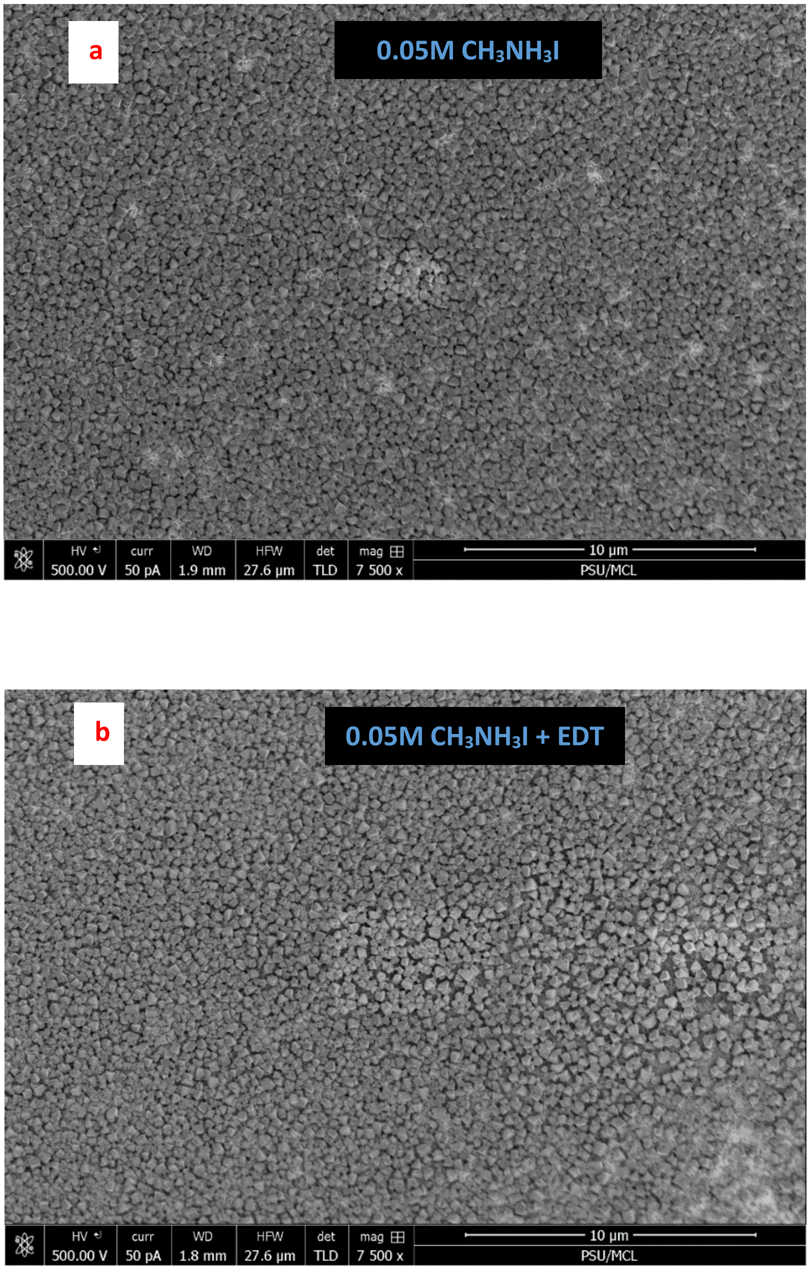

Figure 3.2: SEM Micrographs of perovskite films cast from $PbCl_2$ and 0.05M methylammonium iodide: a) before treatment with EDT and b) after EDT treatment.

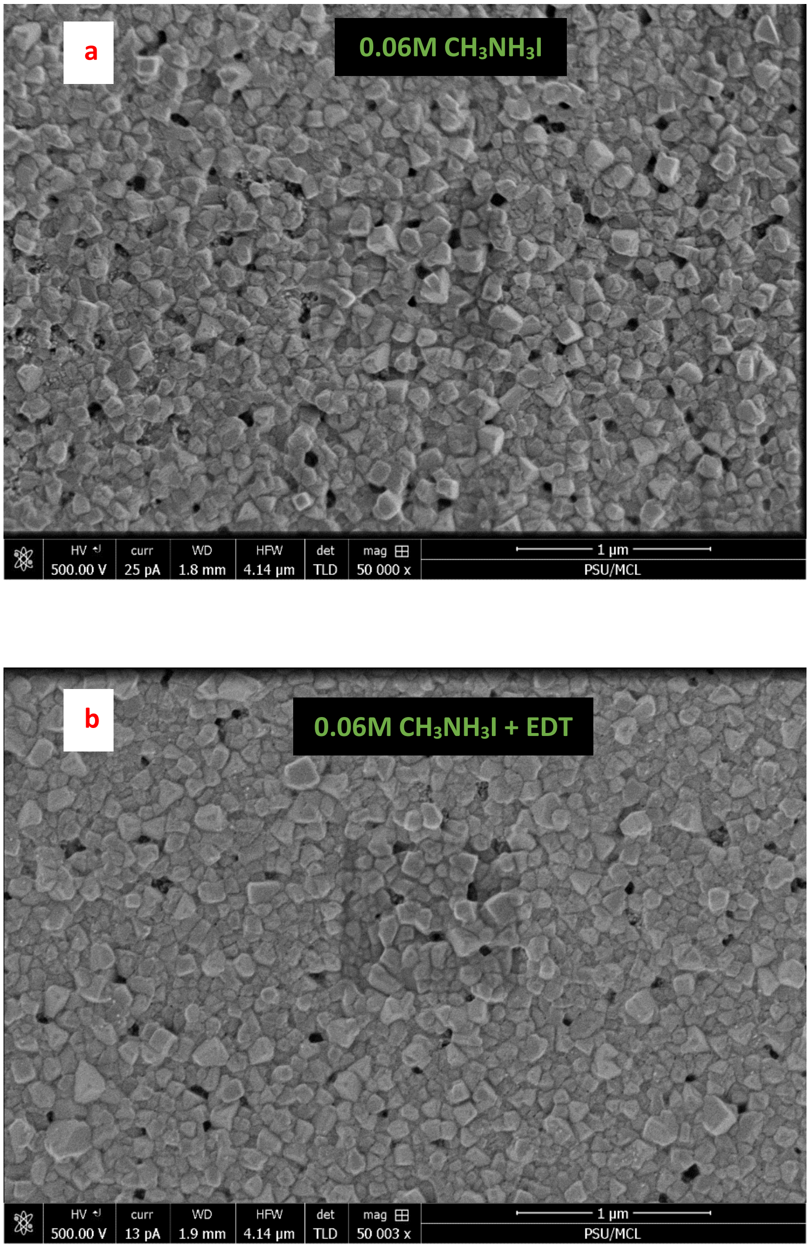

Figure 3.3: SEM Micrographs of perovskite films cast from $PbCl_2$ and 0.06M methylammonium iodide: a) before treatment with EDT and b) after EDT treatment.

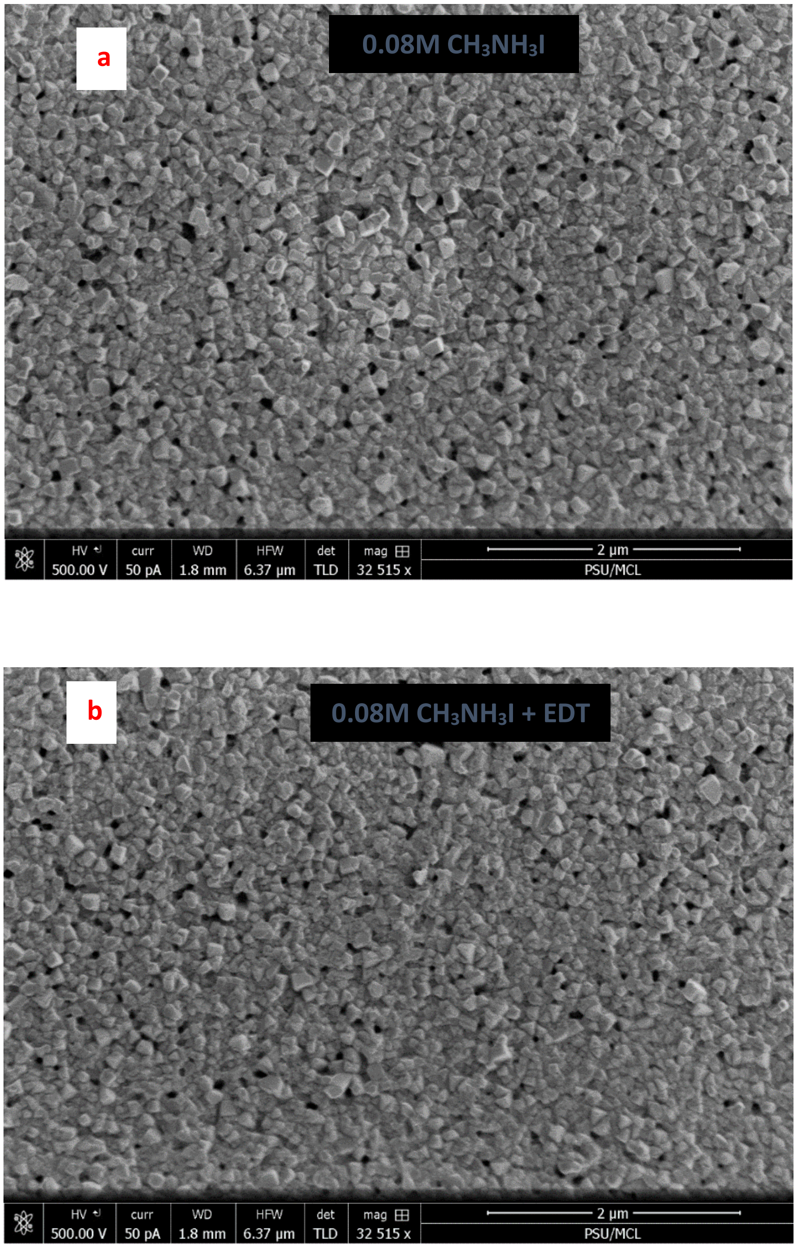

Figure 3.4: SEM Micrographs of perovskite films cast from $PbCl_2$ and 0.08M methylammonium iodide: a) before treatment with EDT and b) after EDT treatment.

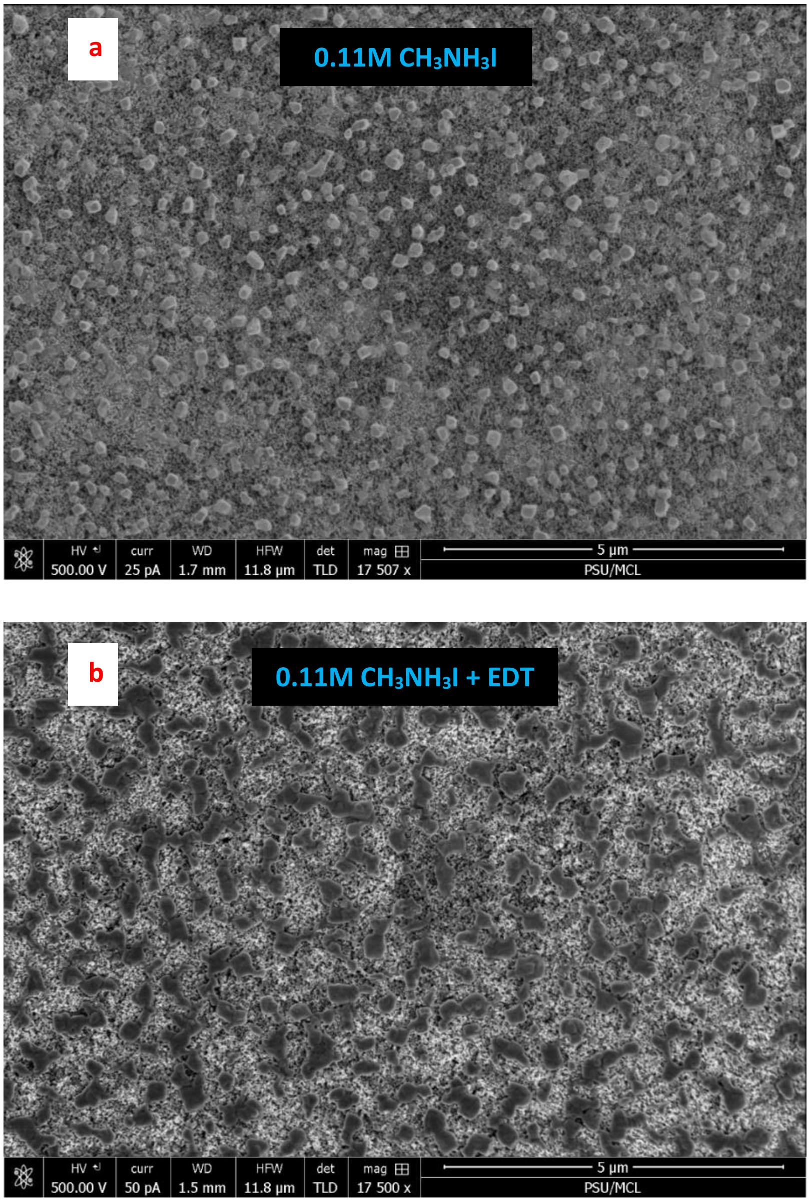

Figure 3.5: SEM Micrographs of perovskite films cast from $PbCl_2$ and 0.11M methylammonium iodide: a) before treatment with EDT and b) after EDT treatment. Like other perovskite films, those cast from 0.11M MAI do not undergo morphological reconstruction upon EDT treatment. However the films exhibit a bimodal morphology consisting of sub 20nm crystals and larger ~200 nm size grains.

UV-Visible Absorption Spectroscopy of Organo-Halide Perovskite Films

To ensure that the optical properties of perovskite films were invariant upon changes in composition or EDT treatment, UV/Visible absorption spectra of all perovskite films were acquired with a Beckman DU 520 UV/Vis spectrometer. The spectra were background subtracted by the glass/mp-Al_2O_3 substrate absorption. UV-Vis absorption spectra of all perovskite films are shown blow in Figure 3.6.

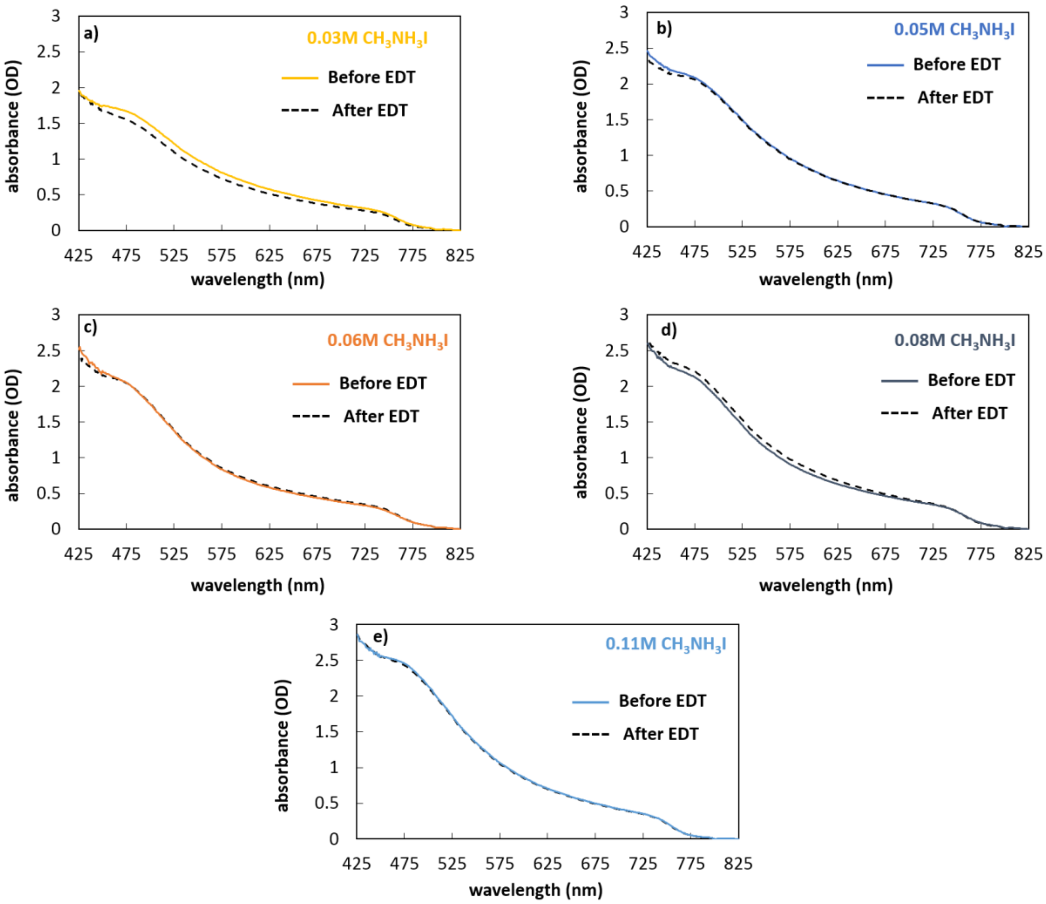

Figure 3.6: UV/Visible absorption spectra of perovskite films cast from a) 0.03M, b) 0.05M, c) 0.06M, d) 0.08M, and e) 0.11M MAI before and after EDT treatment. The data demonstrate that the optical band gap and absorption properties are unaffected by changes in MAI concentration and treatment with EDT.

Fourier-Transport Infrared (FT-IR) Absorption Spectroscopy of Organo-Halide Perovskite Films

FTIR absorption spectra of all perovskite films were acquired with a Digilab Varian FTS 7000 Series FTIR spectrometer equipped with a liquid N_2 cooled MCT detector. All reported spectra were the average of 1000 scans between the spectral range of 2100 – 4500 cm^{-1} where the glass/mp-Al_2O_3 substrate had adequately high optical transmission. The spectra were background subtracted by the glass/mp-Al_2O_3 substrate absorption and baseline corrected by fitting a third-order polynomial more than 200 cm^{-1} from the spectral region represented in the spectra appearing in Figure 3.7.

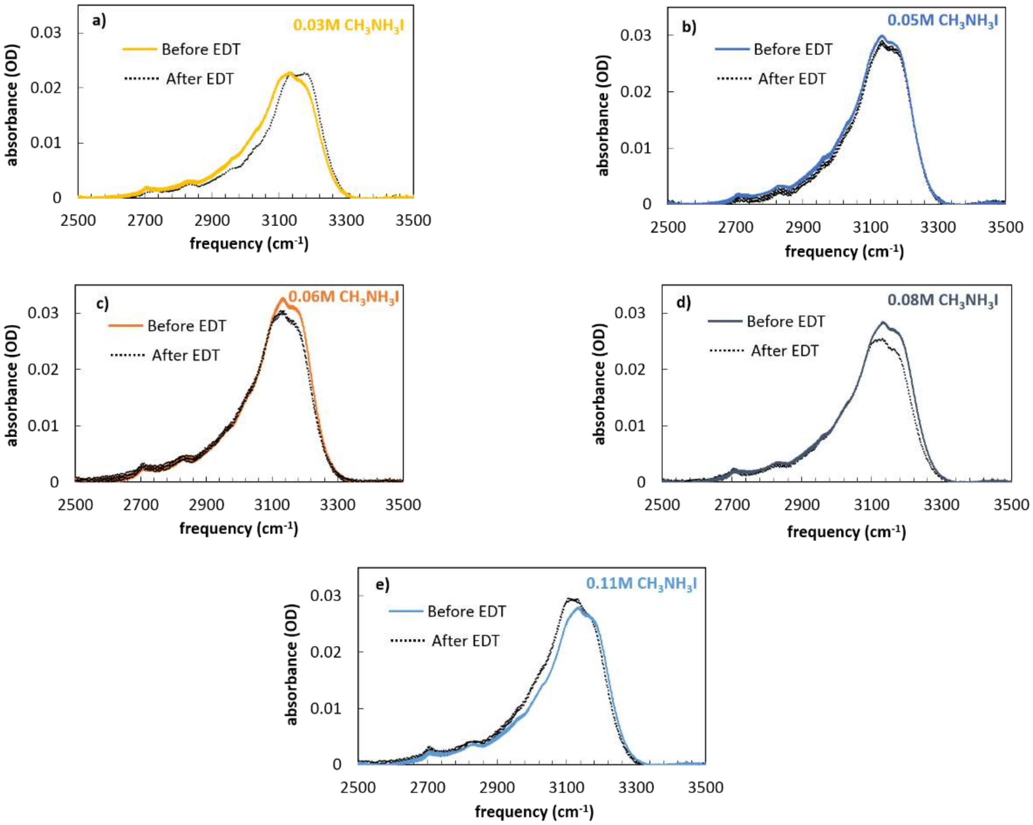

Figure 3.7: FTIR absorption spectra of perovskite films cast from a) 0.03M, b) 0.05M, c) 0.06M, d) 0.08M, and e) 0.11M MAI before and after EDT treatment. No significant change is observed in the spectral region where EDT absorbs strongly (2500-3000cm^{-1}) – indicating that the treatment does not result in large EDT accumulation in the bulk of the films.

X-Ray Diffraction of Organo-Halide Perovskite Films

To ensure that the crystal habit of the perovskite films remained unchanged by changes in precursor concentration or upon exposure to EDT, XRD characterization was performed on all perovskite films used for transient PL experiments. Bragg-Brentano X-ray diffraction patterns were measured with a PANalytical XPert Pro MPD X-ray diffratometer equipped with Cu Kα radiation and a PIXcel 1D detector. Diffraction patters were collected using 0.026° 2θ steps. Data were analyzed using Jade 7.0 software package.

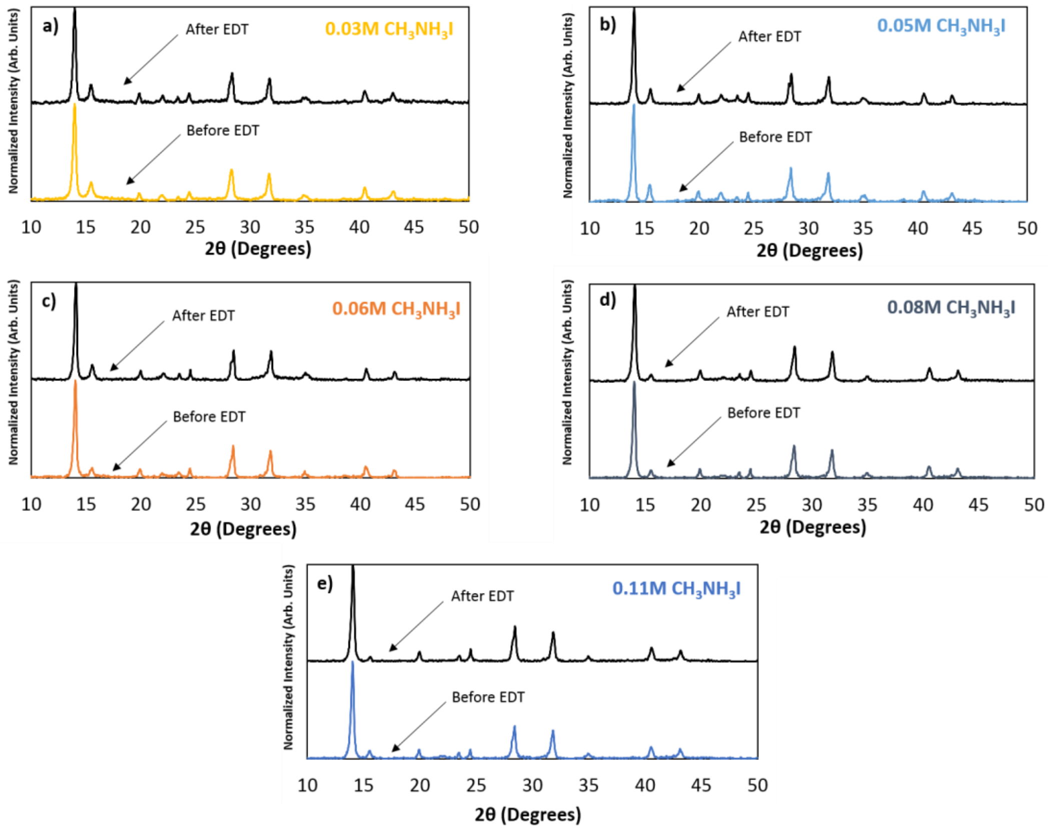

Figure 3.8: Bragg-Brentano diffraction patterns of perovskite films cast from a) 0.03M, b) 0.05M, c) 0.06M, d) 0.08M, and e) 0.11M MAI before and after EDT. The data demonstrate that the bulk perovskite crystal structure is unaffected by changes in MAI concentration and treatment with EDT.

3.2.3 Organo-Halide Perovskite Film Photoluminescence (PL) Spectra, Kinetics Data, Kinetics Fitting, and Excitation Fluence-Dependent PL Kinetics

From Figures 3.1 to 3.5, we are confident that the concentration of MAI used to prepare two-step deposited $CH_3NH_3PbCl_xI_{3-x}$ films strongly influences the morphology (cuboid crystallite size). Therefore, we sought to further investigate the role of this chemically-controlled morphology in the transient photophysics and charge carrier dynamics in identical perovskite films. Photoluminescence (PL) spectroscopy was identified as a sensitive method to characterize the excited-state, charge-carrier dynamics in these perovskite films. PL spectroscopy was performed using a homebuilt spectrometer assembled from the following components. A frequency-doubled Nd:YAG Laser (Surelite, Continuum) was used as the excitation source at 532nm and 16nJ/cm^2 optical energy density. Photoluminescence was collected and coupled into a monochromator (DK240, Spectral Products) using lenses. The output was focused onto a 350 MHz silicon photodiode (DET210, Thorlabs). The signal was amplified using a 200 MHz preamplifier (HVA-200M-40-B, FEMTO) and was digitized using a 200 MHz USB oscilloscope (Pico-5000, Picotech). All spectra were measured with 5nm wavelength resolution. To avoid film degradation, perovskite films were loaded into a gas-tight cryostat which was purged with dry nitrogen for 10-15 minutes prior to exposing the sample to the excitation source.

To measure the average emissive state lifetime $\langle\tau_{avg}\rangle$ in perovskite films, normalized PL transient data were fit to the phenomenological biexponential function shown as equation 3.1.

$$\langle\tau_{avg}\rangle = a \cdot e^{-\tau_1/t} + (1-a) \cdot e^{-\tau_2/t} \tag{3.1}$$

The biexponential function (eq 3.1) represents a linear combination of two exponential functions with short (τ_1) and long (τ_2) lifetimes where the fractional amplitude of each component is controlled by the prefactor a or (1-a). The bieponental fits to the PL data were optimized using the Unconstrained Nonlinear Nelder-Mead simplex algorithm in the Matlab Optimization Toolbox following convolution of the kinetics data with the instrument response function.

Figure 3.9 represents PL kinetics traces measured for the full composition range before the films were treated with EDT. Likewise, Figure 3.10 shows PL kinetics for the fill composition range after treatment with EDT. In both Figs 3.9 and 3.10, the data are shown as a semitransparent line, the biexponential fit is shown as a dark, solid line, and the individual exponential components (τ_1 *and* τ_2) of the bi-exponential fit are shown as dashed lines. Table 3.1 displays the individual lifetimes, amplitudes, and weighted, average lifetimes for all perovskite film PL kinetics data, before and after EDT treatment.

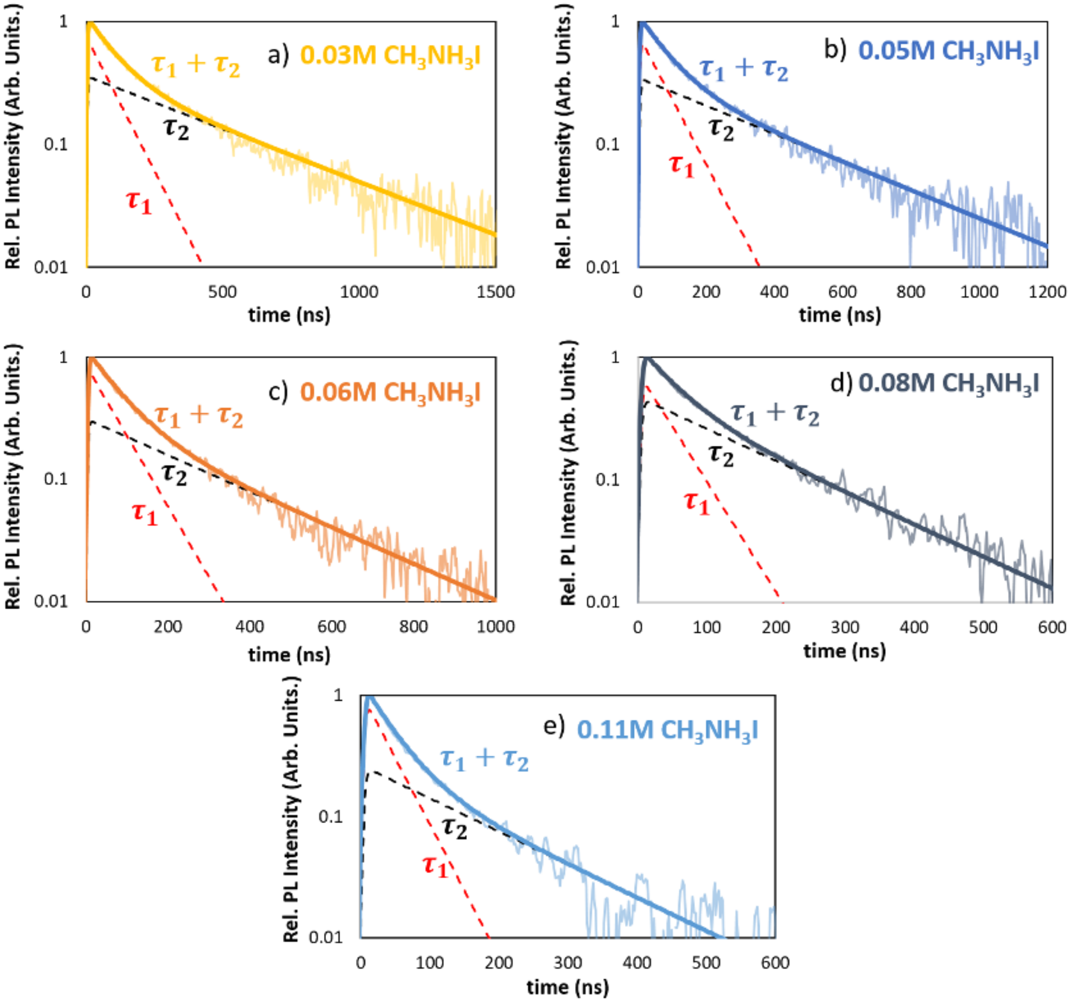

Figure 3.9: PL kinetics traces of perovskite films cast from a) 0.03M, b) 0.05M, c) 0.06M, d) 0.08M, and e) 0.11M MAI *before* EDT treatment. The data are shown as a semitransparent line, the fit of two exponential functions to the data is shown as a solid, bold line, and the fast (τ_1) and slow (τ_2) components of the biexponential fit are shown as dashed lines.

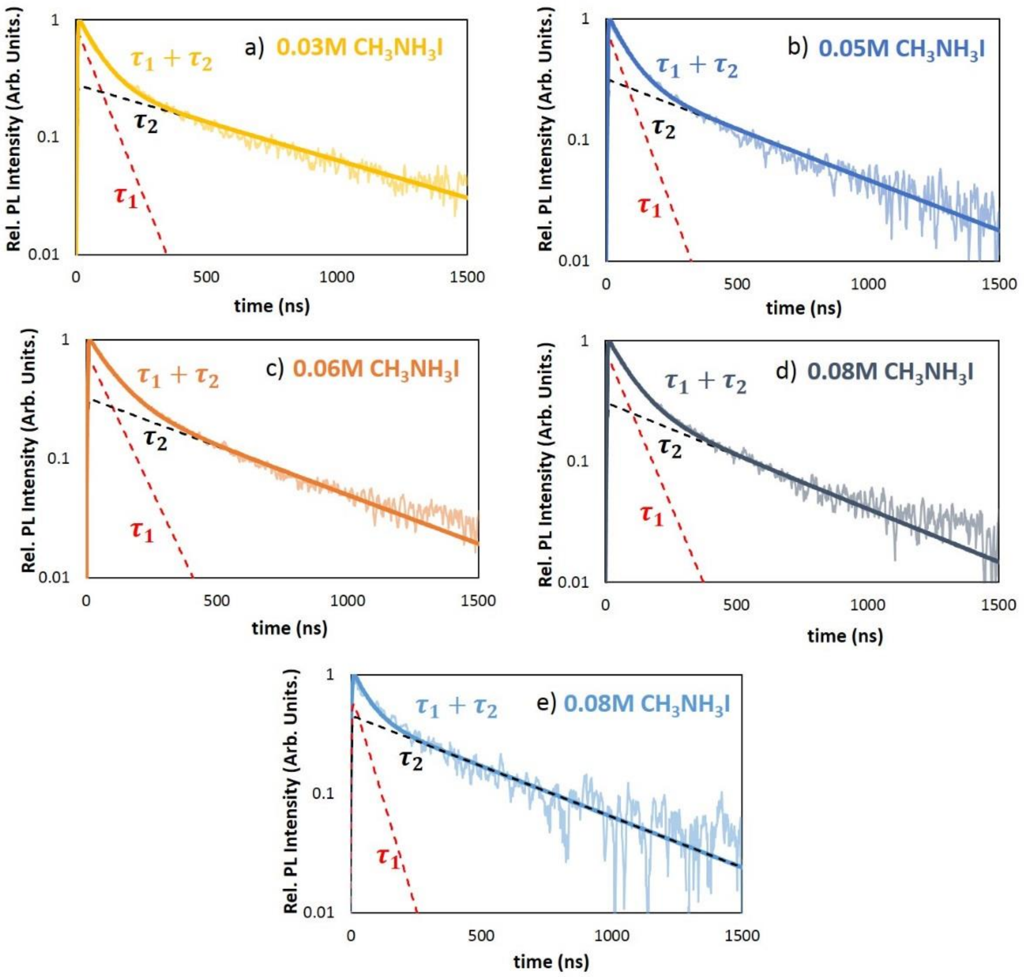

Figure 3.10: PL kinetics traces of perovskite films cast from a) 0.03M, b) 0.05M, c) 0.06M, d) 0.08M, and e) 0.11M MAI *after* EDT treatment. The data are shown as a semitransparent line, the fit of two exponential functions to the data is shown as a solid, bold line, and the fast (τ_1) and slow (τ_2) components of the biexponential fit are shown as dashed lines.

Table 3.1: Analysis of Biexponetial Fit Parameters for Perovskite PL Kinetics Data

	Before EDT				**After EDT**			
CH_3NH_3I Concentration (moles/Liter)	**τ_1 (ns)**	**τ_2 (ns)**	a	Avg τ (ns)	**τ_1 (ns)**	**τ_2 (ns)**	a	Avg τ (ns)
0.03	100.1	504.7	0.666	**235.5**	78.0	675.0	0.742	**231.7**
0.05	81.5	379.2	0.684	**175.6**	73.4	520.6	0.708	**203.9**
0.06	75.2	292.5	0.722	**135.6**	93.4	530.8	0.697	**225.7**
0.08	48.2	166.7	0.597	**95.9**	84.5	493.8	0.717	**200.4**
0.11	39.7	158.9	0.783	**65.6**	59.4	509.8	0.600	**239.6**

Time-integrated photoluminescence spectra were measured for all perovskite films before and after EDT treatment. Within the spectral resolution of the instrument (~5nm), no significant changes in the center wavelength or the energetic distribution of the emission profile were observed upon film casting from different CH_3NH_3I concentrations or upon treatment with EDT, as shown in Figure 3.11. The rigidity of the spectral position and lineshape supports the claim that casting conditions and treatment with EDT only influence non-radiative recombination centers and do not significantly perturb the emissive electronic states at the band edge.

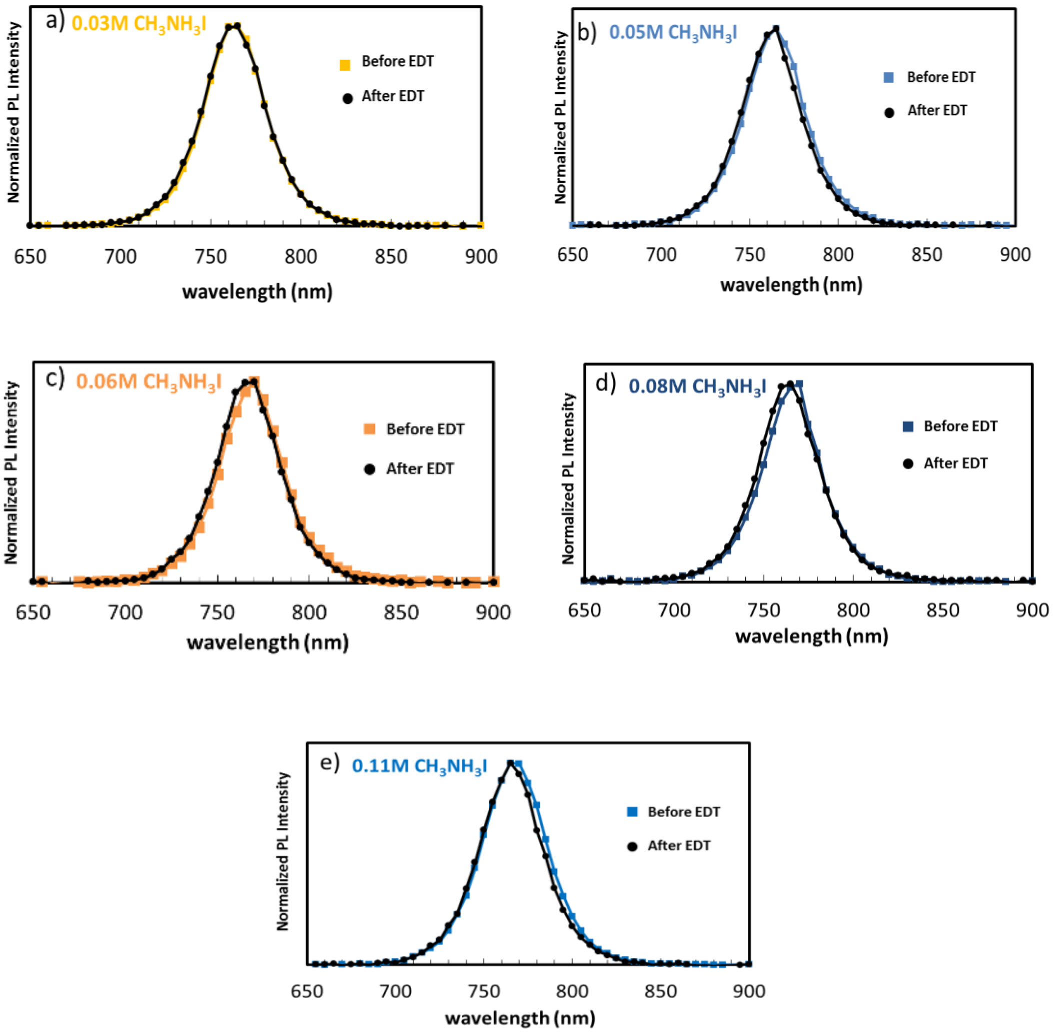

Figure 3.11: Time-integrated PL spectra of perovskite films cast from a) 0.03M, b) 0.05M, c) 0.06M, d) 0.08M, and e) 0.11M MAI before and after EDT treatment. The spectra show that the energy and distribution of the emissive state is unaffected by changes in MAI concentration and treatment with EDT.

To measure electron-hole recombination rates (R_{eh}) as a function of pump fluence, kinetics traces were collected for a perovskite film prepared from 0.11 M CH_3NH_3I after the film was treated with EDT. PL kinetics were measured at the center wavelength of the PL spectrum (765nm – as shown in Fig 3.11) for several excitation energy densities, and the normalized PL transient data were fit to equation (3.2) following convolution of the data with the instrument response. Again, the fit was optimized using the Unconstrained Nonlinear Nelder-Mead simplex algorithm in the Matlab Optimization Toolbox.

$$\frac{I_{eh}(t)}{I_{eh}(0)} = \frac{1}{(\mathbf{n_T} + Ax_0)}\left(\mathbf{n_T} + \frac{AC_1x_0e^{-\gamma t}}{C_1 + x_0(1 - e^{-\gamma t})}\right)\left(\frac{AC_1x_0e^{-\gamma t}}{C_1 + x_0(1 - e^{-\gamma t})}\right) \tag{3.2}$$

Equation 3.2 is the result of a kinetic model developed by Stranks, *et. al.*[11] and the three main fit parameters used in our fitting scheme were: the occupied electron trap density (n_T), total electron trap density (N_T), and the rate of electron-hole recombination not mediated by traps (γ_0), which is related to the total recombination rate (γ) by:

$$\gamma = \frac{n_T\gamma_0}{A + n_T} + \frac{AR_{pop}(N_T - n_T)}{A + n_T} \tag{3.3}$$

where $A \approx 8 \times 10^{16} cm^{-3}$ and $R_{pop} = 2 \times 10^{-10} cm^3 s^{-1}$ as determined by the original authors.[11]

$$x_0 = \frac{N(0)}{A + n_T} \tag{3.4}$$

where N(0) is the initial carrier density which was calculated by $N(0) = j\alpha$ where j is the excitation fluence ($photons/cm^2$) and α is the absorption coefficient at the pump wavelength ($8.8 \times 10^4 cm^{-1}$ at 532nm).

$$C_1 = \frac{n_T}{A} + \frac{R_{pop}(N_T - n_T)}{\gamma_0} \tag{3.5}$$

The bimolecular, electron-hole recombination constant (R_{eh}) was calculated from γ_0, A, and the exciton recombination rate ($R_x = 3.2 \times 10^6\ s^{-1}$) according to eq (3.6):

$$R_{eh} = \frac{\gamma_0 - R_x}{A} \qquad \boxed{3.6}$$

the bimolecular electron-hole recombination constant ($R_{eh} \approx 6 \times 10^{-10}\ cm^3 s^{-1}$) we extract from fitting PL transients measured at low excitation energy density, where higher order annihilation pathways do not compete with bimolecular and trap-assisted pathways, is compatible with other reports. All fluence-dependent PL kinetics traces are shown in Figure 3.15 (B) as dots and the best fit to equation 3.2 is shown as a solid line. The extracted recombination rate γ_0 is plotted against excitation pump fluence in Figure 3.15 (C). All parameters used in the excitation energy dependent PL measurements are included in Table 3.2: experimental values of excitation energy densities, and corresponding photon fluence and initial excited state densities (N(0)) are shown along with values extracted from transient PL data fitting: nT, NT, γ_0, and R_{eh}.

Table 3.2: Parameters from Excitation Energy Density Dependent PL Measurements

Laser Energy Density (μJ /cm^{-2})	**Excitation Fluence (photons/cm^{-2})**	**N(0) (cm^{-3})**	**nT (cm^{-3})**	**NT (cm^{-3})**	**γ_0 (s^{-1})**	**R_{eh} (cm^{3}s^{-1})**
0.02	5.3 x 10^{10}	**4.7 x 10^{15}**	5.6 x 10^{14}	7.9 x 10^{15}	5.1 x 10^{7}	6.0 x 10^{-10}
0.05	1.3 x 10^{11}	**1.2 x 10^{16}**	9.7 x 10^{14}	8.2 x 10^{15}	6.8 x 10^{7}	8.1 x 10^{-10}
0.40	1.1 x 10^{12}	**9.4 x 10^{16}**	1.1x 10^{15}	8.6 x 10^{15}	3.0 x 10^{7}	3.7 x 10^{-9}
1.00	2.7 x 10^{12}	**2.4 x 10^{17}**	8.2 x 10^{15}	7.5 x 10^{15}	4.6 x 10^{8}	5.6 x 10^{-9}
5.01	1.3 x 10^{13}	**2.8 x 10^{18}**	9.7 x 10^{15}	8.1x 10^{15}	5.7 x 10^{9}	7.1 x 10^{-8}

3.3 Results and Discussion

3.3.1 Correlation of Electron-Hole Recombination Rate with Nanocrystallite Surface Area to Volume Ratio

Figure 3.12(A) represents a reiteration of the high-resolution scanning electron microscopy (SEM) images shown in Figs 3.1 – 3.4. Selected micrograph areas from the series of $CH_3NH_3PbCl_xI_{3-x}$ perovskite films were examined and reveal similar cuboidal morphology with the characteristic variation in the dimensions of the cuboids as reported previously by the Gratzel lab.[69]

Time-resolved photoluminescence (PL) spectroscopy has been widely used in the organo-halide perovskite literature to assess the electronic structure of materials with longer PL decays being associated with higher performance materials.[65, 81, 90] Charge carrier lifetimes in excess of hundreds of nanoseconds have been observed in mixed halide perovskites by PL spectroscopy. A kinetic model describing the transition from trap-limited unimolecular to bimolecular charge recombination was developed by Stranks *et al.* from which charge trap densities in high performance materials as low as 10^{15} cm^{-3} were estimated.[39, 91] Furthermore, the role of chlorine in reducing electron-hole recombination rates in $CH_3NH_3PbI_{3-x}Cl_x$ was recently reported.[92]

The PL decay kinetics represented in Figure 3.12(B) on a semi-log plot were measured in $CH_3NH_3PbCl_xI_{3-x}$ perovskite films whose SEM images appear in Figure 3.12(A) following 16 nJ/cm^2 excitation at 532 nm. A phenomenological bi-exponential fit function was used to quantify

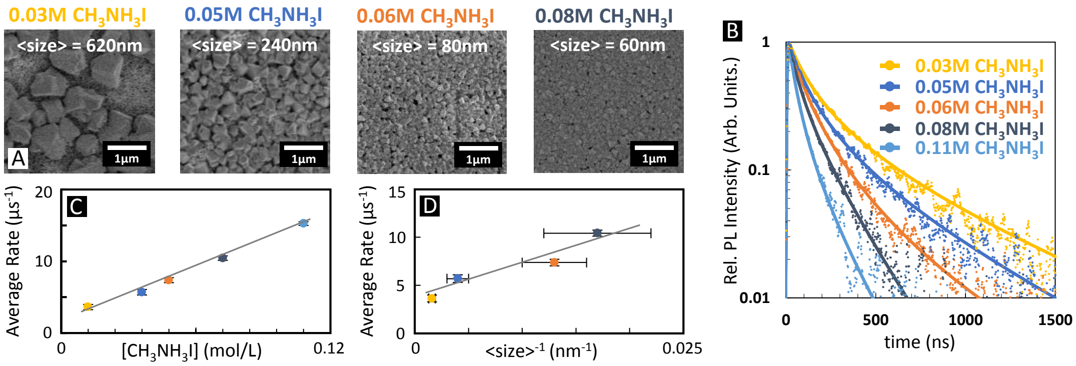

Figure 3.12: (A) SEM images reveal the evolution of the cuboidal morphology of $CH_3NH_3PbI_3$ perovskite films deposited under different concentrations of CH_3NH_3I following a two-step procedure. (B and C) The photoluminescence decays of the corresponding films demonstrate that the charge carrier recombination rates vary amongst the perovskite films. (D) The average charge recombination rate is related to the surface area to volume ratio of the cuboids present in the perovskite films.

the PL decay kinetics.[90, 93] The data reveal a significant variation of the average PL decay lifetimes of the perovskite films as their morphologies vary across the series. Tuning the concentration of CH_3NH_3I in the dip-coat solution from 0.03 to 0.11 moles/Liter causes the average lifetime to vary from about 230 ns to about 60 ns (summarized in Table 3.1).

The inverse of the average charge recombination lifetimes (average rates) obtained from fitting the PL decays are summarized in Figure 3.12(C) and reveal that the lifetimes reported here are comparable to those reported in the literature for high performance perovskite materials.[65, 81, 90] The uncertainty limits of the average rates obtained from the fitting procedure are represented by error bars, which are comparable to the sizes of the symbols in Figure 3.12(C). A linear correlation is observed between the concentration of CH_3NH_3I in the dip-coat solution and the average recombination rates. The correlation indicates that greater densities of charge recombination centers are formed in the presence of higher CH_3NH_3I concentrations in the dip-coat solution, which is consistent with the lower photovoltaic performance of $CH_3NH_3PbI_3$ perovskite solar cells fabricated in a similar manner.[69] It is noteworthy that the increase in average rate is associated with a decrease of the cuboid size across the series of perovskite films examined here.[94-95]

Motivated by the correlation of average recombination rate with cuboid size, we analyzed SEM images of films deposited from various concentrations of CH_3NH_3I to quantify the average cuboid sizes in the series. We reasoned that the surface area to volume ratio of the cuboids is proportional to the inverse of their size. The correlation of average recombination rate with the average inverse cuboid size appears in Figure 3.12(D) showing the rate is indeed proportional to the surface area to volume ratio of the perovskite crystals.

This correlation suggests that the chemical species giving rise to charge recombination centers are principally localized on the surfaces of the perovskite

3.3.2 Approaching the Bulk-Crystalline Radiative-Limit by Chemical Passivation of Nanocrystalline Organo-Halide Perovskite Films

A number of surface passivation strategies involving small organic molecules have been developed to reduce the density of recombination centers at surfaces of lead-based nanocrystals including thiols,[96-101] mercaptopropionic acid[100, 102] and hydrazine.[96, 103] Guided by this prior work, we examined the effect of exposing defective $CH_3NH_3PbCl_xI_{3-x}$ perovskite films to solutions of 1,2-ethanedithiol (EDT). $CH_3NH_3PbCl_xI_{3-x}$ perovskite films were identical to the films that were characterized by SEM imaging and time-resolved PL spectroscopy (Figure 3.12). However, the films were exposed to 0.12 mole/Liter EDT in 2-propanol for 20 seconds and then characterized using the same techniques. The comparison of PL decay traces in Figure 3.13(A) reveals that exposure of the perovskite films to EDT quantitatively eliminates the variation of the charge recombination rates among the set of $CH_3NH_3PbCl_xI_{3-x}$ perovskite films before and after EDT treatment. The variation of average rates among the set of films is reduced to less than 10% (Figure 3.13(B)) – identical within experimental precision determined from multiple PL kinetics traces measured in several films of each type. Because PL decay rates correlate with the density of charge recombination centers in organo-halide perovskites,[39] the data reveal that EDT treatment quantitatively eliminates excess recombination centers in films that were initially exposed to higher concentrations of CH_3NH_3I during conversion to the perovskite phase.

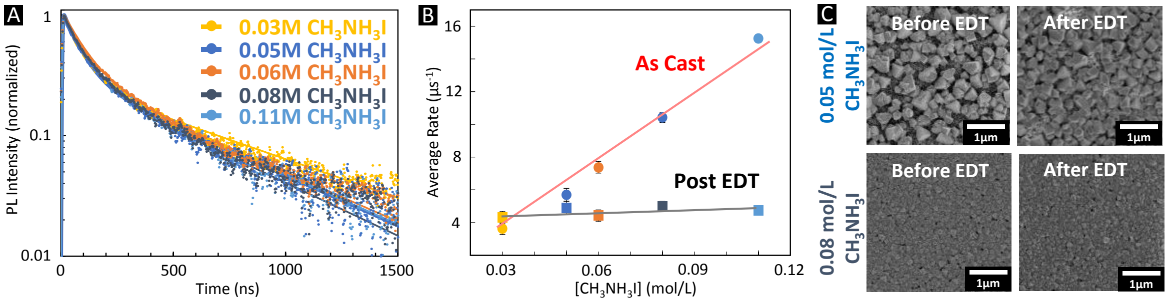

Figure 3.13: (A) Chemical treatment of defective $CH_3NH_3PbCl_xI_{3-x}$ perovskite films with EDT causes their photoluminescence decay traces to converge – indicating that surface passivation quantitatively removes charge recombination centers. (B) Summary of the variation of the average charge recombination lifetimes of perovskite films before and after EDT treatment. (C) SEM images demonstrate that the removal of charge recombination centers does not change the cuboidal morphology of the perovskite films.

The photovoltaic performance of organo-halide perovskite films deposited using similar two-step methods has been correlated with the size of cuboidal structures that form in the films.[69] Therefore, we investigated whether the elimination of excess charge recombination centers in highly defective perovskites might result from reconstruction of the film during the EDT treatment. We hypothesized that because all of the perovskite films exhibit similar PL decays following EDT exposure, their morphologies may have been converted to the same cuboidal size distributions following the treatment. Figure 3.13(C) represents select SEM images of $CH_3NH_3PbCl_xI_{3-x}$ perovskite films that were measured before and after EDT treatment. The full set of SEM images of all films examined in this work before and after EDT treatment appear in the method section 3.2.2. Upon visual inspection, it is evident that the characteristic sizes of the cuboids are not affected by EDT treatment. We conclude therefore that the variation of the PL decay kinetics and the corresponding densities of charge recombination centers among the set of perovskite films are not intrinsic properties of the cuboidal morphologies of the films.

X-ray diffraction was used to determine whether the elimination of charge recombination centers by EDT treatment can be explained in terms of changes in crystalline habit or chemical composition changes in the bulk of the perovskite crystals. Figure 3.14(A) represents Bragg-Brentano XRD diffraction patterns measured in a $CH_3NH_3PbCl_xI_{3-x}$ perovskite film deposited under 0.06 mole/liter CH_3NH_3I dip-coat solution without EDT treatment as a control for comparison to perovskite films deposited under various CH_3NH_3I concentrations and treated with EDT. We find we are able to place the thin film samples in the diffractometer with a precision of ± 0.025 degrees 2θ, which affects the absolute location of the diffraction peaks. Correcting for this variation demonstrates that the diffraction peaks vary by less than 0.01 degrees 2-theta across the set of films – indicating that the bulk structures of the perovskite crystals are unchanged by EDT treatment. Bragg-Brentano XRD diffraction patterns of the complete composition range before and after EDT treatment are represented in Figure 3.8.

Figure 3.14(B) depicts PL spectra measured in $CH_3NH_3PbCl_xI_{3-x}$ films deposited under a 0.03 and 0.11 mole/liter CH_3NH_3I dip-coat solutions before and after EDT treatment. In both cases, the spectra are indistinguishable within experimental precision indicating that the optical bandgaps of the perovskite crystals of both sizes are unchanged by surface passivation with EDT. In total, the data indicate that EDT is segregated primarily to surfaces and grain boundaries in analogy to nanocrystalline inorganic semiconductors such as colloidal quantum dot solids for which similar surface passivation treatments are routinely employed.[96-101]

It is interesting to compare the PL decay kinetics of the nanocrystalline organo-halide perovskite films examined here with corresponding measurements in macroscopic single perovskite crystals.[40, 93] In particular, a bi-exponential PL decay with a 22 ± 6 ns component (~66%) and a 1032 ± 150 ns (~34%) component was recently reported in a $CH_3NH_3PbI_3$ single crystal.[93] This bi-exponential decay is characterized by an average time constant of ~330 ns. Figure 4(A) compares the change in PL decay kinetics before and after EDT treatment

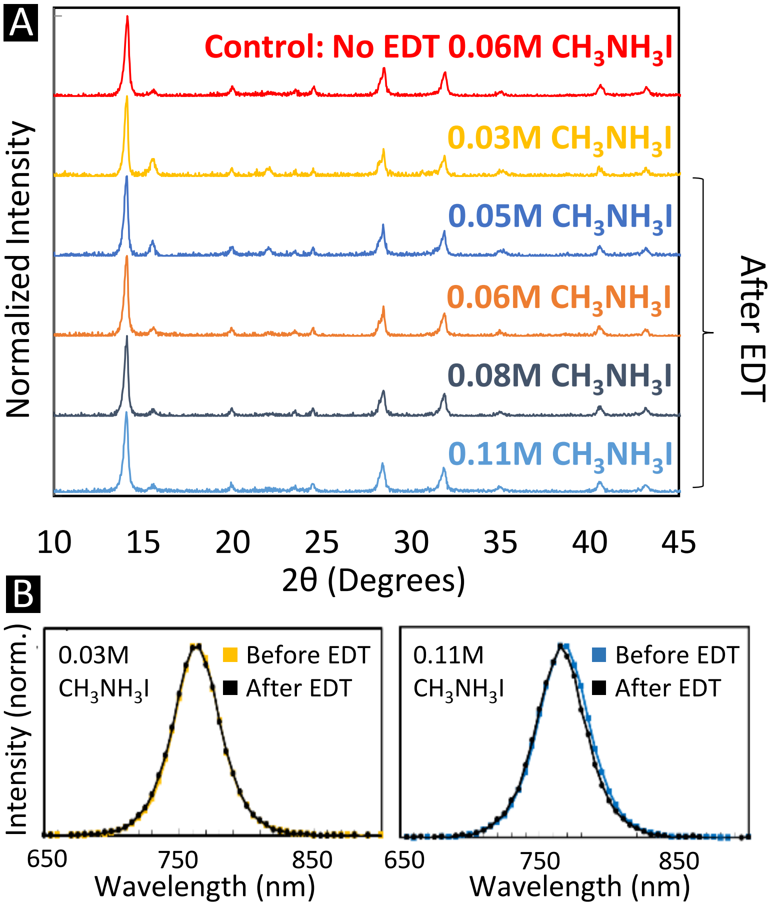

Figure 3.14: (A) X-ray diffraction patterns of CH3NH3PbI3 perovskite films deposited from various CH3NH3I solutions following EDT treatment. (B) PL spectra of 0.03M and 0.11M CH$_3$NH$_3$I perovskite films before and after EDT treatment demonstrating that the interiors of the cores of the perovskite crystals are unchanged by passivation of surface defects.

that were measured in a $CH_3NH_3PbI_3$ nanocrystalline film deposited from a 0.11M CH_3NH_3I solution. The bi-exponential fit of the PL decay after EDT treatment is described by a 60 ± 4 ns component (~60%) and a 510 ± 25 ns component (~40%) with an average time constant of ~240 ns, which is similar to the average lifetime measured in the single crystal. For comparison, analysis of the bi-exponential fit function of the PL decay in the film before EDT treatment reveals an average tine constant of only ~60 ns.

Intrigued by the similarity of the average PL decay time constant reported in bulk perovskite crystals[93] and in the EDT treated $CH_3NH_3PbCl_xI_{3-x}$ nanocrystalline films examined in this work, we measured the excitation energy density dependence of the EDT treated perovskite film deposited from 0.11 M CH_3NH_3I solution and analyzed the results using the kinetic model reported by Stranks *et al.*[39, 91] Pump fluences at 532 nm wavelength in the range of $5 \cdot 10^{10}$ cm^{-2} to $1 \cdot 10^{13}$ cm^{-2} were examined. The PL kinetic decay curves overlaid with corresponding fit functions appear in Figure 3.15(B) on a semi-logarithmic plot and exhibit pseudo first-order behavior at the lowest pump fluence (indicating by the quasi-linear shape of the kinetic trace labeled $5 \cdot 10^{10}$ cm^{-2}). This behavior occurs because the density of photo-generated charges was similar to the density of trap states in the material at the lowest pump fluence examined.[39] At higher pump fluences, a cross-over from pseudo first-order to bimolecular decay kinetics occurs and is indicated by the increased curvature of the kinetic decay curves in Figure 3.15(B).

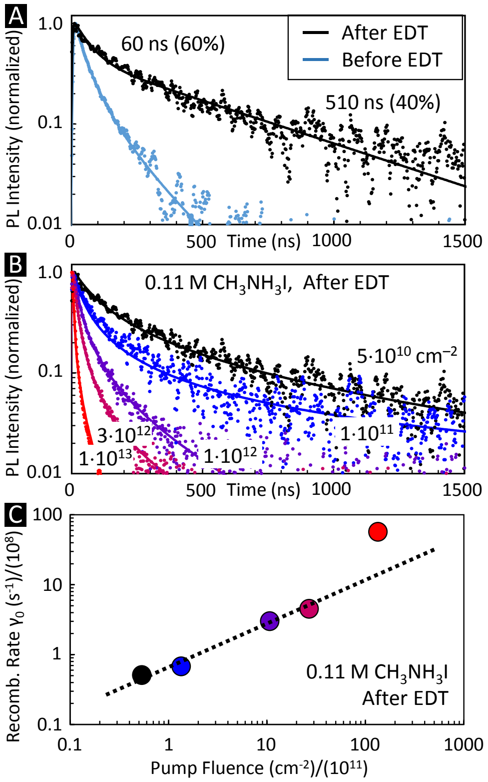

Figure 3.15: (A) Comparison of PL decay kinetics measured in a $CH_3NH_3PbI_3$ film deposited from 0.11M CH_3NH_3I solution before and after surface passivation by EDT showing marked increase in charge recombination lifetime. The time constants obtained from a bi-exponential fit of the data after EDT treatment are indicated. (B) PL decay kinetics measured in the EDT treated $CH_3NH_3PbI_3$ film deposited from 0.11M CH_3NH_3I solution at a variety of pump fluences (indicated). (C) Plot of the charge recombination rate extracted from a kinetic model used to fit the PL decays versus the pump fluence. The recombination rate increases with excitation density and begins to exhibit nonlinear behavior above fluences of $3 \cdot 10^{12}$ cm^{-2} due to the onset of high-order annihilation processes. The dotted line serves as a guide to the eye.

Analysis of the decay curves using the kinetic model reported by Stranks *et al.* permits us to quantify the charge recombination rates not involving traps[39] versus pump fluence, which are summarized in Figure 3.15(C). The uncertainty limits of the recombination rates and pump fluence values are smaller than the symbols represented in the figure. The data reveal the expected inverse relationship of charge recombination lifetime with pump fluence.[95, 104] At pump fluences in excess of $3 \cdot 10^{12}$ cm^{-2}, higher order annihilation processes such as exciton-exciton annihilation and Auger recombination processes lead to nonlinear dependence of the recombination rate with increased pump fluence.[104] Furthermore, adaptation of the kinetic model permits us to extract the constant for bimolecular charge recombination (R_{eh} in reference 39) with a value of $6 \cdot 10^{-10}$ cm^3/s - compatible with prior reports of high performance organo-halide perovskite materials[36-37, 105] given that our excitation density was higher than that used by Stranks *et al.* [39, 91] The detailed fitting procedures and parameters used to adapt the kinetic model developed by Stranks *et al.* are provided in section 3.2.2.

Comparing the PL decay times in our nanocrystalline thin films to those measured in macroscopic single crystals as we have done assumes that charge carrier diffusion does not significantly affect the recombination dynamics.[104] The observation of pseudo first-order recombination with a pump fluence of $5 \cdot 10^{10}$ cm^{-2} in Figure 3.15(B) (the excitation density used throughout this work with the exception of the excitation density dependence study) suggests that carrier diffusion does not significantly influence the recombination kinetics at such low fluence. At higher excitation densities, bimolecular charge recombination is observed, which typically does involve carrier diffusion.

We note that in macroscopic single crystals, surface defects should have little influence on the charge carrier dynamics because carriers have low probability of encountering surfaces. Therefore, the observation of much faster average PL decay kinetics in the unpassivated $CH_3NH_3PbCl_xI_{3-x}$ film deposited from 0.11M CH_3NH_3I solution is not surprising. The ability to extend the PL decay kinetics of such small crystallites into the microsecond time scale (Figure 3.15(A)) and approaching the bulk limit measured in macroscopic single crystals, simply by surface passivation, indicates that the majority of charge recombination centers in the nanocrystalline perovskite films are localized at the surfaces. These observations suggest that the morphology of the perovskite crystallites is not the key material attribute that determines their electronic properties. Rather, the surface chemistry of the crystallites appears to determine the density of charge recombination centers in the material, which then determines the charge carrier lifetime.

It is useful to consider the nature of charge recombination centers on the surfaces of organo-halide perovskites. Prior work suggested that surface exposed iodide or lead ions[79-81] might by responsible for the formation of charge recombination centers. The increased polarizability of surfaces leading to stronger electron-phonon coupling has also been implicated as a possible origin of traps and recombination centers in perovskites.[106] The data reported here reveal that surface defects can be quantitatively removed by reaction with EDT. In the context of colloidal quantum dots, EDT is believed to react with lead-rich surfaces that include under-coordinated Pb^{2+} ions.[96-101] Extending the analogy to organo-halide perovskites, the data suggest that EDT reacts with lead-rich species on the surfaces leading to average charge carrier lifetimes that approach those measured in macroscopic perovskite single crystals. At present we are unable to determine whether such lead-rich species exist at organo-halide perovskite surfaces or whether EDT might etch iodide-rich surfaces thereby exposing lead-rich species with which the molecules then react. The topic of chemical identity of iodoplumbate (PbI_x^{2-x}) species giving rise to organo-halide perovskite defects is the focus of Chapter 5 in this dissertation.

3.4 Conclusion

In summary, we demonstrated that recombination centers limiting charge carrier lifetimes in organo-halide perovskite materials are preferentially located at surfaces rather than in the bulk of the perovskite crystals, even in crystals < 60 nm in size. Furthermore, we showed that surface passivation of the perovskite nanocrystals quantitatively removes excess charge recombination centers. Comparisons of photoluminescence decays from this work with the corresponding measurements in macroscopic single crystals reported in the literature indicate that surface passivation alone provides a means to create nanocrystalline perovskite films with electronic properties approaching the bulk limit. These findings suggest that much of the dependence of perovskite material and device properties on processing conditions and morphology may be explained by how these affect the surface chemistry of the perovskite crystals. These findings further suggest that surface passivation may provide a means to decouple the electronic properties of organo-halide perovskites from the processing conditions used to deposit the films.

CHAPTER 4

Iodoplumbate Precursor Solution Chemistry Influences Electronic Structure of Semiconductor Organo-halide Perovskite Films

This chapter has been adapted from the following publication: Robert J. Stewart, Christopher Grieco, Alec V. Larsen, Grayson S. Doucette, and John B. Asbury; Molecular Origins of Defects in Organo-Halide Perovskites and Their Influence on Charge Carrier Dynamics *J. Phys. Chem. C*, **2016**, 120 (23) pp 12392 – 12402, which has been adapted for the context of this dissertation.

4.1 Introduction

The solar to electrical power conversion efficiencies of lead-based organo-halide perovskite photovoltaics have risen dramatically in recent years.[83, 107-110] These materials are even more remarkable because they exhibit high power conversion efficiencies despite being processed from solution. Recently, two-step deposition approaches have been reported in which a film of the Pb(II) salt precursor is first deposited followed by conversion to the perovskite phase via exposure to the CH_3NH_3I (MAI) precursor in solution or from the vapor phase.[66, 68-69, 83-85, 111-113] Some researchers report that devices fabricated using this approach exhibit superior uniformity and reproducibility[83, 111-112] in comparison to devices fabricated using one-step approaches[114-119]. In such one-step approaches, both the Pb(II) salt and MAI precursors are present together in a single solution from which the perovskite films are deposited.

We hypothesized that the difference in reproducibility and performance of two-step versus one-step deposited organo-halide perovskite films may arise from the solution chemistry of the precursors and how they influence the underlying defect chemistry of the perovskite films. At present, the nature of the defect states principally responsible for controlling the density of charge recombination centers in organo-halide perovskites remains unclear. Several suggestions have been proposed in the literature including interstitial iodide[77] or iodoplumbate anti-site defects[76], surface exposed lead[81] or iodide[79] ions, or enhanced electron-phonon coupling due to polarization of surface states in the presence of photogenerated charges[106]. Ab-initio calculations suggest that many types of defects that contribute mid-gap states in typical covalently bonded solids only contribute electronic states near the conduction or valence bend edges in organo-halide perovskites.[76, 78]

We undertook a systematic study investigating the solution chemistry of organo-halide perovskite precursors and their influence on the electronic properties of the corresponding perovskite films in an effort to gain insight about their defect chemistry and the corresponding influence of the deposition methods. We reasoned that the modest annealing temperatures reported for organo-halide perovskite films may cause some of the iodide or iodoplumbate species formed under equilibrium conditions in precursor solutions to survive the film formation and annealing process, thereby influencing the final densities of charge recombination centers. To identify the principal precursor moieties leading to crystalline defects and to provide insight about approaches to eliminate them, we varied the ratios of MAI to PbI_2 or $PbCl_2$ as a means to systematically tune the concentrations of iodide or iodoplumbate species in precursor solutions. These precursor solutions were then used to cast perovskite films using the one-step deposition method and characterized using time-resolved photoluminescence (TRPL) spectroscopy to measure the emission decay times. These decay times have been used in the literature to assess the electronic structure of perovskite materials, in which higher performance thin-film and single crystal materials are associated with longer decay times.[65, 81, 90, 120-121] The emission decay kinetics were analyzed using a kinetic model developed by Stranks et al.[39, 91] to quantify the recombination rate involving charge recombination centers in the perovskite films. We used this analysis combined with quantitative solution chemistry and materials characterization to correlate the concentrations of solution-phase chemical species with the presence of charge recombination centers in the corresponding perovskite films.

From this analysis, we found remarkably high concentrations of iodoplumbates in precursor solutions used in one-step deposition procedures reported in the literature,[114-119] with the concentration of tetraiodoplumbate (PbI_4^{2-}) uniquely correlated with the densities of charge recombination centers. Our findings indicate that the organo-halide perovskite films deposited using two-step methods may exhibit improved uniformity and reproducibility because they do not require digestion of high concentrations of iodoplumbates during film formation. As a consequence, there is greater latitude in film deposition conditions using the two-step methods to achieve low defect densities in the perovskite films in comparison to those deposited using one-step methods. Furthermore, the comparison of organo-halide perovskite films deposited from precursor solutions using PbI_2 versus $PbCl_2$ as the Pb^{2+} source reveals that the use of $PbCl_2$ suppresses the formation of charge recombination centers in both deposition methods. These results demonstrate that suppression of higher order iodoplumbates is one of the principal origins of lower defect densities and superior electronic properties of mixed-halide perovskites that are reported in the literature[90] in addition to the beneficial effects of chloride on interface states.[92]

4.2 Materials and Methods

4.2.1 Materials Synthesis and Preparation

Materials

The following materials were purchased and used without further purification: hydroiodic acid (Sigma Aldrich, 57wt% in water, distilled, stabilized, 99.95%), methylamine solution (Sigma Aldrich, 40wt% in water), ethyl alcohol (anhydrous, Fisher Scientific), dimethyl sulfoxide (Acros Organics, extra dry over molecular sieve, 99.7%), lead (II) iodide (Alpha Aesar, ultra dry, 99.999%), lead (II) chloride (Sigma Aldrich, trace metal basis, 99.999%), lead (II) nitrate (Sigma Aldrich, trace metal basis, 99.999%), potassium iodide (Sigma Aldrich, anhydrous, 99%), aluminum oxide (Sigma Aldrich, nanoparticles, <50nm particles, 20wt% in isopropanol), and 2-propanol (Sigma Aldrich, anhydrous, 99.5%).

Methylammonium Iodide Synthesis

Methylammonium iodide (MAI) was synthesized according to previously reported.[90] Briefly, dropwise addition of hydroiodic acid (aqueous, 57 wt %) to a solution of methylamine (aqueous, 40 wt %) was stirred at 0°C 3 hrs, and followed by evaporation of the solvent under reduced pressure. The solid was recrystallized from 200 proof ethanol, and the white crystals were heated to 150°C in vacuum overnight to drive off excess solvent. The crystalline solid was stored under vacuum and used without further purification.

Perovskite Film Deposition Procedures

The glass/mesoporous alumina substrates used for all perovskite films examined in this chapter were prepared on glass microscope slides that were sonicated for 5 minutes in each of the following: soap solution, distilled water, 200 proof ethanol, acetone, and isopropyl alcohol. They were then subjected to an oxygen plasma treatment for 5 minutes. The mesoporous aluminum oxide film was deposited by spin coating at 2500 rpm for 30 seconds from a 5 wt % solution of nanoparticles in isopropyl alcohol on the cleaned microscope slides. The films were annealed at 450 °C for 1 h. Prior to deposition of the perovskite film, the substrates were again treated with an oxygen plasma for 5 min to ensure complete removal of stabilizers and other organic materials present in the colloid of Al_2O_3 nanoparticles.

One-Step spin-coat perovskite film deposition followed previously reported methods for high performance materials.[71] Precursor solutions were prepared by dissolving specified mole ratios of $MAI:PbI_2$ or $MAI:PbCl_2$ in anhydrous dimethyl sulfoxide while maintaining a constant lead precursor concentration of 576 ± 2mM. The precursor solution was dripped on glass/ Al_2O_3 substrates and 30 seconds was allowed for the solution to penetrate the mesoporous Al_2O_3 layer before being spun at 2000 rpm for 45s. The resulting films were annealed to form crystalline $CH_3NH_3PbI_3$ perovskite. 1:1 $MAI:PbI_2$ films were annealed at 150°C for 15 minutes, 3:1 $MAI:PbCl_2$ films were annealed for 45 minutes at 100°C. Sub-stoichiometric $MAI:PbX_2$ films required less annealing time while films prepared with excess MAI required extended annealing times. All film fabrication and annealing was performed in a dry-air glovebox, which was found to provide higher performing devices than those prepared in inert, nitrogen atmosphere.[122]

Two-step dip-coat perovskite film deposition followed previously reported methods.[83, 123] $PbCl_2$ was dissolved in anhydrous dimethyl sulfoxide (DMSO) at a concentration of 0.5 moles/Liter $PbCl_2$ or PbI_2 was dissolved in anhydrous N,N-dimethylformamide (DMF) at a concentration of 0.5 moles/Leiter. $PbCl_2$ or PbI_2 films were prepared on mp-Al_2O_3/glass by spin coating the precursor solution at 3000 rpm for 20s and drying the film for 3 minutes at 100^oC. The resulting crystalline film was then submerged into a solution of 6 mg/mL MAI in 2-propanol. Conversion from a white ($PbCl_2$) or yellow (PbI_2) film to black perovskite film occurred almost immediately. The lead salt film were dipped in the MAI/2-propanol solution for 20 seconds and immediately dried with a stream of dry nitrogen to remove excess 2-propoanol, and no subsequent annealing was necessary. All operations were performed in a dry-air glovebox.

4.2.2 UV-Visible Absorption Spectroscopy of Potassium Iodide:Lead (II) Iodide Solutions and Extraction of Iodoplumbate Extinction Coefficients

KI:PbI_2 solutions used to quantify the molar extinction coefficient of iodoplumbate species were prepared by making stock solutions of 770.1mM KI and 271.6 μM PbI_2 in DMSO. Solid KI was dried in a vacuum oven overnight before weighing the solid on an Ohaus Explorer Pro balance (± 0.5mg tolerance) and PbI_2 was weighed on a micro balance (±0.1μg tolerance). Spectroscopic samples were prepared by mixing appropriate volume of stock solutions to achieve the specified KI:PbI_2 mole ratio while maintaining a 100μM or 200μM PbI_2 concentration. Care was taken to limit the exposure of iodide solutions to ambient light to prevent photochemical degradation.

UV-Vis spectra of all KI:PbI_2 solutions (shown in Figures 4.1 and 4.2) were measured with a Perkin-Elmer Lambda 950 spectrometer equipped with the standard detector attachment (Si PMT) with 1nm spectral resolution. Spectra were acquired with samples loaded into a 10mm UV fused quartz cuvettes (Thor Labs). All absorbance spectra were background subtracted with a solution of matching path length and concentration of KI dissolved in DMSO.

From the literature, we find that PbI_2 has a ground state absorption band centered on 290 nm, and PbI_3^- exhibits two bands in the near-UV region centered on 250 nm and 330 nm. PbI_4^{2-} has a peak around 370 nm, making all three iodoplumbate species spectroscopically distinct from each other, although with overlapping peaks.[124-126] The dissociation constant of KI into K^+ and I^- ions in DMSO at room temperature was previously measured as 1.02 moles/liter.[127] Additionally, it was found previously that PbI_2 undergoes identical complexation with iodide ions, regardless of the iodide source (CH_3NH_3I or KI).[126] Therefore, we used this mixture of KI and PbI_2 in DMSO for the quantitative investigation of the influence of solution phase precursors on the electronic structure of organo-halide perovskites in the solid state.

We used the evolution of the proportions of iodoplumbate species as a function of I^- concentration to systematically vary the concentration of PbI_2, PbI_3^- and PbI_4^{2-} species in solution. By maintaining a constant concentration of the Pb^{2+} source in all solutions, we were able to map the changes in absorption of the various species present in the solutions to their corresponding iodide concentration changes – thereby allowing us to quantitatively extract the molar absorption coefficients of all iodoplumbate species. We found that the solution equilibria were strongly affected by the total concentration of PbI_2, and consequently, we used low concentration solutions of PbI_2 (100 µM or 200 µM) to obtain the molar absorption coefficients of the relevant species and then used these results to analyze the coordination chemistry present in the concentrated solutions of CH_3NH_3I/PbX_2 used to deposit organo-halide perovskite films following the one-step, spin-coating approach.

We used solutions of KI and PbI_2 (200 µM) with KI:PbI_2 mole ratios between 100:1 and 400:1 in DMSO to observe the onset of conversion of PbI_2 species into PbI_3^-. Within this concentration regime, PbI_2 and PbI_3^- are the dominant species and little PbI_4^{2-} forms. To obtain the molar absorption coefficient of the PbI_4^{2-} peak at 370 nm, we examined solutions of KI and PbI_2 with much greater KI:PbI_2 mole ratios of 800:1 to 3000:1 while maintaining a total lead II (Pb^{2+}) concentration of 100 µM. This lower concentration was necessary to enable accurate measurement of absorption spectra without artifacts arising from strong absorption of PbI_3^- present in the solutions.

The fits to the absorption spectra F(λ) for each solution can be described as a linear combination of absorption spectra of the individual species, where the absorption of each species is determined by its concentration and molar absorption coefficient ε, which depends on wavelength, λ.

$$F(\lambda) = [PbI_2]\varepsilon_{PbI_2} + [PbI_3^-]\varepsilon_{PbI_3^-} + [PbI_4^{2-}]\varepsilon_{PbI_4^{2-}} \qquad \boxed{4.1}$$

Because all solutions have large excess of I^-, we assume the concentration of PbI^+ is negligible so that the sum of the concentrations of PbI_2, PbI_3^- and PbI_4^{2-} is equal to the total concentration of idoplumbate species. This assumption specifies that

$$[PbI_2] + [PbI_3^-] + [PbI_4^{2-}] = C_{total} \tag{4.2}$$

where C_{total} was 200μM for mole ratios between 100:1 and 400:1 KI:PbI_2 and 100μM for mole ratios between 800:1 and 3000:1 KI:PbI_2. Therefore, for solutions with KI:PbI_2 mole ratios less than 400:1, we divided the measured peak amplitudes of each species by a factor of two so they would reflect the same 100 μM concentration of iodoplumbate species. Because the molar absorption coefficients do not depend on concentration, this multiplier does not affect the fitting results. However, the difference in concentration does affect the slope of the variation in fit amplitudes versus solution composition because the solution equilibria depend sensitively on concentration. The optical path length of 10 mm was common to all measurements of UV absorption spectra and has been taken into account in the molar absorption coefficient calculation.

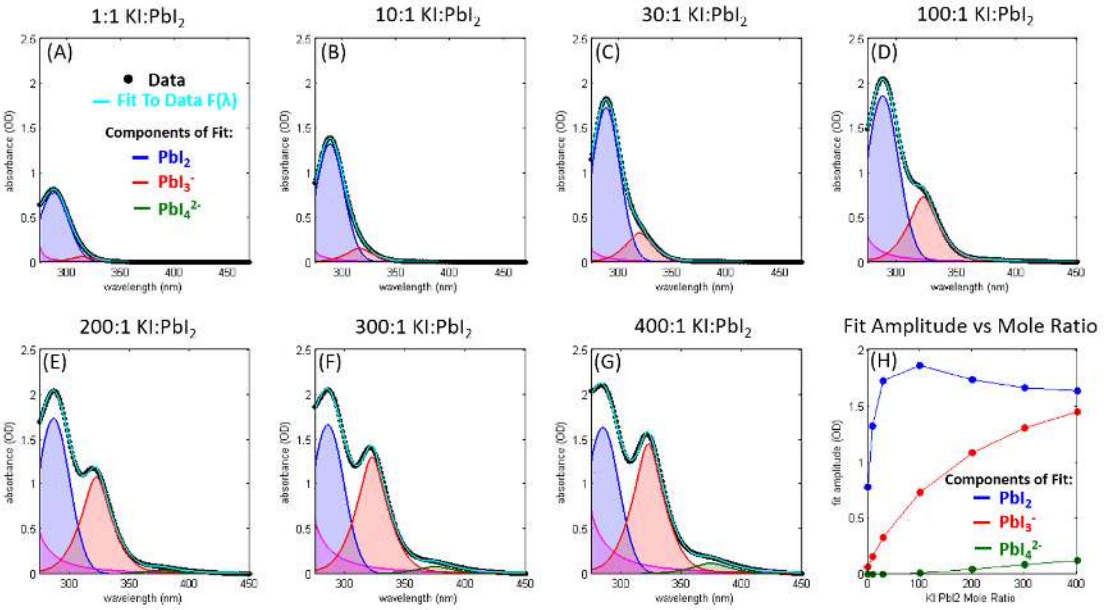

Figure 4.1: Solution UV/Vis absorbance spectra of 0.2 mM (200 μM) PbI_2 mixed with the following concentrations of potassium iodide: (A) 0.2 mM, (B) 2 mM, (C) 6 mM, (D) 20 mM, (E) 40 mM, (F) 60 mM, and (G) 80 mM. Overlaid on the data (black dots) in (A) – (G) are peaks representing the individual absorbing components (PbI_2, PbI_3^-, and PbI_4^{2-}) and the total fit to the data [F(λ)], shown as a cyan line, which is a linear combination of the individual spectral components according to equation 4.1. (H) shows the fit amplitudes versus mole ratio of KI:PbI_2 for each iodoplumbate species (PbI_2, PbI_3^-, and PbI_4^{2-}). To obtain the data shown in Figure 3(B) (in-text), these fit amplitudes were divided by a factor of two in order to reflect the optical density of 100 μM PbI_2 solutions.

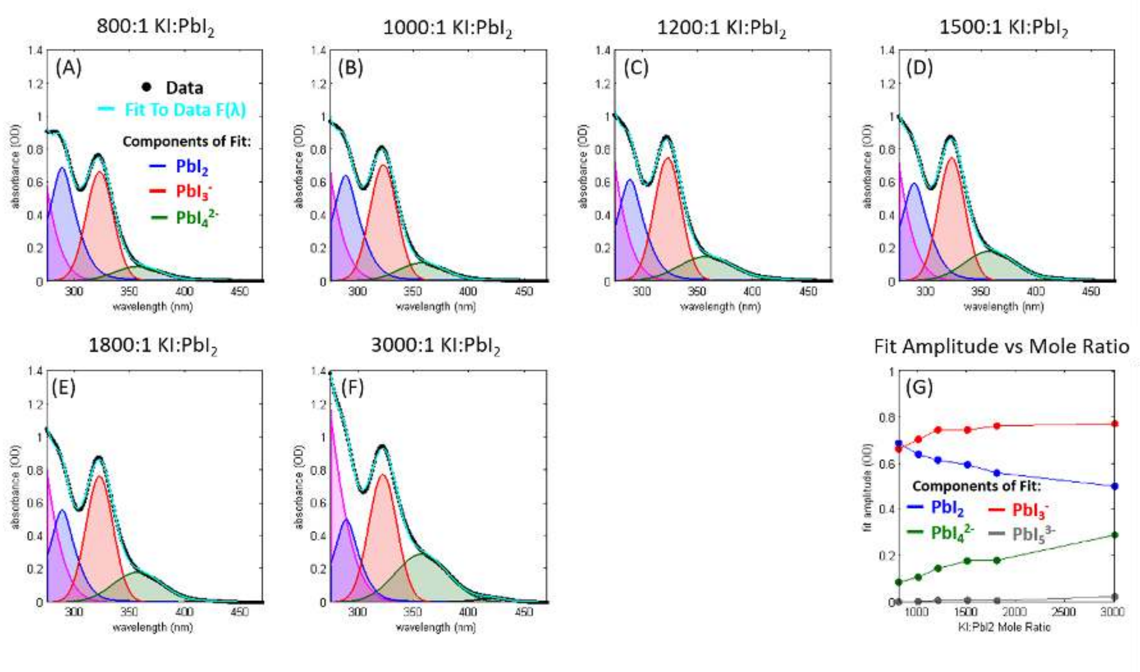

Figure 4.2: Solution UV/Vis absorbance spectra of 0.1 mM (100 μM) PbI$_2$ mixed with the following concentrations of potassium iodide: (A) 80 mM, (B) 100 mM, (C) 120 mM, (D) 150 mM, (E) 180 mM, and (F) 300 mM. Overlaid on the data (black dots) in (A) – (F) are peaks representing the individual absorbing components (PbI$_2$, PbI$_3^-$, and PbI$_4^{2-}$) and the total fit to the data [F(λ)], shown as a cyan line, which is a linear combination of the individual spectral components according to equation 4.1. (G) shows the fit amplitudes versus mole ratio of KI:PbI$_2$ for each iodoplumbate species (PbI$_2$, PbI$_3^-$, and PbI$_4^{2-}$). These data are identical to the data presented in Figure 3(B) (in-text).

The experimental spectra represented in Figures 4.1 and 4.2 are overlaid with fit spectra [F(λ)] that are indistinguishable from the data – indicating the fidelity of the fits. The width and position of the peaks used to fit the spectral data were held constant while fitting the spectra at various concentrations. The only fit parameters were the amplitudes of the individual spectral components and the fit was optimized using the Unconstrained Nonlinear Nelder-Mead simplex algorithm in the Matlab Optimization Toolbox.

It should be noted that all spectra were background subtracted by a solution of KI in DMSO with matching concentration to that used to prepare KI:PbI_2 solution; however, KI has negligible absorption at 270 nm and longer wavelengths. Furthermore, all measurements were conducted with a common path length of 10 mm defined by the quartz cuvettes used in the double-beam spectrometer (Perkin-Elmer Lambda 950). Although DMSO was used as the blank in the measurements, a small tail of the absorption centered below 250 nm appears in the spectra due to imperfect balance of the cuvettes. A fit function was included to account for this tail. We fit the variation in absorption of the three iodoplumbate species (identified by blue, red, and green shaded profiles) to extract the molar absorption coefficients.

The curves overlaid on the data in Figure 4.3 were calculated by varying the molar absorption coefficients so that the calculated change in absorption of all three species best matched the observed variation under the constraint that the sum of the concentrations of all three species must equal 200 or 100 µM. The values of the molar absorption coefficients are constrained in this analysis by the amplitude changes of the absorption of each species. The best fit was found by minimizing the sum of the squares of the residuals between the calculated absorbance values of all three species versus the measured values for all solution compositions. By accounting for the relative absorbance changes and the total concentration of all iodoplumbate species, the fitting procedure results in molar absorption coefficients of PbI_2, PbI_3^- and PbI_4^{2-} of 10,000 ± 500 $M^{-1}cm^{-1}$, 45,000 ± 13,500 $M^{-1}cm^{-1}$, and 13,600 ± 2,720 $M^{-1}cm^{-1}$, respectively. The confidence limits were established by systematically changing the values of the molar absorption coefficient in question away from its optimal value, allowing all other parameters to vary to re-optimize the fit, and repeating until the sum of the squares of the residuals was 50% larger than the value obtained from the global best fit.

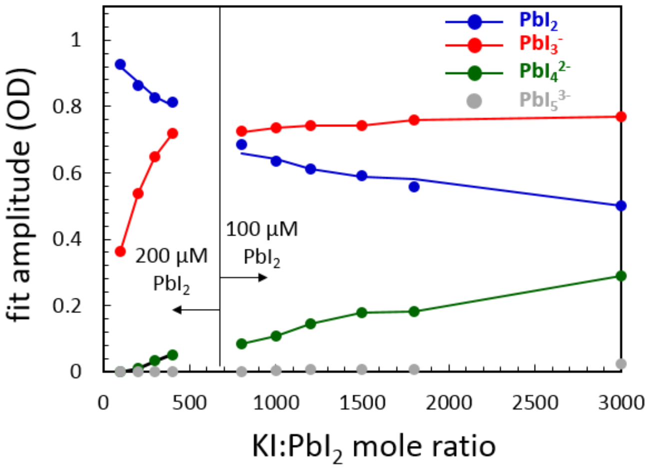

Figure 4.3: The fit amplitudes for each iodoplumbate species extracted from a fitting analysis of the solution spectra in Figures 5.1 and 5.2 from which the molar absorption coefficients of PbI_2, PbI_3^-, and PbI_4^{2-} are obtained. Due to optical density complications, spectra for mole ratios below 400:1 KI:PbI_2 were collected with solutions containing 200µM PbI_2, and mole ratios exceeding 800:1 KI:PbI_2 were measured for samples containing 100µM PbI_2. The molar absorption coefficients for PbI_2, PbI_3^-, and PbI_4^{2-} are: 10,000 $M^{-1}cm^{-1}$, 45,000 $M^{-1}cm^{-1}$, and 13,600 $M^{-1}cm^{-1}$, respectively.

4.2.3 UV-Visible Absorption Spectroscopy and Extraction of Iodoplumbate Concentrations in Solutions Preceding Organo-Halide Perovskite Film Deposition

To quantify the concentrations of iodoplumbate species in film-relevant precursor solutions (~40 wt %), we prepared solutions of PbI_2 or $PbCl_2$ in DMSO at 576 ± 2 mM concentration. When homogenous solutions formed following heating or sonicating, the appropriate mass of solid MAI was added to achieve the specified MAI:PbX_2 mole ratio. In comparison to the KI:PbI_2 solutions described in section 4.2.2 above, the film-relevant MAI:PbX_2 precursor solutions were at least 2500 times more concentrated. Due to the high concentrations, it was necessary that the path length of the optical, liquid-cell required for UV-Visible absorption measurements be three orders of magnitude shorter than the 10 mm cuvette used for the KI:PbI_2 measurements. The home-built liquid cell used in these experiments was composed of two sapphire optical flats mechanically clamped together with no spacer separating the two windows. The resulting path length of the liquid-film was calculated using the etalon interference fringe pattern measured as a function of wavelength (frequency) when the optical beam transmitted the empty cell, according to Figure 4.4. Using this method, the path length for the empty cell was calculated as 2.9 μm. Due to refractive index matching at the liquid/sapphire interface when the cell was loaded with precursor solution, we were unable to observe a clean etalon interference pattern for the loaded cell therefore assumed the loaded cell path length was identical to the path length of the empty cell.

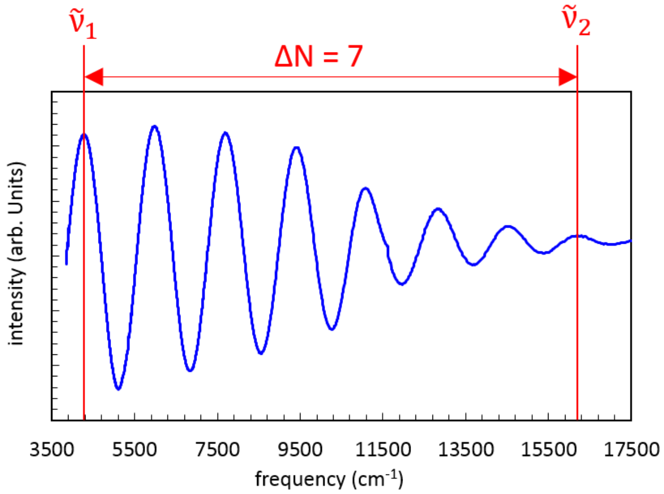

$$\text{Path Length} = \frac{\Delta N}{2(\tilde{\nu}_2 - \tilde{\nu}_1)}$$

$$\text{Path Length} = \frac{7}{2(16339.9\ \text{cm}^{-1} - 4233.5\ \text{cm}^{-1})}$$

$$\text{Path Length} = 2.9 \times 10^{-4}\ \text{cm} = 2.9\ \mu\text{m}$$

Figure 4.4: Calculation of the path length for the liquid-film cell used in the measurement of the film-relevant precursor solution UV/Visible absorbance spectra. The etalon interference fringe pattern was measured for the empty liquid-film cell consisting of two sapphire optical flats pressed together. The path length of the empty cell was calculated as 2.9 µm by measuring the number of interference fringes (ΔN) between two known frequencies ($\tilde{\nu}_1$and $\tilde{\nu}_2$) according to the given equation. Due to refractive index matching at the liquid/sapphire interface in the loaded cell, interference fringes were not observed, and it was necessary to assume to the filled cell path length was identical to the empty cell.

Figure 4.5 displays absorbance spectra of all film-relevant precursor solutions. Absorbance data of 576 mM $PbCl_2$ (Fig. A-D) and 580 mM PbI_2 (Fig. E-G) solutions in DMSO mixed with the appropriate concentration of MAI are shown as black dots, and overlaid on the data are the individual spectral components of lead halide coordination compounds used to fit the spectra with a method identical to that used for the $KI:PbI_2$ absorbance spectra (Figs 4.1 and 4.2).

Table 4.1 displays the fit amplitudes and corresponding concentrations of iodoplumbate species in perovksite film-relevant precursor solutions calculated according to the Beer-Lambert law using extracted quantities for extinction coefficients, liquid-film cell path length, and individual fit amplitudes. The calculated PbI_x^{2-x} concentrations shown in Table 4.1 are those values reported in the correlation with photoluminescence lifetimes in section 4.3 below.

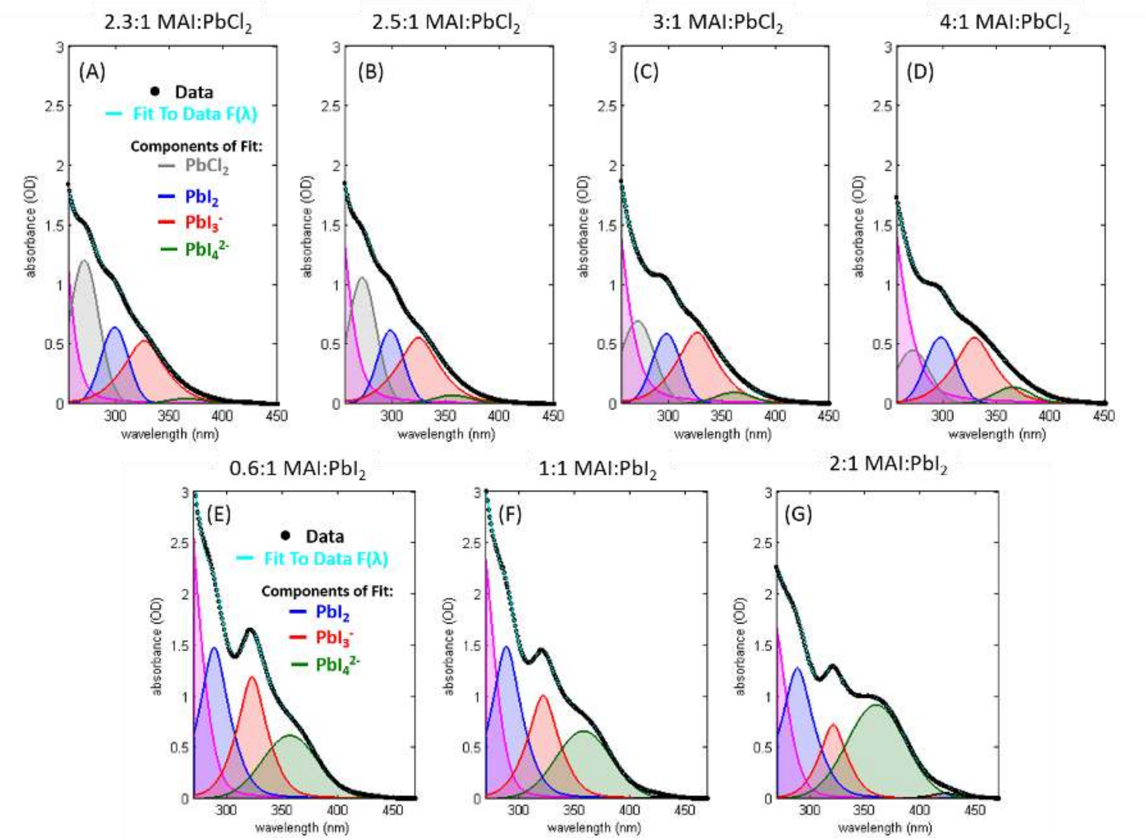

Figure 4.5: UV/Visible absorbance spectra of film-relevant precursor solutions in DMSO measured by transmission through a liquid film (~3 μm thickness) pressed between two sapphire optical flats. The solutions were prepared by mixing 576 mM $PbCl_2$ (Fig. A – D) and 580 mM PbI_2 (Fig. E – G) with the appropriate concentration of CH_3NH_3I to achieve the specified MAI:PbX_2 mole ratio. Overlaid on the data (black dots) are peaks representing the individual absorbing components ($PbCl_2$, PbI_2, PbI_3^-, and PbI_4^{2-}) and the total fit to the data [F(λ)], shown as a cyan line, which is a linear combination of the individual spectral components according to equation 4.1. It should be noted that significant $PbCl_2$ absorption (centered at 270nm) is present in the MAI:$PbCl_2$ solutions which limits the extent of conversion to higher order (PbI_3^- and PbI_4^{2-}) iodoplumbate species - unlike the MAI:PbI_2 solutions, which have significantly larger contribution from PbI_3^- and PbI_4^{2-} absorption.

Table 4.1: Extracted Concentrations from Precursor Solution Analysis (All Values in moles/liter)

	MAI:PbI_2			MAI:$PbCl_2$			
	0.6:1	**1:1**	**2:1**	**2.3:1**	**2.5:1**	**3:1**	**4:1**
MAI	0.3950	0.5919	1.2001	1.3360	1.4241	1.7229	2.3224
PbI_2	0.1052	0.1060	0.0908	0.0446	0.0465	0.0564	0.0762
PbI_3^-	0.0188	0.0159	0.0114	0.0041	0.0047	0.0064	0.0084
PbI_4^{2-}	0.0648	0.0694	0.0961	0.0023	0.0040	0.0069	0.0139

4.2.4 Organo-Halide Perovskite Thin-Film Characterization by X-Ray Diffraction and Transient Photoluminescence Spectroscopy

The experimental procedures for X-ray diffraction and TRPL spectroscopy measurements of organo-halide perovskite films examined here were identical to the procedures recently described in the previous chapter of this dissertation.[48] Briefly, a PANalytical XPert Pro MPD X-ray diffratometer equipped with Cu Kα radiation and a PIXcel 1D detector was used for the X-ray diffraction experiments. All TRPL measurements were made on a homebuilt spectrometer utilizing the second harmonic (532 nm) of a Nd:YAG Laser (Surelite, Continuum) as the excitation source. The PL output from the perovskite films was focused onto the entrance slits of a monochromator (DK240, Spectral Products) and subsequently focused onto a 350 MHz silicon photodiode (DET210, Thorlabs). The signal was amplified using a 200 MHz preamplifier (HVA-200M-40-B, FEMTO) and was digitized using a 200 MHz USB oscilloscope (Pico-5000, Picotech).

PL kinetics traces measured for perovskite films cast using a one-step spin-coat method that has been used to fabricate high-performance photovoltaic devices. The films were prepared from identical precursor solutions to those used in the measurement of iodoplumbate conectration by UV-Vis spectroscopy as described above in section 4.2.3. Emission kinetics were measured at the center wavelength of the PL spectrum (765nm), and the normalized PL transient data were fit to equation (4.3) following convolution of the data with the temporal instrument response. The fit was optimized using the Unconstrained Nonlinear Nelder-Mead simplex algorithm in the Matlab Optimization Toolbox.

$$\frac{I_{eh}(t)}{I_{eh}(0)} = \frac{1}{(n_T + Ax_0)}\left(n_T + \frac{AC_1x_0e^{-\gamma t}}{C_1 + x_0(1 - e^{-\gamma t})}\right)\left(\frac{AC_1x_0e^{-\gamma t}}{C_1 + x_0(1 - e^{-\gamma t})}\right) \tag{4.3}$$

Equation 4.3 is the result of a kinetic model developed by Stranks, *et. al*.[58] and the three main fit parameters used in our fitting scheme were: total electron trap density (N_T), and the total rate of electron-hole recombination (γ), and initial excited state density (N(0)) . As determined by the previous authors, A ≈ 8 x 10^{16}cm^{-3} and R_{pop} = 2 x 10^{-10}cm^{3}s^{-1} .[5] Furthermore,

$$x_0 = \frac{N(0)}{A + n_T} \tag{4.4}$$

Figures 4.6 and 4.7 show PL kinetics traces (data shown as dots) and best-fits to equation 4.3 (red line) following convolution of the data with the instrument response function (blue line) for one-step-deposited perovskite films prepared from $PbCl_2$ and PbI_2, respectively. All fit parameters extracted from fitting PL kinetics traces are included in Table 4.2 below.

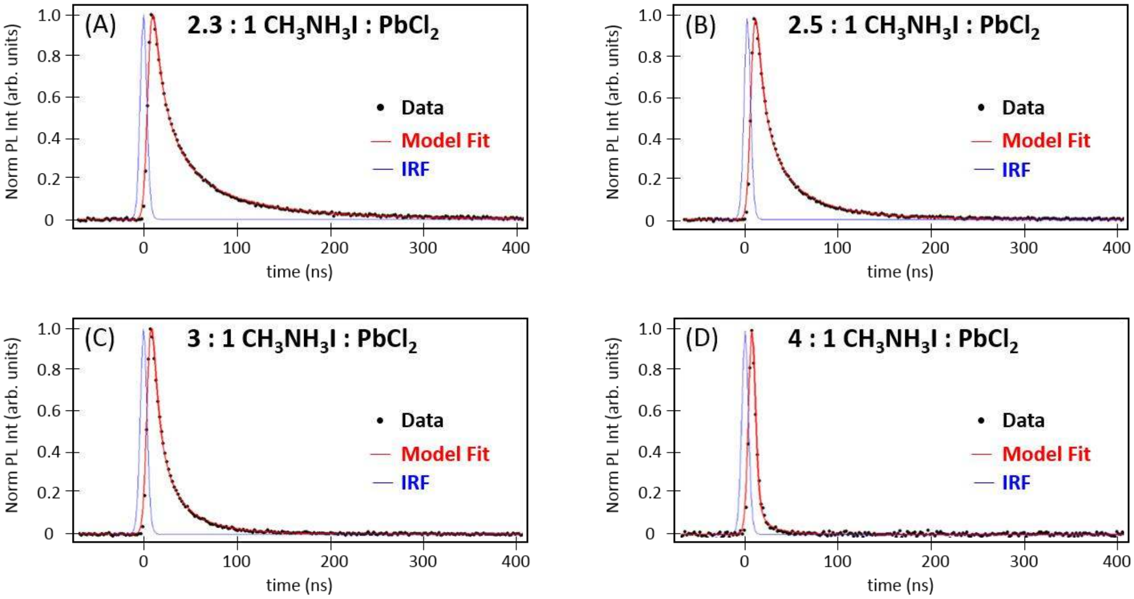

Figure 4.6: PL decay kinetics of $CH_3NH_3PbCl_{3-x}I_x$ films cast using a one-step spin coating method from precursor solutions of (A) 2.3:1, (B) 2.5:1, (C) 3:1, and (D) 4:1 mole ratios of CH_3NH_3I:$PbCl_2$. The data (black dots) are the average of triplicate measurements made on three films prepared separately. Overlaid on the data is the fit to the kinetic model (eq 4.3) as a red line following convolution with the temporal instrument response (blue line).

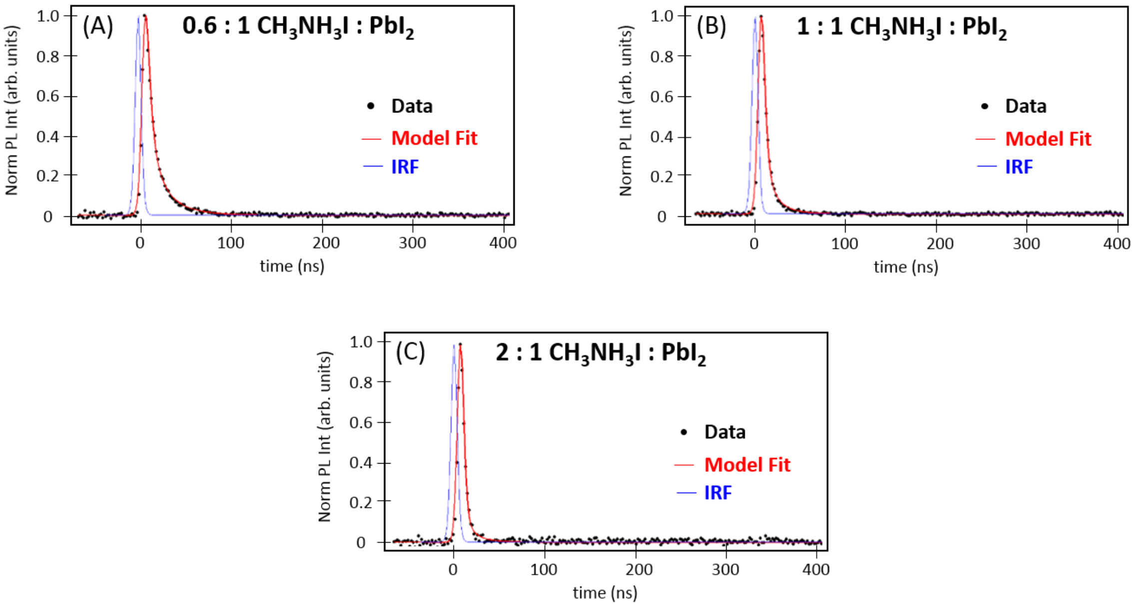

Figure 4.7: PL decay kinetics of $CH_3NH_3PbI_3$ films cast using a one-step spin coating method from precursor solutions of (A) 0.6:1, (B) 1:1, and (C) 2:1 mole ratios of CH_3NH_3I:PbI_2. The data (black dots) are the average of triplicate measurements made on three films prepared separately. Overlaid on the data is the fit to the kinetic model (eq 4.3) as a red line following convolution with the temporal instrument response (blue line).

Table 4.2: Fit Parameter Values Extracted from TRPL Fitting Routine

		γ (s^{-1})	N_T (cm^{-3})	N(0) (cm^{-3})
MAI:PbI$_2$	**0.6: 1**	3.4×10^7	2.4×10^{17}	6.7×10^{15}
	1:1	4.9×10^7	6.7×10^{17}	5.2×10^{15}
	2:1	5.5×10^7	2.7×10^{18}	7.9×10^{15}
MAI:PbCl$_2$	**2.3:1**	9.8×10^6	8.8×10^{16}	4.6×10^{15}
	2.5:1	1.6×10^7	1.4×10^{17}	6.1×10^{15}
	3:1	2.5×10^7	3.3×10^{17}	4.7×10^{15}
	4:1	3.4×10^7	6.3×10^{17}	5.3×10^{15}

4.3 Results and Discussion

Organo-halide perovskite films with the formula $CH_3NH_3PbI_3$ were deposited using two solution-based routes that have been reported in the literature. The first method involved dissolution of two precursors, MAI and PbI_2 (or $PbCl_2$), into the same solution that was then used to cast a solid film in a single spin coating deposition step.[114-119] The concentrations of PbI_2 and $PbCl_2$ in the dimethylsulfoxide (DMSO) solutions were 576 ± 2 mM with appropriate concentrations of CH_3NH_3I dissolved to obtain 1:1 or 3:1 mole ratios, respectively. After annealing at 100 ºC for fifteen minutes, the $CH_3NH_3PbI_3$ perovskite was formed. We will refer to organo-halide perovskites deposited using this method as one-step deposited films. The second method used to form organo-halide perovskites films separated the deposition of the lead precursor, either PbI_2 or $PbCl_2$,[48] from the conversion to the perovskite phase. In this method, a film of neat PbI_2 or $PbCl_2$ was deposited by spin coating a 360 mM solution of PbI_2 or $PbCl_2$ in DMSO onto a mesoporous alumina layer and allowing the film to dry. Then, the film was immersed in a solution of 6 mg/mL CH_3NH_3I dissolved in 2-propanol, which completed the conversion of the film into the perovskite $CH_3NH_3PbI_3$. We will refer to organo-halide perovskites deposited using the second route as two-step deposited films. The second method[48] was recently used to deposit nanocrystalline organo-halide perovskite films with average charge recombination lifetimes approaching the bulk limit reported in macroscopic single crystals of $CH_3NH_3PbI_3$.[40, 93]

Figure 4.8A and 4.8B highlight similarities of the $CH_3NH_3PbI_3$ films deposited using the two approaches. Figure 4.8A depicts visible absorption spectra measured in three $CH_3NH_3PbI_3$ films deposited using: 1) the one-step method from a 1:1 mole ratio solution of $CH_3NH_3I:PbI_2$ in DMSO, 2) the two-step method for which PbI_2 was used as the lead precursor, and 3) the two-step method for which $PbCl_2$ was used as the lead precursor. Importantly, the spectra indicate the formation of $CH_3NH_3PbI_3$ with comparable absorption onsets around 760 nm. The higher energy absorption feature of the local excited state[126] around 550 nm is more prominent in the two-step deposited perovskite films. The inset represents photoluminescence (PL) spectra of the films following excitation at 532 with 16 nJ/cm^2 intensity. Similar to the absorption spectra, the data indicate the formation of organo-halide perovskite films with the same optical bandgap using both deposition routes and lead (II) precursors. Figure 4.8B depicts Bragg-Brentano X-ray diffraction patterns measured in $CH_3NH_3PbI_3$ films deposited using both one-step and two-step approaches.

The diffraction pattern of the one-step deposited film reveals a pure $CH_3NH_3PbI_3$ phase with preferential orientation so that only the (110) and (220) diffraction peaks dominate the pattern. The diffraction pattern of the two-step deposited film for which PbI_2 was the lead precursor also exhibits a pure $CH_3NH_3PbI_3$ phase but with greater diversity of crystallite orientations that cause more reflections to appear in the XRD pattern. The two-step deposited film for which $PbCl_2$ was the lead precursor exhibits a $CH_3NH_3PbCl_3$ phase impurity resulting from incomplete substitution of iodide for chloride in the film. However, the peaks arising from $CH_3NH_3PbI_3$ in the film appear at the same 2θ angles within a precision of $\pm$ 0.01 degrees. This finding reveals that the lattice constants of the $CH_3NH_3PbI_3$ perovskite phase in the film match quantitatively the lattice constants of the perovskite formed using both the one-step method and the two-step method with PbI_2 as the lead precursor. Consequently, we believe the film deposited using the two-step method from the $PbCl_2$ precursor film consists of a physical mixture of two pure phases, $CH_3NH_3PbI_3$ crystals with a minority pure $CH_3NH_3PbCl_3$ phase interspersed among the pure $CH_3NH_3PbI_3$ crystals.

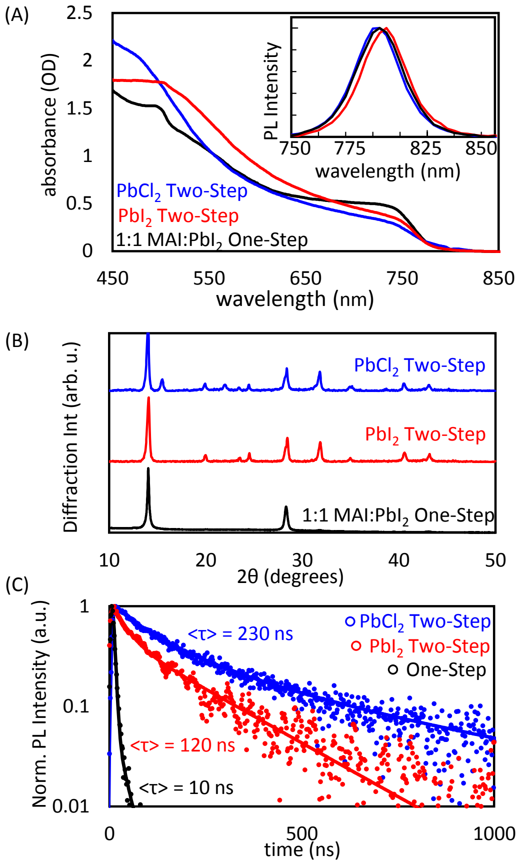

Figure 4.8: (A) Absorption and PL spectra of $CH_3NH_3PbI_3$ films deposited using one-step and two-step methods from both PbI_2 and $PbCl_2$ precursors demonstrating that all films exhibit the same bandgaps. The inset reveals that all films have similar PL spectra indicative of the bandgap of $CH_3NH_3PbI_3$ films. (B) X-ray diffraction patterns of the $CH_3NH_3PbI_3$ films deposited from various methods have similar crystal habits indicating formation of $CH_3NH_3PbI_3$ in all cases. (C) Despite their similarities in bandgap and crystal structure, the perovskite films deposited with various methods have PL lifetimes that differ by more than an order of magnitude. The film deposited using the one-step method exhibits a much higher density of charge recombination centers that cause faster charge recombination.

Despite having similar absorption spectra, emission spectra, and crystalline habits, the PL decay traces represented in Figure 4.8C reveal that the $CH_3NH_3PbI_3$ films deposited using the one-step and two-step methods have remarkably different charge carrier lifetimes. The PL decay kinetics were measured at the peak of the PL spectra of all films (770 nm) following excitation at 532 nm with 16 nJ/cm^2 intensity. This pump intensity is sufficiently low to minimize non-linear annihilation processes in the PL decay kinetics as reported in a previous study.[48] As such, the decay times are related to the charge recombination rates involving a mixture of trap mediated recombination processes and bimolecular charge recombination not involving traps.[39] The PL kinetic curve of the one-step deposited perovskite film decays by a factor 1000 ($\sim e^7$) within 100 ns. The corresponding average time constant of ~10 ns is similar to prior reports of $CH_3NH_3PbI_3$ deposited in a similar manner.[90]

Overlaid on the experimental PL kinetics (dots) in Figure 4.8C are best fit curves that were obtained from empirical biexponential fits to the decay kinetics. Fitting the data with an empirical fit function permitted us to quantify the PL decay times without the need to assume a particular kinetic model. We found that the PL decay curve of the perovskite film deposited using the two-step method from a PbI_2 precursor film was described by a 53 ns (70%) and a 290 ns (30%) biexponential function with an average time constant of 120 ns. It is noteworthy that they PL kinetic trace of the perovskite film deposited using the two-step route but from a $PbCl_2$ precursor film exhibited a significantly slower decay described by a 100 ns (67%) and a 500 ns (33%) biexponential function with an average time constant of 230 ns as reported previously.[48]

Adapting the kinetic model developed by Stranks *et al.*[39, 91] to describe trap-mediated charge recombination in organo-halide perovskites permits us to compare the charge recombination rates involving traps[39] in the perovskite films. The PL decay kinetics of the two-step deposited perovskite film for which $PbCl_2$ was the lead precursor are reproduced from an earlier report.[48] In that report, we obtained the constant for bimolecular charge recombination (R_{eh} in reference 39) with a value of $6\cdot10^{-10}$ cm^3/s.[48] This value is compatible with prior reports of high performance organo-halide perovskite materials.[36-37, 105] In contrast, faster PL decays were observed in both the one-step and two-step deposited perovskite films (with PbI_2 as the lead source) for the same initial density of photogenerated carriers, indicating a higher density of charge recombination centers in the these perovskite films. The procedures and parameters used to adapt the kinetic model by Stranks *et al*. to fit the PL kinetic decay curves have been described elsewhere.[48]

To gain insight about the underlying origin of the difference in charge carrier lifetime with deposition method and selection of the lead precursor, we examined chemical species present in the precursor solutions from which the $CH_3NH_3PbI_3$ films were deposited. Figure 4.9A depicts UV absorption spectra of solutions of PbI_2 dissolved in DMSO at 200 μM and 580 mM concentrations. The lower concentration is sufficiently low to permit absorption measurements in a standard 1.00 cm path length fused silica cuvette. The higher concentration is characteristic of PbI_2 in precursor solutions reported in the literature from which $CH_3NH_3PbI_3$ films were deposited for photovoltaic device studies.[114-119] However, at such high concentration, it is necessary to use a much shorter path length liquid cell (<10μm) to achieve appropriate optical densities and avoid unphysical distortions of the spectra that can arise from low light levels on the photodetectors in absorbance spectrometers.[128] Figure 4.9B depicts UV absorption spectra of $PbCl_2$ dissolved in DMSO at the same concentrations. The higher concentration is matched to that of PbI_2 to quantitatively compare the effects of the halide on the chemical species present in the various precursor solutions.

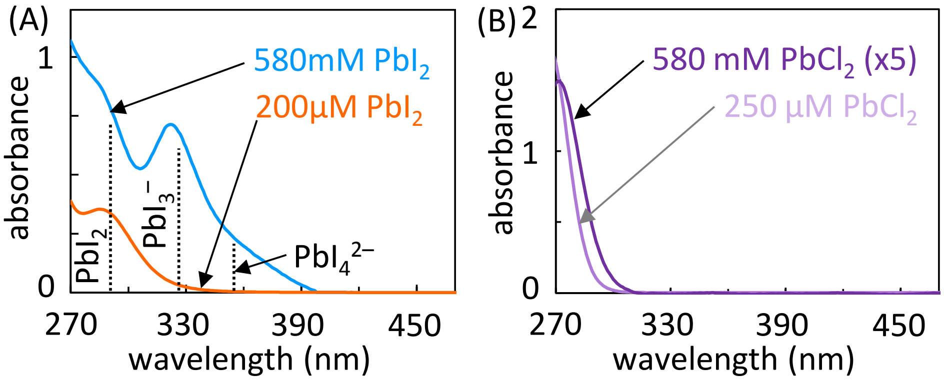

Figure 4.9: UV Absorbance spectra PbI_2 (A) and $PbCl_2$ (B) dissolved in DMSO at lower and higher concentrations. The vertical, dotted lines in 4.9A indicate the peak positions of iodoplumbates PbI_3^- and PbI_4^{2-}. Comparison of Figures 4.9A and 4.9B reveals that the spectrum of $PbCl_2$ undergoes comparatively little change with concentration indicating negligible dissociation into chloroplumbate species. In contrast, the spectrum of PbI_2 depends sensitively on concentration.

We sought to identify the underlying cause of the markedly different average charge carrier lifetimes measured in the $CH_3NH_3PbI_3$ perovskite films deposited using one-step versus two-step deposition methods. The literature suggests several possibilities including the role of chloride in passivating surfaces of perovskite crystals[92] and in favorably affecting the electronic structure in other ways that have yet to be fully clarified.[66, 90] Alternatively, the two-step deposition method may suppress the formation of interstitial iodide,[77] iodoplumbate anti-site defects[76], surface exposed lead[81] or iodide[79] ions, or surface defects that enhance electron-phonon coupling through polarization in response to the presence of photogenerated charges[106].

PbI_2 is known to exhibit complex solution chemistry leading to equilibria with several iodoplumbate species.[129-130] The chemical reactions in eq 4.5 represent equilibria leading to the first few iodoplumbates that form as a result of dissociation of PbI_2 in solution.

$$\begin{aligned} \mathrm{PbI_2} &\rightleftharpoons \mathrm{PbI^+ + I^-} \\ \mathrm{PbI_2 + I^-} &\rightleftharpoons \mathrm{PbI_3^-} \\ \mathrm{PbI_3^- + I^-} &\rightleftharpoons \mathrm{PbI_4^{2-}} \end{aligned} \tag{4.5}$$

In these equilibria, ion pairs form between iodoplumbates and PbI^+ counter ions. UV absorptions of iodoplumbates have been reported for several species including PbI_2 with a peak around 285 nm, PbI_3^- with peaks at 250 and 330 nm, and PbI_4^{2-} with a peak near 370 nm.[129-130] The dotted vertical lines appearing in Figure 4.9A mark the longest wavelength transition of each species. We note that I^- and PbI_3^- have been implicated as possible sources of mid-gap states in organo-halide perovskites on the basis of quantum chemical calculations,[76, 78] although these predictions have not been verified experimentally. We also note that the presence of PbI^+ in the precursor solutions is inferred by the need to maintain charge balance among species in the chemical equilibria represented in eq 4.4. However, PbI^+ has not been observed directly because it is expected to absorb in the UV where solvents such as DMSO and dimethylformamide also absorb.

The spectrum of the lower concentration solution of PbI_2 in DMSO reveals negligible dissociation on the basis of the single absorption feature centered at 290 nm.[126] However, the spectrum of the higher concentration PbI_2 solution in DMSO indicates that a significant fraction of dissolved species dissociate leading to the formation of PbI_3^- and PbI_4^{2-} at substantial concentrations although only PbI_2 and DMSO were combined to form the solution. The data reveal surprisingly high concentrations of chemical species in precursor solutions that may give rise to defects and charge recombination centers.[76, 78] In contrast, solutions of similar concentration of $PbCl_2$ dissolved in DMSO exhibit much less evidence of dissociation and ion pair formation. A more than 2000-fold increase of the concentration of $PbCl_2$ leads to modest broadening of the $PbCl_2$ peak appearing around 270 nm. The lack of increased absorption at longer wavelengths indicates negligible formation of chloroplumbate species in solution. We speculate that the reduced tendency to from chloroplumbates in DMSO solution may arise from the stronger ionic attraction between chloride and Pb^{2+} in $PbCl_2$ because of the smaller ionic radius of the chloride ion. The chloride ion is also a harder Lewis base, which may reduce the ability of DMSO molecules to solvate the ions and stabilize ion-pair formation in solution. The UV spectra of the 580 mM solutions of PbI_2 and $PbCl_2$ were measured in thin 2.9 ± 0.1 μm liquid films sandwiched between optical flats. The spectrum of the high concentration $PbCl_2$ solution was scaled by a factor of five to aid comparison to the peak shape of the lower concentration solution.

Iodoplumbate Molar Absorption Coefficients

The observation that the iodoplumbates PbI_3^- and PbI_4^{2-} can be measured in PbI_2 solutions suggests that these species may exist at high concentrations in solutions from which organo-halide perovskite films are deposited using the one-step approach.[114-119] Furthermore, the absence of such species in the $PbCl_2$ solution and the longer average charge carrier lifetime in the two-step deposited perovskite film suggests that $PbCl_2$ may suppress the formation of iodoplumbates during conversion to $CH_3NH_3PbI_3$. To better understand the chemical transformations that occur during perovskite film formation, we sought to quantify the concentrations of iodoplumbate coordination complexes present in the precursor solutions and then to correlate these species to the densities of defects in the final perovskite films.

As a first step toward this goal, we measured the molar absorption coefficients of PbI_2, PbI_3^- and PbI_4^{2-} in DMSO. Direct measurement of these coefficients from individual solutions is not possible because of the complex equilibria in solution, eq 4.5.[129-130] Fortunately, the dissociation constant of potassium iodide (KI) in DMSO has been reported,[131] which permitted us to vary the concentration of iodide in a systematic way and use the resulting changes in concentration and absorption of iodoplumbates[126] to quantify their absorption coefficients. Therefore, we prepared solutions of KI and PbI_2 in DMSO to systematically vary the concentrations of free iodide and measured the corresponding changes in absorption of PbI_2, PbI_3^- and PbI_4^{2-} species present in the solutions. Figure 4.10A depicts representative UV absorption spectra measured at a range of ratios of KI to PbI_2 sufficient to vary the concentrations of all iodoplumbate species. The total concentrations of Pb(II) species were fixed at either 100 μM or 200 μM among the solutions while the concentrations of KI were varied. We found it necessary to use the lower 100 μM concentration for the solutions with KI:PbI_2 ratios greater than 400:1 because the large molar absorption coefficient of PbI_3^- led to spectral artifacts in the UV spectrometer due to low light levels when 200 μM PbI_2 solutions were used. The complete set of spectra at all concentration ratios are represented in Figure 4.1 and 4.2. As discussed above, superimposed on the spectra in Figures 4.1 and 4.2 are calculated fit spectra resulting from the summation of absorption features of all three iodoplumbate species that match the absorption spectra of these species reported in the literature.[129-130] The detailed fitting procedures and tabulated results are described in the methods section 4.2.2.

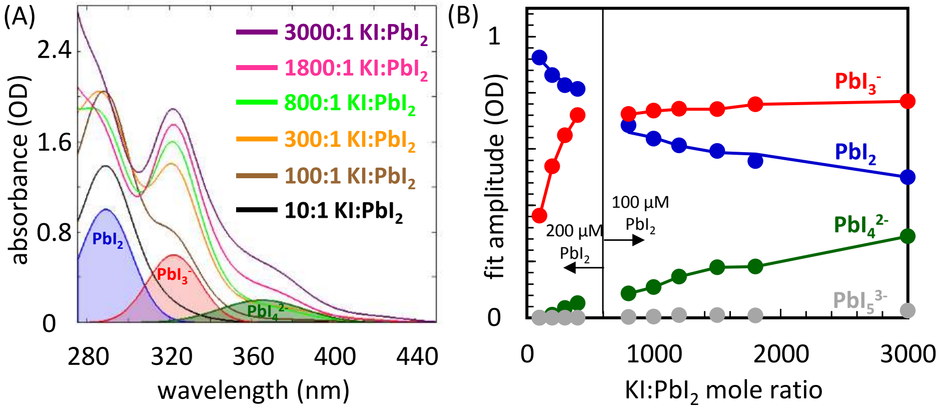

Figure 4.10: (A) UV absorption spectra of PbI$_2$ in DMSO with increasing concentration of KI demonstrating the evolution of solution chemistry with high concentrations of KI versus PbI2. Overlaid on the spectra are example fit functions for the three main complexes (PbI$_2$, PbI$_3^-$, and PbI$_4^{2-}$) absorbing in the spectral window from 270 nm to 450 nm. Panel (B) shows the fit amplitudes for each iodoplumbate species extracted from a fitting analysis of the solution spectra described in Section 4.2.2 from which the molar absorption coefficients of PbI$_2$, PbI$_3^-$, and PbI$_4^{2-}$ are obtained. Due to optical density complications, spectra for mole ratios below 400:1 KI:PbI$_2$ were collected with solutions containing 200µM PbI$_2$, and mole ratios exceeding 400:1 KI:PbI$_2$ were measured for samples containing 100µM PbI$_2$. The spectra and analysis in Figure 4.10 have been corrected to account for the concentration difference, but raw data are shown in Section 4.2.2.

Figure 4.10B depicts the variation of the amplitudes of the fit functions used to describe UV absorption peaks of PbI_2, PbI_3^- and PbI_4^{2-} as the concentration of iodide was varied among the solutions. We note that these solutions are in the 100-200 μM concentration regime where iodoplumbate species do not readily form (Figure 4.9A). Therefore, large excesses of iodide were required to drive the solution equilibria toward PbI_2, PbI_3^- and PbI_4^{2-}, unlike more concentrated solutions. The data in Figure 4.10B exhibit two regimes of behavior. Solutions with mole ratios of KI:PbI_2 in the 100 – 400 range undergo conversion of PbI_2 to PbI_3^- with little growth of PbI_4^{2-}. At much higher KI:PbI_2 mole ratios, the absorption of PbI_3^- grows slowly and the growth of absorption from PbI_4^{2-} is associated with a corresponding loss of PbI_2, similar to the behavior observed by Kamat and coworkers.[126] Assuming Beer-Lambert behavior, the amplitudes of the fit functions for each species are proportional to concentration. Because all solutions had large excesses of I^- and K^+ counter ions, we assumed the concentrations of PbI^+ and Pb^{2+} were negligible so that the sum of the concentrations of PbI_2, PbI_3^- and PbI_4^{2-} (and possibly a small amount of PbI_5^{3-}) accounted for all Pb(II) species in the solutions. Therefore, by fitting the variation in concentrations of the species and comparing to the corresponding changes in amplitudes of the absorption peaks, we could extract the molar absorption coefficient of each species. The molar absorption coefficients for the lowest energy transitions of PbI_2, PbI_3^- and PbI_4^{2-} in DMSO obtained from this analysis are $10{,}000 \pm 500\ M^{-1}cm^{-1}$, $45{,}000 \pm 13{,}500\ M^{-1}cm^{-1}$, and $13{,}600 \pm 2{,}720\ M^{-1}cm^{-1}$, respectively. The detailed fitting procedures used to extract the molar absorption coefficients and uncertainty limits are described in Section 4.2.2.

Quantifying Concentrations of Iodoplumbates

Having established the molar absorption coefficients of iodoplumbate species relevant to lead-halide perovskites, we examined the concentrations of these species in precursor solutions used to deposit $CH_3NH_3PbI_3$ films in which PbI_2 and $PbCl_2$ were used as the Pb(II) sources (Figure 4.11A and 4.11B). The concentrations of PbI_2 and iodoplumbates in the precursor solutions were sufficiently high to require very thin path lengths to avoid artifacts arising from low light levels in the UV spectrometer. To overcome this challenge, we cast thin liquid films sandwiched between optical flats. The thicknesses of the liquid films were measured from the periodicity of low amplitude etalon fringes that appeared in the spectra as a result of interference of reflections from the front and back surfaces of the liquid films (Figure 4.4). We found the liquid films were reproducibly 2.9 ± 0.1 μm thick. From this thickness combined with the molar absorption coefficients, we were able to quantify the concentrations of PbI_2 and iodoplumbates from the UV absorption spectra of the precursor solutions. The procedures by which the liquid films were cast and their UV absorption spectra were measured are provided in Methods Section.

Inspection of the UV spectra of 1:1 MAI:PbI_2 and 3:1 MAI:$PbCl_2$ precursor solutions reveals that PbI_2, PbI_3^- and some PbI_4^{2-} exist at measureable concentrations regardless of whether PbI_2 or $PbCl_2$ were used as the lead source. The dotted vertical lines overlaid on the spectra mark the wavelengths where these species absorb for reference. However, organo-halide perovskite films deposited from solutions containing 3:1 mixtures of MAI and $PbCl_2$ (frequently noted as $CH_3NH_3PbI_{3-x}Cl_x$) exhibit longer charge carrier lifetimes in comparison to films deposited from solutions containing 1:1 mixtures of MAI and PbI_2.[90] We investigated whether this behavior could be traced to suppression of iodoplumbates and associated ion pairing in precursor solutions used in the deposition of these films.

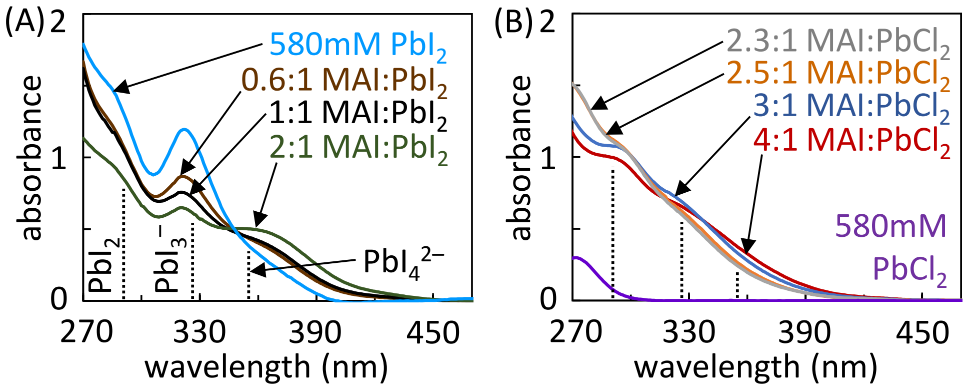

Figure 4.11: UV-Visible Absorbance spectra of film-relevant precursor solutions prepared from 580mM PbI_2 (A) and $PbCl_2$ (B) in DMSO, respectively. Appropriate concentrations of MAI were added to achieve the specified $CH_3NH_3I:PbX_2$ concentration ratios. The spectra of 580mM PbI_2 and 580mM $PbCl_2$ DMSO solutions are reproduced to demonstrate iodoplumbate formation upon addition of MAI to solutions of $PbCl_2$. The dotted vertical lines mark the wavelengths at which PbI_2, PbI_3^- and PbI_4^{2-} absorb.

To quantitatively compare the concentrations of iodoplumbates in precursor solutions including PbI_2 versus $PbCl_2$ as the lead source, we fit the thin liquid film spectra represented in Figure 4.11A and 4.11B with the same model used to fit the UV spectra of KI:PbI_2 solutions appearing in Figure 4.10A. Figure 4.5 represents the UV absorption spectra of the PbI_2 and $PbCl_2$ precursor solutions in individual plots and overlaid with their corresponding best fit spectra. The concentrations of PbI_2 and the iodoplumbates obtained from this analysis are tabulated in Table 4.1. Figure 4.12 depicts the variation of the concentrations of PbI_2, PbI_3^- and PbI_4^{2-} in the precursor solutions for all compositions examined here. The left (right) panel reflects the concentrations of these species in solutions in which PbI_2 ($PbCl_2$) was used as the lead (II) source. We do not have a measure of the dissociation equilibrium constant of MAI in DMSO, although we assume it is of similar order of magnitude to KI in DMSO (1.02 M).[131] However, the concentration of MAI varies only by a factor of 6.7 across the full range of precursor solutions. Therefore, we assume the concentration of iodide is proportional to the concentration of MAI in all solutions. This assumption is reflected in Figure 4.12 where we plot the concentration of MAI in place of iodide.

The data in Figure 4.12 reveal a number of trends that are expected. For example, the addition of MAI to $PbCl_2$ solutions leads to the formation of PbI_2, PbI_3^- and PbI_4^{2-}. Moreover, the addition of increasing amounts of MAI to both PbI_2 and $PbCl_2$ solutions results in monotonic increase of the concentration of PbI_4^{2-}. However, the concentrations of PbI_2 and PbI_3^- exhibit more complex behavior. The concentrations of these species actually decrease with the addition of increasing amounts of MAI to both PbI_2 and $PbCl_2$ solutions. The solution equilibria represented in equation 4.5 demonstrate that PbI_2 and

PbI_3^- are consumed in the reactions to form PbI_4^{2-}. This digestion of PbI_2 and PbI_3^- can be observed qualitatively by the reduction of the absorptions of the precursor solutions in Figure 4.11A (and less clearly in Figure 4.11B) at 290 nm (PbI_2) and 330 nm (PbI_3^-) while the absorption band of PbI_4^{2-} at 370 nm increases with the addition of more MAI. We note that the integrated areas of the spectra represented in Figures 4B are nearly constant regardless of MAI concentration, indicating that similar amounts of $PbCl_2$ were consumed in the formation of PbI_2, PbI_3^- and PbI_4^{2-} for all four solutions.

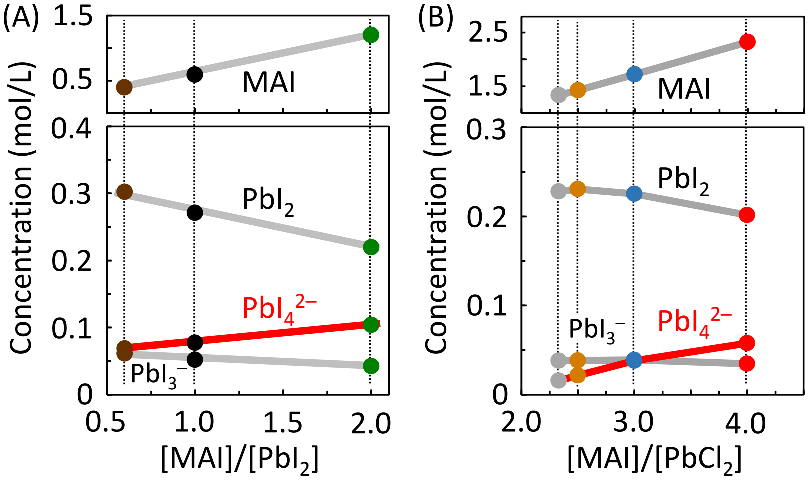

Figure 4.12: Variation of CH_3NH_3I, PbI_2, PbI_3^- and PbI_4^{2-} in precursor solutions of varying composition. Solutions with PbI_2 and $PbCl_2$ as the Pb(II) sources appear in (A) and (B), respectively. The concentrations are obtained from analysis of the UV solution spectra in Figure 4.11A and 4.11B using the Beer-Lambert law. Concentrations of MAI are represented in the upper panels on a different scale for clarity. Importantly, PbI_2 and PbI_3^- are consumed in both solutions as the MAI concentration increases because of the formation of PbI_4^{2-}.

Correlation of Solution Chemistry and Recombination Kinetics

We prepared organo-halide perovskite films from the precursor solutions whose spectra are represented in Figure 4.11A and 4.11B to establish whether excess iodide or iodoplumbates in the solutions are correlated with charge trap densities in the films. Stoichiometric and non-stoichiometric ratios of CH_3NH_3I:PbX_2 (where X = I or Cl) were used to prepare perovskite films via the one-step spin cast deposition method[114-119] on meso-porous Al_2O_3 substrates. All films were characterized by UV-Vis absorption spectroscopy, PL spectroscopy, and X-ray diffraction. Despite a wide range of compositions, we found that all precursor solutions resulted in crystalline perovskite films with well-defined optical band gaps (Figure 4.13A) and uniform, narrow emission spectra (Inset). Additionally, the XRD patterns (Figure 4.13B) reveal that well-ordered perovskite phases were formed from the solutions with the same lattice parameters, although some minor secondary phase impurities such as $CH_3NH_3PbCl_3$ (reflection 14.5^o) and PbI_2 (reflection 12.6^o) were present in the films formed from non-stoichiometric precursor solutions.

Finding that all precursor solutions resulted in the formation of organo-halide perovskites with well-defined absorption and emission spectra, we sought to investigate how the compositional changes influenced charge carrier dynamics in the perovskite films using TRPL spectroscopy. The kinetic model developed by Stranks et al[39] was used to determine electron-hole recombination rates (γ) and trap densities (N_T) in the films prepared from precursor solutions. Figure 4.14A represents experimentally measured TRPL kinetics traces (points) that are overlaid with fit functions calculated from the kinetic model (smooth curves) represented in equation 4.6. Individual kinetics traces and best fit curves from the model are shown in Figure 4.6 and 4.7 for detailed comparison.

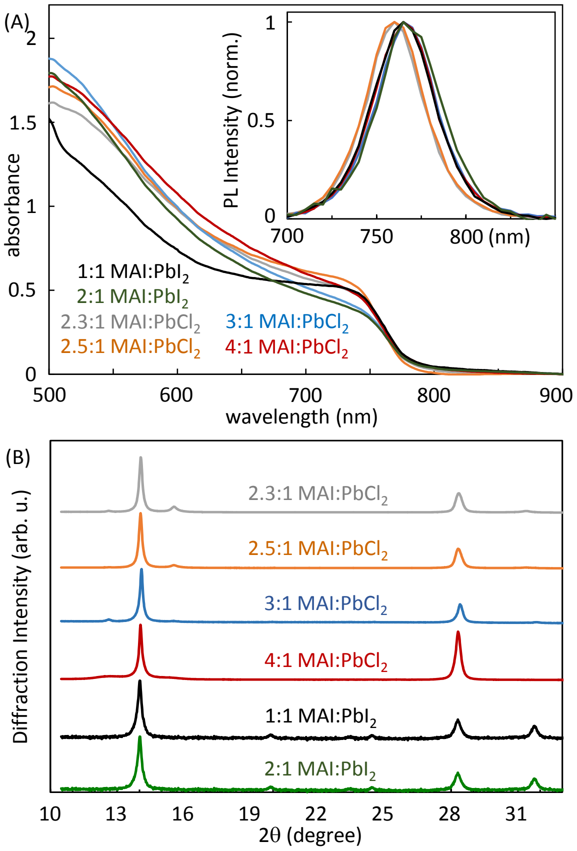

Figure 4.13: (A) Absorption spectra of select $CH_3NH_3PbI_3$ films cast from various precursor solutions reveal that the perovskite films exhibit a consistent bandgap despite different concentrations of MAI. Inset: the corresponding PL spectra are also consistent with $CH_3NH_3PbI_3$ formation. (B) X-ray diffraction patterns also demonstrate formation of $CH_3NH_3PbI_3$. Data for all compositions appear in Section 4.2.

$$\frac{I_{eh}(t)}{I_{eh}(0)} = \frac{1}{Ax_0(n_T + Ax_0)}\left(n_T + \frac{AC_1x_0e^{-\gamma t}}{C_1 + x_0(1-e^{-\gamma t})}\right)\left(\frac{AC_1x_0e^{-\gamma t}}{C_1 + x_0(1-e^{-\gamma t})}\right) \qquad \boxed{4.6}$$

where $x_0 = \frac{N(0)}{A + n_T}$ and $C_1 = \frac{n_T}{A} + \frac{R_{pop}(N_T - n_T)}{\gamma_0}$

Following convolution of the model decay functions described by equation 4.6 with the instrument response, experimental kinetics traces were iteratively fit by varying three parameters: total trap density (N_T), electron-hole recombination rate (γ), and initial excited state density (N(0)). The values and definitions of the other parameters in equation 4.6 were taken directly from reference 39 and are summarized in Section 4.2.4 Because the charge recombination rates measured in the one-step deposited perovskite films are much faster than those we reported recently in two-step deposited perovskites,[48] we do not have an independent measure of the rate of electron-hole recombination not involving traps (γ_0). Therefore, we considered this rate to be a property of the perovskite material and therefore a constant during the fitting procedure. The initial excited state density (N(0)) was varied to account for slight changes in film thickness and excitation fluence. The modifications made to the original model and values of all constants used in the fitting procedure are provided in the Methods Section of this chapter. The parameters obtained from the kinetic modeling of the TRPL kinetics traces are tabulated in Table 4.2.

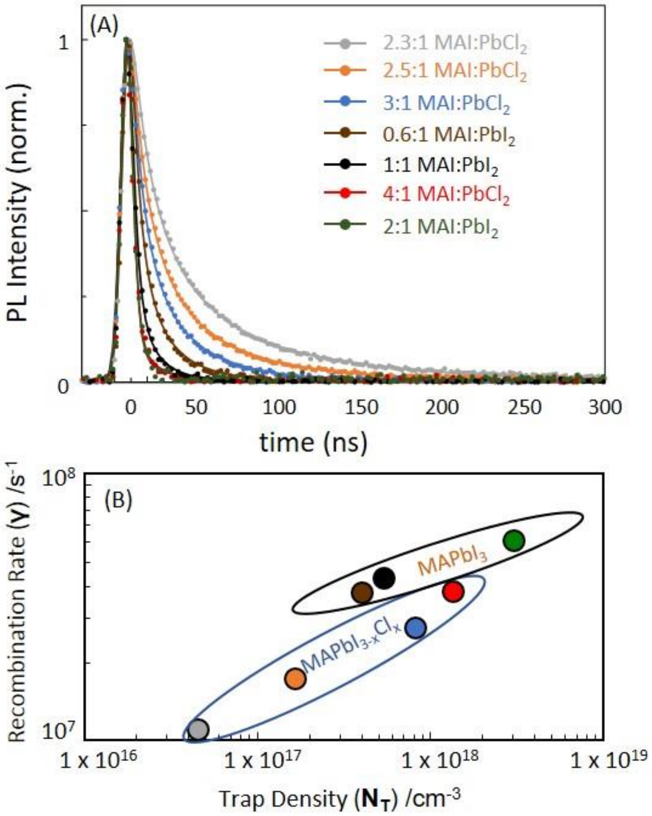

Figure 4.14: (A) TRPL decay curves (points) versus time for $CH_3NH_3PbI_3$ films cast from a variety of precursor solutions. The smooth curves through the data represent best fits from the kinetic model described in the text. (B) The charge recombination rates (γ) plotted versus the total trap densities (N_T) obtained from fitting the data are plotted on a logarithmic scale. The correlation demonstrates that the perovskite films prepared from slightly different precursor compositions have markedly different densities of charge recombination centers, despite having similar optical band gaps and crystal structures.

As a consistency check, we verified whether the changes in charge recombination rates γ measured among the perovskite films of various compositions were correlated with the total trap density N_T obtained by fitting the data with the kinetic model by Stranks et al[39]. Figure 4.14B depicts the correlation of charge recombination rates versus total trap densities of the corresponding perovskite films obtained from this analysis on a logarithmic plot. The correlation reveals that the variation in the charge recombination rates among the perovskite films is a result of tuning the total trap density through control of the precursor solution compositions.

We correlated the charge recombination rates γ obtained from fitting the TRPL decays with the concentrations of iodide and iodoplumbates extracted from fits of the precursor solution UV absorption spectra (Figures 4.11 and 4.12). Correlations of charge recombination rates versus PbI_4^{2-}, PbI_3^-, PbI_2, and MAI concentrations are represented in Figure 4.15A though 4.15D, respectively. The concentrations of MAI in Figure 4.15D already account for the consumption of MAI to form PbI_2 and iodoplumbates in the solutions using $PbCl_2$ as the lead source.

Figure 4.15A indicates that the concentration of PbI_4^{2-} is uniquely correlated with the density of charge recombination centers that determine the charge recombination lifetimes in all films regardless of the lead source used to deposit the films. In contrast, the concentrations of PbI_3^- and PbI_2 are actually anti-correlated with the density of charge recombination centers in the PbI_2-based precursor solutions. Even more complex behaviors are observed for the $PbCl_2$-based precursor solutions. Figure 4A provides the explanation for this behavior. PbI_2 and PbI_3^- are consumed in the reaction to from PbI_4^{2-} as the concentration of MAI increases. If PbI_3^- was the direct precursor to the formation of charge recombination centers in the organo-halide perovskite films, then its concentration would be expected to be proportional to the density of recombination centers regardless of whether PbI_2 or $PbCl_2$ were used as the lead source. The anti-correlation indicates that PbI_2 and PbI_3^- are not the direct precursors to the formation of charge recombination centers.

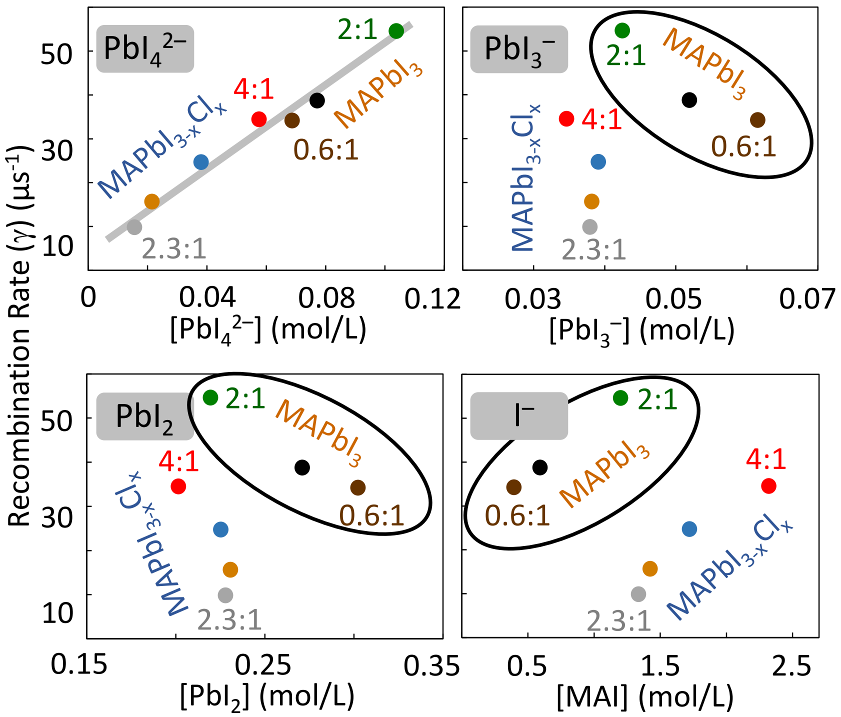

Figure 4.15: Correlation of iodoplumbate and iodide species present in precursor solutions versus charge recombination rates measured in the perovskite films deposited from the corresponding solutions. The charge recombination rates were obtained from fitting the TRPL decays represented in Figure 4.14. The concentrations of chemical species in the precursor solutions were obtained from fitting the absorption spectra represented in Figure 4.12. The correlation plots reveal that PbI_4^{2-} is the only species present in solution that is consistently correlated with charge recombination rate regardless of the lead source.

We note that the MAI concentration (assumed to be proportional to the iodide concentration) is correlated with the variation of the recombination rates in both PbI_2 and $PbCl_2$ series. However, the correlation is not monotonic, indicating that the variation of iodide concentration alone does not explain the change of charge recombination rates measured across both iodide and chloride series. It is difficult to consider interstitial iodide or surface exposed iodide ions as the origin of recombination centers because the density of such species would be expected to be proportional to the concentration of iodide in solution regardless of the source of lead used to cast the perovskite films. The data therefore reveal that iodide is not the direct precursor to charge recombination centers. Instead, the concentration of iodide affects the concentration of PbI_4^{2-}, which is the precursor that directly affects the density of charge recombination centers.

We note that the correlation plots in Figure 4.15 permit us to eliminate possible origins of charge recombination centers. But, they do not directly identify such centers. A recent study of $CH_3NH_3PbI_3$ perovskite films deposited using a two-step dip-coating approach demonstrated that the density of excess charge recombination centers could be quantitatively removed by surface passivation with 1,2-ethanedithiol (EDT).[48] Nanocrystalline films of the organo-halide perovskite passivated in this way exhibited average charge carrier lifetimes that approached the bulk limit measured in macroscopic single crystals.[40, 93] In the context of PbS colloidal quantum dots, EDT is known to be a Lewis base that bonds preferentially to surface exposed lead ions.[96-101] Therefore, the present study combined with these earlier findings suggests that charge recombination centers are located preferentially at the surfaces and that they consist of lead-rich Lewis acidic species. We note that PbI_4^{2-} is not expected to be a Lewis acid. However, it is possible that iodide in highly coordinated iodoplumbates may be replaced by reaction with Lewis bases such as EDT, leading to passivation of the surface defect site associated with the iodoplumbate. Current research efforts seek to investigate the surface chemistry of ligand passivation in an effort to provide further insight regarding the chemical nature of the species that contribute charge recombination centers on the surfaces of organo-halide perovskites. We note that we have not eliminated the possibility that charge recombination centers exist in the bulk as well as on the surfaces of organo-halide perovskites deposited using one-step methods. This issue will be the focus of future work as well.

The role of PbI_4^{2-} as the principal defect precursor in $CH_3NH_3PbI_3$ perovskites may provide a molecular basis from which to consider recent reports in the literature regarding the role of chloride in passivating surfaces of perovskite crystals[92] and in favorably affecting their electronic structure.[66, 90] For example, highly-coordinated iodoplumbates may contribute mid-gap states directly or may increase the polarizability of the surfaces thereby enhancing the electron-phonon coupling as was recently suggested.[106] Replacement of iodide with chloride in the coordination shells of such lead species on the surfaces of perovskites may move the corresponding electronic states back toward the band edges. The presence of chloride is expected to reduce the density of highly coordinated iodoplumbates on the surfaces of perovskite crystals and suppress the corresponding density of charge recombination centers that are associated with iodoplumbate species.

4.4 Conclusions

In summary, we examined the chemical equilibria in precursor solutions relevant to the deposition of lead-based organo-halide perovskite compounds in an effort to determine whether chemical species present in solution are correlated with the density of charge recombination centers in the final perovskite films. To quantitatively establish such correlations, we determined the molar absorption coefficients of iodoplumbate coordination complexes and then used the coefficients to determine the concentrations of the complexes in precursor solutions used to cast perovskite films. Our findings reveal that the chemical equilibria among iodoplumbate species that have been implicated as possible origins of charge recombination centers depend sensitively on the total concentration of lead species in solution. From these findings, we note that reducing the concentration of the Pb(II) species used during perovskite film formation provides a means to decrease the concentration of defect precursors in solutions used to cast perovskite films.

Moreover, we demonstrated that the concentration of tetraiodoplumbate PbI_4^{2-} is uniquely correlated with the density of charge recombination centers in the final perovskite films regardless of the lead precursor used to cast the films. We hypothesize that the relatively low temperatures at which one-step deposited organo-halide perovskite films are annealed may permit iodoplumbate species in solution to survive the film formation process, causing them to contribute to the density of charge recombination centers. In contrast, sequential methods to deposit organo-halide perovskite films appear to suppress the formation of such iodoplumbates by waiting to expose the lead precursor to excess iodide until it is in the solid state.

Two-step deposition methods therefore avoid the need to digest large concentrations of highly-coordinated iodoplumbates during film formation. We speculate that the ability to avoid digestion of high concentrations of iodoplumbates permits the formation of organo-halide perovskite films with low defect densities from a wider distribution of deposition conditions in comparison to perovskite deposited using one-step approaches. In all cases, use of $PbCl_2$ in place of PbI_2 as the lead source results in the formation of perovskite films with lower defect densities for both one-step and two-step deposition methods. The effect is likely a result of suppression of PbI_4^{2-} by starving the film formation reaction of excess iodide during conversion to the $CH_3NH_3PbI_3$ perovskite phase combined with replacement of iodide with chloride in the coordination shells of highly-coordinated lead species that form on perovskite surfaces.

CHAPTER 5

Spectroscopic Investigation of Band-Edge Fine-Structure to Enhance Photocarrier Transport and Photovoltage in Colloidal Quantum Dot Solar Cells

5.1 Preface

The material presented in this chapter highlights a research collaboration between the Asbury Lab and the Sargent Lab (University of Toronto, Department of Electrical and Computer Engineering). The focus of my research in this effort was: assign the optical transition giving rise to transient, mid-IR absorption observed for PbS colloidal quantum dots, tune the mid-IR TA absorption by controlling nanocrystal surface chemistry, and determine the extent of delocalization of a Stokes-shifted sub-gap state identified by mid-IR transient absorption by characterizing this absorption in PbS CQDs suspended as a colloid in organic solvents and diluted in a film of an amorphous, electrically insulating polymer matrix. For me, this research represents a starter project I undertook when I first joined the Asbury lab in 2011; through this work, I was able to develop technical proficiencies in optical photophysics and thin-film physical chemistry, as well as establish a firm knowledge of the field of inorganic semiconductor physical chemistry, which ultimately helped me develop my own independent project in organo-lead-halide perovskites. I would like to acknowledge my collaborators at the University of Toronto and my colleagues at Penn State, Kwang Jeong and Jihye Kim, for their technical contributions to this project and also for the knowledge and guidance they passed along to me.

5.2 Introduction

Colloidal quantum dot (CQD) photovoltaics represent an extremely promising route to achieve a link between 2nd and 3rd generation solar cells, as was discussed in Chapter 1 of this dissertation. CQD electronics are fully processable from solution, which opens the possibility of fabricating complete devices on light-weight and flexible modules - providing a tangible way to eliminate the costly support systems, which account for more than 30 % of the cost of silicon PV modules in use today.[132] Furthermore, as a result of the intrinsic quantum-confined electronic states,[133-135] the optical properties of CQDs can be tuned in such a way to efficiently capture the full solar spectrum; a carefully engineered, multi-junction cell utilizing a series of CQDs with appropriate band-gaps could exhibit high power conversion efficiencies (> 40% PCE).[27]

Researchers have made remarkable progress in increasing the short-circuit current density (J_{SC}) of CQD photovoltaics, with champion solar cells exhibiting J_{SC} values up to 24 mA cm^{-2} under AM 1.5 illumination[136] – levels which are approaching the J_{CS} achieved for single crystal silicon solar cells. However, CQD solar cells still suffer from low photovoltages or open-circuit voltage (V_{OC}), which significantly limits the PCE of these devices. In fact, the V_{OC} is typically lower than expected, based on state-of-the-art, depleted-heterojunction (DH) device architecture (Figure 5.1A),[1] used by our collaborators at University of Toronto to engineer CQD cells producing the record-setting conversion efficiency (11.3% PCE).[137] As shown in Figure 5.1A, V_{OC} is predicted to be bound by the quasi-Fermi level splitting defined by the electron Fermi-level ($E_{F,n}$) of TiO_2, and the hole Fermi-level ($E_{F,p}$) of p-type PbS CQD because the back contact with gold is Ohmic.[138] This large discrepancy between the optical band-gap and electrical band gap represents an energetic loss mechanism which is currently not understood in the field, by is hypothesized to be limited by high density of sub-band gap, non-radiative recombination states, which commonly plague CQD semiconductors.[139] Elimination of this loss mechanism is necessary in order to realize the full potential of CQD photovoltaics.

Figure 5.1B represents the simplified band structure for PbS CQDs solids used as the active layers in CQD DH solar cells. The optical band gap of PbS QDs is established by splitting of $1S_e$ and $1S_h$ states which are typically depicted as the lowest energy states relevant to transport within the bands.[140-143] By optically populating the conduction band ($1S_e$ or higher) with electrons, holes occupy the lowest lying valence band states. In this view, electrons (hole) promoted to higher lying $1P_e$ ($1P_h$) states rapidly cool to $1S_e$ ($1S_h$) states (or lower-lying trap states) at rates that depend on a variety of factors including the nature of the ligands used to passivate quantum dot surfaces or the degree of quantum confinement;[144-148] suggesting that tuning surface chemistry and quantum dot diameter may be two powerful ways to improve the electrical band-gap (V_{OC}) and current conduction pathways (J_{SC}) of CQD photovoltaics. Therefore, a more complete understanding of the electronic structure of CQD solids, and in particular the influence that ligands may have on transport states and electrical band gap, will guide the development of strategies to control the electronic states that determine the maximum quasi-Fermi level differences and so enable higher efficiency CQD photovoltaic devices.

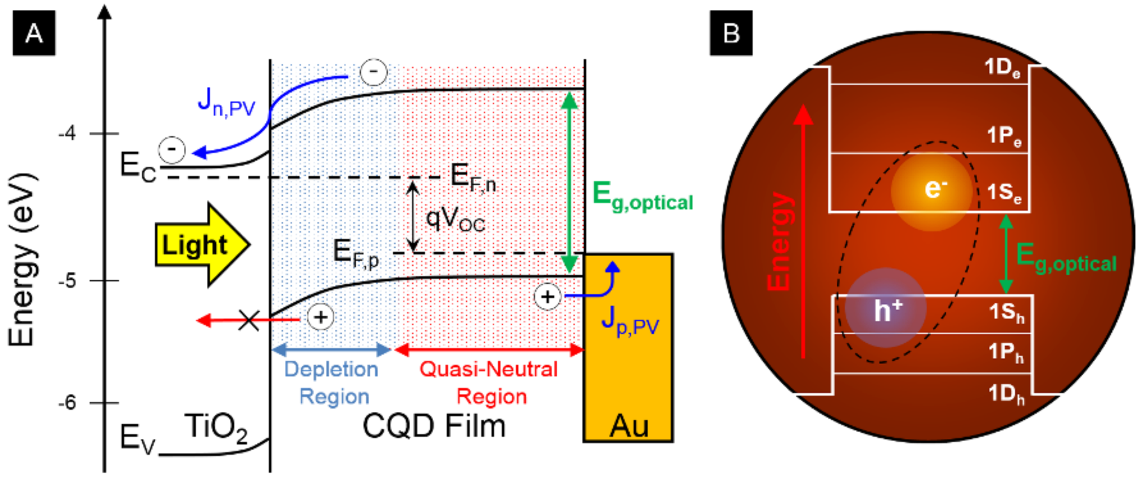

Figure 5.1: A) Spatial band diagram of a depleted-heterojunction device architecture used by the Sargent lab to produce CQD photovoltaics with record-setting power conversion efficiencies (PCE). It is also apartment that the V_{OC} achieved in CQD photovoltaics is less than the optical band-gap ($E_{g,optical}$). Within the depleted-heterojunction architecture, two regions are established: a region where exciton transport is limited by diffusion, and a depletion region where the built-in field drives exciton transport and dissociation at the electron-selective, TiO_2 junction. The V_{OC} achievable within this device (Fig A adapted from reference 1). Figure B) represents an energy level diagram of quantum-confined excitonic states where the conduction band minimum and valance band maximum are established by the $1S_e$ and $1S_h$ states, respectively. It should be noted that in the strong confinement regime, the electron, hole, and exciton wave functions extend beyond the nanocrystal surface; however, for clarity, these wave functions are not drawn to the appropriate scale relative to the quantum dot.

We hypothesized that we could control the activation energy required for photocarrier charge transport through PbS QD thin-films by: a) systematically varying the electronic structure via the quantum size effect,[149] and b) by varying QD surface ligand treatments, including passivation strategies that have produced record power conversion efficiency photovoltaic devices.[150-153] ***With these ideas in mind, the goal of this project was to assign the lowest-energy electronic states capable of supporting charge-transport within CQD solids in an effort to develop design rules for future materials capable of achieving higher photovoltage and photocurrent.***

In this chapter, we show that in CQD solids having produced the best photovoltaic performance to date, photoexcitation is followed by ultrafast relaxation into sub-gap states that provide highly efficient transport paths. The data reveal that photoconductive sub-gap states lie at the Stokes-shifted energy below the optically bright excitonic states of the quantum dots. The successful mediation of transport via dark states explains the remarkably high photocurrent densities seen in these materials, levels that are beginning to approach those of single crystal silicon solar cells. DFT calculations supplied by our collaborators point to the origin of the sub-gap states as being from the delocalized excitonic state manifold that is coupled to the quantum dot surfaces. Our findings provide unexpected approaches to further advance the efficiency of CQD solar cells.

5.3 Methods

5.3.1 Quantum Dot Synthesis, Film Preparation, and Steady-State Spectroscopic Characterization

The Sargent Lab at University of Toronto was responsible for synthesizing all PbS CQD materials in addition to carrying out DFT calculations and performing all electrical measurements, such as: the photoconductivity and temperature-dependent short circuit current density (J_{SC}) measurements. The Asbury Lab received the samples as ~50mg/mL PbS colloids suspended in octane or hexane, where the PbS nanocrystals were capped with oleic acid, unless otherwise specified. We were then responsible for casting thin-films using a layer-by-layer spin-coat deposition of the oleate-capped PbS QDs and performing the solid/liquid ligand-exchange reaction on each subsequent layer to replace the insulating oleic acid capping layer with short-chain surfactants (EDT, MPA, etc.) or halide (Br^-) ions to yield conductive thin-films. Furthermore, we were responsible for performing transient and steady-state optical spectroscopy. All methods will be detailed below.

PbS Colloidal Quantum Dot Synthesis

Cadmium chloride (Sigma-Aldrich, 99.98%) and TDPA (Alfa Aesar, 98%) were dissolved in oleylamine (technical grade, Acros, 80%) by pumping under vacuum for 16 h at 100 °C. The solution was then kept at 80 °C to avoid solidification. In a typical procedure, precursor with a 13.6:1 Cd:TDPA molar ratio was made by dissolving 0.30 g (1.64 mmol) of CdCl2 and 0.033 g (0.12 mmol) of TDPA in 5 ml of oleylamine.

PbS quantum dots synthesis was carried out using a standard Schlenk line technique. Octadecene (ODE) was degassed by pumping under vacuum at 80°C for 8 hours prior to use. 0.45 g PbO, 1.5 mL oleic acid, and 3 mL ODE were mixed in a two-necked flask and pumped under vacuum at 95°C for 16 h to produce lead oleate stock solution. We mixed 4.5 mL lead oleate stock solution and 15 mL ODE and heated to 125°C using a heating mantle under Ar. To this solution, 180 µL TMS in 10 mL ODE was swiftly injected.

For 1.30 eV and 1.22 eV band-gap quantum dots:

For metal halide treatment, 1.0 ml metal halide precursor was introduced into the reaction flask after Sulphur source injection during the slow cooling process. A 6:1 Pb:Cd molar ratio was maintained during the synthesis.

For 1.46 eV band-gap quantum dots:

The Pb:S precursor ratio was adjusted to 4:1 and the injection temperature was increased 160C. The Cd-halide precursor concentration was reduced to one-half that used in A.

For 0.93 eV band-gap quantum dots:

The Pb:S precursor ratio was adjusted to 2.1:1 and the injection temperature was reduced to 90C.

When the reaction temperature reached 30–35 °C, the nanocrystals were isolated by the addition of acetone then centrifugation. The nanocrystals were then purified by dispersion in toluene and reprecipitation with acetone/methanol (1:1 volume ratio), then re-dissolved in anhydrous toluene. The solution was washed with methanol two or three more times before final dispersal in octane (50 mg ml^{-1}).

Thin Film Fabrication

Fabrication procedures for quantum dot films employed previously published fabrication procedures.[136] PbS CQD films were deposited using a layer-by-layer spin-coating process under an ambient atmosphere. For each layer, the CQD solution (50 mg ml−1 in octane) was deposited on the substrates and spin-cast at 2500 r.p.m. Solid-state ligand exchange was performed by flooding the surface with 1% v/v Mercaptopropionic Acid (MPA) in methanol for 3 s before spin-coating dry at 2500 r.p.m. Two washes with methanol were used to remove unbound ligands. For Ethanedithiol (EDT) and 1,6-Hexanedithiol (HDT) 1%v/v solution in acetonitrile was used in place of the MPA solution. Slight variations were made for 0.93 eV and 1.46 eV band-gap materials: a) MPA concentration was increased to 10% v/v in methanol for the 0.93 eV quantum dots; and b) the MPA concentration was reduced to 0.2% v/v in methanol. In addition, the MPA treatment consisted of a 10s soak before spinning dry for a total of 10s for the 1.46 eV.

CQD Thin-Film Photoconductivity Measurements

Photoconductivity measurements were conducted on gold interdigitated electrodes. A two layer thick QD film was applied using identical spin coating techniques to those listed above. Photoconductivity transients were measured across a 5 μm channel under a 6 V applied bias. Optical excitation was achieved using a modulated 640 nm laser with 200 mW/cm2 intensity. The sample was placed in a closed cycle liquid helium cryostat from Advanced Research Systems (ARS-2HW) and was thermally anchored using thermal conductive grease. Initial cooling of the sample was carried out over the course of several hours. Wait times of 30 minutes were used for each temperature step to ensure thermal equilibrium had been reached. Transient measurements were made using an oscilloscope and a 120 KΩ resistor placed in series with the photoconductor.

Optical Spectroscopic Materials Characterization

1) UV/Vis/NIR Absorption spectra were acquired using two spectrometers: Spectra of colloidal suspensions of QD materials were collected using a Varian Cary 500 UV-vis-near-IR spectrophotometer at room temperature. Samples consisted of ~2mg/mL quantum dots in octane solution. UV/Vis/NIR spectra of PbS QDs were acquired using Beckman DU 520 UV/Vis spectrometer. The spectra were background subtracted by the substrate absorption.

2) Photoluminescence spectra were likewise carried out with two spectrometers: Our collaborators in the Sargent lab at University of Toronto measured steady-state photoluminescence spectra at room temperature using a focused 640 nm diode laser with an intensity of approximately 10 W/cm2 for excitation. The emission signal was analyzed on a fiber-coupled Near-IR spectrometer equipped with an InGaAs array detector (Ocean Optics NIR-512). These emission measurements made by the Sargent lab were measured for colloidal samples consisting of ~2 mg/mL quantum dots in octane solution. Transient and time-integrated spectra of thin-film PbS CQDs were measured in the Asbury lab using a home-built spectrometer identical to the instrument discussed in Chapter 2 of this dissertation. Briefly, we used a frequency-doubled Nd^{3+}:YAG Laser (Surelite, Continuum) as the excitation source at 532nm. Sample emission was collected at a right angle to the excitation and

coupled into a monochromator (DK240, Spectral Products) using lenses. The monochromator output was focused onto a 50 MHz InGaAs Avalanche photodiode (APC110C, Thorlabs). The signal was amplified using a 200 MHz preamplifier (HVA-200M-40-B, FEMTO) and was digitized using a 200 MHz USB oscilloscope (Pico-5000, Picotech).

3) Nanosecond (ns) to Microsecond (μs) timescale transient infrared (TRIR) absorption spectroscopy experiments were performed on a homebuilt instrument. A 10 ns duration second harmonic (532 nm) pulse from a Nd^{3+}:YAG laser (Continuum) was used to excite the band-gap of the CQD films. The films were deposited onto a MoO_3 coated gold mirror to be used in a reflective optical geometry. The pulse energy was 1.0 ± 0.02 mJ with a beam diameter of 1 cm. Continuous-wave infrared probe light was generated by a compact ceramic Globar Light Source (Newport) that was focused on the sample and overlapped with the 532 nm excitation laser pulse. The infrared continuum was dispersed in a monochromator (HORIBA Jobin Yvon), and transient absorption measurements were collected by a 1 mm^2 HgCdTe (MCT) single-element detector (Infrared Associates, Inc.) tied to a preamplifier with band-pass frequencies of 1.5 Hz to 1.0 MHz (Infrared Systems Development) and digitized by a 16-bit 20 MHz computer mounted analog-digital converter (National Instruments).

At the same time we made the aforementioned TRIR measurements, we built a new MIR transient spectrometer to improve spectral resolution, time resolution, and sensitivity while allowing for reflective and transmissive optical geometries.[59] This new spectrometer is identical to the instrument discussed in chapter 2. Briefly, borad-band IR light was generated by a silicon nitride emitter (Spectral Products) which was used as the probe source. A 30 Hz frequency-doubled Nd^{3+}:YAG laser (Continuum) was used as the pump, which had a pulse duration of 10 ns and a wavelength of 532 nm. MIR TA spectra of the probe light were obtained by dispersing the light using a monochromator (Spectral Products, DK240) and focusing the output on a 1 mm^2, single element, MCT photodiode with 16 MHz response (Kolmar Technologies, KMPV11-1-J1). The signal was then digitized using a 100 MHz PC oscilloscope (Pico Technology). TRIR measurements made in this geometry were obtained for PbS thin-films cast using identical layer-by-layer, ligand exchange, spin-coating techniques discussed above. However, thin-films were cast onto MoO_3/CaF_2 substrates to permit transmission of the MIR probe through the sample in contrast to the MoO_3/Au substrates which only permitted reflective geometry measurements. Casting thin-films on PbS on optical flats with high transmission in the MIR, NIR, Visible, and UV wavelength regimes also enabled us to make FITR, UV-Vis absorption, and emission measurements on identical samples as those measured in TRIR experiments.

The CQD films studied in these experiments were prepared following the same procedure as that used for films for the electrical measurements. Throughout the experiments, the films were mounted in a vacuum-evacuated cryostat (Janis). For the temperature-dependent kinetic trace measurements, the films were cooled in a liquid nitrogen flow cryostat (Janis) where the temperature was controlled at the cold finger with a temperature controller (Lake

Shore). The temperature of the sample holder was separately monitored using a thermocouple (Omega). All samples were deposited under conditions identical to those used for the electrical measurements.

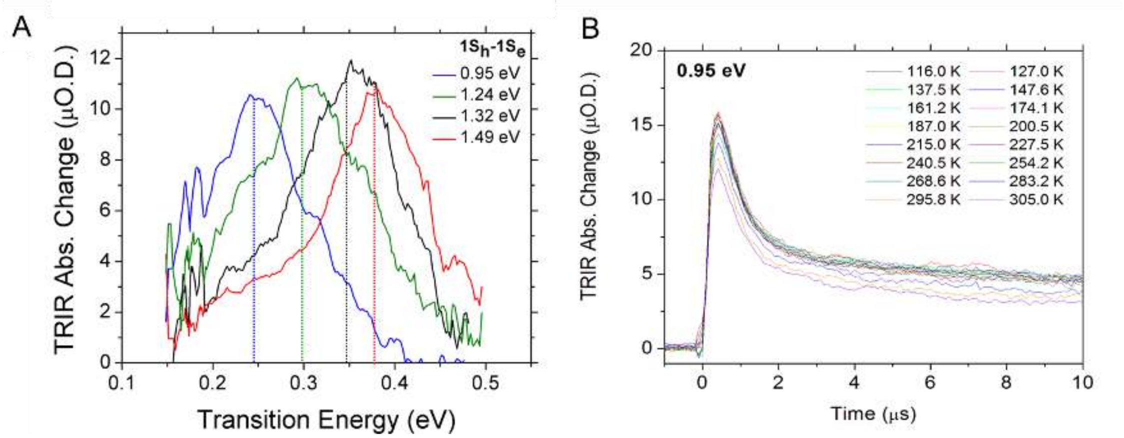

Figure 5.2: A) Shows transient absorbance spectra measured 0.5 μs after optical excitation by a 10 ns pulsed Nd^{3+}:YAG laser (532nm) for a series of PbS CQD thin-films with bandgaps of 1.49, 1.32, 1.25, and 0.95 eV. Dotted vertical lines are meant to indicate the central transition energy for each spectrum and shown that the variation of average mid-IR transition energy is correlated with decreasing optical band-gap. B) Shows example temperature-dependent TRIR decay kinetics measured at the central transition energy for the 0.95 eV band-gap PbS sample. These data were collected by Jihye Kim of the Asbury lab.

5.3.2 Assignment of Transient Mid-IR Absorbance in PbS CQDs

Assignments of 1Se-1Pe Energy Splitting

Our goal of using the size dependent energies of the transient mid-IR electronic transitions (Figure 5.2A) to obtain information about sub-gap states in the CQD solids requires that we identify the nature of the electronic states giving rise to the infrared transient absorption signals. Photoinduced Mid-IR transitions of CdSe quantum dots in solution have been assigned to electron (hole) excitation from 1Se(h) to 1Pe(h) states.[154-156] We hypothesized the photoinduced MIR-IR absorptions measured in PbS CQDs (Fig 5.2A) originated from transitions between the same intraband states, and we therefore, needed an independent measure of the energy splitting between the 1Se(h) to 1Pe(h) states to correlate with the QD side-dependent, transition energy measured in TRIR experiments. The absorption spectra appearing in Figure 5.3 provide independent measures of the first few quantum confined transitions for a series of PbS CQDs with the specified band-gap. Shown below each linear-absorption spectrum is the second derivative of the absorption spectrum, which were used to extract transition energies for all quantum-confined transitions. The second derivative of the linear absorption spectrum is sensitive to changes in concavity, and fitting the local minima of the second derivative spectrum gives us an accurate value for the center frequencies of all ground-state absorption bands.

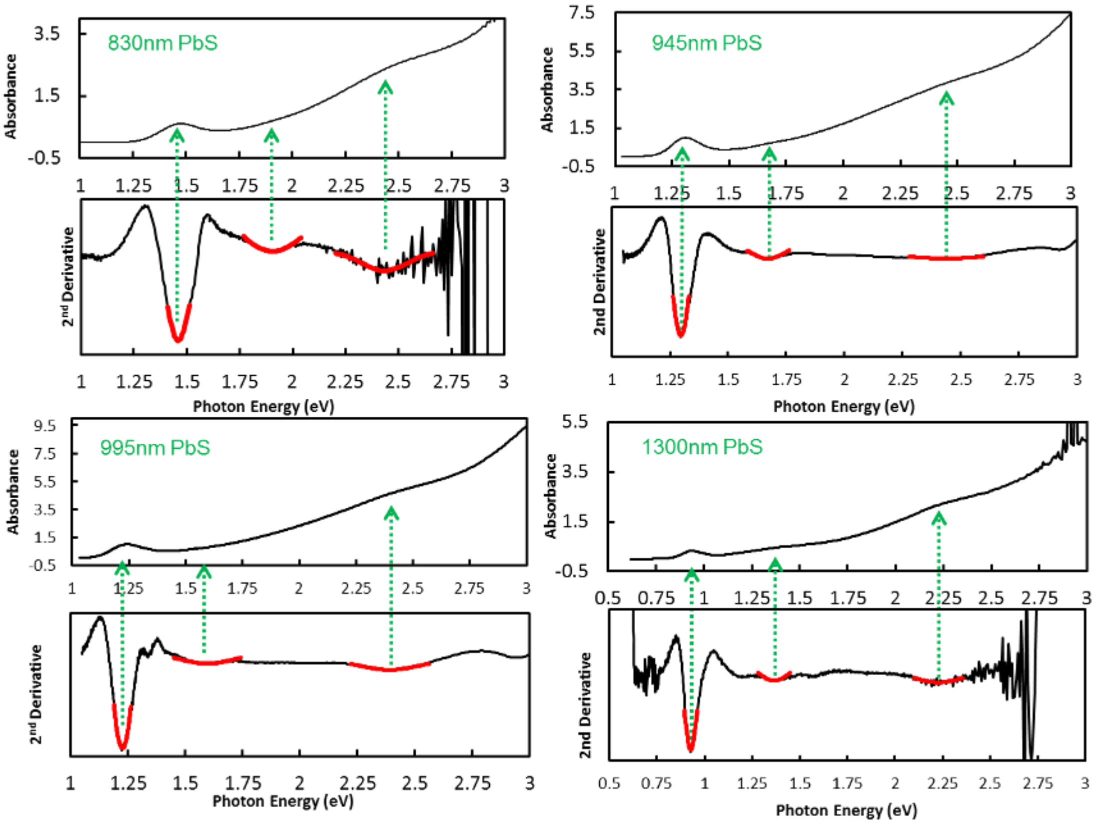

Figure 5.3: Linear absorption and second derivative spectra of a series of PbS CQDs with a variety of optical band-gaps specified by the wavelength of the first exciton absorption. We fit the second derivative spectra to identify the first, second, and third quantum confined optical transitions. The local minima in the second derivative spectra correspond to the concave down regions of the absorption spectra that arise from quantum-confined absorption. The red curves appearing in the second derivative spectra correspond to local best fit functions used to identify the center transition energies of the first three quantum confined transitions.

The first absorption band in PbS CQD semiconductors has been assigned to the $1S_h$-$1S_e$ transition,[157] shown as the yellow transition arrow labeled "E_g" in Figure 5.4A. However, assignments of higher energy transitions have varied in the literature. Therefore, we consider all of the most common assignments of the second and third quantum confined transitions and use them to extract the $1S_e$ – $1P_e$ energy splitting for different sized Pbs quantum dots. Some investigators assigned the second absorption band to forbidden $1S_h \rightarrow 1P_e$ or $1P_h \rightarrow 1S_e$ optical transition[155, 158-160] – labeled as the green transition arrows termed "E_2" in Figure 5.4A. From this assignment, the energy difference between the $1S_e$ – $1P_e$ states taken as the difference between the first and second quantum confined transitions, E_2 - E_g. The energetic splitting of the $1S_e$ – $1P_e$ states calculated from the PbS absorption spectra using this assignment appear as the green open circles in Figure 5.4B. Furthermore, this assignment leads to the conclusion that the third quantum confined transition corresponds to the $1P_h \rightarrow 1P_e$ transition – labeled as the blue transition arrow termed "E_3" in Figure 5.4A. On the basis of this interpretation, assuming symmetric energy splitting of the electron and holes levels, approximately half the energy difference between the first and third quantum confined transitions, ½ (E_3 – E_g), should correspond to the $1S_e$ – $1P_e$ energy splitting (shown as open triangles in the Figure 5.4B).

Alternatively, the second quantum confined transition has been assigned as the $1P_h \rightarrow 1P_e$ transition[157] (labeled as the blue transition arrows termed "E_3" in Figure 5.4A.). Using this interpretation, we conclude that the $1S_e$ – $1P_e$ energy splitting should equal half the energy difference between the first and second quantum confined transitions, ½ (E2 – Eg). The $1S_e$ – $1P_e$ energy splitting calculated for the series of PbS CQDs from this latter assignment is represented as the black bars in Figure 5.4B. It is noteworthy that none of the estimates for the $1S_e$–$1P_e$ energy different from these assignments exhibit the marked variation with quantum dot bandgap that is observed in the mid-infrared electronic transitions appearing in the TRIR spectra displayed in Figure 5.2A (decreasing TRIR transition energy with decreasing PbS band-gap).

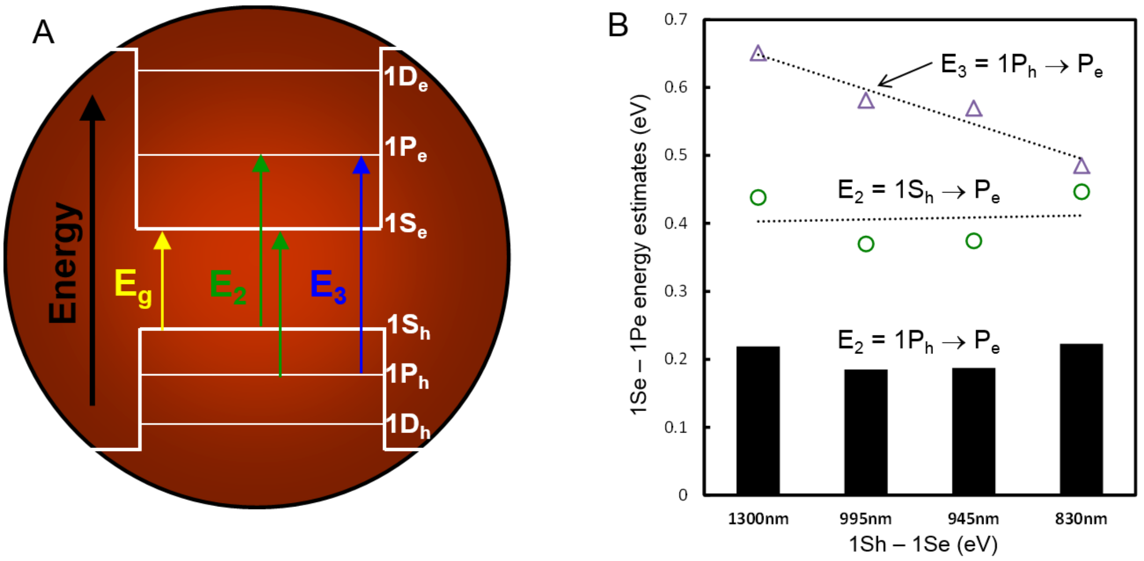

Figure 5.4: A) Shows literature assignments for the first three ground-state optical absorbance bands appearing in PbS CQD spectra in Figure 5.3. B) Estimates of the $1S_e$ – $1P_e$ energy difference for a series of PbS CQDs with the specified band-gaps. These energy estimates come from fitting the spectral features in Figure 5.3 and using the literature assignments for the optical transitions. It should be noted that discrepancies exist for the origin of the second optical transition (E_2) in PbS nanocrystals. If E_2 is interpreted as the optically forbidden $1S_h \rightarrow 1P_e$ or $1P_h \rightarrow 1S_e$ transitions as shown in Figure A, then the $1S_e$ – $1P_e$ splitting energy for this series of PbS is represented by the green circles. However, if E_2 is interpreted as the $1P_h \rightarrow 1P_e$ transitions (shown as E_3 in Figure A) then the $1S_e$ – $1P_e$ splitting energy for this series of PbS is represented by the black bars.

Incorporation of Stokes Shift Energy

Figure 5.5 is a reiteration of the absorption spectra in Figure 5.3 overlaid with corresponding photoluminescence (PL) spectra for identical PbS quantum dots. The Stokes shift (Δ_S) represents the energetic difference between the first absorbance maximum and the emission maximum. It is apparent from the data in Figure 5.5 that there is a decreasing Stokes shift for PbS QDs of increasing optical band-gap.

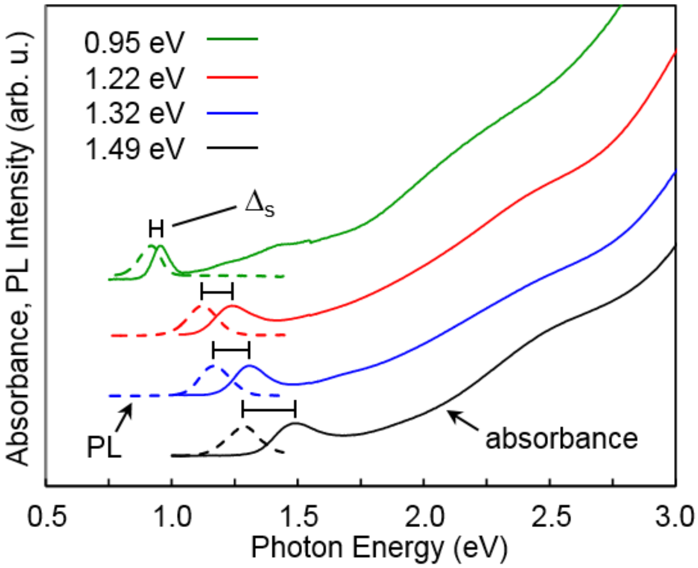

Figure 5.5: Absorbance spectra (identical to Figure 5.3) shown as solid lines and corresponding PL emission spectra measured for identical PbS QDs as a colloid suspended in octane. The data reveal a QD size-dependent Stokes shift (Δ_S) energy where the Stokes shift increases with increasing PbS optical band-gap. This QD, size-dependent Δ_S inspired us to consider incorporating the Stokes shift energy into the correlation with TRIR transition energy because the Mid-IR transient absorption spectra (Figure 5.2A) showed a similar, qualitative trend with PbS QD optical band-gap energy.

We find the best correlation with average TRIR transition energy – extracted from Figure 5.2A – is made when the Stokes shift energy is added to the $1S_e$ – $1P_e$ energy difference for the case using the assignment that second quantum confined absorption represents the transition $1P_h \rightarrow 1P_e$ (black bars in Figure 5.4B). Adapting Figure 5.4B, we show that TRIR energy for a series of PbS CQDs with four different band-gaps is quantitatively correlated with the sum of the Stokes shift energy and the 1Se – 1Pe energy splitting in Figure 5.6. This correlation between TRIR energy, Stokes shift energy and 1Se – 1Pe energy splitting suggests the mid-IR photoinduced absorption results from a transition between a state that lies below the band-edge by an energy equal to the Stokes shift energy (referred to as a sub-gap state) to the 1P intraband state.

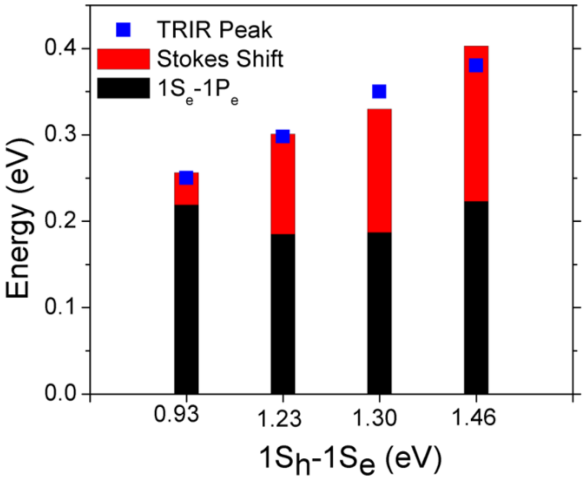

Figure 5.6: Comparison of mid-IR transition energies (blue squares) extracted from the transient infrared absorption spectra (Fig 5.2A) with the sums of 1S-1P energies (black bars) and the Stokes shift energies (red bars) of CQDs of four different bandgaps.

5.4 Results and Discussion

We hypothesized that the Stokes-shifted, sub-band state in PbS CQDs was critical to charge conduction within thin-films of these materials because the lowest-energy states that can form sufficiently delocalized electronic levels in a lightly-doped electronic material often mediate charge transport. Further characterization of the optically dark, sub-band gap state was warranted to provide insight into the ways this state can be tuned by the nanocrystal surface chemistry and the degree of quantum confinement in order to control the charge carrier dynamics in thin-films of PbS CQDs. Therefore, we sought to identify the chemical origins of the Stokes-shifted, sub-gap state, and the relationship of this sub-gap state to CQD surface chemistry, and relate these spectroscopic observables to electrical measurements provided by our collaborators in the Sargent lab.

Superimposed on the broad, transient, mid-IR spectra of electronic transitions are narrow vibrational modes around 0.18 eV (~1400 cm^{-1}) which represent symmetric and asymmetric vibrations of the MPA carboxylate functional group which is coordinated to the nanocrystal surface. The ground-state bleach and induced absorption features from MPA carboxylate surface ligands appear in the mid-IR transient spectrum because optical excitation of the PbS QD semiconductor followed by population of the sub-gap state alters the charge distributions experienced by MPA molecules which suggests the sub-gap state is strongly coupled by the nanocrystal surface. Furthermore, we identified the transition giving rise to the TRIR signal is from a sub-gap state to the 1P level based on energy correlations (Figure 5.6). The 1P level is an excitionic state originating from the PbS semiconductor, and in order for the transition to have sufficiently large oscillator strength to measure in a transient absorption experiment, the sub-gap state must have sufficient wavefunction overlap with the delocalized 1P excitonic state. Therefore, it is expected that the sub-gap level likely has origins in PbS excitoinc states as well, and could provide states sufficiently delocalized to transport charge in CQD films.

The hypotheses with regards to coupling of the sub-gap state with both the quantum dot surface and the core excitonic levels of PbS were supported by density functional theory (DFT) calculations performed by our collaborations in the Sargent Lab. The details of the DFT calculations are beyond the scope of this dissertation, but conclusions of the calculations showed that two noticeably different symmetries exist within the fourfold 1S manifold. It was found that the overlap of the electron and hole states is minimized for even-odd symmetries, and optical transitions between states of even and odd parity are optically forbidden. Furthermore, our collaborators examined the influence of surface passivation on the energies of states in the 1S manifold and for two cases: a perfectly coordinated (perfectly passivated) PbS nanocrystal and an under-coordinated surface – energy level diagrams are shown for the two cases in Figures 5.7A and 5.7B, respectively. In the case of perfect surface passivation, where no crystalline atoms have dangling bonds at the surface, the closest lying electron and hole states have identical symmetry – causing the optical transition between closest lying band states to be optically allowed. It is expected that the Stokes shift between absorption and emission should be minimized in the hypothetical case that all nanocrystal surface dangling bonds be passivated; however, without the use of a thick core-shell nanocrystal system, this limit is unlikely to be experimentally achieved.

In the case of incomplete nanocrystal surface coverage by ligands, even and odd 1S states of the conduction band manifold swap – as demonstrated previously by this reordering of the lowest energy conduction band states results in closest-lying valence and conduction band states that have opposite symmetry – making transitions between the two states optically forbidden. The resulting energetic disparity between the optical and electrical band gaps that is equal to the Stokes shift between absorption and emission, as shown in Figure 5.7

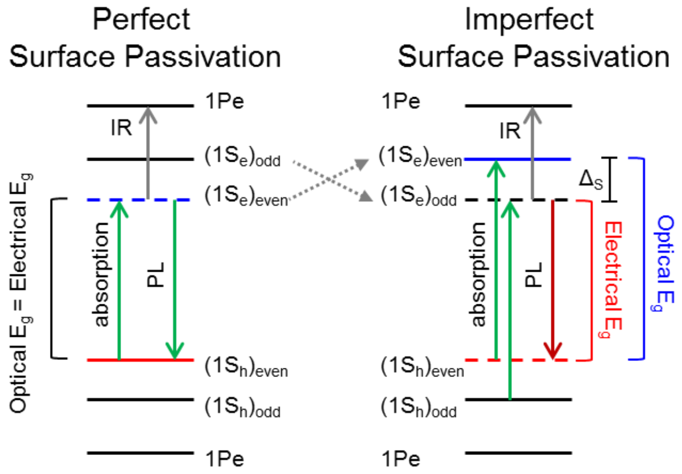

Figure 5.7: Band structure diagrams obtained from DFT calculations indicating distinct states of different symmetry in the 1S manifold. A) The electrical and optical bandgaps are nearly identical in perfectly passivated quantum dots because optical transitions are allowed between closest lying states. B) Imperfect passivation reorders the lowest energy states in the conduction band, causing optical transitions between these states forbidden, and results in large Stokes shift energies. Large reductions in surface coverage cause reordering of the electronic states and large increases of the Stokes shift energies.

We combined the transient infrared spectroscopy study of the Stokes shifted sub-gap states in PbS CQD solids with transient photoconductivity measurements to investigate the involvement of these states in charge transport. Charge carrier cooling occurs on ultrafast time scales following optical excitation of lead and cadmium chalcogenide quantum dots. However, 1S states of quantum dots are conventionally considered the lowest energy high mobility transport states in CQD solids. If electron conduction occurs primarily through $1S_e$ states, then they must be thermally promoted from sub-gap states to $1S_e$ states for electron transport to occur. In this case, the activation energies for electron transport should be equal to the Stokes shift energies of the PbS CQD solids.

We therefore investigated the activation energies for charge transport in PbS CQD thin-films using temperature-dependent transient photoconductivity decays that have been previously employed to study activated electron transport in PbS materials. Employing Arrhenius analysis, the natural logarithm of these decay traces are plotted versus inverse of thermal energy in Figure 5.8A for three PbS CQD solids with varying bandgaps. Activation energies obtained from the temperature-dependent photoconductivity reveal that electron transport in PbS CQD materials is an activated process, but activations energies are significantly lower than experimentally determined Stokes shift energies – suggesting that carrier do not need to be promoted to higher lying excitonic states to undergo efficient charge transport within CQD films.

Seeking confirmation that the Stokes-shifted, sub-gap state is involved in photocarrier transport, we examined activation energies extracted from temperature-dependent TRIR decay kinetics using a similar Arrhenius analysis as for the transient photoconductivity measurements. Charge recombination measured by transient infrared spectroscopy provides a measure of charge transport because recombination occurs via rare recombination centers. Therefore, charge transport is required for photocarriers to recombine. Figure 5.8B represents the logarithms of the rates of charge recombination versus extracted from TRIR kinetics plotted against the inverse thermal energy. The activation energies obtained from this analysis are in quantitative agreement within experimental precision with energies obtained from temperature dependent photoconductivity measurements for all quantum dot sizes. For comparison, the Stokes shift energies of the corresponding PbS quantum dots obtained from analysis of absorption and photoluminescence spectra in Figures 5.3 and 5.5 are included in Table 5.1. In all cases, the activation energies are much smaller than the Stokes shift energies.

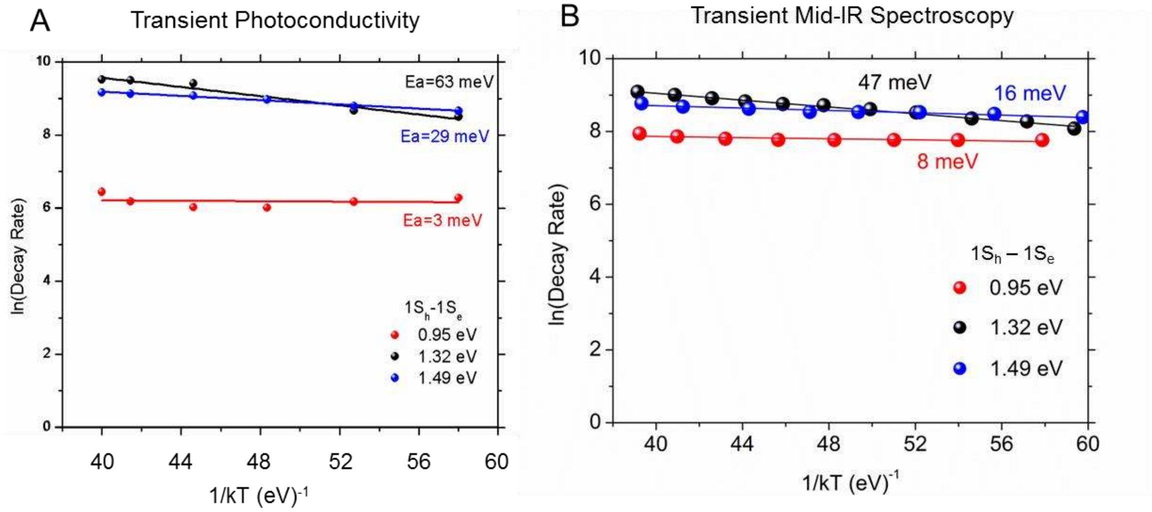

Figure 5.8: Arrhenius plots used to extract activation energies from A) temperature-dependent transient photoconductivity and B) temperature-dependent TRIR spectroscopy experiments for PbS materials with three band-gaps. The activation energies show qualitative agreement for both electrical and optical techniques.

Table 5.1: Comparison of Optical Band Gap, Stokes-shift Energy, and Activation Energies Extracted from Arrhenius analysis of TRIR and Transient Photoconductivity Measurements

PbS Optical Band Gap $1S_h$-$1S_e$ (eV)	Stokes Shift Energy (meV)	TRIR E_a (meV)	Transient Photoconductivity E_a (meV)
0.95	50	8	3
1.32	130	47	63
1.49	190	16	29

5.5 Conclusion

The work presented in this chapter provides optical and electrical evidence to support the inclusion of a previously unrecognized electronic state in PbS colloidal nanocrystals. Our results point to the presence of an electronic state that lies below the conduction band edge by an energy equal to the Stokes shift energy difference between the first optical absorption maximum and the emission maximum. Supported by DFT calculations, we find that direct absorption to this sub-gap state in nanocrystals with incomplete surface passivation is optically forbidden but can be populated following carrier cooling from higher lying states. Correlating the average transition energy from mid-IR transient absorbance experiments with a sum of the Stokes shift energy and the energy splitting between the $1S_e$-$1P_e$ excitionic states reveals that this mid-IR transient absorbance results from promotion of carriers in the sub-gap state to the $1P_e$ level.

Upon comparison of the activation energies extracted from temperature-dependent transient absorption measurements and transient photoconductivity measurements we show that the sub-gap state is responsible for charge transport in CQD thin-films. Not surprisingly, transport within the delocalized sub-gap state is an activated process, but the activation energy measured for a series of PbS thin-films is significantly less than the Stokes shift energy – indicating that promotion of charges to higher lying states is not required for transport. We postulate that the activation energy we measure is a result of nanocrystal polydispersity which corrugates the electronic structure landscape experienced by mobile charges within the thin-film. Our findings reveal that controlling the density of surfaces ligands on nanocrystal surfaces is key minimizing the Stokes shift energy for PbS CQDs. By finding new colloidal nanocrystal synthetic and surface passivation strategies that yield lower density of dangling surface bonds, we expect a reduction in the Stokes-shift energy which is of course correlated with shifting the sub-gap states to an energetic level that is isoenergetic with the optical band edge. Further improvement is CQD surface chemistry and monodispersity are warranted as we believe these are achievable route to realizing higher photovoltages, photocurrents, and power conversion efficiencies in CQD solar cells.

CHAPTER 6

Infrared Spectroscopic Investigation of Protein Electrostatic Microenvironments and their Role in Enzyme Catalysis

The material in this chapter has been adapted from the following publications: C. Tony Liu, Robert J. Stewart, Joshua P. Layfield, Jarrod B. French, Philip Hanoian, John B. Asbury, Sharon Hammes-Schiffer, and Stephen J. Benkovic Probing the Electrostatics of Active Site Microenvironments Along the Catalytic Cycle of *Escherichia coli* Dihydrofolate Reductase; *J. Am. Chem. Soc.*, 2014, 136 (29), pp 10349–10360; and C. Tony Liu, Robert J. Stewart, and Stephen J. Benkovic Too Fast for Catalysis; *Biocatalysis and Biotransformation*, 2013; 31(5); 269-271, which has been adapted for the context of this dissertation.

6.1 Introduction

6.1.1 The Role of Protein Motions in Enzyme Catalysis

The field of enzyme catalysis has experienced a renaissance over the past decade, characterized by a renewal of interest in unraveling the fundamental components involved in the exalted enzymatic efficiency. Enzymes have evolved to be proficient in accelerating a wide variety of chemical transformations, and the majority of enzyme-catalyzed processes, which take seconds or minutes to complete, would otherwise take billions of years in the absence of enzymes.[161] Despite the impressive progress in our understanding of enzyme mechanisms, “designer” or *de novo* enzymes/catalysts derived from static structures are unable to achieve the same degree of catalytic efficiency of naturally-derived enzymes. From recent research advancements in X-ray crystallography, solution NMR, FTIR, ultrafast 2D-IR, FRET, computational simulations, and single molecule techniques, it has become clear that enzymes are flexible entities that can adopt multiple conformations across the protein energy landscape, which can be influenced by different conditions.[162] Moreover, it has been demonstrated that there is a strong correlation between the conformational states of an enzyme and its activity.[163-164] Incorporation of protein flexibility into such calculations should lead to novel design of inhibitors that effectively regulate enzyme activity by manipulating the enzyme’s conformational states and provide unique pharmacophores.[165-166] However, there are some fundamental disagreements regarding the intricate connection between protein motions and the chemical reactions that take place in the enzyme’s active site. As illustrated in Figure 6.1 A (modified from reference 2), the time-scale of available motions in proteins spans roughly 15 orders of magnitude in time from 10^{-15} seconds to 10^{0} seconds. Broadly speaking, the events can be classified into two groups: fast femtosecond (fs; 10^{-15}s) dynamics that reflect the local fluctuations of the protein residues and slow millisecond (ms; 10^{-3}s) motions that involve the collective conformational changes of a protein in transitioning between equilibrium conformations. While bond vibrations occur at fs or ps timescales, most enzyme-catalyzed chemical transformations occur in the ms – s range. Once fully bound, the conversion of the enzyme – substrate(s) complex into the enzyme – product(s) complex is often accompanied by rate constants ranging from 10^{1} to 10^{4} s^{-1} at 25°C.[161] Yet, it has been argued that these millisecond collective conformational fluctuations are too slow relative to the bond-vibrational timescale involved in the cleavage/formation of chemical bonds in the transition state. Consequently, special ‘promoting-mode’ motions in the fs – ps timescales have been proposed to assist enzymatic barrier crossing at the transition state.[167] As shown in Figure 6.1B, there is a substantial temporal disconnection between these proposed fs – ps promoting-mode motions along the enzyme ensemble coordinate and the ms – s enzyme reactions, making it highly unlikely that fs – ps fast motions can greatly affect the energy barrier from the ground state, reactant (Michaelis – Menten) complex to the transition state of the reaction. Furthermore, these fs – ps timescale bond vibrations are likely to exist at the transition state of an uncatalyzed reference reaction taking place in the absence of an enzyme in solution – strengthening the argument that fs – ps motions in an enzyme at the transition state are not likely the cause of enzyme’s catalytic efficacy or the enzyme’s ability to reduce the activation energy barrier of a particular uncatalyzed reaction.[161] For example, with ultrafast, transient, pump – probe IR and stopped-flow Fourier-transform IR (SF-FTIR) spectroscopies, both ps and ms protein motions were observed in the catalytic cycle of coenzyme B 12-dependent ethanolamine ammonia lyase,[168] and there was no indication as to how these motions might contribute to lowering the free energy barrier of the reaction. In this case, conformational motions are coupled to the reaction only in the sense that they both occur in the same temporal dimension, but this does not provide evidence of a casual effect of motions on catalysis. Furthermore, just because two observable events occur at the same timescale it does not mean that they progress forward concurrently, which would be a more convincing evidence for the ‘coupling’ between protein motions and catalysis.

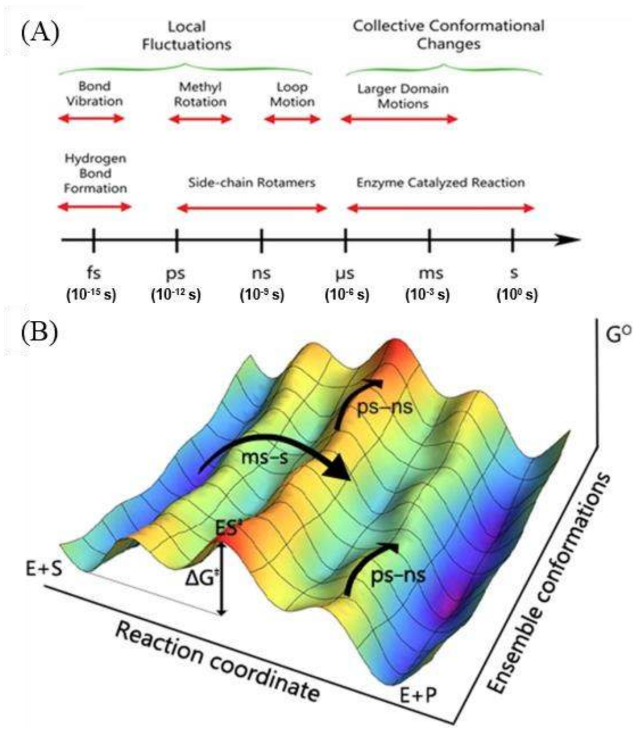

Figure 6.1: A) Timescale of various chemical events and protein motions. b) 3D representation of the free energy landscape of an enzymatic reaction. Multiple conformational changes are expected to occur along the reaction coordinate from free enzyme (E) and substrate (S) to the transition states ($ES^{\ddagger}$) and then to the products (P) through many parallel reaction pathways. Conformational changes occur along both the x and y axes, and different conformations should have different free energies (G^o) associated with them. Both the large scale collective conformational changes and typical enzymatic reactions occur in the ms–s timescale. In contrast, local fluctuations in the ps–ns timescale relate to processes with significantly lower energy barriers than the actual enzymatic reaction.

Using nuclear magnetic resonance (NMR) relaxation experiments, Bhabha et al. showed the loss of millisecond timescale active site loop motions in dihydrofolate reductase coincided with a ~20-fold drop in the rate of the enzyme-promoted hydride transfer reaction.[169] The observed reduction in the rate of hydride transfer is most likely due to changes to the reaction's free energy profile, which is a product of various elements including protein conformational states. However, this does not mean that the conformational changes occurring along the reaction coordinate contribute energetically to overcoming the energy barrier of the reaction. A proposed explanation for the catalytic benefit of these 'promoting-mode' motions is based on the ability to facilitate the compression of reacting substrates.[170] For example, Bandaria et al. applied ultrafast two-dimensional infrared (2D-IR) echo spectroscopy to study a transition-state complex mimic of formate dehydrogenase.[171] They found hydrogen bond fluctuations between four active site residues and a transition state ligand analog (azide, N_3^-) on the order of fs timescale. This was interpreted as motions relevant to the optimized donor – acceptor distance between the reacting substrates in the transition state. This should not be interpreted as invoking fs structural fluctuations to actively push the donor and the acceptor species together, because it has been correctly pointed out that similar compression of reacting species should also exist in the uncatalyzed reaction in solution.[13] There will also be an energetic cost (e.g., from electrostatic repulsion, entropy, and steric) for compressing the distance between reacting substrates. The consequences of such energetic cost (which will increase the energy barrier of the reaction) need to be accounted for when considering the overall effect of promoting-mode motions. It should be noted that there is no convincing evidence in the literature at this moment, experimental or theoretical, that shows protein conformational fluctuations being directly coupled to bond vibrations in the transition state.[163, 172-173] In the midst of a relatively new and controversial issue, it is imperative to establish a clear perspective. The emerging view in the literature is that, collectively, the local fast stochastic thermal motions lead to slower large scale conformational changes that exist in the same temporal space (ms – s) as the enzymatic reactions. More importantly, these slow protein motions are involved in enzymatic reactions are hypothesized to guide the orientation of the reacting species along the reaction coordinate while providing a conducive electrostatic environment for stabilizing the high energy transition state species,[162-163, 174-175] and we believe it is this dynamic electrostatic environment, uniquely established within the enzyme active-site, that provides enzymes with their powerful ability to accelerate chemical reactions. It is for this reason that we feel Infrared Vibrational Stark effect experiments[176] should offer more in-depth analysis of the intimate connection between conformational and electrostatic samplings along the reaction pathway, and the enzymatic reaction. Looking forward, the intrinsic flexibility/motions in enzymes and the resultant, transient, electrostatic environments established by different protein confirmations might be the missing link in the *de novo* design of artificial enzymes capable of biological catalytic efficiency.

6.1.2 The Role of Electrostatic Interactions in Enzyme Catalysis

Electrostatic interactions have been shown to play a vital role in enzymes, such as: assisting in the binding or positioning of ligands within the active-site, as well as stabilizing the transition state in some cases.[163, 173-175, 177-181] Moreover, we hypothesize these electrostatic interactions to be significantly modulated by the conformational changes that occur over the catalytic cycle.[174, 180, 182-183] In particular, the electrostatic environment in the active site is expected to change as the ligands bind, the chemical reaction occurs, and the ligands are released. Quantifying the electrostatic contributions to the individual catalytic steps, as well as the impact of conformational changes on the electrostatic interactions, is a challenging yet important goal in the field of enzyme catalysis.

To gain a better understanding of the catalytic role of electrostatics and conformational motions, we probed the changes in the active site electrostatic environment resulting from structural rearrangements that occur along the catalytic cycle of *Escherichia coli* dihydrofolate reductase (*ec*DHFR). An enzyme responsible for catalyzing the NADPH-dependent conversion of 7,8-dihydrofolate (DHF) to 5,6,7,8-tetrahydrofolate (THF). X-ray crystallography, nuclear magnetic resonance (NMR), theoretical, and photophysical studies have shown that *ec*DHFR exhibits significant structural rearrangements along the catalytic cycle.[179, 184-186] Thus, *ec*DHFR is a highly suitable system for studying how conformational changes can affect the active site electrostatic environment, which can then modulate enzyme catalysis.

Recently, thiocyanate and other vibrational probes have been incorporated into a number of biological systems to investigate the local electrostatic environments.[2, 187-191] Boxer and co-workers have explored the use of nitrile (CN) probes to detect differences in the electric field projected along the CN axis in proteins upon ligand binding, protein folding, and protein–protein association.[2, 176, 192-195] Using this method, they showed that the electrostatic environment in the active site of Δ^5-3-ketosteroid isomerase (KSI) exhibits limited rearrangement upon photoexcitation of a ligand, where this excitation was proposed to mimic the movement of charge during the catalyzed chemical transformation.[192] The authors concluded that the KSI active site is electrostatically preorganized for catalysis in its tertiary protein structure and that major rearrangement is not necessary for catalysis. This observation is not unexpected due to the relatively rigid structure of KSI[196-198] that limits substantial conformational mobility, thereby limiting electrostatic rearrangement. However, calculations have shown that the active site reorganization, manifested as small conformational changes that position the reacting species for chemistry, is still required in KSI to enable the catalyzed proton transfer reactions.[198-199] In contrast to KSI, which exhibits limited protein motion along the catalytic cycle, *ec*DHFR is known to undergo significant conformational changes along the catalytic cycle, suggesting that larger changes in electrostatics could play a more significant role in all steps of the catalytic cycle.

To examine the electrostatic interactions within the active site of *ec*DHFR, we incorporated thiocyanate probes at site-specific locations. Using vibrational and ^{13}C NMR spectroscopic techniques, as well as computer simulations, we analyzed the electrostatics and degree of hydration of the microenvironments surrounding the probes. The electrostatic interactions arising from the active site microenvironments surrounding the small, catalytically nonintrusive, probes led to different observed CN vibrational stretching frequencies and ^{13}C NMR chemical shifts along the catalytic cycle. Experimental data clearly show changes in the active site electrostatic environment due to structural rearrangements. Further insights were obtained through mixed quantum mechanical and molecular mechanical (QM/MM) analyses of classical molecular dynamics (MD) simulations – although the details of these computational experiments will not be the focus of this dissertation. It should be noted that these calculations were able to reproduce the experimentally measured vibrational frequency shifts reported by the probes across the enzyme-catalyzed hydride transfer step of the catalytic cycle.[179, 184]

Moreover, the electrostatic contributions from the active site microenvironments surrounding the probe were decomposed into the major components (individual residues and ligands). In addition, the experimentally validated theoretical model allowed us to examine the electric field along the hydride transfer pathway between the substrate and cofactor, a property that is catalytically important yet unattainable experimentally. This integrated approach provides valuable insights into the interplay between electrostatic and conformational changes along the catalytic cycle of *ec*DHFR.

6.2 Materials and Experimental Methods

6.2.1 Materials

7,8-Dihydrofolate (DHF) and [(4′R)-^{2}H]NADPH (NADPD) were prepared according to previously described procedures.[200-201] β-Nicotinamide adenine dinucleotide phosphate reduced tetra(cyclohexylammonium) salt (NADPH), β-Nicotinamide adenine dinucleotide phosphate hydrate (NADP$^+$), potassium cyanide-^{13}C (99 atom % ^{13}C), methotrexate, methotrexate-agarose, dithiothreitol (DTT), folic acid (≥97%; FOL), sodium phosphate monobasic monohydrate (98–102%), and 5,5′-dithiobis(2-nitrobenzoic acid) (Ellman's reagent) were purchased from Sigma-Aldrich and used without further purification. (6*S*)-5,6,7,8-tetrahydrofolic acid (THF) was obtained from Schircks Laboratories. Sodium phosphate dibasic heptahydrate and 2-nitro-5-thiocyanatobenzoic acid (97%; NTCB) were purchased from EMD and TCI America, respectively. pH values were measured using an Accumet model 13-620-300 standard combination electrode calibrated with VWR certified standard aqueous buffers (pH = 4, 7, and 10). All of the experiments, including kinetics and spectroscopic measurements, were done in pH 7.0 50 mM sodium phosphate buffer unless otherwise specified.

6.2.2 Specific *ec*DHFR Constructs

First, the two native cysteines (C85 and C152) in wild-type (WT) *ec*DHFR were mutated to Ala and Ser, respectively, to generate ΔCys *ec*DHFR using the Stratagene QuikChange site-directed mutagenesis kit and the WT *ec*DHFR template as described elsewhere.[202] Primer sequences were 5′-C GAA GCC ATC GCG GCG GCT GGT GAC GTA CCA G-3′ (C85A) and 5′-C TCG CAT AGC TAT TCA TTC GAA ATC CTC G-3′ (C152S). The choice of amino acid substitution was based on a previous report showing that the C85A/C152S substitution on *ec*DHFR induced minimal perturbation to the enzymatic activity.[203] Selective incorporation of cysteine was achieved through subsequent mutations using the following primers: 5′-CA ATC GGT AGG CCT TGC CCC GGC CGC AAA AAT ATT ATC-3′ (L54C) and 5′-G ATT ATG GGG CGC CAT TGC TGG GAA TCA ATC G-3′ (T46C). Plasmid construction, protein expression, and purification of mutant DHFRs were performed according to published protocols.[202]

6.2.3 SCN and S^{13}CN Labeling

Labeling of the single-cysteine *ec*DHFR constructs (ΔCys L54C and ΔCys T46C, denoted as L54C-CN and T46C-CN, respectively) was achieved using a modified version of a published procedure.[204] Inside an Amicon Ultra-4 10K nominal molecular weight limit (NWML) centrifugal filter tube, approximately 400 μM of each *ec*DHFR construct was mixed with four times excess of NTCB in 4 mL of 0.1 M sodium phosphate buffer at pH

7.4. The mixture was allowed to react at room temperature for 10 min, and reaction progress was monitored by the appearance of the phenolic product using a UV–vis spectrophotometer. The protein mixture was then concentrated by spinning at 5K rpm in a centrifuge at 4 °C. The protein sample was then washed twice with 12 mM KCN in pH 7.0 50 mM sodium phosphate buffer, with a concentration step after each wash. This was followed by washing the protein sample with 50mM pH 7.0 sodium phosphate buffer two more times before concentrating the protein solution down to ~0.8 mL, which was then applied onto a size exclusion column (Econo-Pac 10DG; Bio-Rad) that was pre-equilibrated with pH 7.0 50 mM sodium phosphate buffer. The isolated labeled proteins were concentrated in an Amicon Ultra-4 10K NMWL centrifugal filter tube. The intact masses of SCN labeled and unmodified samples were confirmed by ESI-MS, which yield deconvoluted *m*/*z* values of 17965 (L54C)/17978 (T46C) and 17940 (L54C)/17953 (T46C) Da, respectively. The theoretical molecular weights for the unmodified samples are 17941 (L54C)/17953 (T46C) Da.

Similar preparation procedures were used for the $S^{13}CN$ labeled samples. A mixture containing 10 mM Ellman's reagent and 0.5 M $K^{13}CN$ in pH 7.0 0.1 M sodium phosphate buffer was prepared at room temperature for 15 min. This mixture was then allowed to react with a sample of the unlabeled protein in an Amicon Ultra-4 10K NMWL for 10 min at room temperature. The final concentrations of a typical reaction mixture were 500 μM protein, 5 mM Ellman's reagent, and 0.25 M $K^{13}CN$. The subsequent purification and isolation steps were similar to those for SCN labeling, except that $K^{13}CN$ was used for washes rather than KCN. Successful labeling was confirmed spectroscopically by the release of one equivalent of the phenolic product as well as ^{13}C NMR comparison with the unlabeled proteins.

6.2.4 FTIR Spectroscopy Measurements

FTIR Spectra were obtained at room temperature using a Mattson Research Series FTIR Spectrometer (Madison Instruments, Inc.) equipped with a liquid-nitrogen cooled HgCdTe (MCT) detector (Infrared Associates, Inc.). Cyanylated DHFR samples were mixed with appropriate ligands (1:10 mole equivalents DHFR:ligand) in aqueous buffer and placed in a liquid cell with two CaF_2 windows separated by a 56μm Teflon spacer. All thiocyanate (SCN) stretch absorbance spectra for cyanylated DHFR samples consisted of 2000 scans and were collected with 1.0 cm^{-1} resolution. The SCN stretch absorbance spectra for cyanylated DHFR samples were obtained by subtracting a spectrum of the aqueous buffer solution from the protein spectrum to obtain the absorbance spectra shown in Figure 6.2 B. The baseline for each spectrum was corrected by fitting a 5th order polynomial function to the data (shown as a black, solid line fit to each spectra in Fig 6.2B), as done previously by Fafarman and McMahon.[193, 205] The 5th order polynomial fit functions were obtained by defining roots at least 15 cm^{-1} from the peak maximum, meaning the data and fits were forced to be equal at points more than 15 cm^{-1} from the central frequency.

All published spectra are the averages of two independently prepared protein samples after fitting and subtracting the baseline with the polynomial and normalizing the peak height to unit amplitude. The peak positions obtained from independently prepared protein samples typically differed by less than 0.5 cm^{-1}, substantially less than the changes among peak positions due to variation by protein binding and release of the substrate and cofactor. The IR vs. ^{13}C NMR correlation data are shown in Figure 6.4 and tabulated in Table 6.1, below. The species that appear to exhibit significant hydrogen bonding can be described by a linear expression (slope = -2.6 ± 0.5 cm^{-1}/ppm, R2 = 0.80), which is within one standard deviation from that of EtSCN in non-hydrogen bonding solvents (slope = -1.7 ± 0.5 cm^{-1}/ppm, R2 = 0.68;9 dashed line). In water, hydrogen bonding between a water molecule and acetonitrile induces a 7 cm^{-1} blue shift in the nitrile stretching frequency, which is consistent with the degree of shift we found in the nitrile.

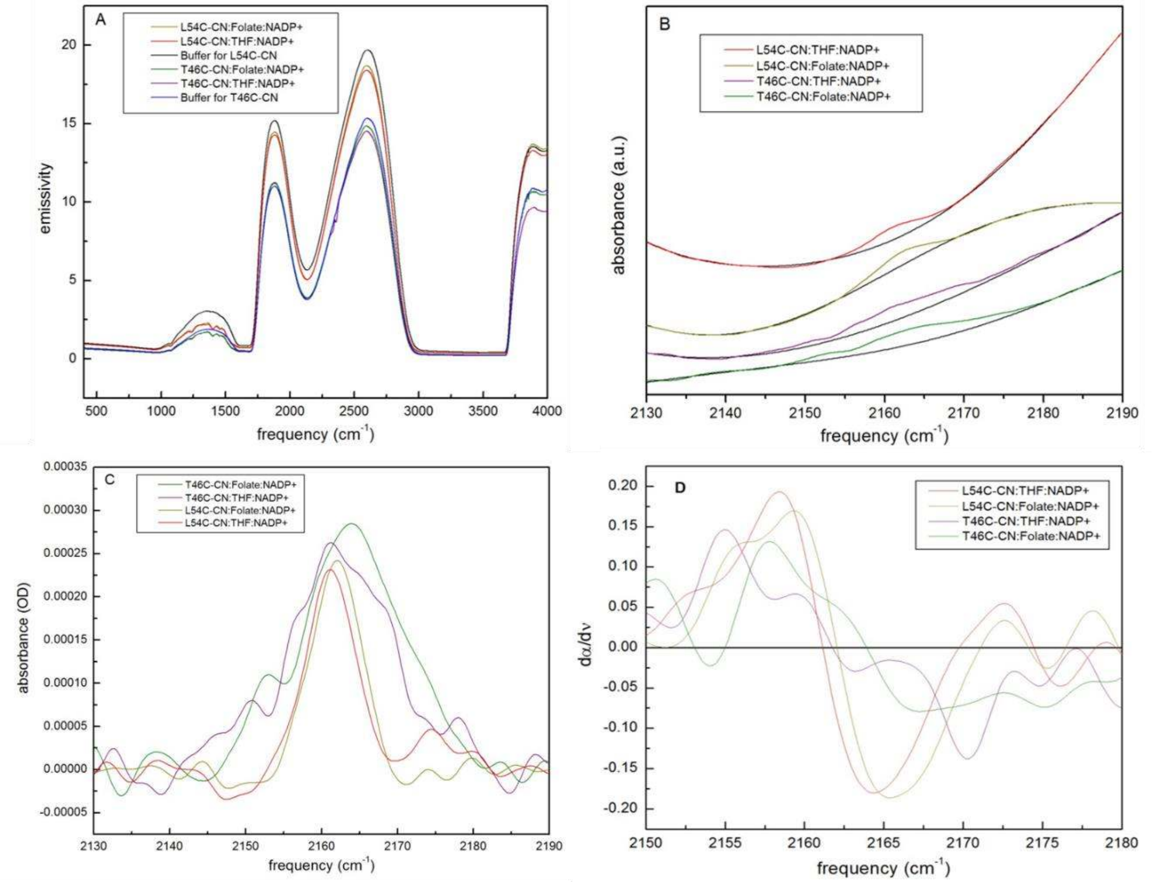

Figure 6.2: Details of FTIR signal processing and analysis. (A) Shows full mid-IR intensity spectra measured for DHFR/buffer/water solutions before the background of matching buffer solution was subtracted to calculate the absorbance spectrum. Intense H_2O absorptions are obvious in these spectra: ($\tilde{\nu}(\mathrm{O-H\ bend}) > 1800\ \mathrm{cm}^{-1}$, $\tilde{\nu}(\mathrm{O-H\ stretch}) \sim 2800 - 3800\ \mathrm{cm}^{-1}$, and $\tilde{\nu}(\mathrm{O-H\ combination}) \sim 1800 - 2800\mathrm{cm}^{-1}$), which necessitates the use of short path length liquid cells. (B) The SCN stretch absorbance spectra following subtraction of the buffer background for the protein samples. Large baseline offsets arise from the bend + stretch combination band of water. The black curves correspond to local best fit 5th order polynomials with roots defined more than 15 cm^{-1} from peak maximum of each spectrum. (C) Represents the SCN stretch band following subtraction of the best fit functions (black line, Fig 6.2A) from raw absorbance spectra

(colored lines, Figure 6.2B). As discussed below, the center frequency has little dependence on the points at which polynomial and data are forced to be equal in our analysis scheme (see Figure 6.3). The first derivative spectra (D) were calculated from the baseline-corrected SCN absorption spectra appearing in Panel C. The node in the first derivative spectrum corresponds to the peaks of the absorption spectra (where the derivate is zero). This analysis scheme was used to identify the center vibrational frequencies of the *ec*DHFR-CN stretch modes with negligible influence from the 5th order polynomial function or background subtraction procedure.

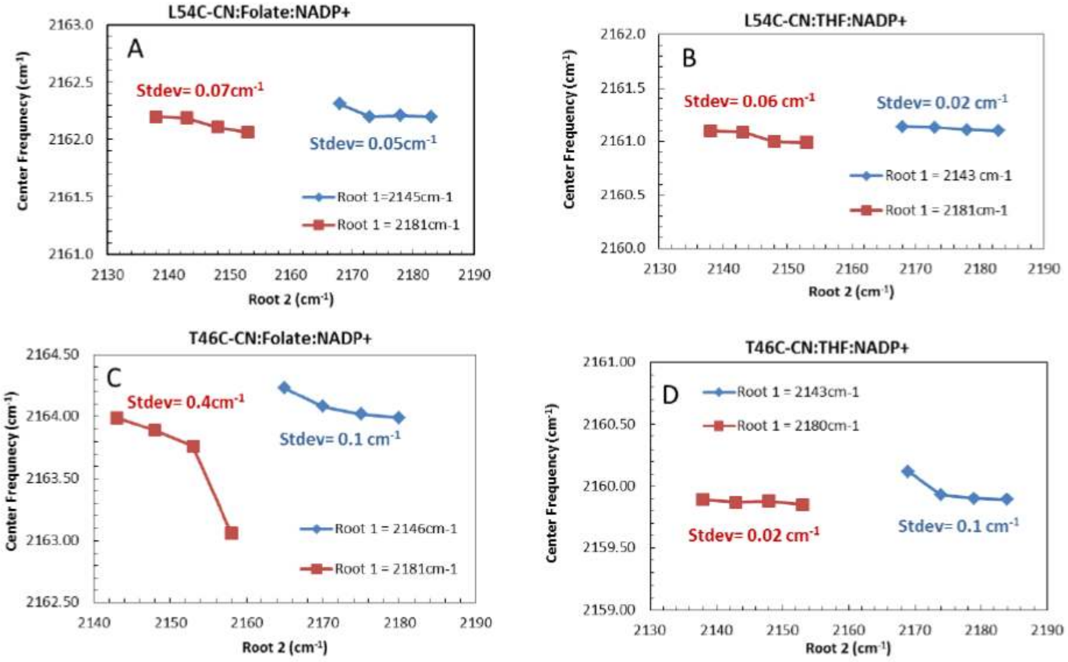

Figure 6.3: Analysis of the sensitivity of the center frequency with definition of 5th order polynomial roots. To quantitatively assess the variation of the center frequencies obtained from the CN stretch peaks versus locations of where the 5th order polynomial is forced to equal the baseline, we systematically varied the position of the roots on either side of the CN stretch peak and plotted the corresponding center frequencies for each protein, substrate and cofactor complex. Panels A – D represent the results of calculating the center frequencies of the CN stretch peaks while holding one root position constant and systematically varying the other root. The root that is held constant is labeling Root 1 in the panels, and the root that is varied is labeled Root 2. Symmetric variation of both roots simultaneously had no effect on the center frequencies obtained from our analysis scheme. We performed this analysis for both roots: we fixed the high frequency root and varied the low frequency pinning point (data appear as squares); we also varied the high frequency root and fixed the low frequency point (data appear as diamonds). Panels A, B, C, and D

show the variation in the center frequency for a variety of root positions for L54C-CN:FOL:NADP+, L54C-CN:THF:NADP+, T46C-CN:FOL:NADP+, and T46C-CN:THF:NADP+ samples, respectively. The standard deviation in the center frequency for each root position is displayed in the figure, with the largest variation in center frequency of 0.4 cm-1 and most variations less than 0.05 cm-1, showing that the center frequency is insensitive to the position of the polynomial roots in comparison to the variation among peak positions due to variation by protein binding and release of the substrate and cofactor. It is noteworthy that the largest variation of the center frequency with the location of roots occurs in the T46C-CN:FOL:NADP+ complex, which has the greatest line width. The lowest extracted frequency in Panel C occurs where the low frequency root is actually within the line width of the CN stretch. Therefore, the experimental uncertainty in frequency is actually substantially less than the 0.4 cm^{-1} standard deviation indicated in Panel C.

6.2.5 ^{13}C NMR Experiments

^{13}C NMR spectra were collected on a Bruker AV-III-600 (150.9 MHz ^{13}C frequency) at 25 °C. Samples were prepared with 1.6 mM of the $S^{13}CN$ labeled protein, 8 mM ligands, and 50 mM potassium phosphate (pH 7.0) in water. A sealed capillary tube containing 1 M acetone in D_2O was inserted into the NMR tube that holds the protein sample. This provided both a locked solvent and an internal standard. Chemical shifts were also checked with an external standard of tetramethylsilane. Spectral data were acquired for ~3000–4000 scans. The 1D ^{13}C NMR spectral data obtained for each sample were compared with its corresponding ^{13}C DEPT 45° (distortionless enhancement by polarization transfer) data to confirm the identity of the assigned peaks. Under the same experimental conditions, we were unable to detect the ^{13}C NMR signals corresponding to the SCN probes for samples containing either the nonisotopically enriched SCN label or the unlabeled proteins. The IR vs. ^{13}C NMR correlation data are shown in Figure 6.4 and Table 6.1 summarizes ^{13}C NMR Shifts, central frequency of vibrational bands, and Full Width at Half Maximum (FWHM) Values for the IR spectra in two *ec*DHFR mutants, L54C and T46C.

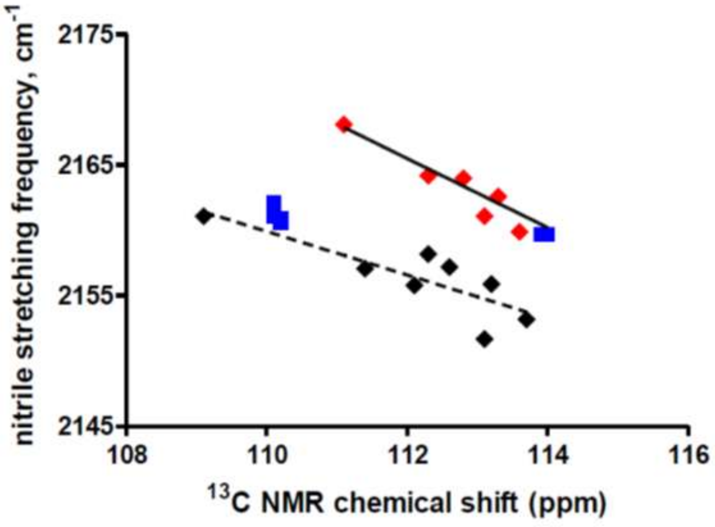

Figure 6.4: Plot of nitrile vibrational stretching frequencies versus the ^{13}C NMR chemical shifts for the labeled *ec*DHFR variants (T46C-CN: ♦ and L54C-CN: ■). The dashed line and the black solid data points are from a previous publication illustrating the expected trend for EtSCN in non-hydrogen bonding solvents.[2] The solid line (slope = -2.6 ± 0.5, R2 = 0.8008) is fit to all data points that exhibit significant deviations (~ 7 cm^{-1}), which can be attributed to specific hydrogen-bonding interactions between the SCN probe and a hydrogen bond donor.

Table 6.1: S^{13}CN NMR Chemical Shifts and FTIR Center Frequency Data

	L54C-CN Complexes		
	^{13}C Chemical Shift (ppm)	IR Frequency (cm^{-1})	FWHM (cm^{-1})
Apoenzyme	113.9 ± 0.1	2159.7	12.6 ± 0.1
E:NADPH	113.7 ± 0.0	2159.7	11.9 ± 0.1
E:NADPH:FOL	110.1 ± 0.1	2162.1	10.95 ± 0.08
E:NADP+:FOL	110.1 ± 0.0	2162.1	6.43 ± 0.07
E:NADP+:THF	110.1 ± 0.2	2161.1	6.2 ± 0.1
E:THF	110.2 ± 0.0	2160.9	8.08 ±0.08
E:NADPH:THF	110.2 ± 0.1	2160.6	6.61 ±0.08

	T46C-CN Complexes		
	^{13}C Chemical Shift (ppm)	IR Frequency (cm^{-1})	FWHM (cm^{-1})
Apoenzyme	112.3 ± 0.2	2164.2	11.56 ± 0.09
E:NADPH	111.1 ± 0.0	2168.1	8.2 ± 0.1
E:NADPH:FOL	112.5 ± 0.2	2164.2	12.07 ± 0.03
E:NADP+:FOL	113.1 ± 0.1	2164	14.1 ± 0.2
E:NADP+:THF	113.6 ± 0.0	2159.9	11.8 ± 0.1
E:THF	112.9 ± 0.1	2161.1	12.2 ± 0.1
E:NADPH:THF	113.3 ± 0.0	2162.6	13.49 ± 0.06

6.2.6 Computational Methods

My collaborators in the Hammes-Schiffer lab (University of Illinois at Urbana-Champaign, Department of Chemistry) were responsible for providing computational support for this experimental work. Using a combination of classical Molecular Dynamics (MD) simulations and mixed Quantum Mechanics/Molecular Mechanics (QM/MM) calculations they were able to reproduce our experimental, vibrational, FTIR spectra of Cyanylated DHFR with very high precision.[55] The theoretical contribution was not the focus of my research in this collaborative effort, and as such, the details of the method are beyond the scope of this dissertation.

6.2.7 Electrostatics Calculations

To assist in the analysis of the vibrational frequency calculations, we calculated the average electric field at the midpoint of the CN bond in the thiocyanate group from our MD simulations. The shift is vibrational frequency of a spectral feature due to an environmental electric field ($\Delta\vec{E}_{env}$) can be described by the vibrational Stark effect:

$$hc\Delta\tilde{v}_{CN} = \Delta\vec{\mu}_{CN} \cdot \Delta\vec{E}_{env} = |\Delta\vec{\mu}_{CN}| \cdot |\Delta\vec{E}_{env}| \cos\theta \quad \boxed{6.1}$$

where *h* is Planck's constant, c is the speed of light in a vacuum, $\Delta\tilde{v}_{CN}$ is the shift in vibrational frequency due to an applied or environmental electric field, $\cdot \Delta\vec{E}_{env}$ is the difference in the electric field vector at the nitrile bond as a result of the change in the environment, $\Delta\vec{\mu}_{CN}$ is the difference dipole moment for the vibrational transition, which in the case of a thiocyanate lies along the C-N bond axis, and θ is the angle between these two vectors. The magnitude of $\Delta\vec{\mu}_{CN}$ is the Stark tuning rate, which is a measure of the sensitivity of the probe to changes in the local electric field. Boxer and co-workers have measured the Stark tuning rate for thiocyanate probes in various environments, including in proteins, to be ~0.7 cm^{-1}/(MV/cm).[193] We emphasize that this equation accounts only for the classical electrostatic effects of the environment and does not account for the quantum mechanical aspects of effects such as specific hydrogen-bonding interactions and polarization. While these phenomena have significant classical components, they also have nonclassical aspects that can be incorporated into the calculations by treating interacting residues quantum mechanically, as will be discussed below.

Recent work explores the role of a local field correction factor[206] that scales the externally applied electric field to obtain the local field experienced by the probe, which is typically larger because of the polarization of the local environment induced by the applied electric field. This local field correction factor has been estimated to be between 1.1 and 1.3 for protein environments,[207-208] but recent investigations have suggested that it may be as large as 1.8.[206] We have not considered the role of the local field correction factor in our analysis of the electric fields in DHFR due to the lack of consensus about its value for a protein environment. Moreover, applying the local field corrections would result in changes that are within the error bars of our calculations.

To calculate the electric field at the nitrile bond, a virtual particle was positioned at the midpoint of the CN axis during the MD trajectory computation. This virtual particle had no electrostatic or van der Waals interactions with other particles, and the bond, angle, and dihedral parameters were set to zero. The configurations from the MD trajectory were saved, and subsequently the forces acting on all particles were recalculated for these configurations when the charge on the virtual particle was set to +1.

The electric field, $\vec{\mathrm{E}}_{\mathrm{VP}}$, at the virtual particle location was calculated as:

$$\vec{\mathrm{E}}_{\mathrm{VP}} = \frac{\vec{\mathrm{F}}_{\mathrm{VP}}}{\mathrm{q}_{\mathrm{VP}}} \qquad \boxed{6.2}$$

where $\vec{\mathrm{F}}_{\mathrm{VP}}$ is the force acting on the virtual particle and q_{VP} is the charge of the virtual particle. The total electric field vector, as well as the component along the CN axis, was calculated for each configuration along the MD trajectory. Calculation of the component of the electric field along the CN axis allows us to calculate the change in the vibrational frequency due to classical electrostatics using equation 6.1. The remaining frequency change can be attributed to the quantum mechanical aspects of specific hydrogen-bonding interactions and polarization effects. These effects can be investigated by using a classical polarizable force field[206, 209-210] or by treating the interacting residues quantum mechanically. We note that the experimentally measured and theoretically calculated frequency shifts can be compared directly, but the breakdown into the classical electrostatics and quantum mechanical aspects is available only from the theoretical calculations.

We also analyzed the contributions of individual residues and ligands to the electric field at the midpoint of the CN bond. Because the classical electric field is the sum of the individual contributions from each atom, the electric field can be decomposed into contributions from each protein residue and ligand. Analysis of the contributions from specific residues provides insight into the impact of conformational changes occurring during the closed to occluded transition associated with hydride transfer.

6.3 Results and Discussion

6.3.1 Thiocyanate Probe Incorporation in Enzyme Active Sites

We generated the T46C-CN and L54C-CN mutants by site-specifically incorporating a thiocyanate probe at each position as shown in Figure 6.5. The T46C-CN probe is situated in close proximity to the junction between the two reacting ligands, DHF and NADPH, allowing us to monitor the microenvironment close to the reaction center.[184] The L54C-CN probe is located ~9 Å from the center of the hydride donor–acceptor (D–A) axis. This probe monitors the folate binding pocket, and its spectral character is expected to respond to the formation of the ternary Michaelis–Menten complex upon folate binding, as well as the release of THF in the enzyme turnover step.

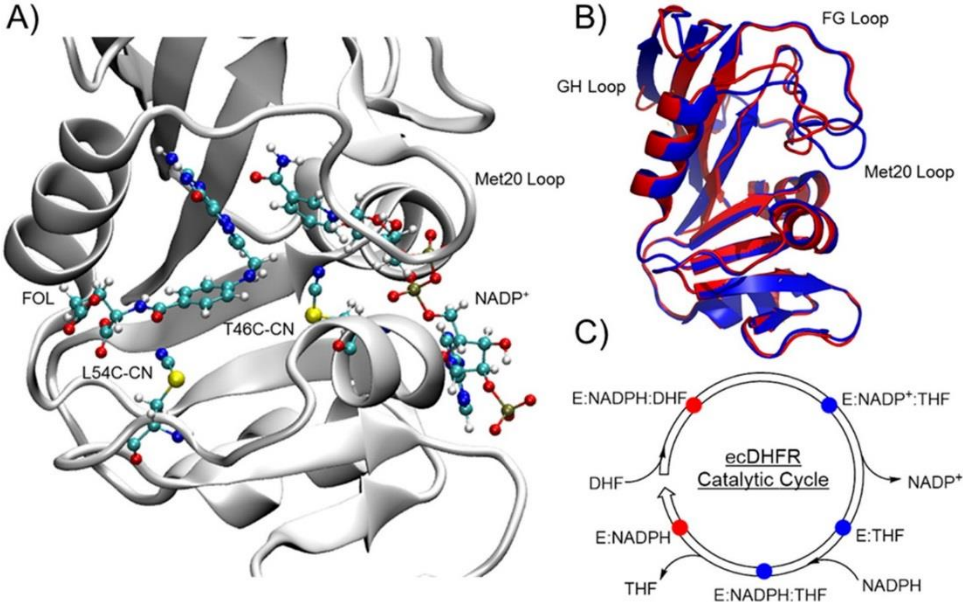

Figure 6.5: (A) Superposition of the T46C-CN and L54C-CN *ec*DHFR mutants in the closed conformation with folate and NADP$^+$ bound, where only the thiocyanate residue is shown for the L54C-CN mutant. (B) *ec*DHFR in the closed (red) and the occluded (blue) conformations exhibited by the (C) five major complexes in its catalytic cycle.

My collaborators in the Benkovic Lab (Pennsylvania State University, Department of Chemistry) evaluated the enzyme activity of the two *ec*DHFR variants to verify their ability to catalyze the NADPH-dependent reduction of DHF and the enzyme turnover rates at pH 7.0 and 25 °C. The catalytic efficiencies of the T46C-CN ($k_{\mathrm{hyd}} = 120 \pm 10\ \mathrm{s}^{-1}$; $k_{\mathrm{cat}} = 6.5 \pm 0.5\ \mathrm{s}^{-1}$) and L54C-CN ($k_{\mathrm{hyd}} = 250 \pm 20\ \mathrm{s}^{-1}$; $k_{\mathrm{cat}} = 28 \pm 3\ \mathrm{s}^{-1}$) variants were comparable to that of WT *ec*DHFR ($k_{\mathrm{hyd}} = 220\ \mathrm{s}^{-1}$; $k_{\mathrm{cat}} = 12\ \mathrm{s}^{-1}$).[169, 211] We also found the ΔCys *ec*DHFR (C85A/C152S; $k_{\mathrm{hyd}} = 215 \pm 8\ \mathrm{s}^{-1}$; $k_{\mathrm{cat}} = 6.3 \pm 0.8\ \mathrm{s}^{-1}$) variant to exhibit activity similar to the WT enzyme. These observations suggest that the incorporation of the SCN probes into the selected locations of the active site does not significantly alter the structure or activity of the enzyme.

It should be noted that we also incorporated the SCN probe at the I50 position (ΔCys-I50C-CN). However, such a modification decreased the hydride transfer rate by ~10 times at pH 7.0 and 25 °C. We felt that the degree of enzyme activity reduction in ΔCys-I50C-CN might result in a less accurate representation of the electrostatic environment in the active site of the WT enzyme. Thus, further investigations were not performed for the ΔCys-I50C-CN construct. It is expected that even small modifications to the crowded active site can have large effects on enzyme activity.

6.3.2 Active Site Microenvironments Along *ec*DHFR Catalytic Cycle

The *ec*DHFR catalytic cycle contains the five major species (Figure 6.5C) that reflect the significant conformational changes in the active site Met20 loop (Figure 6.5B).[179, 184] The Met20 loop moves from a closed conformation in the ternary Michaelis–Menten complex (E:NADPH:DHF) to an occluded conformation in the initial ternary product complex (E:NADP$^+$:THF). The enzyme remains in the occluded conformation in the two subsequent product-containing species (E:THF and E:NADPH:THF), until the Met20 loop reverts back to the closed conformation upon the rate-limiting[211] release of THF to generate E:NADPH (Figure 6.5C). NMR relaxation dispersion experiments have found that the rates of the Met20 loop conformational change are temporally similar to their corresponding enzymatic processes.[179] In other words, the hydride transfer and enzyme turnover rates are similar to the values determined from the NMR experiments for the conformational transitions that connect the relevant enzyme complexes. While the major change in the Met20 loop conformation appears to be induced by the formation of the product THF,[212] other researchers have provided theoretical simulations that show minor structural rearrangements of the ligands and protein, not restricted to the Met20 loop, are necessary to progressively optimize the substrate orientations and the active site environment along the reaction coordinate of the hydride transfer reaction.[163, 183] Herein, we utilized the SCN probe to experimentally monitor the changes in the local microenvironments in two locations in the active site over the five major catalytic species.

The five complexes that constitute the catalytic cycle of *ec*DHFR (Figure 6.6) were generated using 1.5–2.5 mM of the enzyme and at least five times excess of the ligands in pH 7.0 phosphate buffer. These concentrations should be more than sufficient to push the equilibria toward full complexation,[169, 179, 211] thus allowing us to obtain vibrational FTIR spectra of the five major complexes that constitute the *ec*DHFR catalytic cycle, as well as for the apoenzyme (enzyme with ligands or cofactors in active site) and the E:NADPH:FOL complex. Note that the E:NADPH:DHF state is modeled by E:NADP$^+$:FOL, as discussed in the literature.[213] For each enzyme complex, the IR spectrum was obtained in duplicate/triplicate using separately prepared samples, and these spectra were found to be very reproducible (see section 6.2). After correcting the IR data for baseline and subsequently normalizing the amplitude of the peak to 1.0 (Figure 6.2), we determined the maximum frequency ($\tilde{\nu}_{\mathrm{max}}$) from the first derivative of the corrected IR peak (figure 6.2 D). The peak position is a measure of the transition energy between the vibrational ground state and first excited state of the thiocyanate probe. The transition energy is sensitive to the electric field along the CN bond because the vibrational potential energy function is perturbed by the local electrostatic environment (surrounding residues, ligands, and solvent molecules) which modulates the energy difference between the vibrational quantum states. Color coding the frequency of maximum absorption detected in each enzyme complex, illustrates the changes in the local electrostatic interactions experienced by the CN probe over the catalytic cycle for ecDHFR.

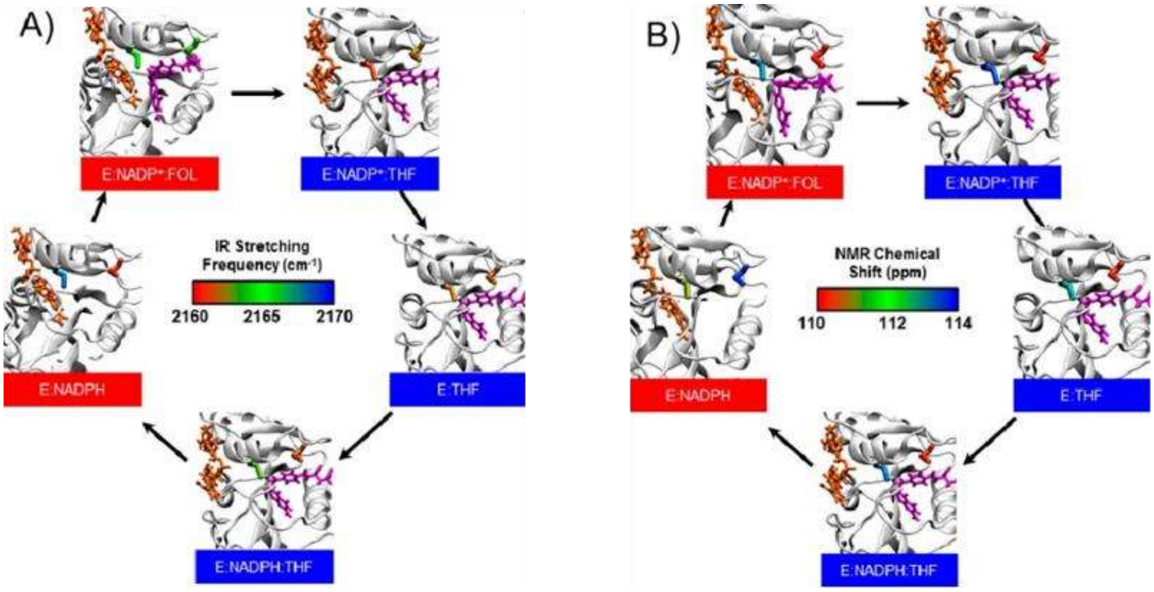

Figure 6.6: (A) FTIR (SCN) and (B) NMR ($S^{13}CN$) measurements along the catalytic cycle of *ec*DHFR. The color scales for the FTIR and NMR data have units of cm^{-1} and ppm, respectively. The cofactor is orange, and the substrate/product is purple in all complexes (the coloring of the cofactor and substrate/product does not correspond to the color scales that represent the NMR shift or IR frequency). Enzyme complex labels in blue are in the occluded conformation, and those in red are in the closed conformation. The measured values for IR frequency and NMR chemical shift are provided in Table 6.1.

Figure 6.6 A indicates that the local environment of each CN probe changes significantly over several key steps in the catalytic cycle: formation of the ternary Michaelis–Menten model ground state complex, the hydride transfer step, and the rate-limiting release of THF. The largest frequency shifts observed for the T46C-CN probe occurred across the two most important steps in the catalytic cycle: (1) upon the conversion between the model Michaelis–Menten E:NADP$^+$:FOL complex and the initial E:NADP$^+$:THF product complex (-4.1 cm^{-1}), which is analogous to the hydride transfer step; (2) across the enzyme turnover step, which is the release of THF (5.5 cm^{-1}). For the L54C-CN probe, the most significant change occurred upon the formation of the ternary E:NADP$^+$:FOL complex (2.4 cm^{-1}). Crystal structures of the WT enzyme have shown that the T46 and L54 residues retain their positions and orientations in the five catalytic complexes, suggesting that the inserted CN probes likely experience limited freedom of movement in the active site.[184] We confirmed with MD simulations that there are no major conformational changes in the probe orientation during 5 ns trajectories. Therefore, the observed changes in the microenvironments as the system moves through the various complexes in the catalytic cycle are likely due to protein conformational rearrangements that induce changes in the electrostatic interactions between the probes and their surroundings. Note also that the redox state of the cofactor (NADPH/NADP$^+$) has very little effect on both the IR and ^{13}C NMR data (Table 6.l).

In many cases, we also observed changes in the peak full-width at half-maximum (FQHM) as shown in Table 6.1. Changes in the peak FWHM usually reflect the variation of chemical environments sampled by the probe as well as the strength of intermolecular interactions such as hydrogen bonding. For example, the L54C-CN probe, which is located in the folate binding site, reported peak widths that are approximately two times smaller in complexes with bound FOL or THF. This observation is consistent with the probe sampling a less fluctuating and more well-defined electrostatic environment resulting from the various interactions that organize the FOL/THF to bind in the active site. There is also some evidence indicating that the E:NADPH complex and the apoenzyme exhibit a greater degree of hydrogen bonding between a solvent water molecule and the L54C-CN probe. One indication of this phenomenon is obtained from inspection of the ^{13}C NMR-IR relationship, which shows that the data for the above two complexes deviate from the rest of the data in a manner that implicates greater specific solvent hydrogen-bonding interactions. MD simulations support the presence of additional solvent hydrogen-bonding interactions in these two complexes for the L54C-CN probe, with a water molecule hydrogen bonded to the nitrile probe in nearly half of the configurations. We also observed a more broad IR peak in the E:NADPH:FOL complex, which can be attributed to the slow reduction of FOL over the course of the IR measurement. This is not unexpected since the L54C-CN probe is located in the folate binding pocket. These trends are less obvious for the T46C-CN probe, which seems to be located in a more fluctuating environment, as indicated by the relative IR peak widths.

We also prepared the isotopically enriched Cys-^{13}CN variants (T46C-^{13}CN and L54C-^{13}CN) to obtain the complementary ^{13}C NMR data for all of the studied complexes. While the magnitude of the observed changes are different because the ^{13}C NMR chemical shift is less sensitive to specific solvent hydrogen-bonding interactions than is the CN vibrational stretching frequency,[2, 194] the ^{13}C NMR data (Figure 6.6 B and Table 6.1) illustrate similar trends to those shown by the corresponding IR data. In particular, we observed a changing microenvironment around the $S^{13}CN$ probes as the enzyme evolves through the catalytic cycle. Similar to the IR data, the microenvironment detected at the T46C-^{13}CN probe exhibits larger changes along the catalytic cycle than that at the L54C-^{13}CN probe. This trend is expected due to the proximity of the T46C-^{13}CN site to the regions of the substrates that undergo the hydride transfer reaction. Overall, the experimental data summarized as Figure 6.6 clearly demonstrate a dynamic electrostatic environment in the active site of *ec*DHFR across its catalytic cycle. The differences in the microenvironments of the two probes and the way they change among the different complexes, especially between the closed and occluded conformations, in the *ec*DHFR catalytic cycle also provide an indication of the highly heterogeneous nature of the enzyme active site.

6.3.3 Computer Simulations

In order to provide further detail of various environmental contributions that give rise to the observed CN stretching vibrational frequency shifts along the catalytic cycle, my collaborators in the Hammes-Schiffer Lab (University of Illinois at Urbana-Champaign, Department of Chemistry) conducted QM/MM simulations to monitor the electrostatic interactions experienced by the probes for the complexes along the catalytic cycle. These data provide information about how the microenvironments of the probes reorganize across individual steps of the catalytic cycle. Experimental IR spectra of the T46C-CN and L54C-CN mutants of *ec*DHFR were simulated for two different complexes along the catalytic cycle: (1) the ternary complex with the reactant analog FOL and $NADP^+$ bound, which mimics the E:NADPH:DHF state prior to hydride transfer; (2) the ternary complex with the product THF and NADP$^+$ bound, which is the E:NADP$^+$:THF state following hydride transfer.

6.3.3.1 Microenvironment Proximal to the Reaction Center

First, the local environment around the T46C-CN probe was examined, which is located near the midpoint between the two bound ligands (Figure 6.5 A). The QM region includes the T46C-CN residue, the substrate (either FOL or THF), and the nearest water molecule to the nitrile nitrogen, as depicted in Figure 6.7 A. The QM region was determined by calculating the CN frequency including the entire probe microenvironment in the QM region for a subset of the configurations sampled and comparing these results to those obtained with smaller QM regions. The details of the procedure used to determine the QM region are beyond this scope of this dissertation, but readers are encouraged to consult the original publication for all computational details.[55]

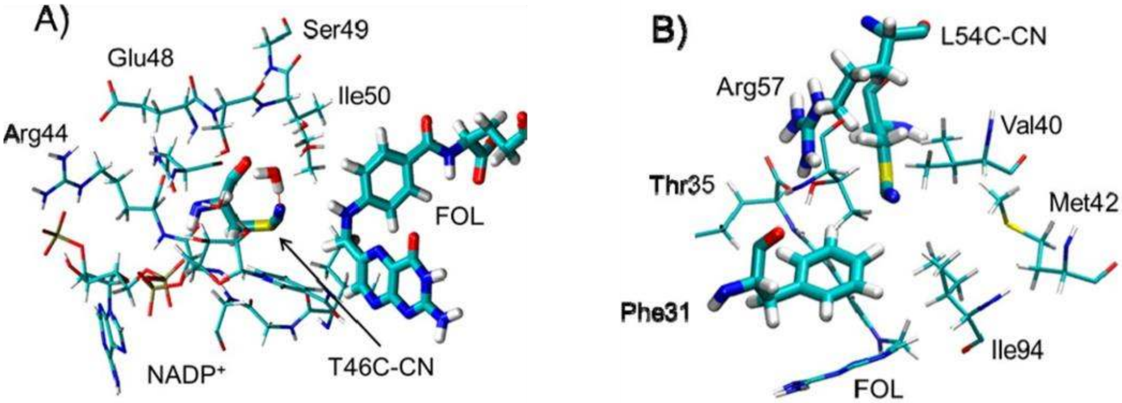

Figure 6.7: Configurations from MD simulations for the (A) T46C-CN and (B) L54C-CN *ec*DHFR mutants. The residues with thicker lines are included in the QM region for the QM/MM calculations of vibrational frequencies.

Figure 6.8 A presents the calculated and experimentally measured IR spectra for the T46C-CN mutant for both the closed (NADP$^+$/FOL) and occluded (NADP$^+$/THF) states. The calculated IR spectrum for the closed conformation (solid black curve) has a maximum at 2165.8 cm^{-1}, which is within 1.8 cm^{-1} of the measured peak in the experiments. The agreement between the calculated and experimental absolute frequencies is potentially fortuitous, but the level of agreement is similar to that calculated in our previous studies of KSI.[214] The FMHM of the calculated IR spectrum for the closed conformation is 11 cm^{-1}, which is in good agreement with the experimentally measured line width of 14 cm^{-1}. The calculated IR spectrum for the occluded product state (solid red curve) has a maximum at 2162.1 cm^{-1}. The calculated shift between these two states is −3.7 cm^{-1}, which is in excellent agreement with the experimentally measured shift of −4.1 cm^{-}

[1]. Note that the MD simulations and CN frequency calculations are performed on the nanosecond time scale. The probe could experience multiple additional conformations on the longer time scale associated with the steady state, equilibrium FTIR measurements. During the MD simulations of 5 ns, no major structural rearrangements of the probe orientation occurred, indicating that we are only sampling a single conformational state. Since the starting configurations for our simulations were based on crystal structures that include the probe, we expect to be sampling the most stable and therefore the dominant configuration of the probe. Moreover, the agreement between the calculated and experimental CN frequency shifts provides further validation of the methodology.

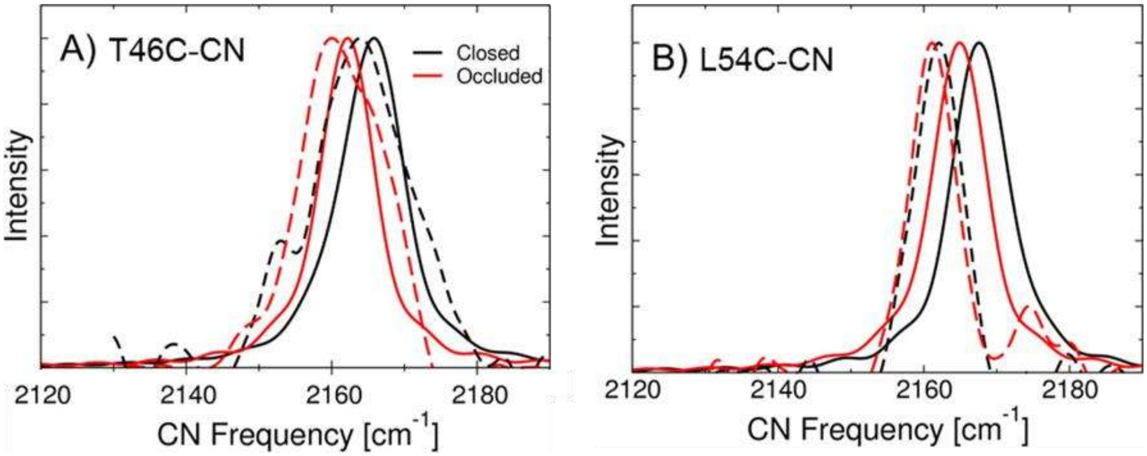

Figure 6.8: Calculated and experimentally measured IR spectra of the CN vibrational stretching frequency for the (A) T46C-CN and (B) L54C-CN *ec*DHFR systems with NADP$^+$/FOL bound (closed conformation; black line) and with NADP$^+$/THF bound (occluded conformation; red line). The solid lines are the simulated spectra from the QM/MM calculations, and the dotted lines are the measured spectra from the FTIR experiments.

In addition to the SCN FTIR spectra, my collaborators calculated the electric field at the midpoint of the CN bond for configurations sampled by the MD trajectory using the methodology described above. From these calculations, we can correlate the measured vibrational frequency shifts to changes in electrostatics from the protein environment. The average projected electric field for the closed ($NADP^+$/FOL) and occluded ($NADP^+$/THF) states are −15.9 and −19.0 MV/cm, respectively. Using the experimental Stark tuning rate of 0.7 cm^{-1}/(MV/cm) in conjunction with equation 6.1, the difference of −3.1 MV/cm corresponds to a shift in the vibrational frequency of −2.2 cm^{-1}. The difference between this frequency shift arising from only classical electrostatics and the actual shift of roughly −4.0 cm^{-1} obtained from both calculations and experiments is attributed to the quantum mechanical aspects of hydrogen-bonding interactions and polarization effects that are not included in the linear relation given by equation 6.1.

Previously, it has been shown both experimentally[2, 193] and computationally[214-215] that significant deviations of ~10 cm^{-1} from the vibrational frequency shifts predicted by equation 6.1 can occur when the nitrile probe participates in specific hydrogen-bonding interactions. According to our MD simulations, the T46C-CN thiocyanate probe is solvent accessible in both the closed and occluded conformations and directly hydrogen bonds to a water molecule, as depicted in Figure 6.7A. In both protein conformations, the nitrile probe is also able to act as a hydrogen-bond acceptor from the amine group in the substrate (FOL/THF) backbone.

Thus, the difference between the frequency shift of −2.2 cm^{-1} predicted from equation 6.1, which includes only classical electrostatic effects, and the shift of −3.7 cm^{-1} obtained from the QM/MM calculations of the full system can be attributed to hydrogen-bonding interactions with the water molecule and polarization effects from the water molecule and the substrate (FOL/THF). To confirm this hypothesis, we performed the QM/MM frequency analysis with only the probe residue (T46C-CN) in the QM region (i.e., switching the water molecule and the substrate from the QM region to the MM region). In this case, the calculated frequency shift between the two states was −2.6 cm^{-1}, which agrees well with the −2.2 cm^{-1} shift obtained from equation 6.1.

Beyond the calculation of the total electric field at the probes, we can decompose the field along the CN axis into contributions from individual residues in the enzymatic complexes. In essence, this methodology allows us to decompose the microenvironment surrounding the CN probe into the constituent parts, which then allows us to identify the major contributing components. For the T46C-CN probe (Figure 6.7 A), the sum of the contributions from the main contributors given in Table 6.2 correspond to a change in electric field along the CN axis of −2.9 MV/cm, which is consistent with the change of −3.1 MV/cm calculated with the entire enzyme. The contributions from the residues in the closed conformation are shown pictorially in Figure 6.9A, where the residues that are colored blue contribute positively and those that are colored red contribute negatively to the total field along the CN bond. For the T46C-CN probe, the NADP$^+$ cofactor and the nearest water molecule are the dominant contributors to the change in the electric field along the CN axis, although Asn18 and Ser49 also make significant contributions (Table 1). The presence of a positive charge on the nicotinamide ring and the short ~4 Å distance between the nitrile nitrogen and the aromatic nitrogen in the nicotinamide ring lead to a strong contribution to the electric field in the closed conformation. After the transition to the occluded conformation, the cofactor is excluded from the active site, and the magnitude of the contribution to the field from the nicotinamide ring is much smaller due to the larger distance of ∼14 Å between the two nitrogen atoms. This effect of the movement of NADP$^+$ on the electric field at the probe demonstrates how atomic motions can significantly alter the local electrostatics in the active site. Moreover, the −3.2 MV/cm change in the electric field contributed by Asn18 and Ser49 is consistent with the structural rearrangement from the closed to the occluded conformation. Specifically, the amide nitrogen of Asn18 is ∼1.5 Å closer to the nitrile probe in the closed conformation than in the occluded conformation, and the hydroxyl group of Ser49 is ∼1.0 Å closer to the nitrile probe in the closed conformation.

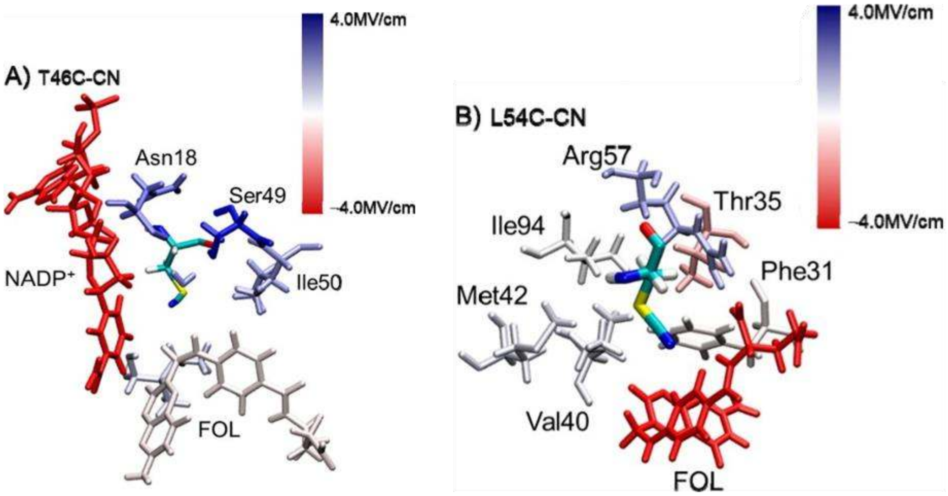

Figure 6.9: Contributions to the calculated electric field along the CN bond at the midpoint of this bond for the (A) T46C-CN and (B) L54C-CN *ec*DHFR systems with NADP$^+$/FOL bound and the Met20 loop in the closed conformation. The color for each residue corresponds to the calculated values in Tables 6.2 and 6.3, respectively, using the color scale provided, although residues contributing a magnitude >4.0 MV/cm are depicted in the darkest color. The residues that contribute negatively to the field are colored red, the residues that contribute positively to the field are colored blue, and the residues that have no net contribution to the field along the CN bond are colored white.

Table 6.2: Calculated Contributions from Specific Residues to the Electric Field along the CN Bond for the T46C-CN ecDHFR Mutant in the Closed and Occluded Conformations

	E_{CN}[a] MV/cm		**ΔE_{CN}[b] ΔMV/cm**
residue	**closed**	**occluded**	**E Field Difference**
	(NADP$^+$/FOL)	**(NADP$^+$/THF)**	
Asn18	2.65	–0.52	−3.17
Ser49	4.23	1.01	−3.22
Ile50	1.79	1.53	−0.26
FOL	–0.66	–3.51	−2.85
NADP$^+$	–19.43	–5.35	14.08
H_2O	2.14	–5.32	−7.46

[a] Component of the electric field along the CN bond

[b] Changes in the electric field along the CN bond in going from the closed conformation (NADP$^+$/FOL) to the occluded conformation (NADP$^+$/THF)

Additionally, following the closed to occluded transition, the CN probe becomes more accessible to the solvent. The contribution to the electric field along the CN axis from the closest water molecule changes by −7.46 MV/cm during this transition. Moreover, the sign of the average electric field along the CN axis due to this water molecule is different for the closed and occluded conformations, with a value of 2.14 MV/cm for the closed conformation and −5.32 MV/cm for the occluded conformation. Analysis of the MD trajectories indicates that a water molecule is hydrogen bonded to the nitrile probe ∼26% of the time in the closed (NADP$^+$/FOL) conformation and ∼52% of the time in the occluded (NADP$^+$/THF) conformation. The positive contribution to the electric field along the CN axis from the nearest water molecule in the closed conformation is due to configurations in which the nearest water molecule has its negatively charged oxygen atom pointing toward the nitrile. These configurations are stabilized by the hydrogen-bonding interaction of the water molecule with the hydroxyl group of Ser49. The negative contribution to the field in the occluded conformation arises from configurations in which a hydrogen atom of the nearest water molecule is oriented toward the probe, forming a hydrogen bond between the water molecule and the CN group. Thus, this computational approach is also able to probe the detailed active site hydration status, which is not easily accessible with experimental means.

6.3.3.2 Microenvironment around Substrate Binding Pocket

We performed the same analysis for the L54C-CN mutant to examine the microenvironment near the folate binding pocket. Figure 6.8 B displays the calculated and experimentally measured vibrational spectra for the L54C-CN mutant in both the closed ($NADP^+$/FOL) and occluded ($NADP^+$/THF) states. The L54C-CN probe is distal from the active site, and it is located in a relatively hydrophobic pocket near the carboxylate tail of the substrate, as shown in Figure 6.5. The QM region used for this mutant includes the L54C-CN residue, Phe31, and Arg57, as depicted in Figure 6.7 B. The QM region was determined by calculating the CN frequency including the entire probe microenvironment in the QM region for a subset of the configurations sampled and comparing these results to those obtained with smaller QM regions. Again, the details of the procedure used to determine the QM region are provided in the original manuscript[55] but are beyond the scope of this dissertation. The calculated frequency shift between the two states for the L54C-CN probe is -2.5 cm^{-1}, which is in reasonable agreement with the shift of -1.0 cm^{-1} measured experimentally.

The calculated average electric fields along the CN probe in the closed and occluded conformations are −8.4 and −13.8 MV/cm, respectively. Using the experimental Stark tuning rate of 0.7 cm^{-1}/(MV/cm) in conjunction with equation 6.1, this shift of −5.4 MV/cm corresponds to a shift in vibrational frequency of −3.8 cm^{-1} due to only classical electrostatic interactions. To model the situation with only classical electrostatic interactions, we calculated the shift in the vibrational frequency when only the residue containing the thiocyanate group (L54C-CN) is treated quantum mechanically and the remainder of the system, including Phe31 and Arg57, is represented as classical point charges. The calculated frequency shift when only the probe residue is treated quantum mechanically is −3.5 cm^{-1}, which is consistent with the value of −3.8 cm^{-1} obtained from equation 1. However, this frequency shift is greater than the shift of −2.5 cm^{-1} calculated with the larger QM region. The greater shift predicted by the purely classical electrostatic model indicates that the polarization effects due to the Phe31 and Arg57 residues decrease the vibrational frequency shift relative to that predicted by classical electrostatics.

Table 6.3 provides the contribution to the electric field along the CN axis for several key residues near the L54C-CN probe. The sum of these contributions is −7.3 MV/cm, which is slightly higher than the change of −5.4 MV/cm calculated with the entire enzyme, indicating that other residues are also contributing to this field. In a similar manner to the analysis for the T46C-CN mutant, the contributions from these residues are illustrated in Figure 6.9 B. The Arg57 residue exhibits the largest change between the two states with a net shift of −6.58 MV/cm. In the closed conformation, the line connecting the midpoint of the CN bond to the protonation site of the positively charged Arg57 is nearly perpendicular to the CN axis, resulting in almost zero contribution to the electric field along the CN axis.

The change in the electric field contribution by Arg57 is likely due to a geometrical shift that moved the positive charge on Arg57 away from this orthogonal orientation with respect to the probe in the occluded conformation. Interestingly, while the substrate exerts a large contribution to the electric field along the CN axis, this contribution remains nearly constant between the two states. The stable orientation of the CN axis relative to the negatively charged carboxylate moiety in the bound substrate results in negligible change in the contribution of the substrate to the electric field at the CN probe.

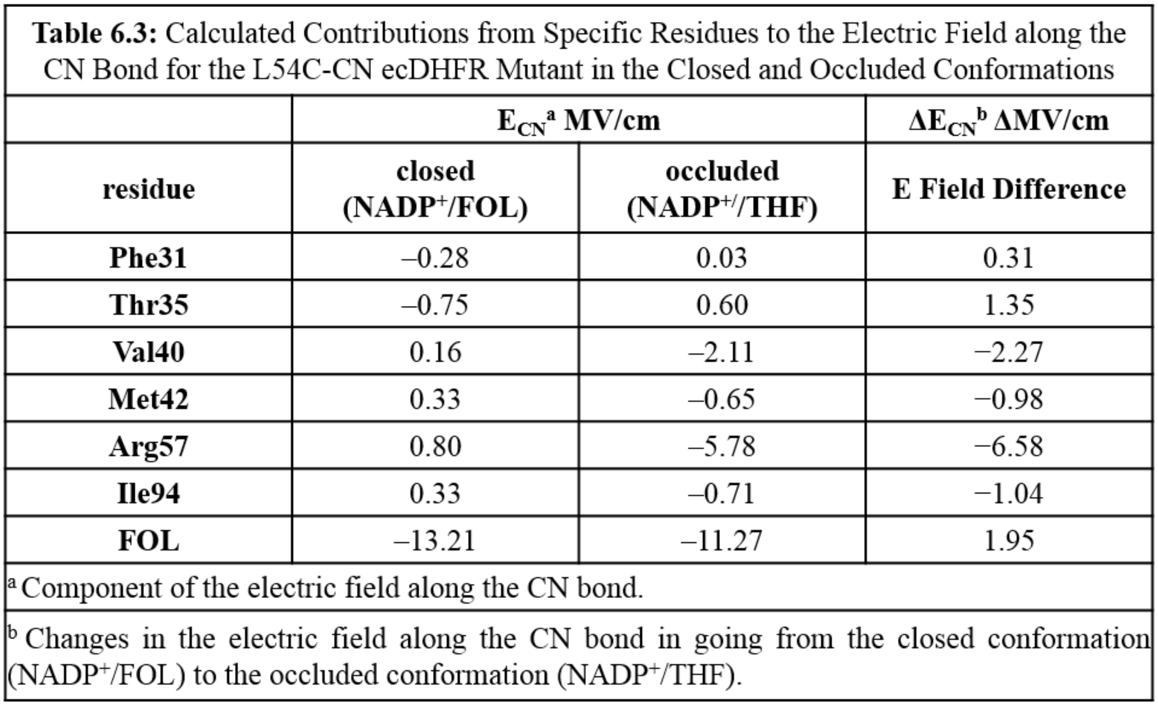

Table 6.3: Calculated Contributions from Specific Residues to the Electric Field along the CN Bond for the L54C-CN ecDHFR Mutant in the Closed and Occluded Conformations

	E_{CN}[a] MV/cm		**ΔE_{CN}[b] ΔMV/cm**
residue	**closed (NADP$^+$/FOL)**	**occluded (NADP$^{+/}$/THF)**	**E Field Difference**
Phe31	–0.28	0.03	0.31
Thr35	–0.75	0.60	1.35
Val40	0.16	–2.11	−2.27
Met42	0.33	–0.65	−0.98
Arg57	0.80	–5.78	−6.58
Ile94	0.33	–0.71	−1.04
FOL	–13.21	–11.27	1.95

[a] Component of the electric field along the CN bond.

[b] Changes in the electric field along the CN bond in going from the closed conformation (NADP$^+$/FOL) to the occluded conformation (NADP$^+$/THF).

6.3.3.3 Electric Field along the Hydride Transfer Donor–Acceptor Axis

While the calculated electric fields along the CN axes of the probes provide a measure of the electrostatic microenvironments within the active site, the electric field along the hydride transfer D–A axis is more directly connected to catalysis. Encouraged by the good agreement between the experimental and the simulated data described above, we applied the same methodology to evaluate the total electric field at the midpoint of the D–A axis and the field projected along the D–A axis in the closed (E:NADP$^+$:FOL) state. The field projected along the D–A axis is −48.9 MV/cm. The negative value of the field indicates that it points from the substrate to the cofactor and that this field will facilitate the transfer of a negatively charged hydride from the cofactor to the substrate. In other words, the projection and the magnitude of the field along the D–A axis in the ternary Michaelis complex is highly favorable for the hydride transfer reaction to occur. The substrate and cofactor contribute a total of −32.4 MV/cm to the field along the D–A axis. The rest of the protein contributes approximately an additional ~31% (−15.4 MV/cm) of the total field. Also, the solvent molecules and ions contribute an additional −1.1 MV/cm to the field along the D–A axis.

This analysis suggests that a major function of the enzyme is to bring the substrate and cofactor into a configuration that realizes the highly favorable field for facilitating the hydride transfer reaction, as shown in Figure 6.6. In the absence of the enzyme, it would be less probable for the reacting species (NADPH and DHF) to achieve the same relative orientation in solution. Moreover, this research provides a new perspective on the role of electrostatic catalytic contributions in DHFR. It is currently impossible to experimentally measure the electric field along the D–A axis, but the calculations provide reasonable estimates. A favorable electric field of −15.4 MV/cm from the protein and −32.4 MV/cm from the ligands along the D–A axis could potentially reduce the free energy barrier by several kcal/mol.[176] While these values suggest a substantial catalytic contribution generated from the active site electrostatic environment, it is important to acknowledge that the full mechanism of catalysis is far more complex than a simplistic evaluation based solely on the electric field along the D–A axis.

We also decomposed this field into the contributions from all of the protein residues, and our analysis identified many residues that contribute to the electric field along the D–A axis. Figure 6.10 depicts the contributions from each of the residues to the field along the D–A axis. The residues that are colored blue contribute positively and those that are colored red contribute negatively to the field pointing from the substrate to the cofactor along the D–A axis. The residues that are shown with side chains contribute to the field with a magnitude >1 MV/cm. The numerical values for the contributions are provided in Table 6.3. Interestingly, there is a strong degree of overlap between the residues that strongly contribute to the field along the D–A axis and the network of coupled motions that has been identified for DHFR catalysis.[216] The residues Ile14, Tyr100, and Asp122 contribute −1.2, −4.2, and −2.4 MV/cm, respectively, and were all implicated in the network of coupled motions. Additional residues that strongly contribute to the electric field along the D–A axis are Lys32 (−3.2 MV/cm), Arg52 (−3.9 MV/cm), and Arg57 (−4.2 MV/cm). The residues that contribute strongly against the field along the D–A axis include Asp27 (5.4 MV/cm), Arg98 (3.4 MV/cm), and His124 (3.0 MV/cm). All of these residues represent potential targets to alter the electrostatic contribution to catalysis.

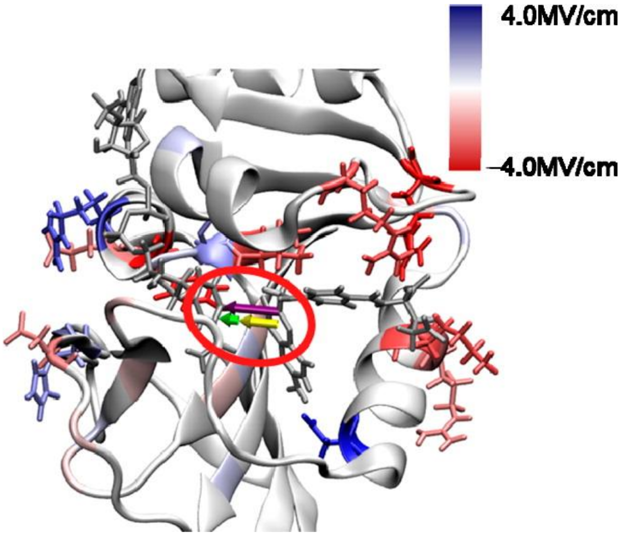

Figure 6.10: Depiction of the component of the electric field along the hydride transfer D–A axis calculated from an MD simulation of WT *ec*DHFR with NADP$^+$/FOL bound and the Met20 loop in the closed conformation. The color for each residue corresponds to the calculated electric field values using the color scale provided, although residues contributing a magnitude >4.0 MV/cm are depicted in the darkest color. The three arrows in the red oval represent the total electric field of −48.9 MV/cm (purple), the field of −32.4 MV/cm resulting from the ligands (yellow), and the field of −16.5 MV/cm resulting from the rest of the system (green) projected along the D–A axis.

6.4 Conclusion

We investigated the changing electrostatic environment at two different thiocyanate probes inserted into the active site of *ec*DHFR for five complexes along the catalytic cycle. Our results illustrate a changing electrostatic environment near the hydride transfer site (T46C-CN) as well as a smaller change in key regions of the folate binding pocket (L54C-CN). The changes in electrostatic environment are associated with conformational changes occurring along the catalytic cycle of *ec*DHFR. Experimental evidence for the changing electrostatic environment includes both IR frequency and ^{13}C NMR measurements, which interrogate the electric field along the CN axis and the total electric field at the probe. These experimental data demonstrate fundamental aspects of the electrostatic landscape for catalysis in *ec*DHFR.

Molecular dynamics simulations provided an atomic-level picture of the local environment experienced by the thiocyanate probes in complexes that model the states prior to and subsequent to the hydride transfer reaction. The QM/MM vibrational frequency calculations reproduced the experimentally measured frequency shifts for these two states, which span the closed to occluded transition associated with hydride transfer. Analysis of the MD trajectories provided insight into the conformational changes occurring between these two states. The factors leading to the vibrational frequency shifts were broken down into classical electrostatic effects, specific hydrogen-bonding interactions, and polarization effects. Thus, the vibrational frequency shifts are not simply a manifestation of the classical electric fields but rather include additional contributions from the environment. Moreover, the electric fields along the CN axis of the probes were decomposed into contributions from specific residues, ligands, and solvent molecules. The electric field along the hydride D–A axis was also calculated with the experimentally validated methodology. The calculations illustrate that the cofactor and substrate, as well as the enzyme, impose a substantial electric field along the D–A axis that facilitates hydride transfer.

Overall, experimental and theoretical data provide evidence for significant electrostatic changes in the microenvironments that constitute the heterogeneous *ec*DHFR active site as the enzyme progresses along the catalytic cycle. The electrostatic interactions between the protein and the ligands assist in orienting the reacting species in a geometry that maintains a large electric field favoring hydride transfer from the cofactor to the substrate. The enzyme active site environment also provides a significant portion (∼1/3) of the total electric field that facilitates the hydride transfer reaction, suggesting the catalytic importance of enzymatic conformational changes that alter the active site electrostatics. Future work will investigate the five trapped states along the catalytic cycle for the two probes studied in this work as well as additional probe sites in the *ec*DHFR system to provide a comprehensive picture of the electrostatic landscape for the entire catalytic cycle.

CHAPTER 7

Prospectus and Conclusion

7.1 Future Direction of Solution-Processed Semiconductors

Utilizing solution-processed semiconductors and other carrier selective transport layers in photovoltaic devices represents one promising route to lowering manufacturing cost of solar cells. However, lowering manufacturing costs only represents half the equation to making solar energy cost competitive with fossil fuel energy on a Levelized Cost of Electricity (LCOE) scale. While driving down manufacturing costs, we must be working simultaneously to increase the power conversion efficiency of these solution-processed, solar energy conversion devices to dramatically increase their LCOE value. Currently, organo-halide perovskites are the most promising technology for generating solar energy at a similar LCOE level as coal and natural gas derived energy. Organo-halide perovskite PV devices have already achieved higher power conversion efficiencies (20% PCE) than any other solution-processed technology to date. Likewise, colloidal quantum dot (CQD) photovoltaics are promising because they offer many tunable parameters that can be controlled to enhance power conversion efficiencies; however, the current state-of-the-art devices can only achieve 11% solar power conversion efficiency.[137] Regardless, both organo-halide perovskite and CQD semiconductors have intrinsic drawbacks requiring significant research and development at the laboratory scale before either of these materials are acceptable for manufacturing at a commercial scale. In this chapter, we will highlight some promising future directions for both materials.

7.1.1 Organo-halide Perovskites

Organo-halide perovskites represent a new class of high-performance, solution-processed, light-harvesting, charge-transport, and highly emissive materials for optoelectronic applications. Organic-inorganic lead halide perovskites, $CH_3NH_3PbI_3$ and $CH_3NH_3PbCl_xI_{3-x}$, were the first materials used to demonstrate respectable photovoltaic energy conversion in 2012.[217] These lead-based semiconductors are still highly researched, and photovoltaics based on these semiconductors are now moving towards commercialization.[218] However, intrinsic drawbacks such as long term stability due to high water solubility and lead toxicity have yet to be resolved for the class of organic-inorganic lead halide perovskites.

Through active research efforts, it is becoming increasing more clear that crystallite surfaces and grain boundaries in organic-inorganic lead halide perovskites strongly influence the photogenerated charge-carrier dynamics as well as the long-term stability of these materials. For instance, deQuilettes et. al. showed that crystallite surfaces and grain boundaries in multicrystalline organo-halide perovskite films showed quenched emission and faster charge-recombination rates that the interior of crystallites.[65] Furthermore, the showed by energy dispersive spectroscopy (EDS) the material existing in the interior of crystallites producing slow charge recombination rates and bring photoluminescence emission is rich in chloride whereas the material at the crystallite surface is rich iodide. Upon treatment with Lewis base compounds such as pyridine, these same authors showed that the PL emission intensity at the iodide-rich surfaces could be brightened – indicating the removal of charge traps and non-radiative recombination pathways. In a separate report, Christians, et. al. showed that systematic exposure of organo-halide perovskite films and

PV devices to humidified air completed degraded the material and the PV power conversion efficiency dropped to 0% within five days. More importantly, alongside the changes in optical absorption properties and device performance, they showed by high resolution electron microscopy that the morphology of the crystallite surfaces were completely reconstructed.[219] These aforementioned findings are just two of several reports that suggest the chemical species at the surface of crystallites play important roles in mediating charge carrier dynamics and are extremely susceptible to reactions with atmospheric chemicals.

The research presented in Chapters 3 and 4 of this dissertation also support the hypothesis that crystallite surfaces mediate charge recombination. We show that the surface area:volume ratio of crystallites in a controlled series of perovskite films is directly correlated with electron-hole recombination rates. Furthermore, we demonstrate that treatment of nanocrystalline organic-inorganic lead halide films with strongly coordinating, Lewis base moieties known to react with lead-containing species at nanocrystalline surfaces can quantitatively recover charge carrier recombination rates. Our research has begun to provide insight into the exact chemical species that exist at the crystallite surface – we find the precursor solution concentration of PbI_4^{2-} is well correlated to the trap density measured from TRPL experiments in a variety of perovskite films cast from different precursor compositions. Through a research initiative that is not presented in this dissertation, we attempted to empirically observe chemical moieties at the surface of nanocrystalline thin-films by surface-specific measurements: x-ray photoelectron spectroscopy (XPS), for example. However, these experiments were unsuccessful in identifying chemical species that are correlated with charge traps – one possible reason for this is because trap densities in organo-halide perovskite films (10^{16} -10^{20} cm^{-3})[38] are approaching the detection limit of modern XPS instruments. Currently, the most sensitive experimental capability we have to track the effect of defects and trap states responsible for charge recombination in organo-halide perovskites is transient optical spectroscopy (Figure 2.8). Future work in discovering the chemical nature of surface defects is expected to take an indirect route and is expected to revolve around systematically tuning the nature of surface ligand and tracking the effect of a series of ligand on the charge recombination rate via transient spectroscopy.

7.1.2 Colloidal Quantum Dots

Colloidal quantum dot (CQD) semiconductors are another class of materials that offer great promise as sensitizers in photovoltaic applications due to their uniquely tunable electronic properties. However, CQD semiconductors have traditionally been plagued by fast charge recombination facilitated by nanocrystal surface defects. The incredibly high surface area in CQDs corresponds to high density of surface defects capable of trapping charge carrier and providing routes to chare recombination. Not only do CQDs provide fast charge carrier recombination, but also cause charge carriers to exhibit low mobilities (μ) in thin-films. This deadly combination of fast charge recombination and low charge mobilities gives rise to short diffusion lengths (equation 1.5) – all of which inhibit charge extraction and lower power conversion efficiencies of CQD PVs. The current state-of-the-art in terms of elongating CQD charge-carrier recombination rates is achieved by a core-shell approach where a thick layer of a wide band-gap semiconductor is overcoated on a narrow band-gap core semiconductor to provide full coordination of surface dangling bonds of the core QD.[220] Although this core-shell technique has been successful in achieving longer excited-state lifetimes, the required thickness of the shell semiconductor prohibits charge carriers from being mobile in solid-state films. Furthermore, the combination of long lifetimes and immobile carriers in core-shell CQDs often leads to nonradiative, Auger-like recombination processes arising from the interaction of free charges with excess excitons generated by continuous photoexcitation – this is the source of excited-state quenching and fluorescence intermittency or "blinking" measured in core-shell CQDs.[221]

One interesting direction to pursue in future research efforts is transition-metal-doped quantum dot (TM-QD) semiconductors. Strategic doping of CQD semiconductors such as CdSe with transition metals such as Mn^{2+} can strategically extend the charge carrier recombination rate by several orders of magnitude while providing unencumbered nanocrystal surfaces capable of allowing efficient charge transfer across interfaces made with adjacent semiconductors or metals. TM-QDs have not been explored for these applications before as the preparation and synthesis of doped QDs with sufficiently high purity and reproducibility for PV and PC applications has only recently been achieved. Additionally, most of the TM-QD applications to date have focused on exploiting the unique magneto-optical properties as diluted magnetic semiconductors rather than electro-optical properties for solar energy conversion.

Perhaps the most important challenges that would need to be overcome before realized TM-QDs as active materials in photovoltaic applications is to provide a methodical investigation of surface passivation strategies to mitigate the effect of nanocrystal surface charge traps that would be counterproductive to charge doping. Beyond complete surface passivation, interesting studies would be to understand the mechanism of change transport through TM-QD solid-state arrays and establish the role of TM^{2+} states in mediating charge transport and recombination within thin-films of TM-QD. Additionally, the unique excited state properties of TM-QDs could yield novel platforms for development of solution-processed, quantum dot lasers and LEDs. Furthermore, investigation of narrow band gap QD semiconductors doped with transition metals expected to have a near-infrared (NIR) ligand-field gap between the ground and excited states (eg: Yb^{3+}/PbS) could provide efficient absorption of all wavelegnts across the solar spectrum while providing unprecedented charge recombination rates. It is acknowledged that PbS QDs can in principle exhibit long excited-state lifetimes and NIR absorption, but utilizing TM-QDs could significantly improve the performance of such NIR QDs for PV applications. Although systems such as Yb^{3+}/PbS are unprecedented and purely hypothetical at this time, it is believed that they could provide the realistic alternative to crystalline silicon solar cells.

7.2 Conclusion

Using principles of physical chemical, optical spectroscopy, materials science, and biophysics, my dissertation research provided fundamental insights into two primary fields: a) charge carrier dynamics in emerging, solution-processed semiconductors for solar energy conversion, and b) the role of protein fluctuations in establishing dynamic electrostatic environments which mediate enzyme catalysis. In summary, research presented in this dissertation demonstrated that recombination centers in organo-halide perovskite semiconductors materials are preferentially located at crystallite surfaces rather than within the bulk of the crystallites. Furthermore, we showed that surface passivation of the perovskite nanocrystals quantitatively removes excess charge recombination centers. This aforementioned work provides a means to create high performance, nanocrystalline perovskite films, which are well suited to form dense networks exhibiting large charge carrier mobilities and recombination lifetimes approaching the bulk crystalline limit. We expect that this powerful combination of highly mobile charges with long lifetimes will enable next-generation materials exhibiting unprecedented charge carrier diffusion lengths.

In order to better understand the molecular or compositional nature of charge recombination centers residing primarily on the surface of perovskite crystallites, we thoroughly characterized the solution-phase chemistry taking place in solutions preceding film deposition. Upon quantitative analysis of these film precursor solutions, we determined the molar absorption coefficients of iodoplumbate coordination complexes and then used the coefficients to determine the concentrations of the complexes in solutions used to cast perovskite films. Our findings reveal that the concentration of tetraiodoplumbate PbI_4^{2-} is uniquely correlated with the density of charge recombination centers in the final perovskite films regardless of the lead precursor used to cast the films. This work suggests that two-step deposition methods where the deposition of the two precursors is temporally separated thus avoiding the need to digest large concentrations of iodoplumbates during film formation. We find films prepared from two-step procedures produces organohalide perovskite films with lower defect densities and longer charge carrier lifetimes than analogous films prepared from one-step deposition routes.

Using similar insights, spectroscopic methods, and materials processing routes, my dissertation research sought to understand and control charge recombination and transport mechanisms in another emerging, solution-processed semiconducting material for photovoltaic applications: colloidal quantum dots. Through collaboration with the Sargent Lab at the University of Toronto, my colleagues and I provided empirical evidence to support the inclusion of a previously unrecognized electronic state in PbS colloidal nanocrystals. Our results suggested an optically-dark, electronic state existed below the conduction band edge in PbS colloidal quantum dot semiconductors, and by controlling the PbS nanocrystal surface chemistry and density of ligand coverage, we could tune the depth of the sub-gap state relative to the conduction band edge. By correlating visible/NIR absorption and emission spectroscopy with transient mid-IR spectroscopy, we made the assignment that this Stokes-shifted, sub-gap states was strongly coupled to the quantum dot surface as well as core excitonic states. Furthermore, quantitative comparison of activation energies extracted form Arrhenius temperature-dependent transient absorption measurements and temperature-dependent transient photoconductivity measurements we show that the sub-gap state is responsible for charge transport in CQD thin-films – avoiding promotion back to excitionic states. We expect that further improvement is CQD surface chemistry and monodispersity are routes to achieving higher photovoltages, photocurrents, and power conversion efficiencies in CQD solar cells.

This dissertation research also presents a tangentially related project in which we used infrared spectroscopy to investigate the electrostatic environment throughout the catalytic cycle for a biologically-active enzyme called DHFR. By selectively incorporating a vibrational probe (thiocyanate) into the amino acid backbone of the protein, we were able to measure variations in the local electrostatic environment (manifest though shifts in SCN vibrational frequency) for five complexes along the catalytic cycle. We found that changes in electrostatic environment are associated with conformational changes of the protein, and electrostatic interactions between the protein and the ligands assist in orienting the reacting species in a geometry that maintains a large electric field favoring hydride transfer direction from the cofactor to the substrate in the catalytic step. Our work provides unprecedented insight that enzyme fluctuations and conformational changes alter the active site electrostatic environment and that it is a result of these these conformational changes and dynamic electrostatic environments that give proteins their catalytic efficacy and prowess.

REFERENCES

1. Pattantyus-Abraham, A. G.; Kramer, I. J.; Barkhouse, A. R.; Wang, X. H.; Konstantatos, G.; Debnath, R.; Levina, L.; Raabe, I.; Nazeeruddin, M. K.; Gratzel, M.; Sargent, E. H., Depleted-Heterojunction Colloidal Quantum Dot Solar Cells. *Acs Nano* **2010,** *4* (6), 3374-3380.
2. Fafarman, A. T.; Sigala, P. A.; Herschlag, D.; Boxer, S. G., Decomposition of Vibrational Shifts of Nitriles into Electrostatic and Hydrogen-Bonding Effects. *J Am Chem Soc* **2010,** *132* (37), 12811-12813.
3. Crabtree, G. W.; Lewis, N. S., Solar Energy Conversion. *Physics of Sustainable Energy* **2008,** *1044*, 309-321.
4. . Energy Information Administration International Energy Outlook 2011 2011.
5. Lewis, N. S., Powering the planet. *Mrs Bull* **2007,** *32* (10), 808-820.
6. Gratzel, M., Photoelectrochemical cells. *Nature* **2001,** *414* (6861), 338-344.
7. Turner, G., Global Renewable Energy Market Outlook 2013. *Bloomberg New Energy Finance* **2013**.
8. Lewis, N. S., Toward cost-effective solar energy use. *Science* **2007,** *315* (5813), 798-801.
9. Agency, I. E., Key World Energy Statistics 2010. 2010.
10. Crabtree, G. W.; Lewis, N. S., Solar energy conversion. *Phys Today* **2007,** *60* (3), 37-42.
11. Lewis, N. S.; Nocera, D. G., Powering the planet: Chemical challenges in solar energy utilization. *P Natl Acad Sci USA* **2006,** *103* (43), 15729-15735.

12. Petit, J. R.; Jouzel, J.; Raynaud, D.; Barkov, N. I.; Barnola, J. M.; Basile, I.; Bender, M.; Chappellaz, J.; Davis, M.; Delaygue, G.; Delmotte, M.; Kotlyakov, V. M.; Legrand, M.; Lipenkov, V. Y.; Lorius, C.; Pepin, L.; Ritz, C.; Saltzman, E.; Stievenard, M., Climate and atmospheric history of the past 420,000 years from the Vostok ice core, Antarctica. *Nature* **1999,** *399* (6735), 429-436.

13. Siegenthaler, U.; Stocker, T. F.; Monnin, E.; Luthi, D.; Schwander, J.; Stauffer, B.; Raynaud, D.; Barnola, J. M.; Fischer, H.; Masson-Delmotte, V.; Jouzel, J., Stable carbon cycle-climate relationship during the late Pleistocene. *Science* **2005,** *310* (5752), 1313-1317.

14. Branker, K.; Pathak, M. J. M.; Pearce, J. M., A review of solar photovoltaic levelized cost of electricity. *Renew Sust Energ Rev* **2011,** *15* (9), 4470-4482.

15. Schmalensee, R.; MIT Energy Initiative, *The future of solar energy : an interdisciplinary MIT study*. p xx, 332 pages.

16. Jean, J.; Brown, P. R.; Jaffe, R. L.; Buonassisi, T.; Bulovic, V., Pathways for solar photovoltaics. *Energ Environ Sci* **2015,** *8* (4), 1200-1219.

17. Green, M. A., Third generation concepts for photovoltaics. *Proceedings of 3rd World Conference on Photovoltaic Energy Conversion, Vols a-C* **2003**, 50-54.

18. International Energy Agency. Renewable Energy Division.; Organisation for Economic Co-operation and Development., Technology roadmap. Solar photovoltaic energy. OECD/IEA,: Paris, 2010; p. 1 online resource (44 p.). http://dx.doi.org/10.1787/9789264088047-en.

19. Grieco, C.; Aplan, M. P.; Rimshaw, A.; Lee, Y.; Le, T. P.; Zhang, W. L.; Wang, Q.; Milner, S. T.; Gomez, E. D.; Asbury, J. B., Molecular Rectification in Conjugated Block Copolymer Photovoltaics. *J Phys Chem C* **2016,** *120* (13), 6978-6988.

20. Pensack, R. D.; Guo, C. H.; Vakhshouri, K.; Gomez, E. D.; Asbury, J. B., Influence of Acceptor Structure on Barriers to Charge Separation in Organic Photovoltaic Materials. *J Phys Chem C* **2012,** *116* (7), 4824-4831.

21. Price, J. S.; Sheng, X.; Meulblok, B. M.; Rogers, J. A.; Giebink, N. C., Wide-angle planar microtracking for quasi-static microcell concentrating photovoltaics. *Nat Commun* **2015,** *6*.

22. Albrecht, S.; Saliba, M.; Baena, J. P. C.; Lang, F.; Kegelmann, L.; Mews, M.; Steier, L.; Abate, A.; Rappich, J.; Korte, L.; Schlatmann, R.; Nazeeruddin, M. K.; Hagfeldt, A.; Gratzel, M.; Rech, B., Monolithic perovskite/silicon-heterojunction tandem solar cells processed at low temperature. *Energ Environ Sci* **2016,** *9* (1), 81-88.

23. Xing, G. C.; Mathews, N.; Lim, S. S.; Yantara, N.; Liu, X. F.; Sabba, D.; Gratzel, M.; Mhaisalkar, S.; Sum, T. C., Low-temperature solution-processed wavelength-tunable perovskites for lasing. *Nat Mater* **2014,** *13* (5), 476-480.

24. Jeong, K. S.; Tang, J.; Liu, H.; Kim, J.; Schaefer, A. W.; Kemp, K.; Levina, L.; Wang, X. H.; Hoogland, S.; Debnath, R.; Brzozowski, L.; Sargent, E. H.; Asbury, J. B., Enhanced Mobility-Lifetime Products in PbS Colloidal Quantum Dot Photovoltaics. *Acs Nano* **2012,** *6* (1), 89-99.

25. Zhao, X. S.; Gorelikov, I.; Musikhin, S.; Cauchi, S.; Sukhovatkin, V.; Sargent, E. H.; Kumacheva, E., Synthesis and optical properties of thiol-stabilized PbS nanocrystals. *Langmuir* **2005,** *21* (3), 1086-1090.

26. Bi, D.; Xu, B.; Gao, P.; Sun, L.; Grätzel, M.; Hagfeldt, A., Facile synthesized organic hole transporting material for perovskite solar cell with efficiency of 19.8%. *Nano Energy* **2016,** *23*, 138-144.

27. Graetzel, M.; Janssen, R. A. J.; Mitzi, D. B.; Sargent, E. H., Materials interface engineering for solution-processed photovoltaics. *Nature* **2012,** *488* (7411), 304-312.

28. Fonash, S. J., Solar Cell Device Physics, 2nd Edition. *Solar Cell Device Physics, 2nd Edition* **2010**, 1-353.

29. Goetzberger, A.; Knobloch, J.; Voss, B., *Crystalline Silicon Solar Cells*. John Wiley & Sons, Inc.: New York, NY, 1998.

30. Bawendi, M. G.; Steigerwald, M. L.; Brus, L. E., The Quantum-Mechanics of Larger Semiconductor Clusters (Quantum Dots). *Annual Review of Physical Chemistry* **1990,** *41*, 477-496.

31. Herz, L. M., Charge-Carrier Dynamics in Organic-Inorganic Metal Halide Perovskites. *Annu. Rev. Phys. Chem.* **2016,** *67*, 65-89.

32. Sze, S. M.; Ng, K. K., *Physics of Semiconductor Devices*. 3rd ed.; John Wiley & Sons, Inc.: 2007.

33. Streetman, B.; Banerjee, S., *Solid State Electronic Devices*. 6th ed.; Prentice Hall: 2005.

34. Herz, L. M., Charge-Carrier Dynamics in Organic-Inorganic Metal Halide Perovskites. *Annual Review of Physical Chemistry* **2016,** *67*, 65-89.

35. Manser, J. S.; Kamat, P. V., Band filling with free charge carriers in organonietal halide perovskites. *Nature Photonics* **2014,** *8* (9), 737-743.

36. Wehrenfennig, C.; Liu, M.; Snaith, H. J.; Johnston, M. B.; Herz, L. M., Charge-Carrier Dynamics in Vapor-Deposited Films of the Organolead Halide Perovskite CH3NH3PbI3-xClx. *Energy Environ. Sci.* **2014,** *7*, 2269-2275.

37. Wehrenfennig, C.; Eperon, G. E.; Johnston, M. B.; Snaith, H. J.; Herz, L. M., High Charge Carrier Mobilities and Lifetimes in Organolead Trihalide Perovskites. *Advanced Materials* **2014,** *26* (10), 1584-1589.

38. Stewart, R. J.; Grieco, C.; Larsen, A. V.; Doucette, G. S.; Asbury, J. B., Molecular Origins of Defects in Organohalide Perovskites and Their Influence on Charge Carrier Dynamics. *J. Phys. Chem. C* **2016**.

39. Stranks, S. D.; Burlakov, V. M.; Leijtens, T.; Ball, J. M.; Goriely, A.; Snaith, H. J., Recombination Kinetics in Organic-Inorganic Perovskites: Excitons, Free Charge, and Subgap States. *Physical Review Applied* **2014,** *2* (3), 034007(8).

40. Nie, W.; Tsai, H.; Asadpour, R.; Blancon, J.-C.; Neukirch, A. J.; Gupta, G.; Crochet, J. J.; Chhowalla, M.; Tretiak, S.; Alam, M. A.; Wang, H.-L.; Mohite, A. D., High-efficiency solution-processed perovskite solar cells with millimeter-scale grains. *Science* **2015,** *347*, 522-525.

41. Shi, D.; Adinolfi, V.; Comin, R.; Yuan, M. J.; Alarousu, E.; Buin, A.; Chen, Y.; Hoogland, S.; Rothenberger, A.; Katsiev, K.; Losovyj, Y.; Zhang, X.; Dowben, P. A.; Mohammed, O. F.; Sargent, E. H.; Bakr, O. M., Low trap-state density and long

carrier diffusion in organolead trihalide perovskite single crystals. *Science* **2015,** *347* (6221), 519-522.

42. Stranks, S. D.; Wood, S. M.; Wojciechowski, K.; Deschler, F.; Saliba, M.; Khandelwal, H.; Patel, J. B.; Elston, S. J.; Herz, L. M.; Johnston, M. B.; Schenning, A. P. H. J.; Debije, M. G.; Riede, M. K.; Morris, S. M.; Snaith, H. J., Enhanced Amplified Spontaneous Emission in Perovskites Using a Flexible Cholesteric Liquid Crystal Reflector. *Nano Letters* **2015,** *15* (8), 4935-4941.

43. Stewart, R. J.; Grieco, C.; Larsen, A. V.; Maier, J. J.; Asbury, J. B., Approaching Bulk Carrier Dynamics in Organo-Halide Perovskite Nanocrystalline Films by Surface Passivation. *J Phys Chem Lett* **2016,** *7* (7), 1148-1153.

44. Pavia, D. L.; Lampman, G. M.; Kriz, G. S.; Vyvyan, J. R., *Introduction to Spectroscopy*. 4 ed.; Brooks/Cole: 2009.

45. Skoog, D. A.; Holler, F. J.; Crouch, S. R., *Principles of Instrumental Analysis*. 6 ed.; Thomson Higher Education: Belmont, CA, 2007.

46. Strong, F. C., Theoretical Basis of the Bouguer-Beer Law of Radiation Absorption. *Anal Chem* **1952,** *24* (2), 338-342.

47. Tkachenko, N. V., *Optical Spectroscopy: Methods and Instrumentation*. Elsevier: Oxford, UK, 2006.

48. Stewart, R. J.; Grieco, C.; Larsen, A. V.; Maier, J. J.; Asbury, J. B., Approaching Bulk Carrier Dynamics in Organo-Halide Perovskite Nanocrystalline Films by Surface Passivation. *J. Phys. Phys. Lett.* **2016,** *7*, 1148-1153.

49. Xing, G. C.; Mathews, N.; Sun, S. Y.; Lim, S. S.; Lam, Y. M.; Gratzel, M.; Mhaisalkar, S.; Sum, T. C., Long-Range Balanced Electron- and Hole-Transport Lengths in Organic-Inorganic CH3NH3PbI3. *Science* **2013,** *342* (6156), 344-347.

50. Diroll, B. T.; Gaulding, E. A.; Kagan, C. R.; Murray, C. B., Spectrally-Resolved Dielectric Functions of Solution-Cast Quantum Dot Thin Films. *Chemistry of Materials* **2015,** *27* (18), 6463-6469.

51. Yu, W. W.; Qu, L. H.; Guo, W. Z.; Peng, X. G., Experimental determination of the extinction coefficient of CdTe, CdSe, and CdS nanocrystals. *Chemistry of Materials* **2003,** *15* (14), 2854-2860.

52. Kortum, G.; Seiler, M., The critical process of choosing colorimetric, spectralphotometric and spectrographic methods for absorption measurements. *Angew Chem-Ger Edit* **1939,** *52*, 687-689.

53. Gratzel, M., Solar energy conversion by dye-sensitized photovoltaic cells. *Inorg Chem* **2005,** *44* (20), 6841-6851.

54. Klein, C.; Nazeeruddin, M. K.; Liska, P.; Di Censo, D.; Hirata, N.; Palomares, E.; Durrant, J. R.; Gratzel, M., Engineering of a novel ruthenium sensitizer and its application in dye-sensitized solar cells for conversion of sunlight into electricity. *Inorg Chem* **2005,** *44* (2), 178-180.

55. Liu, C. T.; Layfield, J. P.; Stewart, R. J.; French, J. B.; Hanoian, P.; Asbury, J. B.; Hammes-Schiffer, S.; Benkovic, S. J., Probing the Electrostatics of Active Site Microenvironments along the Catalytic Cycle for Escherichia coli Dihydrofolate Reductase. *J Am Chem Soc* **2014,** *136* (29), 10349-10360.

56. Noble, D., Ft-Ir Spectroscopy - Its All Done with Mirrors. *Anal Chem* **1995,** *67* (11), A381-A385.

57. Smith, J. P.; Hinson-Smith, V., The endearing FTIR spectrophotometer. *Anal Chem* **2003,** *75* (1), 37a-39a.

58. Stranks, S. D.; Burlakov, V. M.; Leijtens, T.; Ball, J. M.; Goriely, A.; Snaith, H. J., Recombination Kinetics in Organic-Inorganic Perovskites: Excitons, Free Charge, and Subgap States. *Physical Review Applied* **2014,** *2* (3).

59. Rimshaw, A.; Grieco, C.; Asbury, J. B., High Sensitivity Nanosecond Mid-Infrared Transient Absorption Spectrometer Enabling Low Excitation Density Measurements of Electronic Materials. *Applied Spectoscopy* **2016**, Accepted.

60. Rimshaw, A.; Grieco, C.; Asbury, J. B., Note: Using fast digitizer acquisition and flexible resolution to enhance noise cancellation for high performance nanosecond transient absorbance spectroscopy. *Rev Sci Instrum* **2015,** *86* (6).

61. Lakowicz, J. R., *Principles of Fluorescence Spectroscopy*. 2nd ed.; Kluwer Academic Press: New York, NY, 1999.

62. Vardeny, Z.; Tauc, J., Hot-Carrier Thermalization in Amorphous-Silicon. *Phys Rev Lett* **1981,** *46* (18), 1223-1226.

63. Yamada, Y.; Nakamura, T.; Endo, M.; Wakamiya, A.; Kanemitsu, Y., Photocarrier Recombination Dynamics in Perovskite CH3NH3PbI3 for Solar Cell Applications. *J Am Chem Soc* **2014,** *136* (33), 11610-11613.

64. Lawrence, C. J., The Mechanics of Spin Coating of Polymer-Films. *Phys Fluids* **1988,** *31* (10), 2786-2795.

65. deQuilettes, D. W.; Vorpahl, S. M.; Stranks, S. D.; Nagaoka, H.; Eperon, G. E.; Ziffer, M. E.; Snaith, H. J.; Ginger, D. S., Impact of Microstructure on Local Carrier Lifetime in Perovskite Solar Cells. *Science* **2015,** *348*, 683-686.

66. Docampo, P.; Hanusch, F. C.; Stranks, S. D.; Doblinger, M.; Feckl, J. M.; Ehrensperger, M.; Minar, N. K.; Johnston, M. B.; Snaith, H. J.; Bein, T., Solution Deposition-Conversion for Planar Heterojunction Mixed Halide Perovskite Solar Cells. *Adv. Energy Mater.* **2014,** *4*, 1400355(6).

67. Eperon, G. E.; Burlakov, V. M.; Docampo, P.; Goriely, A.; Snaith, H. J., Morphological Control for High Performance, Solution Processed Planar Heterojunction Perovskite Solar Cells. *Advanced Functional Materials* **2014,** *24*, 151-157.

68. Liu, M.; Johnston, M. B.; Snaith, H. J., Efficient planar heterojunction perovskite solar cells by vapour deposition. *Nature* **2013,** *501*, 395-398.

69. Im, J.-H.; Jang, I.-H.; Pellet, N.; Gratzel, M.; Park, N.-G., Growth of CH3NH3PbI3 Cuboids with Controlled Size for High-Efficiency Perovskite Solar Cells. *Nature Nanotech* **2014,** *9*, 927-932.

70. Moore, D. T.; Sai, H.; Tan, K. W.; Smilgies, D.-M.; Zhang, W.; Snaith, H. J.; Wiesner, U.; Estroff, L. A., Crystallization Kinetics of Organic-Inorganic Trihalide Perovskites and the Role of the Lead Anion in Crystal Growth. *Journal of the American Chemical Society* **2015,** *137*, 2350-2358.

71. Dualeh, A.; Tétreault, N.; Moehl, T.; Gao, P.; Nazeeruddin, M. K.; Grätzel, M., Effect of Annealing Temperature on Film Morphology of Organic-Inorganic Hybrid

Pervoskite Solid-State Solar Cells. *Advanced Functional Materials* **2014,** *24* (21), 3250-3258.

72. Grancini, G.; Marras, S.; Prato, M.; Giannini, C.; Quarti, C.; De Angelis, F.; De Bastiani, M.; Eperon, G. E.; Snaith, H. J.; Manna, L.; Petrozza, A., The Impact of the Crystallization Processes on the Structural and Optical Properties of Hybrid Perovskite Films for Photovoltaics. *J. Phys. Chem. Lett.* **2014,** *5*, 3836-3841.

73. Tidhar, Y.; Edri, E.; Weissman, H.; Zohar, D.; Hodes, G.; Cahen, D.; Rybtchinski, B.; Kirmayer, S., Crystallization of Methyl Ammonium Lead Halide Perovskites: Implications for Photovoltaic Applications. *Journal of the American Chemical Society* **2014,** *136*, 13249-13256.

74. Williams, S. T.; Zuo, F.; Chueh, C.-C.; Liao, C.-Y.; Liang, P.-W.; Jen, A. K.-Y., Role of Chloride in the Morphological Evolution of Organo-Lead Halide Perovskite Thin Films. *ACS Nano* **2014,** *8*, 10640-10654.

75. Manser, J. S.; Kamat, P. V., Band Filling with Free Charge Carriers in Organometal Halide Perovskites. *Nature Photonics* **2014,** *8*, 737-743.

76. Buin, A.; Pietsch, P.; Xu, J.; Voznyy, O.; Ip, A. H.; Comin, R.; Sargent, E. H., Materials processing routes to trap-free halide perovskites. *Nano Lett* **2014,** *14* (11), 6281-6.

77. Duan, H. S.; Zhou, H.; Chen, Q.; Sun, P.; Luo, S.; Song, T. B.; Bob, B.; Yang, Y., The identification and characterization of defect states in hybrid organic-inorganic perovskite photovoltaics. *Physical chemistry chemical physics : PCCP* **2015,** *17* (1), 112-6.

78. Yin, W.-J.; Shi, T.; Yan, Y., Unusual Defect Physics in CH3NH3PbI3 Perovskite Solar Cell Absorber. *Appl. Phys. Lett.* **2014,** *104*, 063903(4).

79. Abate, A.; Saliba, M.; Hollman, D. J.; Stranks, S. D.; Wojciechowski, K.; Avolio, R.; Grancini, G.; Petrozza, A.; Snaith, H. J., Supramolecular Halogen Bond Passivation of Organic-Inorganic Halide Perovskite Solar Cells. *Nano Lett* **2014,** *14*, 3247-3254.

80. Li, X.; Dar, I.; Yi, C.; Luo, J.; Tschumi, M.; Zakeeruddin, S. M.; Nazeeruddin, M. K.; Han, H.; Gratzel, M., Improved Performance and Stability of Perovskite Solar Cells by Crystal Crosslinking with Alkylphosphonic Acid w-Ammonium Chlorides. *Nature Chem.* **2015,** *7*, 703-711.

81. Noel, N.; Abate, A.; Stranks, S. D.; Parrott, E. S.; Burlakov, V. M.; Goriely, A.; Snaith, H. J., Enhanced Photoluminescence and Solar Cell Performance via Lewis Base Passivation of Organic-Inorganic Lead Halide Perovskites. *ACS Nano* **2014,** *8*, 9815-9821.

82. Christians, J. A.; Herrera, P. A. M.; Kamat, P. V., Transformation of the Excited State and Photovoltaic Efficiency of CH3NH3PbI3 Perovskite Upon Controlled Exposure to Humidified Air. *Journal of the American Chemical Society* **2015,** *137*, 1530-1538.

83. Burschka, J.; Pellet, N.; Moon, S. J.; Humphry-Baker, R.; Gao, P.; Nazeeruddin, M. K.; Gratzel, M., Sequential deposition as a route to high-performance perovskite-sensitized solar cells. *Nature* **2013,** *499* (7458), 316-9.

84. Liang, K.; Mitzi, D. B.; Prikas, M. T., Synthesis and Characterization of Organic-Inorganic Perovskite Thin Films Prepared Using a Versatile Two-Step Dipping Technique. *Chemistry of Materials* **1998,** *10*, 403-411.

85. Chen, Q.; Zhou, H.; Hong, Z.; Luo, S.; Duan, H. S.; Wang, H.-H.; Liu, Y.; Li, G.; Yang, Y., Planar Heterojunction Perovskite Solar Cells via Vapor-Assisted Solution Process. *J Am Chem Soc* **2014,** *136*, 622-625.

86. Christians, J. A.; Fung, R. C.; Kamat, P. V., An inorganic hole conductor for organo-lead halide perovskite solar cells. Improved hole conductivity with copper iodide. *J Am Chem Soc* **2014,** *136* (2), 758-64.

87. Im, J.-H.; Kim, H.-S.; Park, N.-G., Morphology-photovoltaic property correlation in perovskite solar cells: One-step versus two-step deposition of CH3NH3PbI3. *APL Materials* **2014,** *2*.

88. Burschka, J.; Pellet, N.; Moon, S.-J.; Humphry-Baker, R.; Gao, P.; Nazeeruddin, M. K.; Gratzel, M., Sequential deposition as a route to high-performance perovskite-sensitized solar cells. *Nature* **2013,** *499*, 316-319.

89. Im, J. H.; Jang, I. H.; Pellet, N.; Gratzel, M.; Park, N. G., Growth of CH3NH3PbI3 cuboids with controlled size for high-efficiency perovskite solar cells. *Nature nanotechnology* **2014,** *9* (11), 927-32.

90. Stranks, S. D.; Eperon, G. E.; Grancini, G.; Menelaou, C.; Alcocer, M. J.; Leijtens, T.; Herz, L. M.; Petrozza, A.; Snaith, H. J., Electron-hole diffusion lengths exceeding 1 micrometer in an organometal trihalide perovskite absorber. *Science* **2013,** *342* (6156), 341-4.

91. Hutter, E. M.; Eperon, G. E.; Stranks, S. D.; Savenije, T. J., Charge Carriers in Planar and Meso-Structured Organic-Inorganic Perovskites: Mobilities, Lifetimes, and Concentrations of Trap States. *J. Phys. Chem. Lett.* **2015,** *6*, 3082-3090.

92. Liu, J.; Prezhdo, O. V., Chlorine Doping Reduces Electron-Hole Recombination in Lead Iodide Perovskites: Time-Domain Ab Initio Analysis. *J. Phys. Chem. Lett.* **2015,** *6*, 4463-4469.

93. Shi, D.; Adinolf, V.; Comin, R.; Yuan, M.; Alarousu, E.; Buin, A.; Chen, Y.; Hoogland, S.; Rothenberger, A.; Katsiev, K.; Losovyj, Y.; Zhang, X.; Dowben, P. A.; Mohammed, O. F.; Sargent, E. H.; Bakr, O. M., Low Trap-State Density and Long Carrier Diffusion in Organolead Trihadline Perovskite Single Crystals. *Science* **2015,** *347*, 519-522.

94. Li, Y.; Yan, W.; Li, Y.; Wang, S.; Wang, W.; Bian, Z.; Xiao, L.; Gong, Q., Direct Observation of Long Electron-Hole Diffusion Distance in CH3NH3PbI3 Perovskite Thin Film. *Scientific Reports* **2015,** *5*, 14485(7).

95. D'Innocenzo, V.; Kandada, A. R. S.; De Bastiani, M.; Gandini, M.; Petrozza, A., Tuning the Light Emission Properties by Band Gap Engineering in Hybrid Lead Halide Perovskite. *Journal of the American Chemical Society* **2014,** *136*, 17730-17733.

96. Luther, J. M.; Law, M.; Song, Q.; Perkins, C. L.; Beard, M. C.; Nozik, A. J., Structural, Optical, and Electrical Properties of Self-Assembled Films of PbSe Nanocrystals Treated with 1,2-Ethanedithiol. *ACS Nano* **2008,** *2*, 271-280.

97. Choi, J. J.; Lim, Y.-F.; Santiago-Berrios, M. B.; Oh, M.; Hyun, B.-R.; Sun, L.; Bartnik, A. C.; Goedhard, A.; Malliaras, G. G.; Abruna, H. D.; Wise, F. W.; Hanrath, T., PbSe Nanocrystal Excitonic Solar Cells. *Nano Lett.* **2009,** *9*, 3749-3755.

98. Nagpal, P.; Klimov, V. I., Role of Mid-gap States in Charge Transport and Photoconductivity in Semiconductor Nanocrystal Films. *Nature Comm.* **2011,** *2*, 1492(7).

99. Luther, J. M.; Gao, J.; Lloyd, M. T.; Semonin, O. E.; Beard, M. C.; Nozik, A. J., Stability Assessment on a 3% Bilayer PbS/ZnO Quantum Dot Heterojunction Solar Cell. *Adv. Mater.* **2010,** *22*, 3704-3707.

100. Jeong, K. S.; Tang, J.; Liu, H.; Kim, J.; Schaefer, A. W.; Kemp, K.; Levina, L.; Wang, X.; Hoogland, S.; Debnath, R.; Brzozowski, L.; Sargent, E. H.; Asbury, J. B., Enhanced Mobility-Lifetime Products in Colloidal Quantum Dot Photovoltaics. *ACS Nano* **2012,** *6*, 89-99.

101. Choi, J. J.; Luria, J.; Hyun, B.-R.; Barnik, A. C.; Sun, L.; Lim, Y.-F.; Marohn, J. A.; Wise, F. W.; Hanrath, T., Photogenerated Exciton Dissociation in Highly Coupled Lead Salt Nanocrystal Assemblies. *Nano Lett* **2010,** *10*, 1805-1811.

102. Pattantyus-Abraham, A. G.; Kramer, I. J.; Barkhouse, D. A. R.; Wang, X.; Konstantatos, G.; Debnath, R.; Levina, L.; Raabe, I.; Nazeeruddin, M. K.; Gratzel, M.; Sargent, E. H., Depleted-Heterojunction Colloidal Quantum Dot Solar Cells. *ACS Nano* **2010,** *4*, 3374-3380.

103. Semonin, O. E.; Luther, J. M.; Choi, S.; Chen, H.-Y.; Gao, J.; Nozik, A. J.; Beard, M. C., Peak External Photocurrent Quantum Efficiency Exceeding 100% via MEG in a Quantum Dot Solar Cell. *Science* **2011,** *334*, 1530-1533.

104. Yamada, Y.; Nakamura, T.; Endo, M.; Wakamiya, A.; Kanemitsu, Y., Photocarrier Recombination Dynamics in Perovskite CH3NH3PbI3 for Solar Cell Applications. *Journal of the American Chemical Society* **2014,** *136*, 11610-11613.

105. Johnston, M. B.; Herz, L. M., Hybrid Perovskites for Photovoltaics: Charge-Carrier Recombination, Diffusion, and Radiative Efficiencies. *Acc. Chem. Res.* **2016,** *49*, 146-154.

106. Wu, X.; Trinh, M. T.; Niesner, D.; Zhu, H.; Norman, Z.; Owen, J. S.; Yaffe, O.; Kudisch, B. J.; Zhu, X.-Y., Trap States in Lead Iodide Perovskites. *J Am Chem Soc* **2014,** *136*, 2089-2096.

107. Kojima, A.; Teshima, K.; Shirai, Y.; Miyasaka, T., Organometal Halide Perovskites as Visible-Light Sensitizers for Photovoltaic Cells. *J. AM. CHEM. SOC.* **2009,** *131*, 6050–6051.

108. Park, N.-G., Organometal Perovskite Light Absorbers Toward a 20% Efficiency Low-Cost Solid-State Mesoscopic Solar Cell. *The Journal of Physical Chemistry Letters* **2013,** *4*, 2423−2429.

109. Green, M. A.; Ho-Baillie, A.; Snaith, H. J., The emergence of perovskite solar cells. *Nature Photonics* **2014,** *8*, 506-514.

110. Green, M. A.; Emery, K.; Hishikawa, Y.; Warta, W.; Dunlop, E. D., Solar cell efficiency tables (version 46). *Prog. Photovolt: Res. Appl.* **2015,** *23*, 805-812.

111. Hao, F.; Stoumpos, C. C.; Liu, Z.; Chang, R. P. H.; Kanatzidis, M. G., Controllable Perovskite Crystallization at a Gas-Solid Interface for Hole Conductor-Free Solar Cells with Steady Power Conversion Efficiency. *J. AM. CHEM. SOC.* **2014,** *136*, 16411-16419.

112. Im, J.-H.; Kim, H.-S.; Park, N.-G., Morphology-Photovoltaic Property Correlation in Perovskite Solar Cells: One-Step Versus Two-Steo Deposition of CH3NH3PbI3. *APL Mater.* **2014,** *2*, 081510(8).

113. Ip, A. H.; Quan, L. N.; Adachi, M. M.; McDowell, J. J.; Xu, J.; Kim, D. H.; Sargent, E. H., A Two-Step Route to Planar Perovskite Cells Exhibiting Reduced Hysteresis. *Appl. Phys. Lett.* **2015,** *106*, 143902(5).

114. Lee, M. M.; Teuscher, J.; Miyasaka, T.; Murakami, T. N.; Snaith, H. J., Efficient hybrid solar cells based on meso-superstructured organometal halide perovskites. *Science* **2012,** *338* (6107), 643-7.

115. Etgar, L.; Gao, P.; Xue, Z.; Peng, Q.; Chandiran, A. K.; Liu, B.; Nazeeruddin, M. K.; Gratzel, M., Mesoscopic CH3NH3PbI3/TiO2 heterojunction solar cells. *J Am Chem Soc* **2012,** *134* (42), 17396-9.

116. Ball, J. M.; Lee, M. M.; Hey, A.; Snaith, H. J., Low-temperature processed meso-superstructured to thin-film perovskite solar cells. *Energy Environ. Sci.* **2013,** *6*, 1739-1743.

117. You, J.; Yang, Y. M.; Hong, Z.; Song, T. B.; Meng, L.; Liu, Y.; Jiang, C.; Zhuo, H.; Chang, W.-H.; Li, G.; Yang, Y., Moisture Assisted Perovskite Film Growth for High Performance Solar Cells. *Appl. Phys. Lett.* **2014,** *105*, 183902(5).

118. Yella, A.; Heiniger, L.-P.; Gao, P.; Nazeeruddin, M. K.; Gratzel, M., Nanocrystalline Rutile Electron Extraction Layer Enables Low-Temperature Solution Processed Perovskite Photovoltaics with 13.7% Efficiency. *Nano letters* **2014,** *14*, 2591-2596.

119. Liang, P.-W.; Liao, C.-Y.; Chueh, C.-C.; Zuo, F.; Williams, S. T.; Xin, X.-K.; Lin, J.; Jen, A. K.-Y., Additive Enhanced Crystallization of Solution-Processed Perovskite for Highly Efficient Planar-Heterojunction Solar Cells. *Adv. Mater.* **2014,** *26*, 3748-3754.

120. Piatkowski, P.; Cohen, B.; Ponseca, C. S.; Salado, M.; Kazim, S.; Ahmad, S.; Sundstrom, V.; Douhal, A., Unraveling Charge Carriers Generation, Diffusion, and Recombination in Formadinium Lead Halide Perovskite Polycrystalline Thin Film. *J. Phys. Chem. Lett.* **2016,** *7*, 204-210.

121. Zhumekenov, A. A.; Saidaminov, M. I.; Haque, M. A.; Alarousu, E.; Sarmah, S. P.; Murali, B.; Durson, I.; Miao, X.-H.; Abdelhady, A. L.; We, T.; Mohammed, O. F.; Bakr, O. M., Formadinium Lead Halide Perovskite Crystals with Unprecedented Long Carrier Dynamics and Diffusion Length. *ACS Energy Lett.* **2016,** *1*, 32-37.

122. Pathak, S.; Sepe, A.; Sadhanala, A.; Deschler, F.; Haghighirad, A.; Sakai, N.; Goedel, K. C.; Stranks, S. D.; Noel, N.; Price, M.; Huttner, S.; Hawkins, N. A.; Friend, R. H.; Steiner, U.; Snaith, H. J., Atmospheric Influence upon Crystallization and Electronic Disorder and Its Impact on the Photophysical Properties of Organin-Inorganic Perovskite Solar Cells. *ACS Nano* **2015,** *9*, 2311–2320.

123. Zhang, J.; Pauporte, T., Effects of Oxide Contact Layer on the Preparation and Properties of CH3NH3PbI3 for Perovskite Solar Cell Application. *J. Phys. Chem. C* **2015,** *119*, 14919−14928.

124. Horvath, O.; Miko, I., Spectra, equilibrium and photoredox chemistry of tri- and tetraiodoplumbate(II) complexes in acetonitrile. *J Photoch Photobio A* **1998,** *114* (2), 95-101.

125. Oldenburg, K.; Vogler, A.; Miko, I.; Horvath, O., Photoredox decomposition of tin(II), lead(II), antimony(III) and bismuth(III) iodide complexes in solution. *Inorg Chim Acta* **1996,** *248* (1), 107-110.

126. Stamplecoskie, K. G.; Manser, J. S.; Kamat, P. V., Dual nature of the excited state in organic–inorganic lead halide perovskites. *Energy Environ. Sci.* **2015,** *8* (1), 208-215.

127. Plowas, I.; Swiergiel, J.; Jadzyn, J., Electrical Conductivity in Dimethyl Sulfoxide plus Potassium Iodide Solutions at Different Concentrations and Temperatures. *J Chem Eng Data* **2014,** *59* (8), 2360-2366.

128. Yan, K.; Long, M.; Zhang, T.; Wei, Z.; Chen, H.; Yang, S.; Xu, J., Hybrid Halide Perovskite Solar Cell Precursors: Colloidal Chemistry and Coordination Engineering behind Device Processing for High Efficiency. *Journal of the American Chemical Society* **2015,** *137*, 4460-4468.

129. Oldenburg, K.; Vogler, A.; Miko, I.; Horvath, O., Photoredox Decomposition of Tin(II), Lead(II), Antimony(III) and Bismuth(III) Iodide Complexes in Solution. *Inorg. Chim. Acta* **1996,** *248* (1), 107-110.

130. Horvath, O.; Miko, I., Spectra,equilibrium and photoredox chemistry of tri and tetraiodoplumbate(II) complexes in acetonitrile. *Journal of Photochemistry and Photobiology A: Chemistry* **1998,** *114*, 95-101.

131. Płowaś, I.; Świergiel, J.; Jadżyn, J., Electrical Conductivity in Dimethyl Sulfoxide + Potassium Iodide Solutions at Different Concentrations and Temperatures. *J. Chem. Eng. Data* **2014,** *59*, 2360−2366.

132. Powell, D. M.; Winkler, M. T.; Choi, H. J.; Simmons, C. B.; Needleman, D. B.; Buonassisi, T., Crystalline silicon photovoltaics: a cost analysis framework for determining technology pathways to reach baseload electricity costs. *Energ Environ Sci* **2012,** *5* (3), 5874-5883.

133. Brus, L. E., Electron Electron and Electron-Hole Interactions in Small Semiconductor Crystallites - the Size Dependence of the Lowest Excited Electronic State. *J Chem Phys* **1984,** *80* (9), 4403-4409.

134. Brus, L. E., A Simple-Model for the Ionization-Potential, Electron-Affinity, and Aqueous Redox Potentials of Small Semiconductor Crystallites. *J Chem Phys* **1983,** *79* (11), 5566-5571.

135. Brus, L., Electronic Wave-Functions in Semiconductor Clusters - Experiment and Theory. *J Phys Chem-Us* **1986,** *90* (12), 2555-2560.

136. Ip, A. H.; Thon, S. M.; Hoogland, S.; Voznyy, O.; Zhitomirsky, D.; Debnath, R.; Levina, L.; Rollny, L. R.; Carey, G. H.; Fischer, A.; Kemp, K. W.; Kramer, I. J.; Ning, Z. J.; Labelle, A. J.; Chou, K. W.; Amassian, A.; Sargent, E. H., Hybrid passivated colloidal quantum dot solids. *Nat Nanotechnol* **2012,** *7* (9), 577-582.

137. Kim, G. H.; de Arquer, F. P. G.; Yoon, Y. J.; Lan, X. Z.; Liu, M. X.; Voznyy, O.; Yang, Z. Y.; Fan, F. J.; Ip, A. H.; Kanjanaboos, P.; Hoogland, S.; Kim, J. Y.; Sargent, E. H., High-Efficiency Colloidal Quantum Dot Photovoltaics via Robust Self-Assembled Mono layers. *Nano Letters* **2015,** *15* (11), 7691-7696.

138. Debnath, R.; Greiner, M. T.; Kramer, I. J.; Fischer, A.; Tang, J. A.; Barkhouse, D. A. R.; Wang, X. H.; Levina, L.; Lu, Z. H.; Sargent, E. H., Depleted-heterojunction

colloidal quantum dot photovoltaics employing low-cost electrical contacts. *Appl Phys Lett* **2010,** *97* (2).

139. Yoon, W.; Boercker, J. E.; Lumb, M. P.; Placencia, D.; Foos, E. E.; Tischler, J. G., Enhanced Open-Circuit Voltage of PbS Nanocrystal Quantum Dot Solar Cells. *Sci Rep-Uk* **2013,** *3*.

140. Geyer, S.; Porter, V. J.; Halpert, J. E.; Mentzel, T. S.; Kastner, M. A.; Bawendi, M. G., Charge transport in mixed CdSe and CdTe colloidal nanocrystal films. *Phys Rev B* **2010,** *82* (15).

141. Mentzel, T. S.; Porter, V. J.; Geyer, S.; MacLean, K.; Bawendi, M. G.; Kastner, M. A., Charge transport in PbSe nanocrystal arrays. *Phys Rev B* **2008,** *77* (7).

142. Guyot-Sionnest, P., Electrical Transport in Colloidal Quantum Dot Films. *J Phys Chem Lett* **2012,** *3* (9), 1169-1175.

143. Wehrenberg, B. L.; Yu, D.; Ma, J. S.; Guyot-Sionnest, P., Conduction in charged PbSe nanocrystal films. *J Phys Chem B* **2005,** *109* (43), 20192-20199.

144. Yang, J.; Hyun, B.-R.; Basile, A. J.; Wise, F. W., Exciton Relaxation in PbSe Nanorods. *ACS Nano* **2012,** *6*, 8120-8127.

145. Guyot-Sionnest, P.; Wehrenberg, B.; Yu, D., Intraband Relaxation in CdSe Nanocrystals and the Strong Influence of the surface ligands. *J. Chem. Phys.* **2005,** *123*, 074709(7).

146. Schaller, R. D.; Pietryga, J. M.; Goupalov, S. V.; Petruska, M. A.; Ivanov, S.; Klimov, V. I., Breaking the Phonon Bottleneck in Semiconductor Nanocrystals via Multiphonon Emission Induced by Intrinsic Nonadiabatic Interactions. *Phys. Rev. Lett.* **2005,** *95*, 196401(4).

147. Gao, Y.; Talgorn, E.; Aerts, M.; Trinh, M. T.; Schins, J. M.; Houtepen, A. J.; Siebbeles, L. D. A., Enhanced Hot-Carrier Cooling and Ultrafast Spectral Diffusion in Strongly Coupled PbSe Quantum-Dot Solids. *Nano Lett.* **2011,** *11*, 5471-5476.

148. Miaja-Avila, L.; Tritsch, J. R.; Wolcott, A.; Chan, W.-L.; Nelson, C. A.; Zhu, X.-Y., Direct Mapping of Hot-Electron Relaxation and Multiplication Dynamics in PbSe Quantum Dots. *Nano Lett.* **2012,** *12*, 1588-1591.

149. Miller, E. M.; Kroupa, D. M.; Zhang, J. B.; Schulz, P.; Marshall, A. R.; Kahn, A.; Lany, S.; Luther, J. M.; Beard, M. C.; Perkins, C. L.; van de Lagemaat, J., Revisiting the Valence and Conduction Band Size Dependence of PbS Quantum Dot Thin Films. *Acs Nano* **2016,** *10* (3), 3302-3311.

150. Tang, J.; Brzozowski, L.; Barkhouse, D. A. R.; Wang, X.; Debnath, R.; Wolowiec, R.; Palmiano, E.; Levina, L.; Pattantyus-Abraham, A. G.; Jamakosmanovic, D.; Sargent, E. H., Quantum Dot Photovoltaics in the Extreme Quantum Confinement Regime: The Surface-Chemical Origins of Exceptional Air- and Light-Stability. *ACS Nano* **2010,** *4*, 869-878.

151. Pattantyus-Abraham, A. G.; Kramer, I. J.; Barkhouse, A. R.; Wang, X.; Konstantatos, G.; Debnath, R.; Levina, L.; Nazeeruddin, M. K.; Gratzel, M.; Sargent, E. H., Depleted-Heterojunction Colloidal Quantum Dot Solar Cells. *ACS Nano* **2010,** *4*, 3374-3380.

152. Tang, J.; Kemp, K.; Hoogland, S.; Jeong, K. S.; Liu, H.; Levina, L.; Furukawa, M.; Wang, X.; Debnath, R.; Cha, D.; Chou, K. W.; Fischer, A.; Amassian, A.; Asbury, J. B.; Sargent, E. H., Colloidal Quantum Dot Photovoltaics Using Atomic Ligand Passivation. *Nature Materials* **2011,** *10*, 765-771.

153. Ip, A. H.; Thon, S. M.; Hoogland, S.; Voznyy, O.; Zhitomirsky, D.; Debnath, R.; levina, L.; Rollny, L. R.; Carey, G. H.; Fischer, A.; Kemp, K. W.; Kramer, I. J.; Ning, Z.; Labelle, A. J.; Chou, K. W.; Amassian, A.; Sargent, E. H., Hybrid Passivated Colloidal Quantum Dot Solids. *Nature Nanotech.* **2012,** *7*, 577-582.

154. Pandey, A.; Guyot-Sionnest, P., Intraband spectroscopy and band offsets of colloidal II-VI core/shell structures. *J Chem Phys* **2007,** *127* (10).

155. Wehrenberg, B. L.; Wang, C. J.; Guyot-Sionnest, P., Interband and intraband optical studies of PbSe colloidal quantum dots. *J Phys Chem B* **2002,** *106* (41), 10634-10640.

156. Shim, M.; Shilov, S. V.; Braiman, M. S.; Guyot-Sionnest, P., Long-lived delocalized electron states in quantum dots: A step-scan Fourier transform infrared study. *J Phys Chem B* **2000,** *104* (7), 1494-1496.

157. Trinh, M. T.; Houtepen, A. J.; Schins, J. M.; Piris, J.; Siebbeles, L. D. A., Nature of the second optical transition in PbSe nanocrystals. *Nano Letters* **2008,** *8* (7), 2112-2117.

158. Du, H.; Chen, C. L.; Krishnan, R.; Krauss, T. D.; Harbold, J. M.; Wise, F. W.; Thomas, M. G.; Silcox, J., Optical properties of colloidal PbSe nanocrystals. *Nano Letters* **2002,** *2* (11), 1321-1324.

159. Kang, I.; Wise, F. W., Electronic structure and optical properties of PbS and PbSe quantum dots. *J Opt Soc Am B* **1997,** *14* (7), 1632-1646.

160. Norris, D. J., Electronic Structure in Semiconductor Nanocrystals: Optical Experiment. *Nanocrystal Quantum Dots, Second Edition* **2010**, 63-96.

161. Wolfenden, R.; Snider, M. J., The depth of chemical time and the power of enzymes as catalysts. *Accounts Chem Res* **2001,** *34* (12), 938-945.

162. Henzler-Wildman, K.; Kern, D., Dynamic personalities of proteins. *Nature* **2007,** *450* (7172), 964-972.

163. Hammes, G. G.; Benkovic, S. J.; Hammes-Schiffer, S., Flexibility, Diversity, and Cooperativity: Pillars of Enzyme Catalysis. *Biochemistry-Us* **2011,** *50* (48), 10422-10430.

164. Nagel, Z. D.; Klinman, J. P., A 21(st) century revisionist's view at a turning point in enzymology. *Nat Chem Biol* **2009,** *5* (8), 543-550.

165. Peng, J. W., Communication Breakdown: Protein Dynamics and Drug Design. *Structure* **2009,** *17* (3), 319-320.

166. Lee, G. M.; Craik, C. S., Trapping Moving Targets with Small Molecules. *Science* **2009,** *324* (5924), 213-215.

167. Schwartz, S. D.; Schramm, V. L., Enzymatic transition states and dynamic motion in barrier crossing. *Nat Chem Biol* **2009,** *5* (8), 552-559.

168. Russell, H. J.; Jones, A. R.; Hay, S.; Greetham, G. M.; Towrie, M.; Scrutton, N. S., Protein Motions Are Coupled to the Reaction Chemistry in Coenzyme B12-Dependent Ethanolamine Ammonia Lyase. *Angew Chem Int Edit* **2012,** *51* (37), 9306-9310.

169. Bhabha, G.; Lee, J.; Ekiert, D. C.; Gam, J.; Wilson, I. A.; Dyson, H. J.; Benkovic, S. J.; Wright, P. E., A Dynamic Knockout Reveals That Conformational Fluctuations Influence the Chemical Step of Enzyme Catalysis. *Science* **2011,** *332* (6026), 234-238.

170. Nunez, S.; Antoniou, D.; Schramm, V. L.; Schwartz, S. D., Promoting vibrations in human purine nucleoside phosphorylase. A molecular dynamics and hybrid quantum mechanical/molecular mechanical study. *J Am Chem Soc* **2004,** *126* (48), 15720-15729.

171. Bandaria, J. N.; Dutta, S.; Nydegger, M. W.; Rock, W.; Kohen, A.; Cheatum, C. M., Characterizing the dynamics of functionally relevant complexes of formate dehydrogenase. *P Natl Acad Sci USA* **2010,** *107* (42), 17974-17979.

172. Peters, B., Transition-State Theory, Dynamics, and Narrow Time Scale Separation in the Rate-Promoting Vibrations Model of Enzyme Catalysis. *J Chem Theory Comput* **2010,** *6* (5), 1447-1454.

173. Kamerlin, S. C. L.; Warshel, A., At the dawn of the 21st century: Is dynamics the missing link for understanding enzyme catalysis? *Proteins* **2010,** *78* (6), 1339-1375.

174. Kosugi, T.; Hayashi, S., Crucial Role of Protein Flexibility in Formation of a Stable Reaction Transition State in an alpha-Amylase Catalysis. *J Am Chem Soc* **2012,** *134* (16), 7045-7055.

175. Doshi, U.; McGowan, L. C.; Ladani, S. T.; Hamelberg, D., Resolving the complex role of enzyme conformational dynamics in catalytic function. *P Natl Acad Sci USA* **2012,** *109* (15), 5699-5704.

176. Suydam, I. T.; Snow, C. D.; Pande, V. S.; Boxer, S. G., Electric fields at the active site of an enzyme: Direct comparison of experiment with theory. *Science* **2006,** *313* (5784), 200-204.

177. Hammes-Schiffer, S.; Benkovic, S. J., Relating protein motion to catalysis. *Annu Rev Biochem* **2006,** *75*, 519-541.

178. Henzler-Wildman, K. A.; Thai, V.; Lei, M.; Ott, M.; Wolf-Watz, M.; Fenn, T.; Pozharski, E.; Wilson, M. A.; Petsko, G. A.; Karplus, M.; Hubner, C. G.; Kern, D., Intrinsic motions along an enzymatic reaction trajectory. *Nature* **2007,** *450* (7171), 838-U13.

179. Boehr, D. D.; McElheny, D.; Dyson, H. J.; Wright, P. E., The dynamic energy landscape of dihydrofolate reductase catalysis. *Science* **2006,** *313* (5793), 1638-1642.

180. Garcia-Meseguer, R.; Marti, S.; Ruiz-Pernia, J. J.; Moliner, V.; Tunon, I., Studying the role of protein dynamics in an S(N)2 enzyme reaction using free-energy surfaces and solvent coordinates. *Nat Chem* **2013,** *5* (7), 566-571.

181. Warshel, A.; Sharma, P. K.; Kato, M.; Xiang, Y.; Liu, H. B.; Olsson, M. H. M., Electrostatic basis for enzyme catalysis. *Chem Rev* **2006,** *106* (8), 3210-3235.

182. Benkovic, S. J.; Hammes, G. G.; Hammes-Schiffer, S., Free-energy landscape of enzyme catalysis. *Biochemistry-Us* **2008,** *47* (11), 3317-3321.

183. Liu, C. T.; Hanoian, P.; French, J. B.; Pringle, T. H.; Hammes-Schiffer, S.; Benkovic, S. J., Functional significance of evolving protein sequence in dihydrofolate reductase from bacteria to humans. *P Natl Acad Sci USA* **2013,** *110* (25), 10159-10164.

184. Sawaya, M. R.; Kraut, J., Loop and subdomain movements in the mechanism of Escherichia coli dihydrofolate reductase: Crystallographic evidence. *Biochemistry-Us* **1997,** *36* (3), 586-603.

185. Antikainen, N. M.; Smiley, R. D.; Benkovic, S. J.; Hammes, G. G., Conformation coupled enzyme catalysis: Single-molecule and transient kinetics investigation of dihydrofolate reductase. *Biochemistry-Us* **2005,** *44* (51), 16835-16843.

186. Wong, K. F.; Selzer, T.; Benkovic, S. J.; Hammes-Schiffer, S., Impact of distal mutations on the network of coupled motions correlated to hydride transfer in dihydrofolate reductase. *P Natl Acad Sci USA* **2005,** *102* (19), 6807-6812.

187. Waegele, M. M.; Culik, R. M.; Gai, F., Site-Specific Spectroscopic Reporters of the Local Electric Field, Hydration, Structure, and Dynamics of Biomolecules. *J Phys Chem Lett* **2011,** *2* (20), 2598-2609.

188. Weitman, H.; Roslaniec, M.; Frimer, A. A.; Afri, M.; Freeman, D.; Mazur, Y.; Ehrenberg, B., Solvatochromic effects in the electronic absorption and nuclear magnetic resonance spectra of hypericin in organic solvents and in lipid bilayers. *Photochem Photobiol* **2001,** *73* (2), 110-118.

189. Taft, R. W.; Kamlet, M. J., Linear Solvation Energy Relationships .8. Solvent Effects on Nmr Spectral Shifts and Coupling-Constants. *Org Magn Resonance* **1980,** *14* (6), 485-493.

190. Getahun, Z.; Huang, C. Y.; Wang, T.; De Leon, B.; DeGrado, W. F.; Gai, F., Using nitrile-derivatized amino acids as infrared probes of local environment. *J Am Chem Soc* **2003,** *125* (2), 405-411.

191. Kim, H.; Cho, M., Infrared Probes for Studying the Structure and Dynamics of Biomolecules. *Chem Rev* **2013,** *113* (8), 5817-5847.

192. Jha, S. K.; Ji, M. B. A.; Gaffney, K. J.; Boxer, S. G., Direct measurement of the protein response to an electrostatic perturbation that mimics the catalytic cycle in ketosteroid isomerase. *P Natl Acad Sci USA* **2011,** *108* (40), 16612-16617.

193. Fafarman, A. T.; Sigala, P. A.; Schwans, J. P.; Fenn, T. D.; Herschlag, D.; Boxer, S. G., Quantitative, directional measurement of electric field heterogeneity in the active site of ketosteroid isomerase. *P Natl Acad Sci USA* **2012,** *109* (6), E299-E308.

194. Bagchi, S.; Fried, S. D.; Boxer, S. G., A Solvatochromic Model Calibrates Nitriles' Vibrational Frequencies to Electrostatic Fields. *J Am Chem Soc* **2012,** *134* (25), 10373-10376.

195. Bagchi, S.; Boxer, S. G.; Fayer, M. D., Ribonuclease S Dynamics Measured Using a Nitrile Label with 2D IR Vibrational Echo Spectroscopy. *J Phys Chem B* **2012,** *116* (13), 4034-4042.

196. Zhao, Q. J.; Abeygunawardana, C.; Mildvan, A. S., C-13 NMR relaxation studies of backbone and side chain motion of the catalytic tyrosine residue in free and steroid-bound Delta(5)-3-ketosteroid isomerase. *Biochemistry-Us* **1996,** *35* (5), 1525-1532.

197. Zhao, Q. J.; Li, Y. K.; Mildvan, A. S.; Talalay, P., Ultraviolet Spectroscopic Evidence for Decreased Motion of the Active-Site Tyrosine Residue of Delta(5)-3-Ketosteroid Isomerase by Steroid-Binding. *Biochemistry-Us* **1995,** *34* (19), 6562-6572.

198. Chakravorty, D. K.; Soudackov, A. V.; Hammes-Schiffer, S., Hybrid Quantum/Classical Molecular Dynamics Simulations of the Proton Transfer

Reactions Catalyzed by Ketosteroid Isomerase: Analysis of Hydrogen Bonding, Conformational Motions, and Electrostatics. *Biochemistry-Us* **2009,** *48* (44), 10608-10619.

199. Chakravorty, D. K.; Soudackov, A. V.; Hammes-Schiffer, S., Proton transfer reactions in ketosteroid isomerase. *Abstr Pap Am Chem S* **2009,** *238*.

200. Blakley, R. L., Crystalline Dihydropteroylglutamic Acid. *Nature* **1960,** *188* (4746), 231-232.

201. Jeong, S. S.; Gready, J. E., A Method of Preparation and Purification of (4r)-Deuterated-Reduced Nicotinamide Adenine-Dinucleotide Phosphate. *Anal Biochem* **1994,** *221* (2), 273-277.

202. Cameron, C. E.; Benkovic, S. J., Evidence for a functional role of the dynamics of glycine-121 of Escherichia coli dihydrofolate reductase obtained from kinetic analysis of a site-directed mutant. *Biochemistry-Us* **1997,** *36* (50), 15792-15800.

203. Rajagopalan, P. T. R.; Zhang, Z. Q.; McCourt, L.; Dwyer, M.; Benkovic, S. J.; Hammes, G. G., Interaction of dihydrofolate reductase with methotrexate: Ensemble and single-molecule kinetics. *P Natl Acad Sci USA* **2002,** *99* (21), 13481-13486.

204. Fafarman, A. T.; Webb, L. J.; Chuang, J. I.; Boxer, S. G., Site-specific conversion of cysteine thiols into thiocyanate creates an IR probe for electric fields in proteins. *J Am Chem Soc* **2006,** *128* (41), 13356-13357.

205. McMahon, H. A.; Alfieri, K. N.; Clark, C. A. A.; Londergan, C. H., Cyanylated Cysteine: A Covalently Attached Vibrational Probe of Protein-Lipid Contacts. *J Phys Chem Lett* **2010,** *1* (5), 850-855.

206. Fried, S. D.; Wang, L. P.; Boxer, S. G.; Ren, P. Y.; Pande, V. S., Calculations of the Electric Fields in Liquid Solutions. *J Phys Chem B* **2013,** *117* (50), 16236-16248.

207. Wortmann, R.; Bishop, D. M., Effective polarizabilities and local field corrections for nonlinear optical experiments in condensed media. *J Chem Phys* **1998,** *108* (3), 1001-1007.

208. Andrews, S. S.; Boxer, S. G., Vibrational stark effects of nitriles I. Methods and experimental results. *J Phys Chem A* **2000,** *104* (51), 11853-11863.

209. Ren, P. Y.; Ponder, J. W., Polarizable atomic multipole water model for molecular mechanics simulation. *J Phys Chem B* **2003,** *107* (24), 5933-5947.

210. Lamoureux, G.; Harder, E.; Vorobyov, I. V.; Roux, B.; MacKerell, A. D., A polarizable model of water for molecular dynamics simulations of biomolecules. *Chem Phys Lett* **2006,** *418* (1-3), 245-249.

211. Fierke, C. A.; Johnson, K. A.; Benkovic, S. J., Construction and Evaluation of the Kinetic Scheme Associated with Dihydrofolate-Reductase from Escherichia-Coli. *Biochemistry-Us* **1987,** *26* (13), 4085-4092.

212. Weikl, T. R.; Boehr, D. D., Conformational selection and induced changes along the catalytic cycle of Escherichia coli dihydrofolate reductase. *Proteins* **2012,** *80* (10), 2369-2383.

213. Osborne, M. J.; Schnell, J.; Benkovic, S. J.; Dyson, H. J.; Wright, P. E., Backbone dynamics in dihydrofolate reductase complexes: Role of loop flexibility in the catalytic mechanism. *Biochemistry-Us* **2001,** *40* (33), 9846-9859.

214. Layfield, J. P.; Hammes-Schiffer, S., Calculation of Vibrational Shifts of Nitrile Probes in the Active Site of Ketosteroid Isomerase upon Ligand Binding. *J Am Chem Soc* **2013,** *135* (2), 717-725.

215. Waegele, M. M.; Gai, F., Computational Modeling of the Nitrile Stretching Vibration of 5-Cyanoindole in Water. *J Phys Chem Lett* **2010,** *1* (4), 781-786.

216. Agarwal, P. K.; Billeter, S. R.; Rajagopalan, P. T. R.; Benkovic, S. J.; Hammes-Schiffer, S., Network of coupled promoting motions in enzyme catalysis. *P Natl Acad Sci USA* **2002,** *99* (5), 2794-2799.

217. Lee, M. M.; Teuscher, J.; Miyasaka, T.; Murakami, T. N.; Snaith, H. J., Efficient Hybrid Solar Cells Based on Meso-Superstructured Organometal Halide Perovskites. *Science* **2012,** *338* (6107), 643-647.

218. Jacoby, M., Commercializing low-cost solar cells. *Chem Eng News* **2016,** *94* (18), 30-34.

219. Christians, J. A.; Herrera, P. A. M.; Kamat, P. V., Transformation of the Excited State and Photovoltaic Efficiency of CH3NH3PbI3 Perovskite upon Controlled Exposure to Humidified Air. *J Am Chem Soc* **2015,** *137* (4), 1530-1538.

220. Peng, X. G.; Schlamp, M. C.; Kadavanich, A. V.; Alivisatos, A. P., Epitaxial growth of highly luminescent CdSe/CdS core/shell nanocrystals with photostability and electronic accessibility. *J Am Chem Soc* **1997,** *119* (30), 7019-7029.

221. Efros, A. L.; Rosen, M., Random telegraph signal in the photoluminescence intensity of a single quantum dot. *Phys Rev Lett* **1997,** *78* (6), 1110-1113.

VITA

Robert J. Stewart graduated Cum Laude from Canisius College (Buffalo, NY) with a bachelor's degree in chemistry and a minor in physics. Under the guidance of Professor Timothy Gregg, he carried out research in homogenous catalysis, specifically, investigating the mechanism of cyclopropanation of substitutes allenes mediated by chiral rhodium catalysts. In the summer of 2011, Robert joined the Asbury Lab at Penn State University. With Professor John Asbury, his research focused on the spectroscopic and photophysical investigation of solution-processed semiconductors to enable the integration of these materials into emerging opto-electronic devices. His work led to one of the first reports demonstrating that charge recombination centers in organo-halide perovskite films are primarily located at the boundaries of crystallites, and post-processing, chemical treatments can be used to modify crystal surfaces to significantly improve charge carrier lifetimes and the long-term stability of nanocrystalline perovskite films. While at Penn State, Robert had the opportunity to present posters and seminars at several professional conferences including: The National Meeting of SPIE Optics + Photonics (2014, San Diego) and the 250th ACS National Meeting and Exposition (2015, Boston) where he won the Division of Physical Chemistry Student Seminar Honorarium. This dissertation serves to complete his work as a doctoral candidate at Penn State University.